Title

New Insights into Foraminiferal Carbonate Clumped Isotope Geochemistry

Author

Tandy, Hannah

Publication Date

2025

UNIVERSITY OF CALIFORNIA

Los Angeles

New Insights into Foraminiferal Carbonate Clumped Isotope Geochemistry

A dissertation submitted in partial satisfaction of the requirements for the degree Doctor of Philosophy in Geochemistry

by

Hannah Tylee Tandy

2025

ABSTRACT OF THE DISSERTATION

New Insights into Foraminiferal Carbonate

Clumped Isotope Geochemistry

by

Hannah Tylee Tandy

Doctor of Philosophy in Geochemistry

University of California, Los Angeles, 2025

Professor Aradhna K. Tripati, Chair

Temperature reconstructions of past oceanic conditions and climates are vital to our understanding of the earth system and climate feedbacks. Foraminiferal tests are one of the most widely used archives of past climate. Several studies have previously reported that the clumped isotope composition (Δ_{47}) of core-top foraminifera record seawater temperatures, and this proxy is increasingly being applied to foraminifera in order to reconstruct Cenozoic ocean temperatures. In this thesis, I examine multiple aspects of foraminiferal clumped isotope thermometry that are less well constrained and in my last two chapters I apply this proxy to early Cenozoic samples for temperature reconstructions in a hothouse climate.

The first chapter presents an investigation of thermal and non-thermal effects on core-top foraminifera in a dataset composed of 260 samples that includes both new data and a meta-analysis of published data. It shows that Δ_{47}-temperature regressions through a composite foraminiferal dataset, mixed layer planktics, epifaunal benthics, and infaunal benthics are

indistinguishable from inorganic calcite. It also reports possible effects of bottom water carbonate saturation on both planktic and benthic foraminifera. Benthic carbonate ion effects are investigated in detail and a multivariate regression relating Δ_{47} to temperature and $\Delta[CO_3^{2-}]$ reported. We apply the calculated regressions to published Δ_{47} data for the Cenozoic to discuss impacts to interpretations and show these can yield reasonable temperature and seawater $\delta^{18}O$ estimates for key intervals that had previously been controversial if carbonate ion effects on benthic foraminifera are considered.

The second chapter is an investigation of the potential impacts of dissolution on foraminiferal Δ_{47}. We report data for multiple species from a core-top transect at the Ontong Java Plateau and from dissolution impacts. It shows evidence that in some species, dissolution elevates Δ_{47}, and biases Δ_{47}-temperatures to colder values. Specifically**,** in three species surveyed from core-tops, Δ_{47} values increase by ~0.01 ‰ below the carbonate saturation horizon. In dissolution experiments, some species show evidence for an increase in Δ_{47} with mass loss, while no change was resolved in others. Multiple mechanisms for dissolution impacts on Δ_{47} and correction methods are explored.

The third chapter applies clumped isotope paleothermometry to constrain temperatures across the Paleocene-Eocene Thermal Maximum (PETM), a hyperthermal event characterized by an injection of isotopically light carbon into the atmosphere at Site 1263 on Walvis Ridge in the South Atlantic. This site has higher clay contents and lower porosity, making recrystallization impacts minimal (~10%), including in the clay layer. We report planktic foraminiferal and fine fraction isotopic data and derive sea surface temperature (SST) and seawater composition estimates and compare this record to published proxy-based temperature estimates and climate model predictions. Clumped isotope data show evidence for Late Paleocene SST of ~18.8 ˚C and a minimum warming of 3-4 ˚C. When dissolution and recrystallization impacts on Δ_{47} are

considered, a baseline SST of ~20.5 ˚C and a warming of ~7 ˚C are calculated, which supports a change in temperature that is larger than most published estimates. Other non-thermal impacts on the reconstruction are estimated to be minimal. Discrepancies with other carbonate-based proxies can be mostly reconciled if seawater chemistry is considered, including pH effects on carbonate $\delta^{18}O$ and Mg/Ca, and changes in seawater $\delta^{18}O$ and Mg/Ca. The results are broadly consistent with climate model simulations for 3X and 6X CO_2 that are part of DeepMIP.

Chapter 4 investigates clumped isotope changes across the PETM but over a suite of global oceanic sites. Non-thermal influences, especially recrystallization and dissolution, contribute variably to each site, and this chapter systematically explores the possible impacts of each of these factors to the interpretation of clumped isotope temperature estimates, and comparisons with other proxy reconstructions and model temperatures. In particular, at high-latitude Site 690, in the Southern Ocean, Δ_{47} data from fine fraction records Late Paleocene SST of 13.4 ˚C and a PETM warming of ~1.2 ˚C; if a recrystallization correction of up to 10% and other non-thermal effects are considered, then Late Paleocene SSTs increase to 15.3 ˚C with a PETM warming of ~5.3 ˚C. At Site 1263, first reported in chapter 3, the data support late Paleocene temperatures of 18.8 °C and a PETM warming of ~4 ˚C. If 10 % recrystallization and other non-thermal corrections are factored in, then late Paleocene SSTs of 18.8 ˚C and a PETM anomaly of ~7 ˚C is estimated, largely due to the impact of dissolution on peak PETM samples. For low-latitude Site 1209, late Paleocene temperatures are estimated at 20.8 ˚C. These values are relatively cold and implausible for a hothouse world. If 10% recrystallization impacted samples, SSTs increase to 23.5 ˚C, and if 25% recrystallization and other effects are considered, then more plausible tropical SSTs of 25.4 ˚C are estimated. The PETM temperature anomaly at this site increases from 1.7 ˚C to 4.2 ˚C following corrections for dissolution effects. In the North Atlantic, at mid-latitude Site 1409, Late Paleocene SSTs of 19.9 ˚C are estimated, with values

increasing to 21.6 ˚C assuming 10 % recrystallization and other non-thermal corrections. Lastly, in the Equatorial Pacific Site 865, late Paleocene temperatures are estimated as 24.0 ˚C and increase to 27.0 ˚C if 25% recrystallization is assumed, and 32.6 ˚C if 50 % recrystallization is assumed. These reconstructions are used to evaluate equator-to-pole temperature and seawater $\delta^{18}O$ gradients, and climate sensitivities to forcing, and could be used for model parameterization.

The dissertation of Hannah Tylee Tandy is approved.

Tina Irene Treude

Robert Alfred Eagle

Abby Kavner

Aradhna K. Tripati, Committee Chair

University of California, Los Angeles

2025

DEDICATION

I dedicate this thesis to my friends and family who supported me through the trials of my dissertation, as well as a global pandemic. I would not have stayed sane without you all <3.

TABLE OF CONTENTS

FIGURES

CHAPTER 1

TABLES

ACKNOWLEDGEMENTS

I thank B. Elliot for help with machine running and training. H. Taylor, K. Miguel, and J. Rubi thank you for being great lab assistants and helping with samples and machine running. I would also like to acknowledge all the undergraduates and high school students who I worked with over the years on sample preparation. F. Swain, D. Ramirez, S Chung, S. Zheng, M Tharpe, S. Nguyen, T. Khan, L. Archuleta, N. Rodkin, B. Amato, S. Gwak, A. Beck, G. Toranzo, C. Martinez, L. Avila, L. Savage and C. Ulloa thank you all so much for all your hard work! I thank H. Carroll for teaching me statistics and R and her support over the years. M. Guillermic thank you for editing help and teaching me foraminiferal processing. R. Flores thank you for being a sounding board for my thoughts on projects and for all the lab assistance. L. Martin-Silverstone assisted with CT scanning at the University of Bristol. I thank J. Zachos and others for sharing samples. I acknowledge all my co-authors on these projects and especially A. Subhas and D. Schmidt for their assistance in the dissolution project development and interpretation, and my committee members for their support. Finally, I'd like to thank my advisor A. Tripati for providing me with this opportunity. This work was funded with support by the Schlanger IODP Fellowship as well as The Center for Diverse Leadership in Science which is supported by the Packard Foundation, Sloan Foundation, Silicon Valley Community Foundation, the Waverley Street Foundation, and NSF (RISE-228198). This work was also funded by Heising-Simons Foundation grant 2022-3314, DOE BES grant DE-FG02-83613ER16402, and NSF grants EAR-0949191, EAR-1352212, and RISE-228198 to A. Tripati and RISE-2024426 to R. Eagle.

VITA

EDUCATION AND CERTIFICATIONS

University of California, Los Angeles (UCLA)

- Doctor of Philosophy in Geochemistry Exp. 2025
- Master of Science in Geochemistry 2022

Princeton University

- Bachelor of Arts Geosciences, High Honors 2018

PUBLICATIONS

Submitted

Aradhna Tripati*, **Hannah Tandy***, Alexandra Villa*, Randon J. Flores, Alexandrea Arnold, Hannah Carroll, Maxence Guillermic, Ingrid Maradiaga, Cristian Blair, Bisrat Zerehaimanot, Dana Brown, Robert Ulrich, Cristian-Roman Palacios, Mohan Kuppusamy, Raquel Bryant, Jules de La Cruz, Fengming Chang, Robert A. Eagle, Ceara Tomaiso, A. Nele Meckler, Thomas M. Marchitto, Rosemarie E. Came, Jean Lynch-Stieglitz. (submitted) Clumped isotope thermometry in foraminifera as a tool in paleoceanography: New planktonic and benthic data and constraints on non-thermal effects, *Paleoceanography and Paleoclimatology*
*Joint-first author

Hannah Tandy, Randon J. Flores, Adam V. Subhas, Daniela N. Schmidt, Khushboo Tanya Khan, Soyoun Gwak, Lina Savage, Robert A. Eagle, Aradhna Tripati. (submitted) Dissolution effects on clumped isotope signatures in foraminifera, *Paleoceanography and Paleoclimatology*

In preparation

Hannah Tandy, Maxence Guillermic, Maria Tharpe, Sydney Zheng, Gabriela Toranzo, Sydney Nguyen, Lorna Avila, Cynthia Ulloa, Robert Eagle, James Zachos, Clay Kelly, Aradhna Tripati. (In preparation) Paleocene-Eocene Thermal Maximum Subtropical Atlantic Ocean Warming and Hydrology Constrained by Clumped Isotopes, *PNAS*

Hannah Tandy, Alberto Perez-Huerta, Richard Kozdon, Annabella Amato, Diasy Ramirez, Sarah Chung, Forrest Swain, Lyndsey Archuleta, Natasha Rodkin, Adam Beck, Gwyneth Stolo, Tyler Vollmer, J. Voon, G. Jesmok, Robert Eagle, Clay Kelly, Timothy Bralower, James Zachos, Aradhna Tripati. (In preparation), Planktic Foraminifera and Coccolithophore-Based Estimates of Clumped Isotope Temperature During the Late Paleocene to Early Eocene, *Paleoceanography and Paleoclimatology*

Mohan Kuppusamy*, Dharmendra Singh*, Aradhna Tripati*, Maxence Guillermic*, Daniel Gebregiorgis, **Hannah Tandy**, Alexandrea Villa, Kirellos Sefein, Gabriela Toranzo, Cameron

Brown, Dana Brown, Simon Crowhurst. (In preparation) Deep Pacific Ocean Temperatures and Cryospheric Evolution at the Eocene-Oligocene Transition from Clumped Isotopes, *Science Advances*

Maxence Guillermic, **Hannah Tandy**, Cristian Hyde, Mohan Kuppusamy, Sydney Nguyen, Aradhna Tripati. (In preparation) Miocene to Recent Water Temperature Profiles of the Equatorial Pacific using Clumped Isotopes. *Paleoceanography and Paleoclimatology*

Nirmal B, Weiyu Chen, Gwyneth Stolo, Shawronna Sengupta, Maxence Guillermic, **Hannah Tandy**, Cristian Hyde, Sruthy Rose Baby Yeizal, Shitha Premaraj, Mohan Kuppusamy, Aradhna Tripati. (In preparation) Miocene to Recent Ocean Temperatures in the South Atlantic. *Paleoceanography and Paleoclimatology*

Daniel Sepulveda, **Hannah Tandy**, Randy Flores, Abel Aragon, C. Martinez, Aradhna Tripati. (In preparation) Paleoclimatology and Paleoenvironment of Seymour Island, Antarctic Peninsula, from the Late Cretaceous to the Eocene using Stable Isotope Geochemistry and Clumped isotopes on Bivalve Fossils. *Paloceanography and Paleoclimatology*

HONORS AND AWARDS

Center for Diverse Leadership in Science Fellow, UCLA 2019 - Present

Constantine and Perina Panunzio Citizenship Award, UCLA 2023

Schlanger International Ocean Drilling Program (IODP) Fellow, 2021 - 2022

The Bearded Lady Project: Currano Scholarship Student Research Award, Paleontological Society 2021

GSA Graduate Student Research Grant Awardee, GSA 2021

Regent's Fellowship, UCLA 2019 - 2020

Graduate Dean Scholarship, UCLA 2019 - 2020

INTRODUCTION

Accurate constraints on past ocean temperatures are critical to understanding ocean-climate interactions and Earth's climate history. A temperature proxy that has emerged as a potentially transformative tool in the geosciences is carbonate clumped isotope thermometry, which is based on the abundance of ^{13}C-^{18}O bonds in carbonate minerals (Eiler, 2007; Ghosh et al., 2006; Schauble et al., 2006). Carbonate "clumped" isotope geochemistry examines the proportion of heavy isotopes that are bound to each other forming heavy isotope "pairs" or clumps, for example, the multiply-substituted isotopologue $^{13}C^{18}O^{16}O$. Due to zero point energy differences, molecules with heavy isotope clumps have distinct physical and chemical properties from those without, enabling their use as tracers of equilibrium and kinetic processes.

A key aspect of clumped isotope thermometry is that in principle, it is based solely on thermodynamics. Clumped isotope thermometry relies on internal isotopic exchange between isotopes in a single phase. This means that, in theory, all that is needed to determine mineral formation temperatures is the clumped isotope composition of the solid, and not the water from which it grew.

An initial study of clumped isotopes in planktonic and benthic foraminifera and coccoliths was published four years after the geothermometer was developed (Tripati et al., 2010). This study found no evidence for differences between synthetic calcite and foraminifera calibrations, nor between cultured coccolithophores and inorganic calcite, and did not find discernible taxon-specific fractionations (Tripati et al., 2010). Since then, multiple paleoceanographic reconstructions have been published (e.g. Agterhuis et al., 2022; Evans et al., 2018; Leutert et al., 2020, 2019; Meckler et al., 2022; Tripati et al., 2014).

The existing body of work illustrates the power of clumped isotope thermometry when applied to foraminifera; however, proxy use in paleoceanography over the past decade has been

limited due to major challenges in applying this proxy to foraminifera. One major issue has been large sample sizes, with 3-8 mg $CaCO_3$ used to perform a single replicate analysis (Ghosh et al., 2006; Tripati et al., 2010). Another issue relates to interlaboratory offsets (see Bernasconi et al., 2021, 2018; Dennis et al., 2011; Petersen et al., 2019; Tang et al., 2014 for discussion).

In this dissertation, we built on recent developments in the field to lay the foundation for more widespread use of clumped isotope thermometry in foraminiferal archives as a tool in paleoceanography and applied clumped isotopes to a study of sea surface temperatures in the early Cenozoic. In Chapter 1, we reported Δ_{47} data for 124 new samples and reprocessed data from 136 published samples. This facilitated a meta-analysis of clumped isotope data for 260 core-top planktic and benthic foraminiferal samples from several major ocean basins to assess if there was evidence for ecological, taxonomic, regional, or depth-dependent isotope effects. We derived calibrations with significant data representation for both planktic and benthic foraminifera - where previously relatively little benthic data has been published - and compared results to synthetic calcite. In Chapter 2, we investigated dissolution effects on the clumped isotope paleothermometer in foraminifera through in-situ ocean sediments of a depth transect in the Ontong Java Plateau. We found evidence for increased Δ_{47} values with dissolution in three of the six species included in the study (*G. siphonifera, P. obliquiloculata*, and *G. tumida*). In Chapter 3, we applied our findings from the previous chapters to clay-rich sediments from Site 1263 located on Walvis Ridge and developed a time series across the Paleocene-Eocene Thermal Maximum (PETM) for temperatures. We found evidence for sea surface temperatures warming in the region by ~7 °C over the PETM, from a baseline of ~20 °C, more than previously estimated, and the impact of different assumptions on carbonate-based proxies and proxy-model agreement is discussed. In Chapter 4, we further investigate late Paleocene through early Eocene temperatures using clumped isotopes at five sediment cores with variable amounts of

recrystallization and explore how clumped isotope temperature reconstructions compare to other proxy-derived temperatures and model simulations for the early Cenozoic.

REFERENCES

Agterhuis, T., Ziegler, M., de Winter, N. J., & Lourens, L. J. (2022). Warm deep-sea temperatures across Eocene Thermal Maximum 2 from clumped isotope thermometry. *Communications Earth & Environment*, *3*(1), 1–9. https://doi.org/10.1038/s43247-022-00350-8

Bernasconi, S. M., Müller, I. A., Bergmann, K. D., Breitenbach, S. F. M., Fernandez, A., Hodell, D. A., et al. (2018). Reducing Uncertainties in Carbonate Clumped Isotope Analysis Through Consistent Carbonate-Based Standardization. *Geochemistry, Geophysics, Geosystems*, *19*(9), 2895–2914. https://doi.org/10.1029/2017GC007385

Bernasconi, S. M., Daëron, M., Bergmann, K. D., Bonifacie, M., Meckler, A. N., Affek, H. P., et al. (2021). InterCarb: A Community Effort to Improve Interlaboratory Standardization of the Carbonate Clumped Isotope Thermometer Using Carbonate Standards. *Geochemistry, Geophysics, Geosystems*, *22*(5), e2020GC009588. https://doi.org/10.1029/2020GC009588

Dennis, K. J., Affek, H. P., Passey, B. H., Schrag, D. P., & Eiler, J. M. (2011). Defining an absolute reference frame for 'clumped' isotope studies of CO2. *Geochimica et Cosmochimica Acta*, *75*(22), 7117–7131. https://doi.org/10.1016/j.gca.2011.09.025

Eiler, J. M. (2007). "Clumped-isotope" geochemistry—The study of naturally-occurring, multiply-substituted isotopologues. *Earth and Planetary Science Letters*, *262*(3–4), 309–327. https://doi.org/10.1016/j.epsl.2007.08.020

Evans, D., Sagoo, N., Renema, W., Cotton, L. J., Müller, W., Todd, J. A., et al. (2018). Eocene greenhouse climate revealed by coupled clumped isotope-Mg/Ca thermometry. *Proceedings of the National Academy of Sciences*, *115*(6), 1174–1179. https://doi.org/10.1073/pnas.1714744115

Ghosh, P., Adkins, J., Affek, H., Balta, B., Guo, W., Schauble, E. A., et al. (2006). 13C–18O bonds in carbonate minerals: A new kind of paleothermometer. *Geochimica et Cosmochimica Acta*, *70*(6), 1439–1456. https://doi.org/10.1016/j.gca.2005.11.014

Leutert, T. J., Auderset, A., Martínez-García, A., Modestou, S., & Meckler, A. N. (2020). Coupled Southern Ocean cooling and Antarctic ice sheet expansion during the middle Miocene. *Nature Geoscience*, *13*(9), 634–639. https://doi.org/10.1038/s41561-020-0623-0

Meckler, A. N., Sexton, P. F., Piasecki, A. M., Leutert, T. J., Marquardt, J., Ziegler, M., et al. (2022). Cenozoic evolution of deep ocean temperature from clumped isotope thermometry. *Science*, *377*(6601), 86–90. https://doi.org/10.1126/science.abk0604

Petersen, S. V., Defliese, W. F., Saenger, C., Daëron, M., Huntington, K. W., John, C. M., et al. (2019). Effects of Improved 17O Correction on Interlaboratory Agreement in Clumped Isotope Calibrations, Estimates of Mineral-Specific Offsets, and Temperature Dependence of Acid Digestion Fractionation. *Geochemistry, Geophysics, Geosystems*, *20*(7), 3495–3519. https://doi.org/10.1029/2018GC008127

Schauble, E. A., Ghosh, P., & Eiler, J. M. (2006). Preferential formation of 13C–18O bonds in carbonate minerals, estimated using first-principles lattice dynamics. *Geochimica et Cosmochimica Acta*, *70*(10), 2510–2529. https://doi.org/10.1016/j.gca.2006.02.011

Tang, J., Dietzel, M., Fernandez, A., Tripati, A. K., & Rosenheim, B. E. (2014). Evaluation of kinetic effects on clumped isotope fractionation (Δ47) during inorganic calcite

precipitation. *Geochimica et Cosmochimica Acta*, *134*, 120–136. https://doi.org/10.1016/j.gca.2014.03.005

Tripati, A. K., Eagle, R. A., Thiagarajan, N., Gagnon, A. C., Bauch, H., Halloran, P. R., & Eiler, J. M. (2010). 13C–18O isotope signatures and 'clumped isotope' thermometry in foraminifera and coccoliths. *Geochimica et Cosmochimica Acta*, *74*(20), 5697–5717. https://doi.org/10.1016/j.gca.2010.07.006

Tripati, A. K., Sahany, S., Pittman, D., Eagle, R. A., Neelin, J. D., Mitchell, J. L., & Beaufort, L. (2014). Modern and glacial tropical snowlines controlled by sea surface temperature and atmospheric mixing. *Nature Geoscience*, *7*(3), 205–209. https://doi.org/10.1038/ngeo2082

Chapter 1: Clumped isotope thermometry in foraminifera as a tool in paleoceanography: New planktic and benthic data and constraints on non-thermal effects

Aradhna Tripati[*], Hannah Tandy[*], Alexandra Villa[*], Randon J. Flores, Alexandrea Arnold, Hannah Carroll, Maxence Guillermic, Ingrid Maradiaga, Christian Blair, Bisrat Zerehaimanot, Dana Brown, Robert Ulrich, Cristian-Roman Palacios, Mohan Kuppusamy, Dharmendra Pratap Singh, Raquel Bryant, Jules de La Cruz, Fengming Chang, Robert A. Eagle, Ceara Tomaiso, Thomas M. Marchitto, Rosemarie E. Came, Jean Lynch-Stieglitz

*joint first author

Key Points:

- 124 new samples and 136 reprocessed samples are reported and compared to 118 synthetic calcite samples to explore the scope of non-thermal effects in foraminifera
- We define temperature regressions for Δ_{47} in foraminifera, inorganic calcite synthesized between 0-50 °C and multivariate regressions for benthic foraminifera
- Regressions applied to published Δ_{47} data for the Cenozoic yield reasonable temperature and seawater $\delta^{18}O$ estimates for intervals that had been controversial

Abstract

The carbonate "clumped" isotope thermometer (Δ_{47}) in foraminifera is increasingly being used to reconstruct ocean temperature. Here we address several less understood aspects of the proxy using a large dataset comprising new and reprocessed data. The Δ_{47}-temperature relationship can be described in foraminifera (n = 260) by $\Delta_{47} = 0.0374 \pm 0.0013\ 10^6/T^2 + 0.1744 \pm 0.0154$, and in inorganic calcite (n = 118) by $\Delta_{47} = 0.0392 \pm 0.0014\ 10^6/T^2 + 0.1547 \pm 0.0165$. Dataset-related differences can explain only 11% of the variance; all non-thermal effects explain up to 13% of the variance. We address the paucity of benthic data with new samples, establishing with more certainty the proxy temperature sensitivity is indistinguishable from planktics and inorganic calcite. The large benthic foraminiferal dataset allows us to resolve a previously uncharacterized correlation of Δ_{47} with $[CO_3^{2-}]$ that is small ($\Delta\Delta_{47}/\Delta CO_3^{2-}$ slope = 0.00019 ± 0.00004, n = 66; $R^2 = 0.315$, $p < 0.01$). We report a multivariate regression to account for both temperature and $\Delta[CO_3^2]$ for all benthics (epifaunal and infaunal), with Δ_{47} (‰) = 0.152 ± 0.049 + 0.03865 ± 0.00376 x $10^6/T^2$ + 0.000150 ± 0.0000601 $\Delta[CO_3^{2-}]$. We apply these regressions to published benthic Δ_{47} values over the Cenozoic, with the multivariate benthic equation yielding temperature and $\delta^{18}O_{sw}$ values more consistent with independent proxy data, models, and broader understanding of ocean and cryosphere dynamics under different conditions, including across the Eocene-Oligocene Transition and the Early Eocene Climatic Optimum. In total, this work enables the application of clumped isotopes to foraminifera with a more realistic understanding of uncertainties.

Plain Language Summary

Carbonate clumped isotopes (Δ_{47}) is an emerging proxy for temperature. Several calibration studies have examined the relationship between Δ_{47} and temperature in core-top foraminifera but

have used small datasets. Here we measure new samples and restandardize published data for foraminifera and synthetic calcite using best practices and explore controls on the proxy using results for 260 samples (>2500 analyses). We confidently demonstrate with a large dataset that foraminiferal Δ_{47} shows a temperature dependence like inorganic calcite, report a robust temperature calibration relationship, and discuss evidence for a possible carbonate ion effect on benthic foraminifera that merits further examination. We then apply the new calibrations to address some puzzling aspects of published Cenozoic benthic foraminiferal temperature and $\delta^{18}O_{sw}$ reconstructions.

1. Introduction

Accurate constraints on past ocean temperatures are critical to understanding ocean-climate interactions and Earth's climate history. However, employing proxies for temperature requires frameworks for disambiguating thermal effects from chemical, biotic, and/or diagenetic imprints. Therefore, a large body of work has focused on calibrating and applying temperature proxies, including $^{18}O/^{16}O$ ratios ($\delta^{18}O$) in foraminifera (Zachos et al., 1994, 2001, 2008), Mg/Ca (Anand et al., 2003; Elderfield and Ganssen, 2000; Lea et al., 1999; Mashiotta et al., 1999; Nürnberg et al., 1996; Pak et al., 2004), the alkenone unsaturation index (Conte et al., 2001, 2006; Müller et al., 1998; Sachs et al., 2000), and TEX_{86} (J.-H. Kim et al., 2008; Leider et al., 2010; Powers et al., 2010; Schouten et al., 2007; Tierney and Tingley, 2014). Each of these approaches leverages a temperature tracer recorded in sedimentary material and compounds produced by different types of organisms. Although each temperature proxy has been applied to provide information on the history of the oceans (e.g., Bard, 2000; Bard et al., 1997; de Garidel-Thoron et al., 2005; Koutavas, 2002; Lea et al., 2002; Martin and Lea, 2002), limitations exist, such as kinetic effects, unconstrained species-specific vital effects, the need for regional and

latitudinal specific calibrations, the influence of changing seawater chemistry, and/or poor preservation potential.

More recently, a temperature proxy has emerged as a potentially transformative tool in the ocean sciences is carbonate clumped isotope thermometry, which may be robust to some of these limitations (Came et al., 2007; Ghosh et al., 2006; Leutert et al., 2019; Meckler et al., 2022; Meinicke et al., 2020; Peral et al., 2018; Piasecki et al., 2019; Thiagarajan et al., 2011; Tripati et al., 2010, 2014). The clumped isotope thermometer stands out because of its basis in thermodynamics (Ghosh et al., 2006; Schauble et al., 2006; Tripati et al., 2015). In calcite, aragonite, dolomite, other carbonates, and different chemical species of dissolved inorganic carbon (DIC), heavier isotopes of C and O (^{13}C, ^{18}O) are rare relative to the lighter isotopes (^{12}C, ^{16}O). Carbonate "clumped" isotope geochemistry examines the proportion of these heavy isotopes that are bound to each other forming heavy isotope "pairs" or clumps, for example, the multiply-substituted isotopologues $^{13}C^{18}O^{16}O$ (the predominant species used for temperature reconstructions, to date) or $^{12}C^{18}O^{18}O$.

Since the first studies of clumped isotope systematics in foraminifera were published (Grauel et al., 2013; Tripati et al., 2010), the use of the temperature proxy in paleoceanography has been limited because of the large sample sizes needed for the analyses (Table 1.1), and the presence of interlaboratory offsets (see Bernasconi et al., 2018, 2021; Dennis et al., 2011; Petersen et al., 2019; Tang et al., 2014 for discussion). The work of multiple labs has been addressing these issues, including the use of consistent standardization and more accurate methods for isotope ratio calculations (Dennis et al., 2011; Bernasconi et al., 2021; Daeron et al., 2016; Upadhyay et al., 2021; Lucarelli et al., 2023) and sample size reduction (Grauel et al., 2013; Upadhyay et al., 2021). Building on these advances, downcore records have been published for foraminifera (e.g., Tripati et al., 2014; Leutert et al., 2019; Meckler et al., 2022).

However, recent work has highlighted the need for additional work to improve clumped isotope calibrations for foraminifera, particularly for benthics (Daeron and Gray, 2023; Rohling et al., 2024). To date, the exploration of potential chemical and biological biases has been limited, and the scope of non-thermal effects that we know confound other proxies are unresolved for clumped isotopes. For example, studies have shown for oxygen isotopes and Mg/Ca ratios in foraminifera, carbonate ion effects can be important (Bemis et al., 1998; Elderfield et al., 2006; Spero et al., 1997).

Thus, in this study, we build on these developments in the systematics of other proxies to similarly advance the foundation for more widespread use of clumped isotope thermometry in foraminifera as a tool in paleoceanography. We recognize that a key aspect underpinning the nuanced application of temperature proxies has been the development of large datasets (Anand et al., 2003; Elderfield et al., 2006), as well as meta-analysis (e.g., Bemis et al., 1998; Daeron and Gray, 2023; Elderfield et al., 2006) to allow for the intensive characterization of thermal and non-thermal effects to understand the circumstances in which proxy application may be limited. Therefore, here we utilize current analytical methods and report new Δ_{47} data for 124 core-top foraminiferal samples, including data on previously unstudied species. Next, we reprocess data from published studies on foraminiferal samples (n = 136) using updated data handling practices including use of the IUPAC parameter set (Daëron et al., 2016; Petersen et al., 2019), and carbonate-based standardization onto the Intercarb-Carbon Dioxide Equilibrium Scale (I-CDES or I-CDES$_{90}$) reference frame (Bernasconi et al., 2021; Lucarelli et al., 2023; Upadhyay et al., 2021). These data were generated on multiple models of mass spectrometer and carbonate preparation systems and together allow us to report a novel combined dataset. We report a combined benthic foraminiferal dataset that is composed of 42 monospecific samples and 25 mixed benthic foraminiferal samples. We conduct a meta-analysis to assess if there are

interlaboratory related effects or other non-thermal effects, including evidence for ecological, taxonomic, regional, or depth-dependent isotope effects. We derive calibrations for planktic and benthic foraminifera (and different subsets of these taxa) and compare them to synthetic calcite. We use this dataset to determine benthic multivariable regressions that account for a dependence of Δ_{47} on both temperature and $\Delta[CO_3^2]$. These calibrations are used to reevaluate published reconstructions of deep ocean temperature and $\delta^{18}O$ from Δ_{47}.

1.1 Background on clumped isotope thermometry

Carbonate clumped isotope thermometry has the potential in paleoceanography to be similarly impactful as oxygen isotope thermometry. For over 50 years, the primary isotopic tool used to constrain past ocean temperatures has been the $\delta^{18}O$ of foraminifera (Shackleton and Opdyke, 1973; Zachos et al., 1994, 2001, 2008). For example, foraminiferal $\delta^{18}O$ has been used to provide critical constraints on how temperature, ice volume, salinity, water column structure, and ocean circulation have responded to past changes in greenhouse gas concentrations. However, a longstanding challenge in such applications has been accurately partitioning the thermodynamic fractionation of oxygen isotopes in carbonates from the effects of changing water $\delta^{18}O$. In contrast, carbonate clumped isotope thermometry is not sensitive to water $\delta^{18}O$. All that is needed to determine mineral formation temperatures is the clumped isotope composition of the solid, not the water from which it grew.

Clumped isotope thermometry relies on internal isotopic exchange between isotopes in a single phase, instead of relying on an isotopic exchange reaction between different phases (e.g., $CaCO_3$ and H_2O for the carbonate-water oxygen isotope thermometer). As with oxygen isotope thermometry, zero-point energy differences between isotopic species (or isotopologues) form the basis of the clumped isotope thermometer. For carbonate minerals that have grown in

equilibrium, the paired measurement of clumped isotopes and $\delta^{18}O$ in carbonate minerals can therefore yield both carbonate formation temperature and fluid $\delta^{18}O$. However, the low abundance of clumped (multiply-substituted) isotopologues ($^{13}C^{18}O^{16}O$ and $^{12}C^{18}O^{18}O$, for example), and the low temperature sensitivity of the relevant isotope exchange reactions, measurements need to be made with high precision and accuracy. Further, robust application of the geothermometer necessitates mineral equilibrium being achieved and reliable quantification of temperature dependencies, and if appropriate, corrections for kinetic isotope effects.

An initial study of clumped isotopes in planktic and benthic foraminifera and coccoliths was published four years after the geothermometer was developed (Tripati et al., 2010). Using error-in-variable regression models (a Deming regression), this study found no evidence for differences between synthetic calcite and foraminifera calibrations, nor between cultured coccolithophores and inorganic calcite, and did not find discernible taxon-specific fractionations (Tripati et al., 2010). Several calibration studies have validated those initial findings and have also made instrumental advancements by reducing sample requirements and using different methods and instrumentation for sample analysis as well as different regression models (Meinicke et al., 2020; Peral et al., 2018; Piasecki et al., 2019). Multiple studies have evaluated different models for estimation of seawater calcification temperature (e.g., Daëron and Gray, 2023; Tripati et al., 2010). Although foraminiferal measurements are challenging, there is a growing literature of applied studies using clumped isotope thermometry to reconstruct ocean temperature and $\delta^{18}O$ (e.g., Agterhuis et al., 2022; Evans et al., 2018; Leutert et al., 2019, 2020; Meckler et al., 2022; Tripati et al., 2014; Taylor et al., 2023).

1.1.1 Challenges in applying clumped isotopes to foraminifera

While the growing body of work is demonstrating the power of clumped isotope thermometry when applied to foraminifera, proxy use in paleoceanography is still limited because of several issues. Recent major technological advances in applying this proxy to foraminifera have resolved the issue of large sample sizes (Table 1.1). While initially 3-8 mg $CaCO_3$ were used to perform a single replicate analysis and at least three replicates required, with typical sample sizes of 9 to 30 mg (Ghosh et al., 2006; Tripati et al., 2010), a major step forward has involved reduction in sample sizes that are similar to Mg/Ca analyses with 0.1 to 0.5 mg required for a single replicate, and 3 to 50 replicates, with typical total sample sizes of 2.5 to 5 mg (Table 1.1). These small sample measurements (total sample sizes of 2.5 to 5 mg, including replicates) have been made on a MAT 253 isotope ration mass spectrometer (IRMS) with a kiel device (Grauel et al., 2013; Meckler et al., 2014; Meinecke et al., 2020, Piasecki et al., 2019), the Nu-Perspective IRMS and NuCarb or in-house carbonate reaction and purification devices (Anderson et al., 2021; Defliese and Tripati, 2020; Upadhyay et al., 2021). These advances make employment of the proxy on foraminifera more feasible.

For carbonate-hosted tracers, it has also been important for the community to investigate inter-lab differences (Greaves et al., 2008; Rosenthal et al., 2004) and understand whether they are associated with sample preparation or with the specific analytical technique used (Barker et al., 2003, 2005; Bian and Martin, 2010; Martin and Lea, 2002). In clumped isotopes, interlaboratory offsets have been reduced through updated data handling practices including use of the IUPAC parameter set (Daëron et al., 2016; Petersen et al., 2019), and carbonate-based standardization onto the I-CDES reference frame (Bernasconi et al., 2021; Lucarelli et al., 2023; Upadhyay et al., 2021; Anderson et al., 2024).

1.2 Overview of this study

In this study, we leverage advances, best practices, and instrumentation that have been shown to yield highly precise, accurate, and intercomparable data (Bernasconi et al., 2021; Upadhyay et al., 2021; Lucarelli et al., 2023; Daeron and Gray, 2023). First, we utilize current analytical methods that have been shown to yield highly precise, accurate, and intercomparable data, with all data reported on the I-CDES reference frame (Bernasconi et al., 2021; Upadhyay et al., 2021; Lucarelli et al., 2023). We report Δ_{47} data for new foraminiferal samples (n = 124; 82 planktic foraminiferal samples and 42 benthic foraminiferal samples) which includes data on previously unstudied species. We reprocess data from published studies on foraminiferal samples (n = 136) using different types of instrumentation. This facilitates a substantial combined dataset comprised of 260 core-top planktic and benthic foraminiferal samples, with 29 species and 2569 replicate analyses, from several major ocean basins (Table 1.1).

We evaluate the use of multiple calcification temperature methods, including different $\delta^{18}O$-based calcification temperature equations. We conduct a meta-analysis to assess if there are interlaboratory related effects or other non-thermal effects, including evidence for ecological, taxonomic, regional, or depth-dependent isotope effects, and show non-thermal effects can explain only 13% of the data variance. We derive calibrations with significant data representation for both planktic and benthic foraminifera - where previously relatively little benthic data has been published - and compare results to synthetic calcite. We derive Δ_{47}-temperature calibrations for foraminiferal samples to compare material specific differences and report limits for accuracy and precision of reconstructions. We validate prior findings of no significant deviation from foraminiferal test Δ_{47} temperature sensitivity to inorganic calcite precipitates (118 samples; 641 analyses; grown in experiments at temperatures between 4 and 50 °C; Table 1.2). The analysis of benthic foraminiferal data indicates a weak carbonate ion effect,

and we report a new multivariate regression relating Δ_{47} to both temperature and carbonate saturation. Finally, we apply our novel calibrations. We analyze profile temperature reconstructions and show that modern hydrographic profiles are reasonably constrained using data from multiple taxa, show the impact of the use of our new calibrations on reconstructed temperatures on Cenozoic temperatures, and make recommendations for future studies.

2 Materials and Methods

2.1 Sample and locality information

Samples are from the four major ocean basins (Arctic, Atlantic, Indian, Pacific), the Gulf of Mexico, and the Mediterranean Sea (Figure 1.1, Table 1.S.1). Figure 1.1 shows locality information for the 49 sites. A total of 29 foraminifera taxa were studied (13 benthic, 15 planktic), and assemblages of mixed benthic species. The species included in this study live in a range of habitats, spanning Atlas temperatures from -1.5 °C to 29.6 °C (Levitus et al., 2010). Data for 124 foraminifera samples are newly reported and were run in the Eagle-Tripati clumped isotope laboratory at UCLA, while 136 samples from five previous publications (Breitenbach et al., 2018; Meinicke et al., 2020; Peral et al., 2018; Piasecki et al., 2019; Tripati et al., 2010) were projected into the I-CDES reference frame for this work (Table 1.1, Table 1.S.2).

2.2 Methods for new samples measured in the Eagle-Tripati laboratory

2.2.1 Sample Preparation

Core-top sediment samples from 47 different sites were suspended in deionized (DI) water for a minimum of 24 hours using a rotating wheel (Table 1.S.1). Fine and coarse fraction were separated using a 63 μm sieve and dried overnight at 30 °C (≤ 50 °C to prevent bond reordering). A total of 16 different taxa, both planktic and benthic, and mixed benthic species, were hand-picked from different size fractions at these sites. Tests were translucent and intact.

We aimed for a minimum weight of picked foraminifera of 3 mg to have sufficient material for several replicate analyses.

Picked samples underwent a cleaning procedure to remove potential contaminants, adapted from the cleaning procedure for Mg/Ca analysis from Barker et al. (2003), as described in Tripati et al. (2010), with a focus on removing infill and adhering sediment. Briefly, foraminiferal shells are cracked open, rinsed and ultrasonicated using methanol and DI water until the cleaning water is clear. Each ultrasonication step consisted of 4 intervals lasting 15 seconds to ensure that the water did not heat up. Samples were then placed inside an oven to dry overnight at 30 °C (< 50 °C). Samples were homogenized using a mortar and replicates were weighed and stored in a desiccator until the day of analysis. Additional details on sample preparation are provided in the Supplement (S2).

2.2.2 Measurement Procedure

Aliquots of cleaned samples that ranged from 0.46 to 0.52 mg were measured in single analyses, with 3 to 20 replicates measured per sample. A total of 720 new analyses of 124 foraminifera samples were made. Samples were analyzed from 2017 to 2023 on two Nu Perspective Dual inlet mass spectrometers with secondary electron suppression. These were run on instrument configurations “2” (Nu Perspective 2014, acid bath 90 °C), “3A” (Nu Perspective 2014, Nu Carb, 70 °C) and “3B” (Nu Perspective 2016, Nu Carb, 70 °C) that were shown in Upadhyay et al. (2021) and Lucarelli et al. (2023) to yield statistically indistinguishable results from each other.

Every 4 to 5 sample measurements, a carbonate standard was measured and Δ_{47} values are reported on the Inter-Carbon Dioxide Equilibrium Scale (I-CDES$_{90}$, Bernasconi et al. 2021) at 90 °C. A total of seven standards were used, including ETH-1, ETH-2, ETH-3, ETH-4, CM

Tile, Carmel Chalk, and Veinstrom (Upadhyay et al., 2021; Lucarelli et al., 2023). ETH-1 and ETH-2 were used for non-linearity corrections while ETH-1, ETH-2, and ETH-3 and the remaining in-house standards were utilized for $\delta^{13}C$ and $\delta^{18}O$ drift corrections and empirical transfer function (ETF) calculations. ETH-4 was used as a consistency standard and not included in any standard corrections. Depending on standard drift during a correction interval, we utilized either 10 or 20-point moving averages for drift, nonlinearity, and empirical transfer function corrections for each correction interval, following published studies (Meckler et al., 2014; Upadhyay et al., 2021; Lucarelli et al., 2023). The Brand parameter set was used for calculations (Daëron et al., 2019; Petersen et al., 2019). Calculations to determine Δ_{47}, $\delta^{13}C$, and $\delta^{18}O$ use publicly available software (Easotope - John and Bowen, 2016) and further details on clumped isotopes are provided in the supplementary material (Section S1).

2.2.3 Accuracy and precision of data and data archiving

Standard values for each instrumental configuration are typically within 0.005‰ of values reported by Bernasconi et al. (2021) as described in Upadhyay et al. (2021) and Lucarelli et al. (2023). Long-term absolute mean error in standard Δ_{47} across instruments is 0.0002‰ (or 0.03% in percent terms), and is normally distributed (Upadhyay et al., 2021; Lucarelli et al., 2023). The average Δ_{47} standard deviation (1 s.d.) among standard replicates for all instruments is 0.021‰ (Upadhyay et al., 2021; Lucarelli et al., 2023).

Similar values are reported for samples. For samples, average Δ_{47} reproducibility is 0.022‰ (1 s.d.) and 0.009‰ (1 s.e.) (Supplemental Table 1.S.1). The ranges for samples are 0.001-0.049‰ (1 s.d.) and 0.000-0.029‰ (1 s.e.). Standard and sample data for new measurements are provided using the recommended EarthChem template (Petersen et al., 2019) and archived online with manuscript acceptance.

2.2.4 Quality control

Data quality control followed published procedures described in Parvez et al. (2023). Although in the laboratory, samples are routinely screened based on Δ_{48} or Δ_{49} values that are indicative of high organic content, all samples reported for this study fell within initial screening bounds, so no replicates were excluded based on this criteria. Replicates with incomplete gas transfer and Δ_{47}, $\delta^{13}C$, and $\delta^{18}O$ values that fall outside of a SD range of ±0.5‰ for $\delta^{13}C$ and $\delta^{18}O$ and ±0.05‰ for Δ_{47} are also flagged. Similar screening thresholds for Δ_{47} were reported by Meckler et al. (2014), Upadhyay et al. (2021), and Lucarelli et al. (2023). Data were screened based on instrument source stability, pumpdown times and leaks in the acid digestion system, and standard data quality during correction intervals as described in Parvez et al. (2023). Of the new analyses conducted for this study, 720 replicates were included, and 52 replicates excluded.

2.3 Reprocessed datasets from publications

2.3.1 Core-top foraminiferal datasets

Five published foraminiferal datasets (Breitenbach et al., 2018; Meinicke et al., 2020; Peral et al., 2018; Piasecki et al., 2019; Tripati et al., 2010) were reprocessed onto the I-CDES$_{90}$ reference frame as part of this study. The foraminiferal data include 24 different taxa (10 benthic, and 14 planktic) and mixed benthic samples from Tripati et al. (2010) and Piasecki et al. (2019) (Table 1.1, 1.S.2, 1.S.3). After discussion with S. Bernasconi about Grauel et al. (2013) and the reprocessing of their dataset, data from the study were not included, as the measurements only included the use of two marble (high-temperature) standards with low Δ_{47} values, with no carbonate standard with high Δ_{47} values used for their corrections.

2.3.2 Synthetic calcite datasets

We compare our foraminiferal data to synthetic calcite to assess if there are differences between the two groups. Since growth temperatures for foraminiferal samples occupy a much narrower range of temperature than many synthetic calcite precipitates used for calibration purposes, we limit the data used for synthetic calcite to 4 to 50 °C.

A total of 118 synthetic calcite samples comprising 641 replicates were utilized for this comparison: we include 11 new measurements of synthetic calcite analyzed in the same manner as foraminiferal samples on the I-CDES$_{90}$ reference frame (Table 1.2, Supplemental Table 1.S.4), 19 samples were reprocessed as part of this study (Defliese and Tripati, 2020; UCLA samples from Tang et al., 2014; Tripati et al., 2015) and 85 additional synthetic calcite samples from other studies (Table 1.2, Supplemental Table 1.S.4). Synthetic calcite calibration samples from other studies include samples that were reprocessed using Brand parameters in the Petersen et al. (2019) study (Defliese and Lohmann, 2015; Kelson et al., 2017; Kluge et al., 2015; Tulane samples from Tang et al., 2014), as well as Anderson et al. (2021), Lucarelli et al. (2023), Jautzy et al. (2020), and Swart et al. (2021).

2.3.3 Data reprocessing for published datasets

The Tripati et al., (2010) dataset for foraminifera and Tripati et al. (2015) dataset for synthetic calcite were reprocessed for use in this study in the Easotope software (John and Bowen, 2016) with updated parameter values (Daëron et al., 2016) and standard values (Bernasconi et al., 2021; J. Lucarelli et al., 2023) on the CDES absolute reference frame. Gas standards are used for the nonlinearity correction step and a combination of gas and carbonate standards for the ETF to project onto the CDES reference frame (see methods section 2.1.2). We

use these new Δ_{47} (CDES) values, along with the transfer functions (Supplemental Table 1.S.5) constructed from Bernasconi et al. (2021) to project values into the I-CDES$_{90}$ reference frame.

We also reprocessed data from the Petersen et al. (2019) study (Defliese et al., 2015; Kelson et al., 2017; Kluge et al., 2015; Tang et al., 2014). These datasets were initially brought onto the CDES reference frame at 25 °C (Dennis et al., 2011) using ETH carbonate standards (Bernasconi et al., 2018) and acid fractionations associated with Brand parameters (Daëron et al. 2016). We use these originally published Δ_{47} CDES values in concert with the methodology described in Bernasconi et al. (2021) to project values into the I-CDES$_{90}$ reference frame.

We reprocessed data from Defliese and Tripati (2020) and Tang et al. (2014) that were measured at UCLA as part of this study in Easotope on I-CDES$_{90}$. Data from Anderson et al. (2021), Lucarelli et al. (2022A), Jautzy et al. (2020), and Swart et al. (2021) were already in I-CDES$_{90}$ and were not reprocessed.

2.4 Ecological and Hydrographic data

Foraminiferal Δ_{47} values were compared to estimates of calcification temperature, that in turn are constrained by independent datasets (i.e., habitat, ocean atlas-derived calcification temperatures, oxygen-isotope derived calcification temperatures). We also use multiple methods to probe secondary (non-thermal effects). We use Δ_{47}-temperature regression models to estimate vertical profiles of temperature and compare results to ocean atlas temperatures.

2.4.1 Habitat

Species were classified by depth habitats including mixed-layer, mixed-layer to thermocline, and thermocline for planktic species, and epifaunal and infaunal for benthic species. Specific depth habitats and ranges for different taxa were taken from Rippert et al. (2016) and Schiebel and Hemleben (2017) and references therein. We note that calcification depths of

foraminifera vary seasonally and can evolve with ontogeny, as well as depend on factors influencing feeding patterns (Schiebel and Hemleben, 2017). Ocean basins sampled in the complete dataset include the Arctic, Atlantic, Indian, and Pacific Oceans, as well as the Mediterranean Sea and the Gulf of Mexico.

2.4.2 Calcification temperatures

Calcification temperatures for each sample were calculated for new and reprocessed samples, so that we could ensure the same methods were consistently used (Supplemental Table 1.S.3). Three methods were utilized and a comparison of results is provided in the supplemental material (Section S3). Briefly, method 1 uses the literature on calcification depths of foraminifera species in geographical regions in conjunction with WOA temperature data (version 13V2; Levitus et al., 2010) to estimate calcification temperatures. Method 2 consists of combining measured $\delta^{18}O$ of foraminiferal tests with seawater $\delta^{18}O$ (at assumed foraminiferal calcification depths and growth seasons) from a database (LeGrande and Schmidt, 2006), in combination with published taxon-specific $\delta^{18}O$-temperature relationships. For the latter, we referred to the most data-rich study on planktic taxon-specific $\delta^{18}O$-temperature relationships from Malevich et al. (2019) that compiles data from >2600 core top samples from five taxa and reports Bayesian regression models that are taxon-specific as well as a pooled calibration. They examined both annual and seasonal data, with similar errors for each. For our calcification temperature estimates, in the case of taxa for which species-specific calibrations were provided, we used the seasonal hierarchical model to estimate calcification temperatures and used the pooled calibration for all other planktic species. To estimate calcification temperatures of benthic taxa, we implemented equation 9 of Marchitto et al. (2014) for epifaunal species and mixed benthics, and the same equation modified by 0.47 ‰ for infaunal species as the authors suggest.

Method 2, presented in the figures and the text, uses assumed calcification depths and oxygen isotope measurements, to estimate calcification temperatures for planktic foraminifera. Additionally, isotopic calcification temperatures were estimated using Method 2, but with equations from Kim and O'Neil, (1997) and Shackleton (1974). Method 3 uses theoretical values of $\delta^{18}O_{calcite}$ to develop vertical profiles and compares them to measured $\delta^{18}O_{calcite}$ values to determine the minimum and maximum calcification depths.

2.4.3 Salinity

Estimated salinity is calculated using published decadal averaged seawater salinity from the WOA18 gridded dataset (Zweng et al., 2019). Salinity is averaged for each species at each site over their site specific assumed calcification depths.

2.4.4 Bottom water saturation state

Bottom water saturation state was compared to benthic foraminiferal data to assess carbonate ion effects on calcification, with the caveat that infaunal taxa may inhabit environments with values that differ in composition from bottom waters. For these comparisons, calcite saturation state ($\Delta[CO_3^{2-}]$) is calculated as the difference between the in-situ carbonate-ion concentration ($[CO_3^{2-}]$) and the carbonate-ion concentration at saturation ($[CO_3^{2-}]_{sat}$). Carbon system data was obtained from the nearest neighbor sites from the World Ocean Circulation Experiment and the Global Ocean Data Analysis Project (Olsen et al., 2019) and carbonate-ion concentration was calculated via Ocean Data Viewer (http://woce.nodc.noaa.gov/wdiu) using best practices by Dickson et al. (2007).

2.5 Statistical Models

We used multiple statistical methods for this work. One method was used for developing regressions between Δ_{47} and temperature. Multiple approaches were applied for comparing subsets of data to assess if different models are needed (i.e., for foraminifera relative to synthetic calcite, or planktics relative to benthics). We used different approaches to assess if non-thermal effects are substantial (i.e., carbonate ion effects).

2.5.1 Regressions between Δ_{47} and calcification temperature

We fit regressions between Δ_{47} and calcification temperature utilizing Deming models. Among multiple analyzed frequentist regression models, Deming models are known to outperform other errors in variable models (i.e., York models), with higher levels of accuracy and precision for datasets of these sizes and similar error structures (Román-Palacios et al., 2021). Regression parameters from these models are generally congruent with Bayesian-derived estimates (Román-Palacios et al., 2021). We use Deming models to investigate potential non-thermal effects and differences between data subsets through confidence interval (CI) comparison.

2.5.2 Use of R-based model selection for investigation of non-thermal effects

We used a model selection approach to determine whether non-thermal factors substantially impact isotopic signatures in foraminifera. Deming regressions are strictly univariate, so we substituted multivariate ordinary least squares (OLS) linear models in R version 4.1.2 (R Core Team, 2022). The potential suite of non-thermal variables consisted of lab/dataset, salinity, depth, region, photosymbiont presence, habitat, genus, ocean, and bottom water saturation state. Because this constitutes a large number of potential variables (set within a model as predictor variables) that could feasibly impact the final Δ_{47} value, with an unknown

potential for interactions between variables, we employed automated model selection using the multithreaded implementation of the 'dredge' function in R package MuMIn version 1.47.1 (Bartoń, 2022). All numerical predictor variables were scaled and centered (i.e., z-scored) prior to building models, as differences in the absolute magnitude of predictor variables can lead to erroneous results in effect size calculations. Scaling the response variable was found to be unnecessary.

We report coefficients from linear models fit to z-scored data, which provides an estimate of the per mil change in Δ_{47} for each 1 standard deviation (1 σ) increase in the predictor variable(s) of interest. Uncertainty around coefficients is given in standard error in permil units. The effect size, partial eta squared (η^2), is used to evaluate how much variation in foraminiferal Δ_{47} is explained by each model component (fit to z-scored data) and determine whether those effects are small (partial $\eta^2 = 0.01$), medium (partial $\eta^2 = 0.06$), or large (partial $\eta^2 >= 0.14$) when all other variables in the model are held constant. The calculation for η^2 is mathematically similar to the calculation for R^2 and may therefore be interpreted in a similar manner for individual model components. Note that we report effect sizes calculated using Type II (non-sequential) sums-of-squares as implemented in the *car* package for R (Fox and Weisberg, 2019). This means that the impact of each predictor variable on foraminiferal Δ_{47} is evaluated individually in turn, while all other predictor variables are held constant. Effect sizes may therefore add up to >1. As η^2 is calculated using a one-sided hypothesis, we report one-sided 95% confidence intervals. Where final models include only a single predictor variable (temperature), partial η^2 is equivalent to η^2, and so η^2 is reported. Linear model F-statistics are reported with the numerator and denominator degrees of freedom listed as subscripts in that order.

A ‘full’ model was constructed for each subset of data (by lab/dataset, habitat, etc.) which contained all relevant candidate predictor variables. The ‘dredge’ function then examined every possible combination of predictor variables and determined the most likely reduced models. Candidate reduced models were manually checked for goodness-of-fit and extraneous terms were dropped if warranted. To determine whether dropping extraneous terms improved model fit, a hypothesis testing approach, followed by examination of the Akaike Information Criterion (AIC), was used to select between the reduced model identified by ‘dredge’ and a simplified model with terms dropped. If hypothesis testing and AIC indicated that two reduced models were equally likely to fit the data, we defaulted to the simpler model (e.g., the model with fewer terms or without interactions). Effect sizes and confidence intervals for final model components were calculated using R package effectsize version 0.7.0.5 (Ben-Shachar et al., 2020), with non-sequential (Type II) sums-of-squares calculated in R package car version 3.1-1 (Fox and Weisberg, 2019). Full details of this method are available in the Supplementary information (Section S5). We also use OLS for directly investigating non-thermal dependences (i.e., regressions between Δ_{47} residuals and bottom water $\Delta[CO_3^{2-}]$). Individual comparisons between data subsets are done using ANCOVA-type analyses (performed in Graphpad Prism). Tests for multicollinearity confirm PCA results, with the additional ability to include categorical predictors, and show no evidence of problematic degrees of correlation between predictor variables including temperature, dataset, depth, carbonate saturation, salinity, and photosymbiont presence/absence.

2.6 Temperature reconstruction

We reconstruct temperatures using core-top data for multiple species of foraminifera at several locations to evaluate the fidelity of using this approach to constrain hydrographic profiles

in different oceanographic regimes. Temperatures were estimated using the full foraminiferal regression from the meta-analysis (labelled "All Foraminifera" in Table 1.3).

3 Results and Discussion

3.1 Sensitivity of regression to calcification temperatures estimated using different methods

Figure 1.2 shows Δ_{47} values for calibration samples compared to $\delta^{18}O$-based calcification temperatures estimated using the species-specific Bayesian model (method 2). Supplemental Table 1.S.3 contains the calcification temperature estimates from different methods, and water isotope values and the supplement compares results from these different methods in more detail. Briefly, although all three methods yield results that are broadly similar, there are some notable differences. Calcification temperatures derived from method 1 (the WOA13 values) show more scatter than those estimated using either methods 2 or 3 (oxygen isotope-based estimates) as is evidenced by a lower Pearson's correlation coefficient (see supplementary material S4). Differences between the Atlas (method 1) and isotopic temperatures (method 2) reach up to 13.4 °C for the same sample, which is a *Trilobatus sacculifer* from the Equatorial Pacific from Tripati et al. (2010). In contrast, calcification temperatures derived from method 2 and method 3 yield small differences for most samples (max = 5.1 °C). Method 2 allows for the use of the species-specific Bayesian model for carbonate $\delta^{18}O$ temperature estimates and decreases the temperature estimate error for planktic samples. If we solely examine the new dataset generated at UCLA on 124 foraminiferal samples, we reach similar conclusions with the largest Pearson's correlation from Method 2 (r = 0.898) and relatively small differences between Method 2 and 3 (mean = 0.0077 °C, SD = 1.7 °C).

We conclude from our meta-analysis that the differences between methods are generally small, with the smallest offsets between Method 2 and Method 3 and the largest offsets between

Method 1 and Method 3. Results from Method 2 exhibited the strongest correlation between temperature and Δ_{47}, both in the new dataset generated at UCLA and the overall meta-analysis. The method is similar to what was used by Meinicke et al. (2020) and what is recommended by Daeron and Gray (2023). Given Method 2 has the strongest correlation between temperature and Δ_{47}, both in the new dataset generated at UCLA and the overall meta-analysis, it was the method utilized for calcification temperature estimation in this study.

We also compare multiple models for estimating isotopic calcification temperatures utilizing Method 2. Figures 1.S.1 and 1.S.2 compare calcification temperatures for planktics (from Malevich et al., 2019) and benthics (derived from Marchitto et al., 2014) estimated using Method 2 to atlas temperatures (Method 1), and are modelled after Figure 1.7 from Daeron and Gray (2023). Figures 1.S.3-1.S.6 are similar to these but utilize Method 2 but show isotopic calcification temperatures derived using the equations of Kim and O'Neil (1997) or Shackleton (1974). Figure 1.S.7 shows a histogram of the differences between isotopic temperatures and atlas temperatures. In our analysis, there are fewer benthic foraminiferal samples with large offsets between isotopic and atlas temperatures when the isotopic equation of Marchitto et al. (2014) is used (Figure 1.S.2), in contrast to when equations from Kim and O'Neil (1997) or Shackleton (1974) are utilized (Figures 1.S.4 and 1.S.6). We find the use of the temperature relationships from Malevich et al. (2019), in contrast to Kim and O'Neil (1997) and Shackleton (1974), yields relatively few planktic samples from cold waters (<10 ^{o}C) that have isotopic temperatures that are not within uncertainty of atlas temperatures (Figure 1.S.1 compared to Figures 1.S.3 and 1.S.5). At warmer temperatures, there are more planktic foraminiferal samples that are offset, irrespective of choice of δ^{18}O-calibration (Figure 1.S.1); such samples are described by Daeron and Gray (2023) as being isotopically "discordant" and in this analysis, are dominated by *P. obliquloculata* and *G. ruber* (Figure 1.S.1). We speculate that the offset could

reflect possible non-thermal effects on planktic foraminiferal Δ_{47}. We note that the data for *P. obliquloculata* are for sites at a range of water depths, and thus dissolution could be a contributing factor, but that is not the case for samples of *G. ruber*, as these are from shallower sites.

3.2 Δ_{47}-Temperature calibration

Figure 1.2 and Table 1.3 show the relationship between temperature and Δ_{47} for the UCLA only full foraminiferal dataset (n = 124), for the meta-analysis of the foraminiferal data, and the synthetic calcite data. Figure 1.3 and Table 1.3 also report results for different ecological subgroups of data that are well-defined (e.g., planktic, benthic, mixed-layer planktics, epifaunal vs infaunal benthics) (also reported in Supplemental Table 1.S.5 with other subgroups of data). Results are compared to a regression for synthetic calcite grown at ≤ 50 °C (Tables 1.3, 1.S.3). Pearson's correlation results for all of the populations indicate a strong correlation between temperature and Δ_{47}, consistent with multiple prior studies (e.g., Ghosh et al., 2006; Hill et al., 2014; Petersen et al., 2019; Schauble et al., 2006; Tripati et al., 2015). For example, the meta-analyses of the foraminiferal data and synthetic calcite support a correlation that is significant at the >99% level (r = 0.873, t = 28.7, $p < 0.001$, and r = 0.917, t = 24.4, p < 2.2e-16, respectively).

When comparing foraminiferal results to synthetic carbonates, we see no significant differences between synthetic carbonates and foraminifera overall or between synthetic carbonates and different subgroups of foraminifera excluding mixed benthics (Figures 1.2 and 1.3, Table 1.3). The regression through all foraminiferal data from UCLA (n = 124) is: $\Delta_{47} = 0.0353 \pm 0.0015\ 10^6/T^2 + 0.1973 \pm 0.0187$ while a regression for the full dataset (n = 260) is: $\Delta_{47} = 0.0374 \pm 0.0013\ 10^6/T^2 + 0.1745 \pm 0.0154$. For epifaunal benthics (n = 19) the regression is $\Delta_{47} = 0.\ 0317 \pm 0.0052\ 10^6/T^2 + 0.2474 \pm 0.0674$. For infaunal benthics (n = 23), the regression is $\Delta_{47} = 0.0365 \pm 0.0055\ 10^6/T^2 + 0.186 \pm 0.0696$. For mixed layer planktics, the regression is

Δ_{47} = 0.0423 ± 0.0024 $10^6/T^2$ + 0.1194 ± 0.0282. For synthetic calcite (n = 118), the regression between temperature and Δ_{47} yields the equation with standard error: Δ_{47} = 0.0393 ± 0.0014 $10^6/T^2$ + 0.1547 ± 0.0165.

3.3 Non-thermal effects in foraminifera

To constrain the potential scope of non-thermal effects in this proxy, we build on the body of literature derived from in-depth studies of other foraminiferal proxies such as $\delta^{18}O$ and Mg/Ca (e.g., Anand et al., 2003; Gray and Evans, 2019; Lea et al., 1999; Russell et al., 2004; Stirpe et al., 2021). One group of effects are biological in origin. In some cases, taxon-specific calibrations have been argued to be a better fit (e.g., Bemis et al., 1998; Malevich et al., 2019; Skinner and Elderfield, 2005), while others suggested the use of pooled calibrations (e.g., Anand et al., 2003; Malevich et al., 2019). Recent work surveying cryptic species of foraminifera has shown there are genotype-specific biological controls on shell geochemistry, leading to suggestions that regional calibrations of proxies may also potentially be useful (Darling et al., 2017; Sadekov et al., 2016). Additionally, basinal differences have been identified for Mg/Ca (i.e., a local intercept for Mg/Ca-temperature calibration equations are adjusted to yield modern temperatures from core-top values; Skinner and Elderfield, 2005).

Seawater chemistry has been identified in some studies as being important for proxy systematics. In particular, carbonate chemistry and salinity have been described in the literature as affecting foraminiferal $\delta^{18}O$ and/or Mg/Ca. Carbonate ion effects on oxygen isotopes (Spero et al., 1997) and Mg/Ca (Lea et al., 1999; Russell et al., 2004) have been noted from culturing of planktic foraminifera. Salinity effects have also been reported on Mg/Ca (Ferguson et al., 2008; Gray and Evans, 2019; Hoogakker et al., 2009; Lea et al., 1999). Bottom water carbonate saturation is thought to impact Mg/Ca ratios in benthic foraminifera (Dawber and Tripati, 2012;

Elderfield et al., 2006; Yu and Elderfield, 2008), and potentially oxygen isotopes (Bemis et al., 1998).

These factors have mostly not yet been examined for clumped isotopes in foraminifera. Studies of Δ_{47} have concluded that taxonomic effects have not been detectable (Tripati et al., 2010; Peral et al., 2018; Meinecke et al., 2020, Daëron and Gray, 2023). Similarly, carbonate ion effects have been explored in benthic foraminifera in two studies using relatively small sample sizes; they were not detectable (Tripati et al., 2010; Piasecki et al., 2019). Another study probed for and found no evidence for salinity effects in foraminifera (Peral et al., 2018). The potential scope of carbonate ion and salinity effects in foraminifera has been explored with theory and the mechanisms associated with clumped isotope effects linked to DIC speciation shown to, in principle, be limited across most oceanic conditions (Hill et al., 2014; Tripati et al., 2015). Thus, we hypothesize that non-thermal effects are likely to be weak.

3.3.1 Methodological

Our meta-analysis shows that despite methodological differences, for foraminiferal data, there is strong agreement between most labs when data are placed on the I-CDES reference frame. Clumped isotope measurements involve examination of low abundance isotopic species, and thus are counting statistics limited, and necessitate accurate and precise measurements. Thus, part of our work for this study has involved recalculating available data determined using different methods on the same I-CDES reference frame using published standard values.

Between studies, the instrumentation used varies – including carbonate digestion systems and associated reaction temperatures, mass spectrometers (with distinct signal to noise, and mass spectrometric corrections), and frequency of standards run and standardization approaches. Different labs have variable measurement procedures, with a range of integration times (less than

400 seconds - to 1200 seconds or more), sample sizes (sub-mg or larger for a single analysis), and replication (3 or less to >8). Standard corrections differ, with some labs averaging standard values over multiple days or weeks for corrections, while other labs characterize short-term drift. Some datasets necessitated the use of transfer functions to convert from CDES to I-CDES reference frames (Tripati et al., 2010; Breitenbach et al., 2018; Peral et al., 2018), which uses average standard δ^{47} values. However, this should contribute < 3 ppm for δ^{47} values within ± 18 ‰ of ETH-1 (Bernasconi et al., 2021).

These foraminiferal calibration data come from six clumped isotope laboratories (Table 1.1) that utilize different instruments and analytical methods. There is particularly strong agreement between data from Tripati et al. (2010), Breitenbach et al. (2018), Meinicke et al. (2020), and this study (Eagle-Tripati lab), that overlap with each other including at the extremes of the highest and lowest temperatures. All of these datasets show more variability at warmer temperatures, which could reflect the larger sample density relative to cold regions.

Each dataset included in this study has regression slopes and intercepts that fall within the 95% confidence intervals of each other (Supplemental Table 1.S.6). Within the foraminiferal data synthesis for 260 samples, dataset-related (i.e., methodological artifacts) account for up to 11% of the variance from our non-thermal R-model based effect size testing. This largely comes from two datasets that are amongst the three smallest in terms of sample numbers (Peral et al., 2018 - 27 samples; Piasecki et al., 2019 - 13 samples). The relatively small sample sizes could potentially explain these offsets, although we cannot preclude that differences in instrumentation and/or standardization during the specific intervals that samples were run may also be a contributing factor. At low temperatures, both the Peral et al. (2018) and reprocessed Peral et al. (2022) results are offset from the other studies, with a slightly steeper slope, while the Piasecki et

al. (2019) benthic foraminiferal values are positively offset from other studies, especially at higher temperatures, and exhibit a shallower slope (Supplemental Table 1.S.6).

3.3.2 Biological

3.3.2.1 Ecology

Here, if we subdivide benthic foraminiferal data by habitat (Figures 1.3 and 1.4), we see that the slopes and intercepts of both the infaunal and epifaunal species individually fall within the 95% confidence intervals of planktic regression slope and intercept. While the mixed benthic species regression does not overlap with the planktic regression 95% CI, this is likely a result of low data density at warmer temperature, an artifact of how measurements were combined between species (e.g., Piasecki et al., 2019), potential mixing effects, or a combination of these factors. It is also possible that some of the data are offset due to other potential non-thermal effects that the benthic population is sampling (e.g., a carbonate ion saturation effect, discussed further below).

3.3.2.2 Taxon-specificity

Temperature proxies including foraminiferal $\delta^{18}O$ and Mg/Ca show that interspecific offsets exist for multiple taxa (e.g., Bemis et al., 1998; Jentzen et al., 2018; Marchitto et al., 2014; Regenberg et al., 2009). Previous studies looking for such effects in Δ_{47} have suggested that there are little to no vital effects on this thermometer (Tripati et al., 2010; Grauel et al., 2013; Peral et al., 2018; Meinicke et al., 2020, Daëron and Gray, 2023). However, this previous work on Δ_{47} has investigated relatively small numbers of species, with limited numbers of localities sampled for each species (typically $n < 7$). Here, with our new data and the meta-analysis, we assess taxon-specific effects using data for 29 species, with $n>20$ for five species.

Our analysis indicates that taxon-specific offsets are not resolvable when subgroups of data are examined (Figure 1.5). If grouped by genus, mean residuals (Δ_{47} observed minus Δ_{47} predicted from the calibration for all foraminifera) for 14 taxa are smaller than +/-0.005 ‰, and for all but one taxa are less than +/-0.01 ‰. At the genus level, residuals are indistinguishable from a normal distribution at the 95% confidence level for 10 out of 12 genera, the exceptions being *Trilobatus* and *Uvigerina* where there is a skewness of -0.10 and -2.03 respectively. The skew in the data for *Uvigerina* (n = 9) is driven by a single point that lies far outside the rest of the samples. *Trilobatus* comprises two species and when these are looked at individually, each species is not distinguishable from a normal distribution at the 95% confidence level (*Trilobatus sacculifer:* W = 0.94203831, p = 0.09396572; *T. trilobus:* W = 0.97780615, p = 0.88903859), but when combined reflect a larger trend in the overall dataset of a minor skew to the left (Figure 1.S.9).

If considered at the species-level, mean species residuals for 17 taxa are smaller than +/-0.005 ‰, and for all but 5 taxa are less than 0.01 ‰. Residuals are indistinguishable from a normal distribution other than *N. pachyderma* (Shapiro-Wilk test, p > 0.05). For the five species represented at a large number of localities (*P. obliquiloculata, T. sacculifer, G. tumida, G. bulloides, G. ruber)*, mean residuals are less than 0.005 ‰ (Figure 1.5, 1.S.9). All but one species exhibit residuals within +/-0.02 ‰, which is the long-term standard deviation for standards reported for different instruments and by multiple labs (e.g., Meckler et al., 2014; Bernasconi et al., 2021; Upadhyay et al., 2021). These residuals are normally distributed for all taxa that have a large number of samples.

We note that the taxa with larger residuals and non-normal distributions could bias the regression, and thus, we assessed impacts of individual species on the slope and intercept of the overall calibration line by removing species individually from the calculation and reporting the

resulting values, following the approach of Meinecke et al. (2020). When using this approach, both slopes and intercepts remain well within error of the primary regression, suggesting that individual taxa are not unduly influencing the regression (Supplemental Table 1.S.6).

We investigated other potential biological effects on Δ_{47} associated with mineralogy and photosymbionts. *H. elegans* is an aragonitic species of foraminifera and was measured in multiple studies. However, we do not observe any systematic offsets of data from this species (Figure 1.5, Supplemental Table 1.S.6). Photosymbiosis in foraminifera affects both calcification rates and microenvironments (de Nooijer et al., 2014) and has the potential to cause disequilibrium isotopic values (e.g., Spero et al., 1997). We do not observe systematic offsets when comparing non-photosymbiont bearing species and photosymbiont bearing species at the 95% confidence interval (Figure 1.S.10).

3.3.2.3 Oceanic region

Given basin-specific Mg/Ca calibrations (e.g., Skinner et al., 2007) and region-specific genotypes (Sadekov et al., 2016; Darling et al., 2017), we explored whether geography impacted calibration in the meta-analysis. For all regions with large numbers of samples (Atlantic Ocean, Pacific Ocean, Indian Ocean, Gulf of Mexico), 95% confidence intervals overlapped with the broader foraminiferal calibration (Figure 1.S.11). The Arctic Ocean contains only a small number of samples and a limited temperature range so the uncertainties in a basinal calibration are large, and additional calibration material from this region (and other high latitude areas) are critical.

3.3.3 Seawater Chemistry

Given evidence for seawater chemistry impacts on Mg/Ca, we explore if there are discernable effects of seawater chemistry on Δ_{47} in foraminifera. We first used PCA to assess

how much variance in hydrographic parameters as potential predictors can be attributed to different factors, and whether any potential model components are strongly correlated with one another. We find no evidence of such correlations between hydrographic parameters, when investigating temperature, salinity, carbonate saturation, and depth (Figure 1.S.12). Below, we describe the relationship between Δ_{47} residuals and salinity. We also examine if in benthic foraminifera, Δ_{47} is correlated with saturation state.

3.3.3.1 Salinity

Salinity variation has been shown to affect Mg/Ca sensitivity by around 4.5 % per salinity unit depending on the species (e.g., Ferguson et al., 2008; Hönisch et al., 2013). A small salinity effect on Δ_{47} associated with the salinity-dependence of dissolved inorganic carbon (DIC) speciation has been predicted from theory, but was not thought to be impactful over the salinity range of the oceans (Tripati et al., 2015). Consistent with this prediction, previous studies on clumped isotopes in foraminifera that had small sample sizes suggest no detectable correlation with salinity (Grauel et al., 2013; Peral et al., 2018).

We examined the larger dataset to see if a salinity effect was detectable. Foraminifera from this study cover a salinity range of 33.0 to 38.8 PSU and as a whole similarly show no clear correlation of salinity with Δ_{47} residuals (Pearson's correlation *p*-value = 0.77, Figure 1.S.13). These results support theoretical predictions (Tripati et al., 2015). However, Pearson's correlation between the two variables has a *p*-value of 0.01 for the benthic data. This correlation does not appear in the planktic data. Analysis of the correlation between temperature and salinity ranges in the benthic data suggest that the correlation observed may be due to offsets in temperature trends observed in section 3.2.2 rather than a true salinity effect (Figure 1.S.13).

3.3.3.2 Carbonate saturation effects on benthics

Seawater carbonate chemistry has been shown to impact benthic foraminiferal Mg/Ca (Elderfield et al., 2006). A number of approaches have been used to detect such an effect, including direct comparisons of benthic Mg/Ca to seawater $\Delta[CO_3^{2-}]$, a comparison of temperature-corrected Mg/Ca to $\Delta[CO_3^{2-}]$, as well as the use of a multiple linear regression to examine the sensitivity to temperature and carbonate ion (Elderfield et al., 2006). Based on culturing studies, a carbonate ion effect in $\delta^{18}O$ has been observed in planktic foraminiferal calcite and coral aragonite (Spero et al., 1997). In benthic foraminifera, disequilibrium in $\delta^{18}O$ can systematically vary between taxa, linked to carbonate ion (Bemis et al., 1998; Ishimura et al., 2012; Rathman and Kuhnert, 2008). For $\delta^{18}O$, this disequilibrium is hypothesized to be related to changes in the isotope composition of the dissolved inorganic carbon pool as a function of pH (Zeebe, 1999).

When we compare benthic Δ_{47} residuals ($\Delta_{47observed}$ minus $\Delta_{47calculated}$ using the foraminiferal temperature calibration equation from our meta-analysis) to $\Delta[CO_3^{2-}]$ (Figure 1.6), we find a significant positive correlation, consistent with a weak sensitivity of benthic Δ_{47} to changing carbonate ion (Figure 1.6B; slope = 0.00019, R^2 = 0.315, p <0.01). We note that the correlation largely reflects a significant relationship in the epifaunal benthic foraminiferal data significant at the >95% confidence level (Figure 1.6C; slope = 0.00018, R^2 = 0.315, p = 0.043, n = 19), and in the mixed benthics data (Figure 1.6E; slope = 0.00022, R^2 = 0.482, p <0.01, n = 24). The data showing this trend were generated as part of this study and by Piasecki et al. (2019) (Figure 1.6A). No significant correlation is found at the >95% confidence level in the infaunal benthic data (Figure 1.6D).

If we directly compare benthic Δ_{47} to $\Delta[CO_3^{2-}]$, a significant but weak (p=0.01, R^2=0.09) is observed in the meta-analysis (Figure 1.S.14). This pattern is similar to what was reported for

benthic Mg/Ca (Elderfield et al., 2006). However, different sub-groups of the benthic foraminiferal data (e.g., epifaunal benthics, infaunal benthics, etc.) do not exhibit significant linear correlations, but this may not be surprising if an effect is present but relatively weak.

We developed benthic multivariable regressions that account for a dependence of Δ_{47} on both temperature and $\Delta[CO_3^2]$, in the form of Δ_{47} (‰) = $\beta 0 + \beta 1 \times 10^6/\text{Temperature (K)}^2 + \beta 2 \times \Delta[CO_3^{2-}]$ (Table 1.4 and Figure 1.7). These analyses also support sensitivities of Δ_{47} to $\Delta[CO_3^{2-}]$ that are generally similar in magnitude to those derived using other methods (e.g., regressing Δ_{47} residuals against $\Delta[CO_3^{2-}]$), with values of 0.0017 for all benthic foraminifera, 0.0015 for all benthic foraminifera (epifaunal and infaunal benthics), 0.0019 for epifaunal benthic foraminifera, and 0.0013 for infaunal benthic foraminifera (Figure 1.7, Table 1.4).

3.3.4 R-based model selection

3.3.4.1 Evaluation of non-thermal effects in UCLA dataset

The benthic foraminiferal dataset from the Eagle-Tripati lab at UCLA (n = 42) is best explained by a model with temperature as the sole predictor ($F_{1,40} = 64.6$, SE = 0.01, Adjusted $R^2 = 0.608$, $p < 0.00001$; Supplemental Table 1.S.7). If planktic foraminiferal Δ_{47} from the UCLA dataset is considered, the signal is best explained by an additive model containing temperature, bottom water carbonate saturation (i.e., a dissolution effect), and photosymbiont presence/absence ($F_{3,78} = 50.9$, SE = 0.01, Adjusted $R^2 = 0.649$, $p < 0.00001$; Supplemental Table 1.S.7). Temperature explains the vast majority of the variation in Δ_{47} (Partial $\eta^2 = 0.57$, lower 95% CI 0.46; Supplemental Table 1.S.7), followed by bottom water carbonate saturation and photosymbiont presence/absence, which both have a "medium" effect, and return the same effect size and lower 95% CI (Partial $\eta^2 = 0.06$, lower 95% CI 0.0). Temperature has a large positive effect of 0.029 ± 0.003 ‰ on Δ_{47} for each 1 σ increase. Bottom water carbonate saturation in the

linear model exhibits a slight positive effect of 0.006 ± 0.003 ‰ on Δ_{47} per 1 σ increase in carbonate ion saturation. Photosymbiont presence produces a slight positive offset in Δ_{47} relative to taxa who lack photosymbionts of 0.009 ± 0.004 ‰.

3.3.4.2 Statistical model investigation of non-thermal effects in meta-analysis of benthic and planktic foraminifera

Benthic foraminiferal Δ_{47} in the meta-analysis (n = 67) is best explained by the additive effects of temperature, bottom water carbonate saturation, and salinity ($F_{3,63}$ = 54.4, SE = 0.01, Adjusted R^2 = 0.708, p <0.00001). Temperature again explains the vast majority of the variation in Δ_{47} (Partial η^2 = 0.60, lower 95% CI 0.47; Supplemental Table 1.S.7), followed by carbonate saturation (Partial η^2 = 0.25, lower 95% CI 0.11), and salinity (Partial η^2 = 0.08, lower 95% CI 0.01). Temperature has a positive effect on Δ_{47} of 0.022 ± 0.002 ‰ for each 1 σ increase; carbonate saturation has a slight positive effect of 0.009 ± 0.002 ‰; and salinity has a slight negative effect of 0.005 ± 0.002 ‰. We found no evidence of a significant effect of benthic foraminiferal habitat (epifaunal versus infaunal) on the final Δ_{47} signal (Estimate = -0.0001, Std err = 0.004, t = -0.033, p = 0.97).

For the meta-analysis, planktic foraminiferal Δ_{47} (n = 193) is explained by multiple variables. Model selection identified three-way interactions between temperature, dataset, and bottom water carbonate saturation; and temperature, bottom water carbonate saturation (i.e., dissolution), and photosymbiont presence/absence ($F_{23,169}$ = 31.6, SE = 0.01, Adjusted R^2 = 0.786, p <0.00001). Temperature explains the vast majority of the variation in Δ_{47} (Partial η^2 = 0.62, lower 95% CI 0.55; Supplemental Table 1.S.6), followed by the interaction between dataset and bottom water carbonate saturation (Partial η2 = 0.21, lower 95% CI 0.11); dataset alone and the three-way interaction between temperature, dataset, and carbonate saturation (Partial η2 =

0.15, lower 95% CI 0.07); (Both: Partial η^2 = 0.14, lower 95% CI 0.06); carbonate saturation alone (Partial $\eta 2$ = 0.10, lower 95% CI 0.04) and the two-way interaction between temperature and carbonate saturation (Partial η^2 = 0.06, lower 95% CI 0.01), with all other combinations having an effect size of 0.04 or less.

3.3.4.3 Statistical model investigation of non-thermal effects in full foraminiferal dataset

R-based model selection indicates that temperature effects vastly outweigh non-thermal signals in the full foraminiferal dataset (n = 260) (Supplemental Table 1.S.6). Non-thermal effects can account for up to 13% of the variance in the dataset if all other variables are held constant. Foraminiferal Δ_{47} is best explained by temperature, plus the effects of three two-way interactions (foraminiferal type and bottom water carbonate saturation; dataset and depth; dataset and photosymbiont presence/absence; $F_{20,239}$ = 60.8, SE = 0.01, Adjusted R^2 = 0.822, p <0.00001; Supplemental Table 1.S.6). Temperature has a positive effect on Δ_{47} of 0.028 ± 0.001 ‰ for each 1 σ increase. The interaction between dataset and depth accounts for 13% of the variance (Partial η^2 = 0.13, lower 95% CI 0.06, followed by dataset alone, which accounts for 10% of the variance in Δ_{47} (Partial η^2 = 0.10, lower 95% CI 0.03). All other model terms have a partial η^2 of 0.05 or less.

3.4 Vertical profiles of temperature reconstructed from core-top planktics

We assess the utility of using foraminiferal Δ_{47}-derived temperature estimates in reconstructing oceanic water column thermal properties in different oceanographic regions. For planktics, Δ_{47}-temperature estimates are calculated using the full foraminiferal regression from the meta-analysis. We compared WOA temperature profiles with Δ_{47}-reconstructed temperatures from multiple species we analyzed from the Arctic Ocean, North Atlantic, Indian Ocean, and Western Equatorial Pacific (Figure 1.8; Figures 1.S.15-1.S.17). Reconstructed temperatures are

plotted at assumed calcification depths for each taxa at each site (Figure 1.8, Supplemental Table 1.S.2). A cross comparison of Δ_{47}-temperature and expected temperature based on calcification depth shows good agreement (slope of 0.99 ± 0.03, $R^2 = 0.75$ and $p < 0.001$).

Most Δ_{47}-temperatures plot within error of measured water temperature profiles. With the exception of the Arctic data, there is little indication of seasonality being resolvable using this method because typically, the uncertainty in Δ_{47}-temperatures is greater than the seasonal extremes of temperatures at the sites chosen. Interestingly, in the case of near freezing temperatures, our results show no systematic offset from the measured site temperatures which suggests that there is no observed isotopic offset introduced by calcification at these cold temperatures in foraminifera suggested in other studies (Tripati et al., 2010), although it should be noted that samples in this region are limited only to the species *N. pachyderma*.

3.5 Recalculating Cenozoic bottom water temperatures using new calibrations

Daeron and Gray (2023) and Rohling et al. (2024) discuss some of the differences between published reconstructions of bottom water temperatures from benthic foraminiferal Δ_{47} and $\delta^{18}O$, including discrepancies between proxy predictions for the Late Paleocene, Eocene, Eocene-Oligocene transition, and Pleistocene, highlighting the importance of utilizing new calibration data and constraints from carbonate chemistry in such calculations. Thus, here we apply the new calibrations to benthic foraminiferal data and evaluate Δ_{47}-temperatures and seawater water $\delta^{18}O$. We recalculate Cenozoic temperatures with low-resolution benthic Δ_{47}-data from Meckler et al. (2022) for the North Atlantic from IODP Expedition 342 (Sites 1406, 1407, 1409, and 1410) on the CENOGRID timescale (Westerhold et al., 2020). We recalculate Eocene-Oligocene temperatures using benthic Δ_{47}-data from Taylor et al. (2023) for ODP Site 1218 and IODP Sites U1333 and U1334 from the Pacific and the ages reported therein.

Below, we discuss results from the different calibration approaches for the Pleistocene (Section 3.5.1), Eocene-Oligocene transition (Section 3.5.2), Early Eocene Climatic Optimum (Section 3.5.3), and Paleocene (Section 3.5.4). We also calculate the potential scope of impacts on benthic reconstructions for the PETM (Section 3.5.5). In each section, we compare the originally published benthic Δ_{47}-reconstructions that utilize the planktic calibration of Meinicke et al. (2020) to values calculated using (1) the new Δ_{47}-temperature calibrations and (2) the new benthic multivariate Δ_{47} calibration that also factor changes in carbonate chemistry into estimates of temperature and seawater $\delta^{18}O$ (Supplemental Table 1.S.8-1.S.10). For the latter, to constrain changes in carbonate chemistry, one can use site- or region-specific estimates of bottom water carbonate saturation based on Li/Ca or B/Ca data from benthic foraminifera (Lear and Rosenthal, 2006, Yu et al., 2007), which is the approach we use in Section 3.5.2 (the Eocene-Oligocene transition) because Li/Ca data were available. Another approach that may be less accurate is to utilize a combination of constraints on two different carbonate system parameters using proxy and/or carbon cycle model calculations (e.g., Meckler et al., 2022; Roberts and Tripati, 2009; Tyrell and Zeebe, 2004). This first-order calculation of the impact of $[CO_3^{2-}]$ on Δ_{47}-temperatures is what we utilize for the other sections. We calculated $[CO_3^{2-}]_{in\ situ}$ using CO_2sys excel (v. 2.3. Pierrot et al. 2016) and published constraints on pCO_2 and Total alkalinity (Supplemental Table 1.S.8). pCO_2 was interpolated from a 50 points average record from Hönisch et al. (2023) based phytoplankton and boron isotopes. Total alkalinity was interpolated using the published record from Tyrell and Zeebe (2004). The precipitation constant for calcite (Ksp, Mucci et al. 1983) was calculated using a constant salinity of 35 and the published temperature from clumped isotopes. $[CO_3^{2-}]_{sat}$ was then determined for Ω=1 and $[Ca^{2+}]$ interpolated from Horita et al. (2002).

3.5.1 Cooler Pleistocene temperatures calculated using new benthic Δ_{47}-temperature calibrations

Pleistocene temperatures estimated by Meckler et al. (2022) range from -0.3 °C to 3.4 °C, and average 1.6 °C (Figure 1.9, Supplemental Table 1.S.9). All of the new Δ_{47}-temperature calibrations yield cooler estimates of Pleistocene temperatures (Figure 1.9, Supplemental Table 1.S.9). For example, the "all foraminifera-MB" regression gives similar values to the temperature calibration from Anderson et al. (2021) for the Pleistocene, with Δ_{47}-temperatures ranging from -1.8 to 1.6 °C for the "all foraminifera-MB" and -1.5 to 1.9 °C using the Anderson et al. (2021) regression. Temperatures calculated using the "all benthics" calibration range from -5.1 to 0.5 °C and the "infaunal" regression from -2.3 to 1.3 °C. The "all benthics (infaunal + epifaunal)" and "epifaunal" regressions yield similar results to each other for the Pleistocene, with temperatures ranging from -3.1 to 0.6 °C for "all benthis (infaunal + epifaunal)" and from -3.8 to 0.3 °C for "epifaunal". The full foraminifera calibration supports temperatures in between -2.2 to 1.3 °C.

Estimates of $\delta^{18}O_{sw}$ from these calibrations are lower than those estimated from Meckler et al. (2022), with values of 0.44 ‰ for the "all foraminifera - MB" calibration, 0.71 ‰ for the "All benthic (infaunal + epifaunal)" regression, 0.85 ‰ for the "epifaunal" regression, and 0.54 ‰ for the "infaunal" regression (Figure 1.9, Supplemental Table 1.S.9). For the "compiled benthic", "All benthics (infaunal + epifaunal)", and "epifaunal" regressions, the average $\delta^{18}O_{sw}$ is negative (Figure 1.9, Supplemental Table 1.S.9). Note that negative $\delta^{18}O_{sw}$ values for the Pleistocene are not likely given that average global ice-volumes are expected to be between interglacial and glacial extremes, which should lead to positive $\delta^{18}O_{sw}$ values (Cramer et al., 2011).

3.5.1.1 Pleistocene temperatures from the new benthic multivariate Δ_4-calibration

Figure 1.11 shows Pleistocene values of temperature that are calculated using the "All benthic (infaunal + epifaunal)" multivariate calibration. Pleistocene Δ_{47}-temperatures for the Atlantic range from -0.7 °C to 3.0 °C, in better agreement with the temperature estimates from Meckler et al. (2022) (Figure 1.11, Supplemental Table 1.S.8). Estimates of $\delta^{18}O_{sw}$ range from -0.09 to 1.14 ‰ and average 0.55 ‰. The positive $\delta^{18}O_{sw}$ predicted by the multivariate regression is in better agreement with estimates of ice volumes from the Pleistocene (Cramer et al., 2011).

3.5.2 Cooler Eocene-Oligocene bottom water temperatures from the new benthic Δ_{47}-temperature calibrations

We recalculate tropical Pacific Ocean bottom water temperatures using benthic Δ_{47} data from Taylor et al. (2023) (that used the planktic calibration of Meinicke et al., 2020) for ODP Site 1218 and IODP Sites U1333 and U1334. These sites were located at a paleodepth of 3500 to 4000 m. This transition is associated with the permanent establishment of large ice sheets on Antarctica and a ~1 km deepening of carbonate compensation depth in the Pacific Ocean (Coxall et al., 2005). It is thought that the deepening of the carbonate compensation depth was global (Tripati et al., 2005) and associated with a rise in $[CO_3^{2-}]$ (Pusz et al., 2011). Taylor et al. (2023) report late Eocene Δ_{47}-temperatures of 11.0 °C and Earliest Oligocene temperatures of 9.7 °C, with a change across the Early Oligocene Oxygen Isotope Step (EOIS, absolute temperature of 6.5 °C) of -4.7 ± 0.9 °C.

We apply the new foraminiferal Δ_{47}-temperature calibrations, with recalculated values shown in Supplemental Tables 1.S.9-1.S.10 and Figure 1.9. Overall, all of the new (non-multivariate) benthic Δ_{47}-T calibrations result in absolute temperatures that are cooler by ~2-2.5 °C, compared to what was originally reported by Taylor et al. (2023) using the planktic

calibration of Meinicke et al. (2020). The amplitude of changes in temperature and $\delta^{18}O_{sw}$ are slightly larger or similar to what was published by Taylor et al. (2023).

3.5.2.1 Lower $\delta^{18}O_{sw}$ values using the new benthic Δ_{47}-temperature calibrations

The Taylor et al. (2023) estimates of late Eocene $\delta^{18}O_{sw}$ are 0.35 ‰ to 0.89 ‰ for the early Oligocene. They report an increase of $\delta^{18}O$ seawater of 0.07 ‰ over EOIS and a change of 0.54 ‰ across the transition. As reference, a change of 0.6 ‰ across the transition is estimated to lead to a change of ice volume on the order of 70 %–110 % relative to modern. The new benthic benthic Δ_{47}-temperature calibrations yield absolute $\delta^{18}O_{sw}$ values are ~0.4 to 0.6 ‰ lower, and the changes in $\delta^{18}O_{sw}$ are slightly larger or similar to what was published (Supplemental Table 1.S.9).

A puzzling pattern emerges when looking at calculated changes in $\delta^{18}O_{sw}$ in more detail, specifically if we look at the values of $\delta^{18}O_{sw}$ associated with the EOIS from the different calibrations. We would expect a positive change in $\delta^{18}O_{sw}$ associated with the oxygen isotope step, given the growth of ice, yet some of the new regressions, from “all benthic-MB", “all benthic”, “infaunal” and “epifaunal”, yield negative changes in $\delta^{18}O_{sw}$ associated with the EOIS, although they do give positive changes across the broader EOT. For example, the “all benthic-MB” calibration gives late Eocene mean temperatures of 9.3 °C, a temperature change associated with the EOIS of -4.6 °C and an associated $\delta^{18}O_{sw}$ change of 0.04 ‰, and a change across the EOT of 0.53 ‰ (Supplemental Table 1.S.9). The “epifaunal” calibration yields 9.6 °C, with a -5.5 °C change and a -0.18 ‰ $\delta^{18}O_{sw}$ change across the EOIS, and a 0.47 ‰ change across the transition.

3.5.2.2 Reasonable Δ_{47}-T and $\delta^{18}O_{sw}$ values from the new benthic multivariate Δ_4-calibration

The most robust absolute values and patterns of change in temperature and $\delta^{18}O_{sw}$ are reconstructed using the All benthic (infaunal + epifaunal) multivariate equation. To apply the multivariate calibration, we utilize a series of constraints. Estimates of the increase in $[CO_3^{2-}]$ derived from Li/Ca ratios in benthic foraminifera associated with the Oi-1 glaciation range from ~36 umol/kg at ODP Site 1218 in the equatorial Pacific Ocean (Lear et al., 2010; Lear and Rosenthal, 2006) to ~29 umol/kg at ODP Site 1263 in the South Atlantic on Walvis Ridge (Peck et al., 2010). Modern carbonate profiles in this region have a bottom water $[CO_3^{2-}]$ = 81 µmol/kg (GLODAP database corrected from anthropogenic inputs, modern profiles), $[CO_3^{2-}]_{sat}$ = 87 µmol/kg, and a $\Delta[CO_3^{2-}]$ = -6 µmol/kg. If we apply the estimated change in $[CO_3^{2-}]$ from ODP Site 1218 across the Eocene-Oligocene Transition, we calculate a $\Delta[CO_3^{2-}]$ from -6 to 30 µmol/kg.

Compared to Taylor et al. (2023), the absolute temperatures are cooler, the amplitude of cooling associated with the EOIS is reduced, and changes in $\delta^{18}O_{sw}$ with the EOIS are positive and reasonable in magnitude (Supplemental Table 1.S.10). At ~33.65 Ma, the coolest temperatures of the transition are reconstructed, with absolute bottom water temperatures estimated as 3.9 °C, instead of 6.5 °C. We estimate a cooling of 4.1 °C associated with the EOIS (Figure 1.9), rather than the 4.7 °C change reported by Taylor et al. (2023). These calculations use a pre- EOIS value of $\Delta[CO_3^{2-}]$ = -6 µmol/kg, and EOIS value of $\Delta[CO_3^{2-}]$ = 30 µmol/kg. The recalculated $\delta^{18}O_{sw}$ values (Figure 1.9, Supplemental Table 1.S.10) support a positive excursion associated with the EOIS, as expected based on evidence for a major expansion of continental ice. The absolute values change from an average of -0.47 to 0.21 ‰ post-transition, with a change of 0.67 ‰, which is similar to the change in Taylor et al. (2023). The calculations do

change the $\delta^{18}O_{sw}$ prior to the EOIS which is still closer to but still higher than anticipated based on theoretical calculations of and ice-free world (e.g., -0.9 to –1.2 ‰, Cramer et al., 2011), that could support the presence of some ice storage before this time.

3.5.3 Cooler Early Eocene Climatic Optimum temperatures from the new benthic Δ_{47}-temperature calibrations

Some of the warmest temperatures in the Cenozoic occurred during the Early Eocene Climatic Optimum (EECO; ~52 Ma), based on benthic foraminiferal $\delta^{18}O$ (Zachos et al. 2001). For the interval from 53 to 51 Ma, published (Meckler et al., 2022) Δ_{47}-temperatures for the Atlantic Ocean range from 10.4 to 20.6 °C and $\delta^{18}O_{sw}$ values range from –1.6 to 0.7 ‰, while average EECO temperatures estimated using benthic Δ_{47} are 16.2 °C and $\delta^{18}O_{sw}$ estimates average –0.3 ‰. These Δ_{47}-temperatures use the Meinicke et al. (2020) calibration and are 2-3 °C warmer than foraminiferal $\delta^{18}O$-based estimates, prompting studies to suggest there may be uncertainties in the calibration used, effects relating to carbonate chemistry, and/or warm saline deep water (Meckler et al., 2022; Daeron and Gray, 2023; Rohling et al., 2024).

Using the new benthic Δ_{47}-temperature regressions yields temperatures that are about ~1°C cooler, with temperatures ranging from 8.6 to 23.7 °C for the Early Eocene (Figure 1.9, Supplemental Table 1.S.9). Average EECO temperatures of 14.6 °C and seawater $\delta^{18}O_{sw}$ values of -0.64 ‰ are estimated using the “all foraminifera” calibration, while values of 15.3 °C and -0.51 ‰ are reconstructed using the “all benthics (infaunal + epifaunal)” calibration, values of 16.1°C and -0.34 ‰ from the “epifaunal” calibration and 15.0 °C and -0.58 ‰ from the “infaunal” calibration (Figure 1.9, Supplemental Table 1.S.9). With a pH correction for carbonate $\delta^{18}O$ as described in Meckler et al. (2022), the $\delta^{18}O_{sw}$ decreases further and is closer to expected ice-free predictions of the early Eocene of ~ 0.9 ‰ (Figure 1.11, Supplemental Table

1.S.9) (Cramer et al., 2011). These new temperature estimates are slightly higher than Mg/Ca-derived bottom water temperatures at ODP Site 1263 in the Atlantic, where an average bottom water temperature of 14°C was reported (Lauretano et al., 2018) and are still warmer than $\delta^{18}O$-based temperatures (Meckler et al., 2022; Daeron and Gray, 2023; Rohling et al., 2024).

3.5.4 Cooler Paleocene temperatures from the new benthic Δ_{47}-temperature calibrations

Similar to the early Eocene, the Paleocene is characterized by warm global temperatures and ended with the first of a series of hyperthermals defining the transition into the Eocene, the Paleocene-Eocene Thermal Maximum (PETM) (Zachos et al. 2001). For the interval from 65 to 56 Ma, published (Meckler et al., 2022) Δ_{47}-temperatures for the Atlantic Ocean range from 10.9 to 19.9 °C and $\delta^{18}O_{sw}$ values range from -0.35 to 1.33 ‰, while average temperatures estimated using benthic Δ_{47} are 15.2 °C and $\delta^{18}O_{sw}$ estimates average 0.45 ‰. These Δ_{47}-temperatures use the the Meinicke et al. (2020) planktic calibration and are also 2-3 °C warmer than foraminiferal $\delta^{18}O$-based estimates (Meckler et al., 2022; Daeron and Gray, 2023; Rohling et al., 2024).

Applying the new benthic Δ_{47}-temperature regressions to the published Δ_{47} data yields temperatures that are about ~1.5 °C cooler than what was originally reconstructed (Figure 1.9, Supplemental Table 1.S.9). Average Paleocene temperatures of 13.6 °C and seawater $\delta^{18}O_{sw}$ values of 0.10 ‰ are estimated using the “all foraminifera” calibration, while values of 14.2 °C and 0.61 ‰ are reconstructed using the “all benthics (infaunal + epifaunal)” calibration, values of 14.9 °C and 0.22 ‰ from the “epifaunal” calibration and 13.9 °C and 0.37 ‰ from the “infaunal” calibration (Figure 1.9). With a pH correction for carbonate $\delta^{18}O$ as described in Meckler et al. (2022), the $\delta^{18}O_{sw}$ values decrease to be closer to ice-free predictions (Figure 1.11e, Supplemental Table 1.S.9). These new estimates are similar to Mg/Ca-derived bottom

water temperatures at during the Paleocene (e.g. Cramer et al., 2011) although still warmer than $\delta^{18}O$-based temperatures (Meckler et al., 2022; Daeron and Gray, 2023; Rohling et al., 2024).

3.5.5 Potential effects on Paleocene-Eocene Thermal Maximum (PETM) Δ_{47}-temperatures

Although there currently are no clumped isotope reconstructions published for the PETM, here, we conduct a preliminary assessment of the potential magnitude of effects on Δ_{47}-temperatures. We used $[CO_3^{2-}]$ from Zeebe and Zachos (2007) from nine sites, $[CO_3^{2-}]_{sat}$ based on site paleodepths, and the epifaunal benthics multivariable regression to explore the magnitude of potential temperature biases (Table 1.5). Temperature biases from site-specific $\Delta[CO_3^{2-}]$ values were calculated for three temperatures (15, 20, 35 °C), and are presented in Table 1.5. For example, the bias in temperature from $\Delta[CO_3^{2-}]$ ranging from -25 to -5 µmol/kg could lead to a PETM temperature overestimation by 3.2 to 4.3 °C, at a reconstructed temperature of 15°C (Table 1.5). Coupling Δ_{47} with site-specific estimates of $\Delta[CO_3^{2-}]$ would facilitate the most accurate determinations of temperature.

3.6 Key takeaways and recommendations for future studies

By roughly doubling the amount of foraminiferal calibration data through new analyses where we measured small samples using the latest analytical procedures and instrumentation, and utilizing the I-CDES reference frame, we are able to rigorously determine temperature calibrations for foraminiferal Δ_{47} with reduced uncertainties and also compare results to a large compilation of synthetic calcite Δ_{47} data over a similar temperature range. We observed no significant difference between the synthetic calcite regression and the composite foraminiferal calibration, consistent with prior findings.

We investigated non-thermal effects using multiple statistical methods and found evidence for weak dependencies on carbonate chemistry. R model selection analysis indicated

the carbonate ion saturation of bottom waters has an impact on the Δ_{47} of planktic foraminifera which could result from dissolution. For benthic foraminiferal reconstructions, we found epifaunal and infaunal data have overlapping confidence bands. The benthic foraminiferal data analyzed here shows a correlation between Δ_{47} residuals and carbonate ion saturation within the overall dataset and in epifaunal benthic foraminifera.

For planktic reconstructions, we recommend use of the composite foraminiferal calibration for temperature reconstructions due to the large sample size (n = 260) and the relevant temperature range for paleoceanographic reconstructions ($\Delta_{47} = 0.0374 \pm 0.0013\ 10^6/T^2 + 0.1744 \pm 0.0154$). We applied this calibration (and others) to core-top planktics to assess the ability of the thermometer to accurately constrain vertical hydrographic profiles for several regions, and this equation typically yields results that are the most accurate. Future studies should investigate any potential species-specific dissolution effects through analysis of transect data or dissolution experiments, and planktic reconstructions could explore the possible scope for dissolution impacts.

For benthic reconstructions, we recommend using the all foraminiferal calibration (no mixed benthics) ($\Delta_{47} = 0.0383 \pm 0.0013\ 10^6/T^2 + 0.1635 \pm 0.0154$) or the all benthics calibration (infaunal + epifaunal) ($\Delta_{47} = 0.0342 \pm 0.0034\ 10^6/T^2 + 0.2149 \pm 0.0431$), given the uncertainties associated with the mixed benthic samples. If $\Delta[CO_3^{2-}]$ can be constrained, through modeling and/or with proxy constraints from Li/Ca or B/Ca, the multivariate all benthics (infaunal + epifaunal) calibration can be used ($\Delta_{47} = 0.03865 \pm 0.00376\ 10^6/T^2 + 0.1518 \pm 0.0493 +0.0001495 \pm 0.0000601$). We also suggest combining estimates of Δ_{47}-temperature derived using this approach with carbonate $\delta^{18}O$ estimates that factor in pH effects on carbonate $\delta^{18}O$, similar to the approach described in Meckler et al. (2022) to calculate seawater $\delta^{18}O$.

4 Conclusions

This study presents new clumped isotope data for foraminiferal core-tops made using recently established best practices with a meta analysis of published data reported on the same reference frame. By performing a meta analysis of planktic and benthic foraminiferal species, we determine possible factors that contribute to variance in Δ_{47}. The lab-specific data and meta-analysis do not show any species-specific offsets. Notably, non-thermal effects, including foraminiferal type and bottom water saturation, dataset and depth, and dataset and photosymbiont presence/absence, only explain ~13% of the variance. However, we show there is evidence for a weak carbonate ion effect on benthic foraminifera.

The regressions described in this study allow for benthic Δ_{47}-based temperature reconstructions to align more reasonably with published $\delta^{18}O$ estimates of bottom water temperatures and inferred climatologies throughout the Cenozoic. In particular, the application of a multivariate regression accounting for a weak carbonate ion effect in benthic foraminifera allows for a first-order investigation of how changes in $\Delta[CO_3^{2-}]$ affect Δ_{47}-based reconstructions for the Pleistocene, Eocene-Oligocene Transition, Early Eocene Climatic Optimum, and late Paleocene. We find that applying this calibration brings both temperature and calculated $\delta^{18}O_{sw}$ into better agreement with model-based deconvolution of benthic foraminiferal carbonate $\delta^{18}O$.

Based on our reconstructions we recommend the use of the composite foraminiferal calibration due to the sample size for planktonic foraminifera reconstructions ($\Delta_{47} = 0.0374 \pm 0.0013\ 10^6/T^2 + 0.1744 \pm 0.0154$), and the regression of the benthic foraminiferal calibration with mixed benthics removed for benthic reconstructions ($\Delta_{47} = 0.0342 \pm 0.0034\ 10^6/T^2 + 0.2149 \pm 0.0431$). For benthic foraminifera, when constraints on $\Delta[CO_3^{2-}]$ are available, we recommend

the multivariate all benthic (infaunal + epifaunal) calibration for reconstructions (Δ_{47} = 0.03865 ± 0.00376 $10^6/T^2$ + 0.1518 ± 0.0493 +0.0001495 ± 0.0000601).

Acknowledgments

We thank Eagle-Tripati lab members past and present for their work running standards, efforts in data entry and mass spectrometry, and contributions to discussions, Cynthia Ulloa, Lina Savage, Lorna Avila, and T.-Y. Chiang with sample preparation, and Ben Elliott for analytical support. This work was funded by Heising-Simons Foundation grant 2022-3314, DOE BES grant DE-FG02-83613ER16402, and NSF grants EAR-0949191, EAR-1352212, and RISE-228198 to Aradhna Tripati and RISE-2024426 to Robert Eagle. All UCLA and Fort Valley State University early career researchers were supported from fellowships granted by The Center for Diverse Leadership in Science supported by the Packard Foundation, Sloan Foundation, Silicon Valley Community Foundation, the Waverley Street Foundation, and NSF (RISE-228198). Hannah Tandy received support from a Schlanger IODP Fellowship, Alexandrea Arnold from a Cota-Robles Fellowship, Hannah Carroll from a NIH IRACDA Fellowship, and Robert Ulrich from an NSF GRFP.

Open Research

All data are in the Supplementary information associated with this paper. In addition, on publication, all data will be archived in Pangaea and EarthChem.

5 Figures

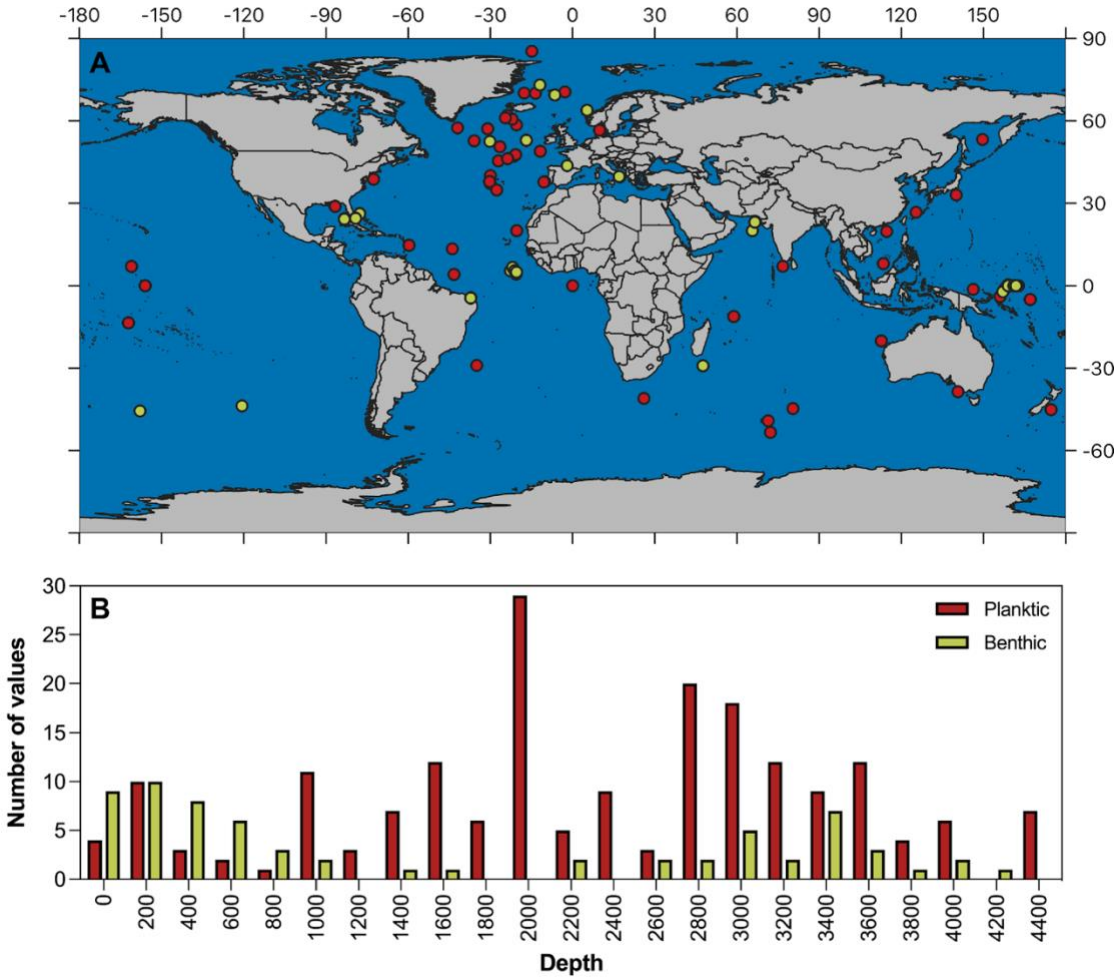

Figure 1.1 Locality information for core-top samples used in this study. Map shows sites and histogram shows water depths. Site information is in Table 1.S.1.

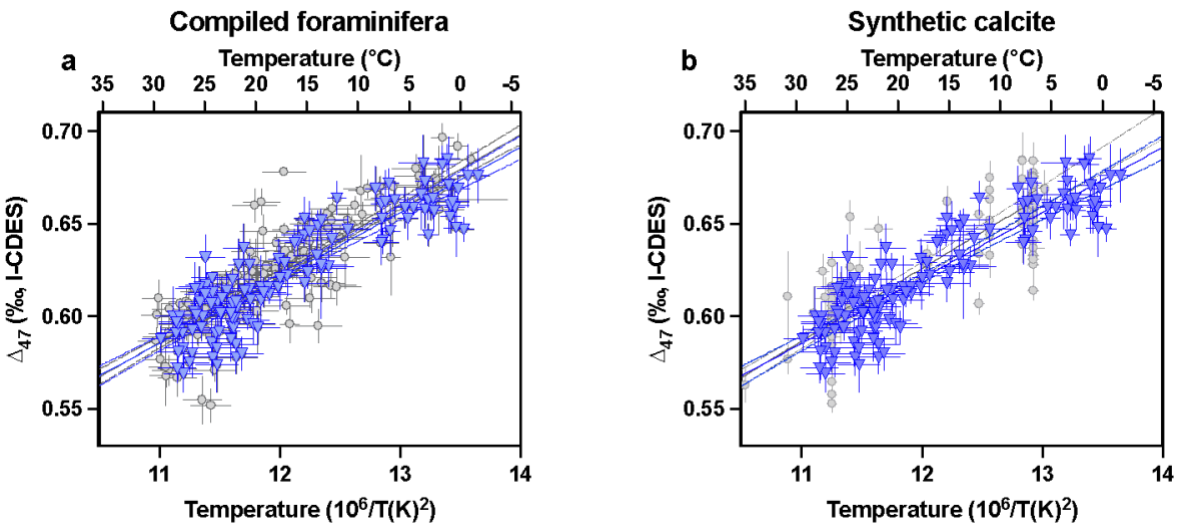

Figure 1.2: Calibration data from this work, including new calibration data (blue) and a meta-analysis of all data (grey) standardized to be on the same reference frame (I-CDES). (a) New calibration data for small foraminiferal samples from the Eagle-Tripati Lab (blue; n = 124) compared to a meta-analysis of all data (grey; n = 260), (b) New foraminiferal data compared to a meta-analysis of synthetic calcite from a similar temperature range (yellow; 0 to 50 ˚C; n = 118). Also shown are 95% confidence bands for the regressions. Individual point errors and coefficient errors are reported as SE. The regression through all foraminiferal data from UCLA (n = 124) is: $\Delta_{47} = 0.0353 \pm 0.0015\ 10^6/T^2 + 0.1973 \pm 0.0187$ while a regression for the full dataset (n = 260) is: $\Delta_{47} = 0.0374 \pm 0.0013\ 10^6/T^2 + 0.1745 \pm 0.0154$. For synthetic calcite (n = 118), the regression between temperature and Δ_{47} yields the equation with standard error: $\Delta_{47} = 0.0393 \pm 0.0014\ 10^6/T^2 + 0.1547 \pm 0.0165$. Regression parameters for all groups of data are in Table 1.3.

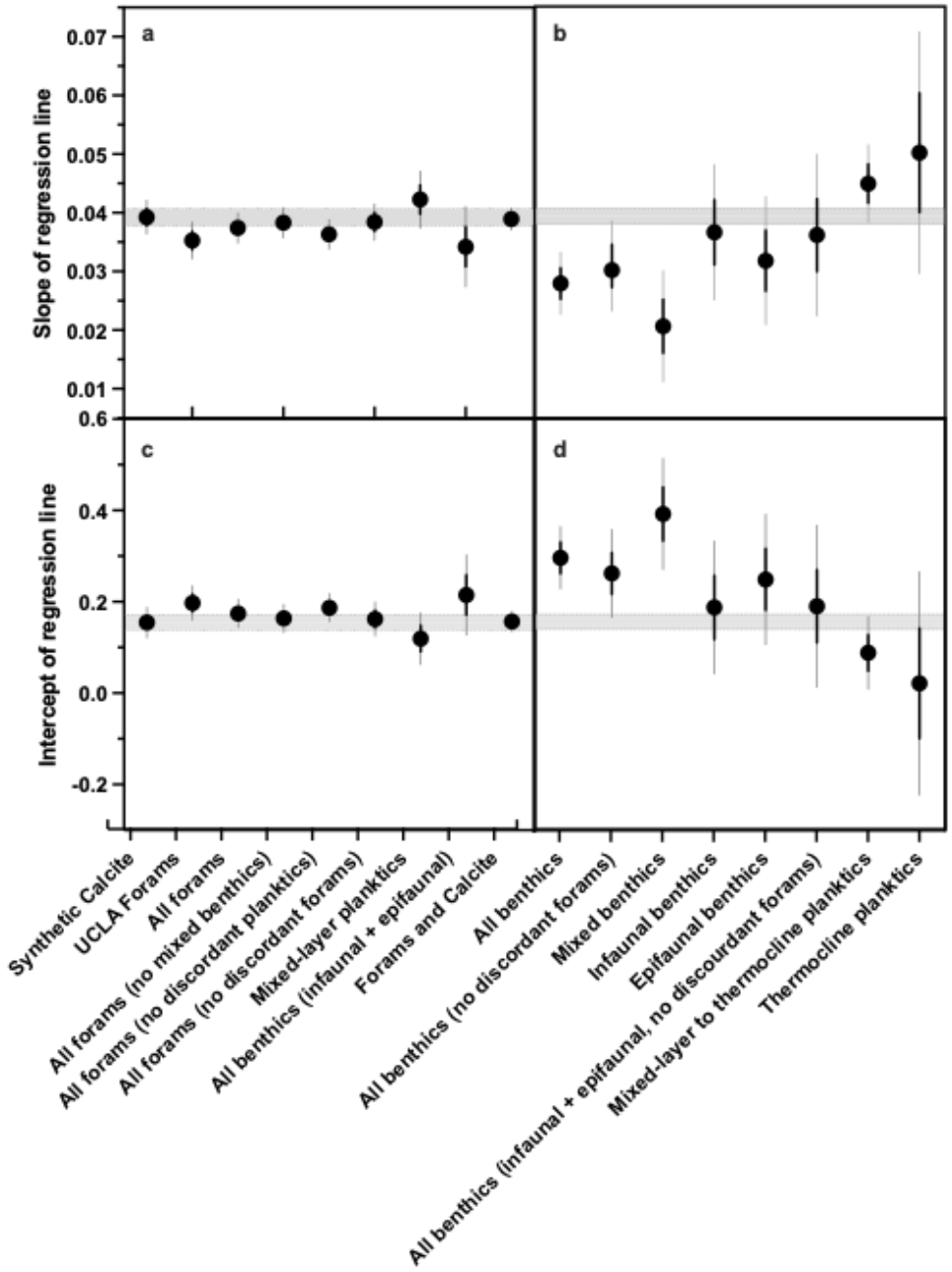

Figure 1.3: Slope and intercept for Δ_{47}-temperature regressions for different data subsets from this study. Results show that regression parameters for datasets that are well constrained (i.e., taxonomically well-defined, with precise estimates of calcification temperature, and with a high n) and other datasets are are indistinguishable from inorganic calcite (horizontal grey bar). These datasets include results for samples that were measured at UCLA, the full foraminiferal dataset, mixed-layer planktics, epifaunal benthics, and infaunal benthics, epifaunal and infaunal benthics, and all foraminiferal data excluding mixed benthics. Panels A and B show slope and intercept for samples that are well constrained, respectively. Panels C and D show slope and intercept for regressions through datasets that contain more poorly constrained samples. Poorly constrained sample groups include groups with low n, groups that are taxonomically more variable, and groups that contain mixed benthic samples. 1 SE is shown in black, 95% CI in gray. Horizontal gray bar is the SE band of the synthetic regression parameters.

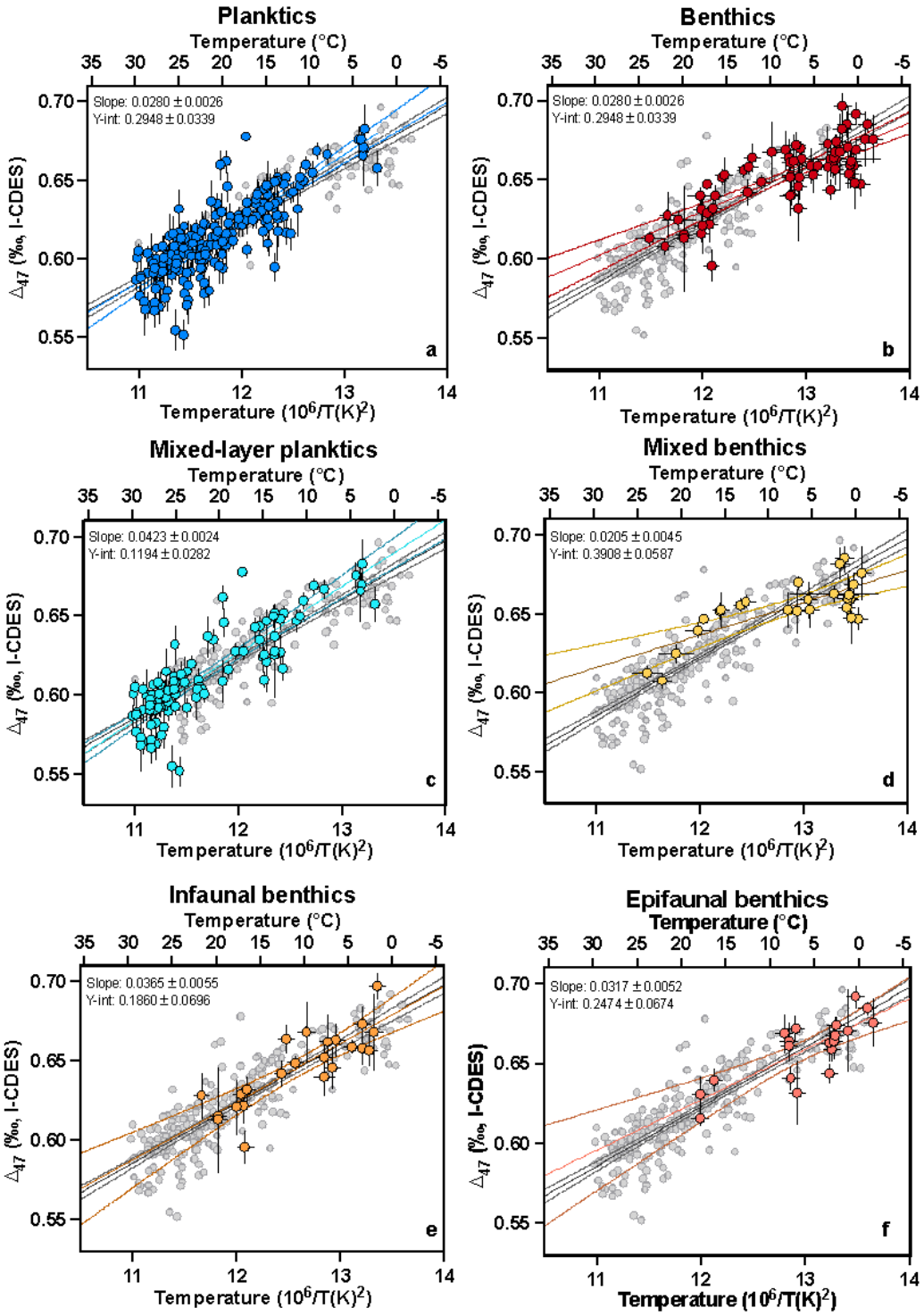

Figure 1.4: Regressions through subsets of core-top foraminiferal data and foraminiferal compilation. All subsets are plotted on top of the foraminiferal compilation (grey) with subsets highlighted as follows: a) Planktic foraminifera b) Benthic foraminifera c) Mixed-layer planktics d) Mixed benthics e) Infaunal benthics f) Epifaunal benthics. 95% confidence interval is also shown.

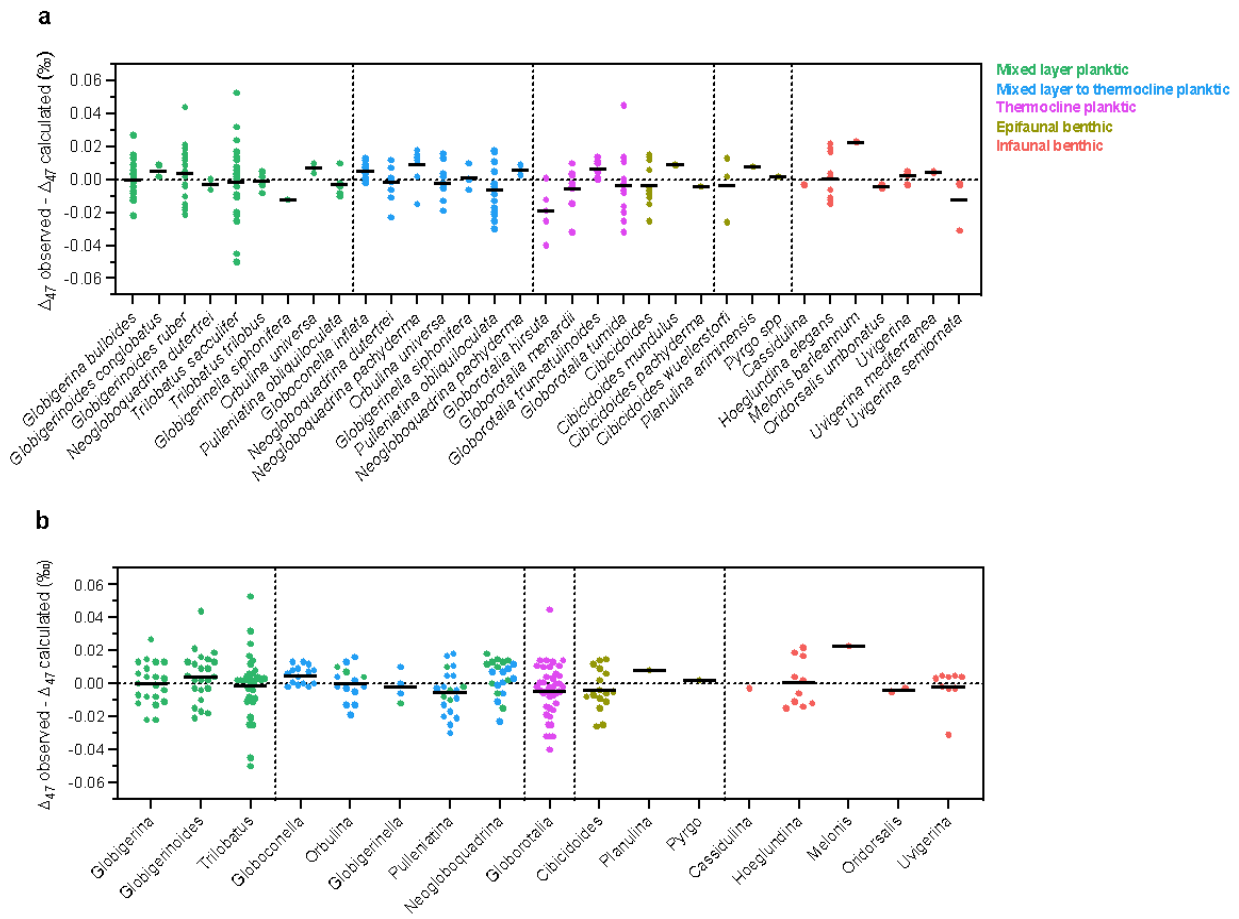

Figure 1.5: Δ_{47} residuals for different taxa calculated as $\Delta_{47observed}$ minus $\Delta_{47calculated}$ using the foraminiferal calibration equation from our meta-analysis. a) Species-specific residuals. b) Grouped genus residuals.

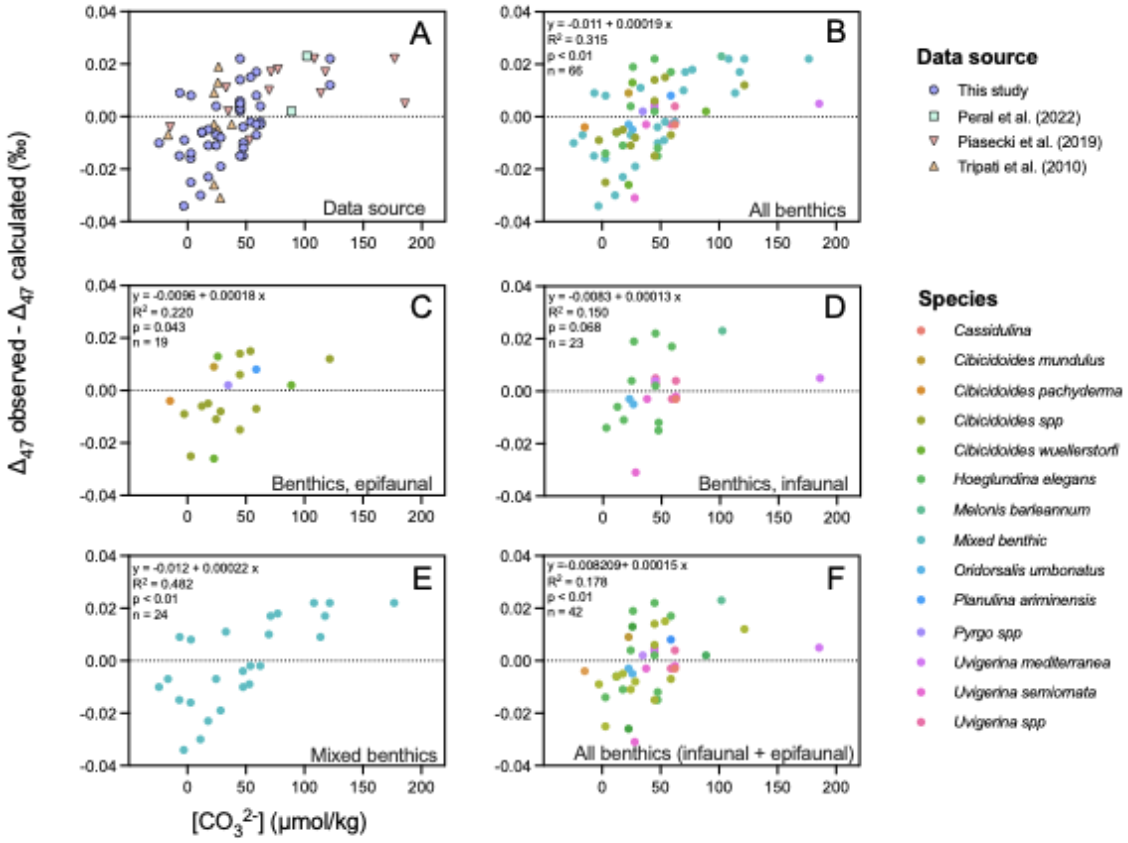

Figure 1.6: Benthic Δ_{47} residuals vs. $\Delta[CO_3^{2-}]$. Residuals calculated as $\Delta_{47observed}$ minus $\Delta_{47calculated}$ using the foraminiferal calibration equation from our meta-analysis. a) Benthics separated by study, b) all benthics, c) epifaunal benthics, d) infaunal benthics, e) mixed benthics, f) all benthics (infaunal + epifaunal).

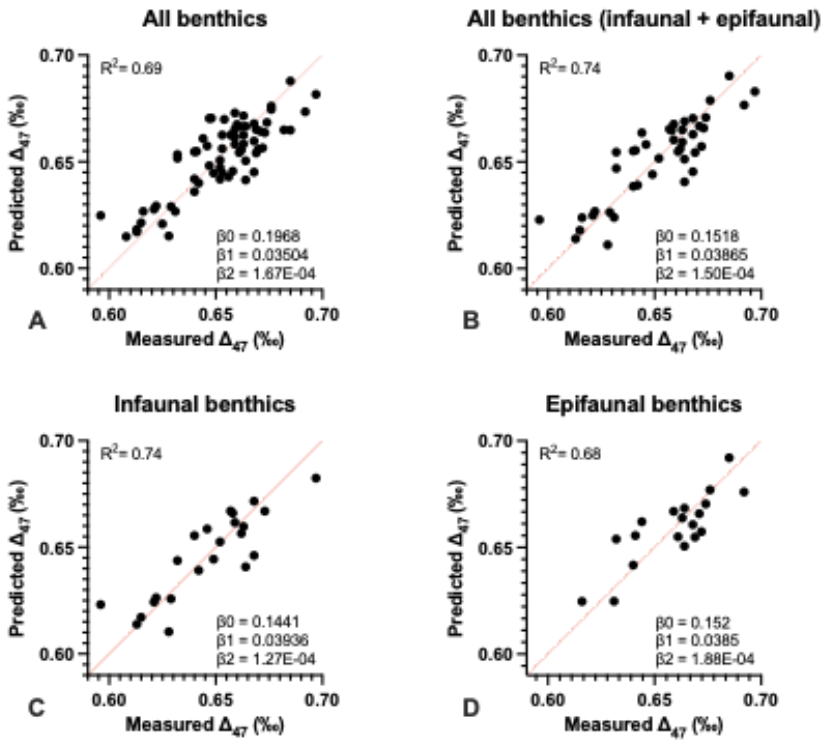

Figure 1.7: Predicted Δ_{47} compared to measured Δ_{47} for benthics. Predicted Δ_{47} is from a multivariate regression of the form Δ_{47} (‰) = β0 + β1 x $10^6/T^2$ + β2 x $\Delta[CO_3^{2-}]$ (regression parameters in Table 1.4). a) all benthics, b) all benthics (infaunal + epifaunal), c) infaunal benthics, and d) epifaunal benthics. There are at least two different ways, in theory, that Δ_{47} could be affected by bottom water carbonate saturation. First, a small effect has been predicted from theory and observed in experiments for Δ_{47}, with a difference in the equilibrium isotopic composition of DIC species at pH between 7 and 11 of ~0.03 to 0.05 ‰, that was predicted to give rise to effects of less than 0.02 ‰ for the Cenozoic, and lower Δ_{47} at elevated pH (Hill et al., 2014; Tripati et al., 2015). A second effect, with increasing Δ_{47} associated with increased pH, could arise from a possible CO_2 hydrolysis effect that increases with precipitation rate (Guo, 2020; Lucarelli et al., 2022; Tripati et al., 2015). Experimental studies have observed this effect only at low temperature and elevated pH (pH > 9.5) with decreased effect size in the presence of carbonic anhydrase recently shown to be active in some benthic foraminiferal species (de Goeyse et al., 2021; Lucarelli et al., 2022).

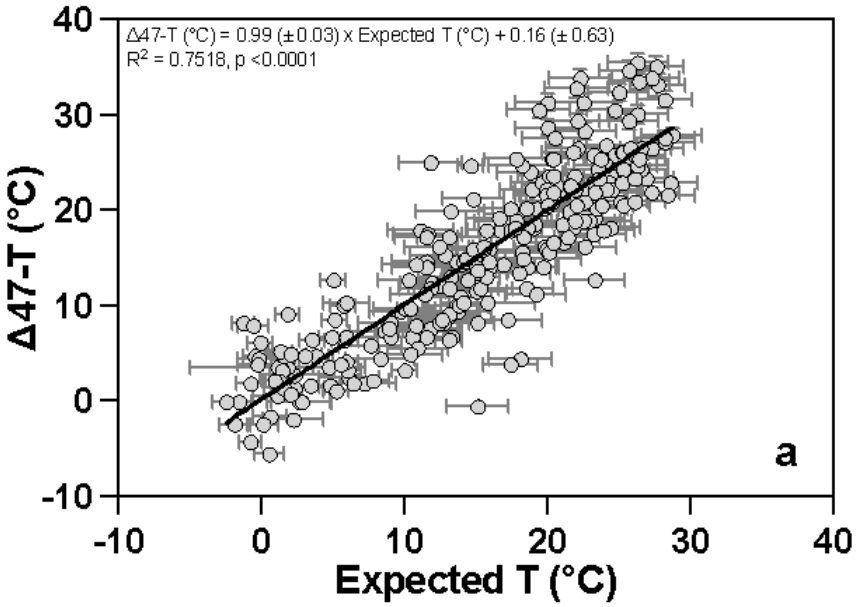
Δ47-T (°C) = 0.99 (±0.03) x Expected T (°C) + 0.16 (±0.63)
R2 = 0.7518, p <0.0001
Δ47-T (°C)
Expected T (°C)
a

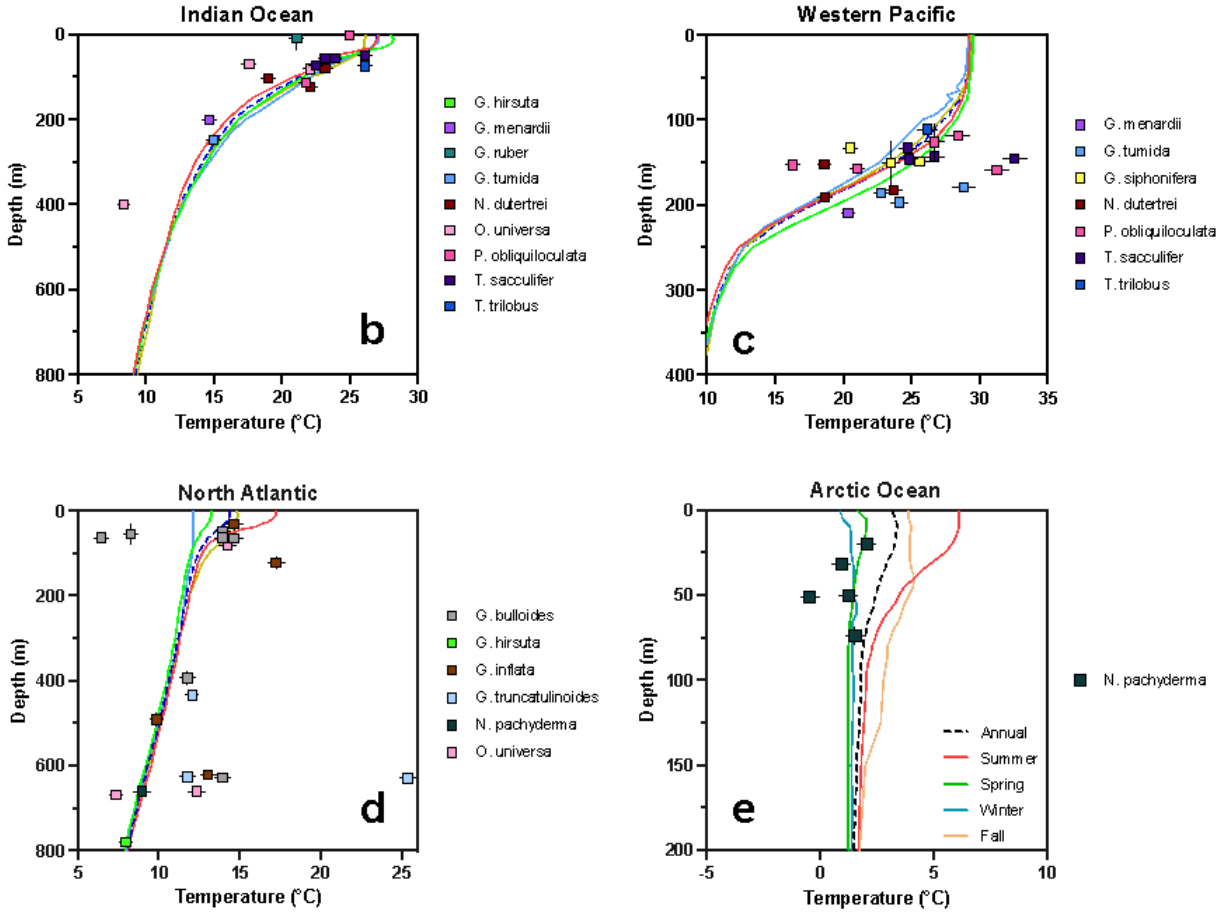
Indian Ocean
Depth (m)
Temperature (°C)
b
G. hirsuta
G. menardii
G. ruber
G. tumida
N. dutertrei
O. universa
P. obliquiloculata
T. sacculifer
T. trilobus
Western Pacific
c
G. menardii
G. tumida
G. siphonifera
N. dutertrei
P. obliquiloculata
T. sacculifer
T. trilobus
North Atlantic
d
G. bulloides
G. hirsuta
G. inflata
G. truncatulinoides
N. pachyderma
O. universa
Arctic Ocean
e
N. pachyderma
Annual
Summer
Spring
Winter
Fall

Figure 1.8: Reconstructed Δ_{47}-temperatures a) Comparison of Δ_{47}-temperature with $\delta^{18}O$-based calcification temperatures (method 2) for all core-top samples. Linear regression has a slope of 0.99 ± 0.03, $R^2 = 0.75$ and $p < 0.001$ ($n = 260$). Reconstructed temperature profiles based on clumped isotopes temperature for b) the Indian Ocean, c) Western Pacific, d) North Atlantic and e) Arctic Ocean.

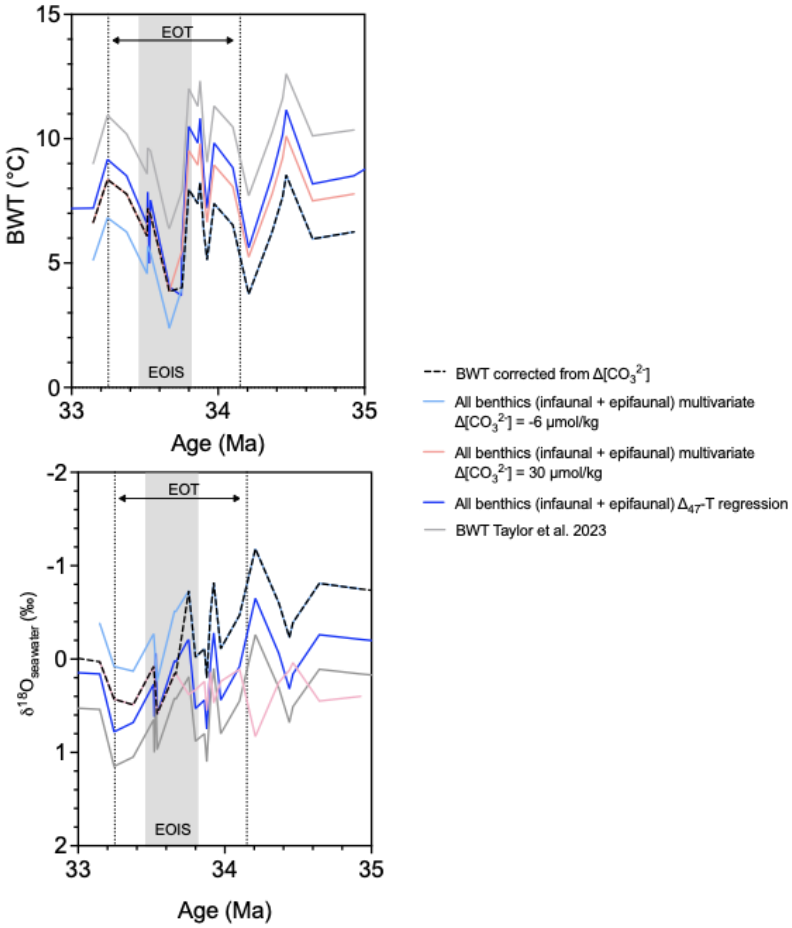

Figure 1.9: Reconstructed Δ_{47}-based estimates of bottom water temperatures and $\delta^{18}O_{sw}$ for the Eocene-Oligocene Transition. Temperatures are cooler for all of the new regressions from this study (colored lines), and most $\delta^{18}O_{sw}$ values lower, compared to Taylor et al. (2023) (grey line). The multivariate regression shows the largest $\delta^{18}O_{sw}$ increase across the EOT. Light blue and pink lines show Δ_{47}-temperatures based on the all benthic (infaunal + epifaunal) multivariate equation at different $\Delta[CO_3^{2-}]$. The dashed line combines these lines to correct for $\Delta[CO_3^{2-}]$ across the event. The dark blue line shows the non-multivariate Δ_{47}-temperatures with no correction for $\Delta[CO_3^{2-}]$.The grey line shows original reconstruction from Taylor et al. (2023) that used planktic calibration from Meinicke et al. (2020) for comparison. All calculations use Δ_{47} data from Taylor et al. (2023).

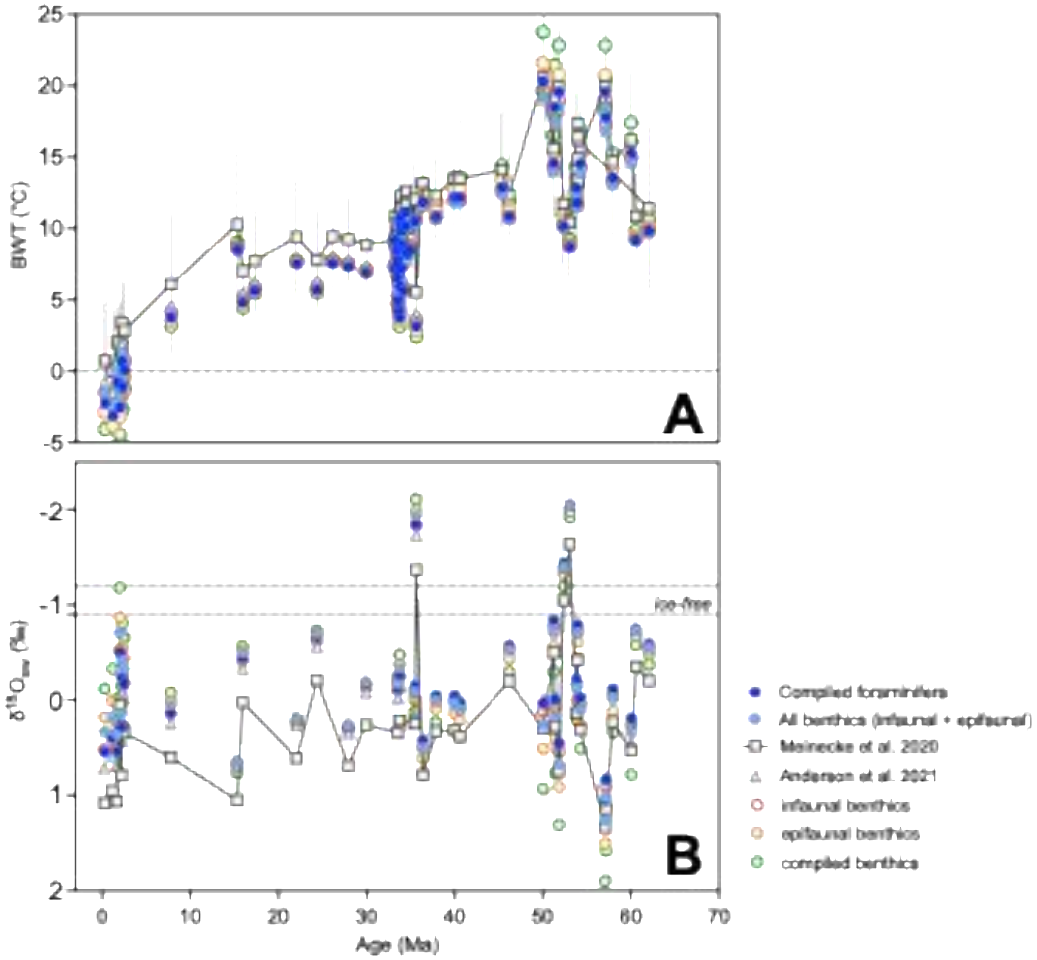

Figure 1.10: Comparison of recalculated bottom water temperatures and $\delta^{18}O_{sw}$ with clumped isotope data from Meckler et al. (2022). A) Bottom water temperature (BWT) reconstructions. B) $\delta^{18}O_{sw}$ reconstructions. Temperatures calculated with the new regressions from this study temp to decrease temperatures relative to the Meinicke et al. (2020) calibration. $\delta^{18}O_{sw}$ estimates also decrease with the new calibrations, however the decrease does not itself reconcile the deviation from ice-free predicted $\delta^{18}O_{sw}$ in the early Cenozoic.

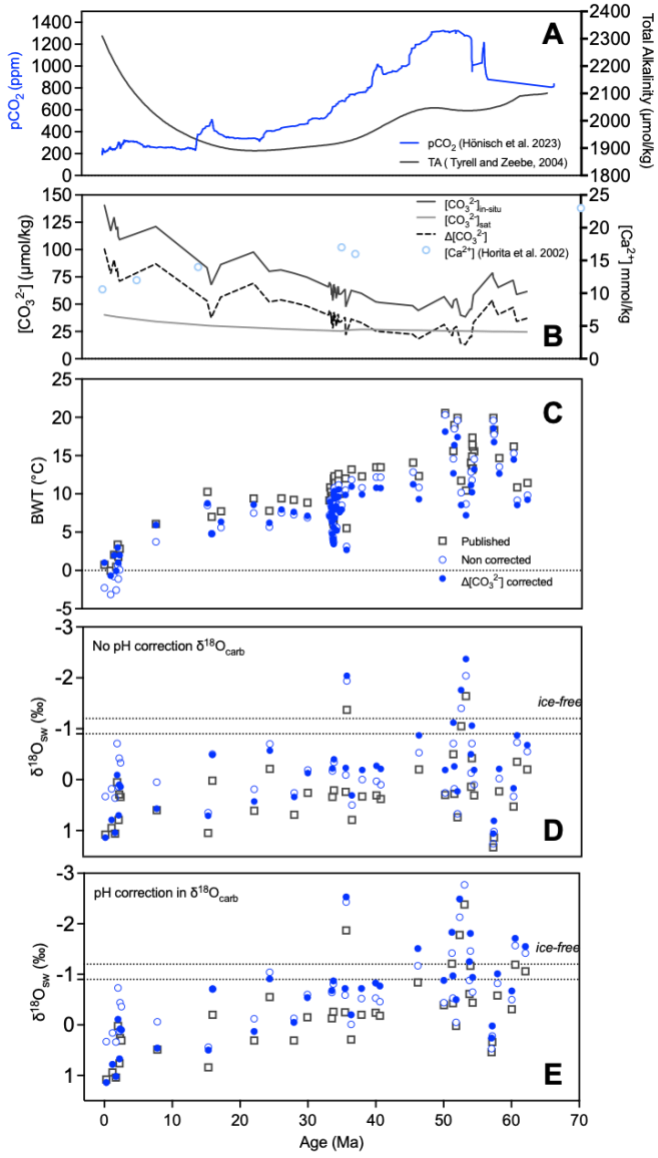

Figure 1.11: Comparison of recalculated bottom water temperatures and $\delta^{18}O_{sw}$ with clumped isotope data from Meckler et al. (2022). pCO2 estimates and TA estimates used to calculate $\Delta[CO_3^{2-}]$ B) $[CO_3^{2-}]$ values calculated as described in section 3.5.4a C) BWT reconstructions using the All benthic (infaunal + epifaunal) equations where non-corrected are the results of the deming regression, and corrected are results from the multivariate regression. D) $\delta^{18}O_{sw}$ reconstructions with E) $\delta^{18}O_{sw}$ reconstructions with a pH correction in $\delta^{18}O_{carb}$ as described in Meckler et al. (2022).

6 Tables

Publication	Ecology	# samples	# of analyses	Mass/replicate (mg)	# replicates	Integration time (seconds)
Tripati et al., 2010	planktic, benthic,	34	58	4-8	1-5	640-1280
Grauel et al., 2013	planktic, benthic	42	618	0.15-0.2	2-47	156
Peral et al., 2018	planktic, benthic	27	248	2-3	4	480
Breitenbach et al., 2018	planktic	19	158	0.12-0.24	1-12	208
Meinicke et al., 2020	planktic	43	830	0.1-0.13	15-30	400
Piasecki et al., 2019	benthic	13	582	0.1-0.4	1-43	400
This study New measurements	planktic, benthic	124	720	0.25-0.52	3-20	1200
This study Foraminifera meta-analysis	**planktic, benthic**	**260**	**2569**			

Table 1.1 Sources of clumped isotopic data from foraminifera used in this study. Data for 260 core-top foraminifera are reported (based on 2569 analyses), comprised of 124 new foraminifera samples measured for this study, and 136 samples reported in prior publications (Tripati et al., 2010; Peral et al., 2018; Breitenbach et al., 2018; Meinicke et al., 2020; Piasecki et al., 2019). The dataset from Grauel et al. (2013) was excluded based on the PI from the measuring laboratory not being confident in the standardization of the dataset. Coccolith bulk measurements from Tripati et al. (2010) were not included in this study. Foraminifera calcification temperatures are recalculated with multiple methods as described in section 2.4.2. All published datasets were updated to the same standardization reference frame (I-CDES$_{90}$).

Publication	# samples	# analyses	Mass/replicate (mg)	# replicates	Integration time (seconds)
Anderson et al., 2021	10	87	0.4 - 0.6	8-10	1800
Defliese et al., 2015	3	12	4-6	4	640
Defliese and Tripati 2015	2	19	0.25-0.5	7-12	640-1600
Jautzy et al., 2020	4	85	0.08 - 0.1	19-24	700
Kelson et al., 2017	30	108	6-9	2-7	1560
Kluge et al., 2015	6	18	5 – 8	1-5	1456
Lucarelli et al., 2022a	4	36	0.48-0.52	5-12	1200
Swart et al., 2021	6	73	5-8	3-14	2436
Tang et al., 2014	32	101	25	1-24	1200
Tripati et al., 2015	7	13	5 – 8	1-4	1200
This study New measurements	11	89	0.48 - 0.52	6-13	1200
This study Synthetics meta-analysis	**115**	**641**			

Table 1.2 Sources of clumped isotopic data from synthetic calcite used in this study. Data for 118 samples of synthetic calcite grown from 0 to 50 ºC are reported (based on 641 analyses), comprising 11 new samples measured for this study, and 104 samples reported in prior publications. All published datasets were updated to the same standardization reference frame (I-CDES$_{90}$).

Datasets included	N	slope	s.e.	CI range	intercept	s.e.	CI range
UCLA Foraminifera	124	0.03527	0.00154	0.03222 to 0.03833	0.1973	0.019	0.1602 to 0.2344
All foraminifera	260	0.03739	0.00128	0.03487 to 0.03991	0.1745	0.015	0.1441 to 0.2049
All foraminifera, no mixed benthics	235	0.0383	0.00128	0.03579 to 0.04084	0.1635	0.015	0.13310 to 0.19390
Synthetic calcite <50 °C	118	0.03926	0.00143	0.03643 to 0.04208	0.1547	0.017	0.1219 to 0.1874
All benthics	67	0.028	0.00264	0.02267 to 0.03324	0.2948	0.034	0.2272 to 0.3625
All benthics, no mixed benthics	42	0.0342	0.00336	0.02740 to 0.04099	0.2149	0.043	0.12770 to 0.30210
All infaunal benthics	23	0.0365	0.00552	0.02505 to 0.04799	0.186	0.07	0.04126 to 0.3307
All epifaunal benthics	19	0.0317	0.00515	0.02081 to 0.04254	0.2474	0.067	0.1053 to 0.3895
All planktics	193	0.0423	0.00191	0.03854 to 0.04609	0.1166	0.023	0.07203 to 0.1612
All mixed-layer planktics	99	0.0423	0.00242	0.03746 to 0.04706	0.1194	0.028	0.063466 to 0.1754
All foraminifera and synthetic calcite	381	0.03894	0.00092	0.03713 to 0.04075	0.1566	0.011	0.1350 to 0.1782

Table1 1.3: Regression parameters for foraminiferal calibration dataset and synthetic calcite dataset.

Δ_{47} (‰) = β0 + β1 x $10^6/T^2$ + β2 x $\Delta[CO_3^{2-}]$						
All benthics						
Parameter estimates	Variable	Estimate	Standard error	P value	R^2	n
β0	Intercept	0.1968	0.0415	<0.0001	0.6926	67
β1	$10^6/T^2$	0.03504	0.003138	<0.0001		
β2	$\Delta[CO_3^{2-}]$	0.0001673	0.00004572	0.001		
All benthics (epifaunal and infaunal benthics)						
Parameter estimates	Variable	Estimate	Standard error	P value	R^2	n
β0	Intercept	0.1518	0.04932	0.0038	0.7427	42
β1	$10^6/T^2$	0.03865	0.00376	<0.0001		
β2	$\Delta[CO_3^{2-}]$	0.0001495	0.00006014	0.0173		
All infaunal benthics						
Parameter estimates	Variable	Estimate	Standard error	P value	R^2	n
β0	Intercept	0.1441	0.06748	0.0453	0.743	23
β1	Temperature	0.03936	0.005239	<0.0001		
β2	$\Delta[CO_3^{2-}]$	0.0001271	0.00007825	0.1199		
All epifaunal benthics						
Parameter estimates	Variable	Estimate	Standard error	P value	R^2	n
β0	Intercept	0.152	0.09113	0.1147	0.6838	19
β1	Temperature	0.03851	0.006841	<0.0001		
β2	$\Delta[CO_3^{2-}]$	0.000188	0.0001059	0.0949		

Table 1.4: Multivariable regressions between Δ_{47} (‰), temperature T (K) and $\Delta[CO_3^{2-}]$ (µmol/kg).

Sites	**1266C**	**999**	**1001**	**690**	**1209B**	**1210B**	**1211C**	**1220B**	**1221C**
$[CO_3^{2-}]$ (µmol/kg)	*37*	*<37*	*<37*	*48*	*52*	*54*	*58*	*49*	*50*
$[CO_3^{2-}]$sat (µmol/kg)	*62*	*55*	*57*	*57*	*59*	*62*	*63*	*63*	*67*
$\Delta[CO_3^{2-}]$ (µmol/kg)	*-25*	*-18*	*-20*	*-9*	*-7*	*-8*	*-5*	*-14*	*-17*
Possible biases:									
T = 15 (°C)	4.3	3.9	4.0	3.4	3.3	3.3	3.2	3.7	3.8
T = 20 (°C)	4.5	4.1	4.2	3.6	3.4	3.5	3.3	3.9	4.0
T = 35 (°C)	5.2	4.7	4.9	4.1	4.0	4.1	3.9	4.5	4.7

Table 1.5: Estimates of potential PETM temperature biases on temperatures, assuming a carbonate ion effect on calcification as described by the multivariable regression for epifaunal benthics. $[CO_3^{2-}]$ for individual sites over the PETM estimated from Zeebe and Zachos (2007). $[CO_3^{2-}]_{sat}$ is based on site paleodepths, and the epifaunal benthics multivariable regression is used to explore the magnitude of potential temperature biases.

Supporting Information for:

Chapter 1: Clumped isotope thermometry in foraminifera as a tool in paleoceanography: New planktonic and benthic data and constraints on non-thermal effects

S1. Background on Clumped Isotopes

In $CaCO_3$ and dissolved inorganic carbon (DIC), the heavier isotopes of C and O (^{13}C, ^{18}O) are rare relative to the lighter isotopes. Carbonate 'clumped' isotope geochemistry examines the proportion of ^{13}C and ^{18}O atoms bound to each other forming heavy isotope "pairs'' or clumps (Ghosh et al., 2006). Due to zero-point energy differences, molecules with heavy isotope clumps have distinct physical and chemical properties from those without, enabling their use as tracers of equilibrium and kinetic processes (Schauble et al., 2006). Crucially, instead of relying on an isotopic exchange reaction between different phases (e.g., $CaCO_3$ and H_2O for the carbonate-water oxygen isotope thermometer), clumped isotope thermometry relies on internal isotopic exchange between isotopes in a single phase. This means that, in theory, all that is needed to determine mineral formation temperatures is the clumped isotope composition of the solid, and not the water from which it grew.

The relevant isotope exchange for calcite that produces a multiply-substituted carbonate ion group with a mass of 63 amu is described by Reaction S1:

$$Ca^{13}C^{16}O_3 + Ca^{12}C^{18}O^{16}O_2 = Ca^{13}C^{18}O^{16}O_2 + Ca^{12}C^{16}O_3 \quad \text{(Reaction S1)}$$

In practice, for carbonate clumped isotope thermometry, the abundance of ^{13}C-^{18}O bonds in a sample is measured on CO_2 liberated from carbonates when reacted with phosphoric acid using gas source mass spectrometry, as is done to measure carbonate $\delta^{18}O$ and $\delta^{13}C$ (Ghosh et al., 2006). Specifically the multiply-substituted isotopologue $^{13}C^{18}O^{16}O$ that dominates the mass-47 isobar is of interest, with Δ_{47} defined (Eiler and Schauble, 2004) as (Equation S1):

$\Delta_{47} = (R47_{sample}/R47_{stochastic} - 1) \times 1000$ (Equation S1)

$R47_i$ is the ratio of 47/44 CO_2 measured in the sample relative to what would be predicted for a stochastic distribution, reported in units of per mil (‰).

S2. Sample Preparation

Core-top sediment samples were transferred into 150 ml containers and filled with approximately 75 ml of deionized (DI) water. The water and sediment mixture was then placed on a rotating wheel for a minimum of 24 hours to disaggregate the sediment. The sediment-liquid solution was wet-sieved over a 63 µm sieve using DI water through a power spray. Fine fraction (< 63 µm) and coarse fraction (> 63 µm) was dried overnight at 30 °C (< 50 °C to prevent bond reordering). The coarse fraction was separated by a series of dry sieves into different size fractions (150-180 µm, 180-212 µm, 212-250 µm, 250-300 µm, 355-400 µm, >400 µm).

Each sample consists of foraminiferal tests hand-picked under a microscope, targeting translucent and intact tests, and omitting tests that were damaged, showed evidence for secondary calcite overgrowth, presented an oxide coating, and/or carbonate infill. A total of 16 different taxa, both planktonic and benthic, were picked from these sites. We aimed for a minimum weight of picked foraminifera of 3 mg to have sufficient material for several replicate analyses given instrumental conditions at the time of analysis.

Picked samples underwent a cleaning procedure to remove potential contaminants, adapted from the cleaning procedure for Mg/Ca analysis from Barker, Greaves, and Elderfield (2003), as described in Tripati et al. (2010), with a focus on removing infill and adhering sediment. Briefly, foraminiferal shells are crushed and then collected into a 1.5 ml conical vial, rinsed with reagent-grade methanol using a 20-200 µml pipette, and ultrasonicated twice in a DI water bath for 4 intervals of 15 seconds while ensuring that the water does not heat to more than 30 °C. Samples are then rinsed with DI water and again ultrasonicated at least 5 times until the

cleaning water is clear. Samples are then placed inside an oven to dry overnight at 30 °C (< 50 °C) and subsequently stored in a desiccator until they are run.

Species names were updated to match the World Registry of Marine Species (Ahyong et al., 2022) where necessary. Specifically, *Cibicides wuellerstorfi* and *Planulina wuellerstorfi* was updated to *Cibicidoides wuellerstorfi*, *Cibicidoides pachyderma* is updated to *Cibicides pachyderma*, and *Globigerinoides sacculifer* was updated to *Trilobatus sacculifer*.

S3. Determination of calcification temperatures

Method 1 *– Atlas – Assumed calcification depths and WOA T*

This method uses the literature on calcification depths of foraminifera species in geographical regions in conjunction with WOA temperature data (version 13V2; Levitus et al., 2010) to estimate calcification temperatures. The WOA dataset interpolates data to standard depth intervals and regions and can be used to develop vertical profiles of mean annual temperature and seasonal temperatures. We took estimates of calcification depth and season of growth for each taxa in a given basin, and compared results to vertical temperature profiles. This method is sensitive to the availability of representative temperature data, and assumptions of calcification depth.

Method 2 *– Isotopic – Assumed calcification depths and oxygen isotope measurements*

A second approach that is used in the main text and figures and tables in the paper combines measured $\delta^{18}O$ of foraminiferal tests with seawater $\delta^{18}O$ (at assumed foraminiferal calcification depths and growth seasons) from a database (LeGrande and Schmidt, 2006), in combination with published taxon-specific $\delta^{18}O$-temperature relationships. To estimate calcification temperatures for planktonic foraminifera, we referred to the most data-rich study on taxon-specific $\delta^{18}O$-temperature relationships from Malevich et al. (2019) that compiles data from >2600 core top samples from five taxa and reports Bayesian regression models that are

taxon-specific as well as a pooled calibration. They examined both annual and seasonal data, with similar errors for each. For our calcification temperature estimates, in the case of taxa for which species-specific calibrations were provided, we used the seasonal hierarchical model to estimate calcification temperatures and used the pooled calibration for all other planktonic species. To estimate calcification temperatures of benthic taxa, we implemented equation 9 of Marchitto et. Al, (2014) for epifaunal species and mixed benthics, and the same equation modified by 0.47 ‰ for infaunal species as the authors suggest. A caveat is that this method is sensitive to the choice of equation used for calculating oxygen isotopes and to assumptions of calcification depth.

Method 3 *– Profile – No assumed calcification depth, with carbonate* $\delta^{18}O$ *matched to theoretical values*

This method contrasts with the other two methods in that the calcification depth is not assumed. With this approach, theoretical values of $\delta^{18}O_{calcite}$ values are calculated and vertical profiles developed and compared to measured $\delta^{18}O_{calcite}$ values to determine the minimum and maximum calcification depths. Calcification temperatures were then determined by taking the WOA temperatures that correspond to the minimum and maximum calcification depth. Theoretical $\delta^{18}O_{calcite}$ profiles are determined by using vertical profiles of water temperature from WOA data in conjunction with vertical profiles of $\delta^{18}O_{sw}$ (LeGrande and Schmidt, 2006), and calculated using oxygen isotope fractionation relationships reported for the calcite-water system (Kim and O'Neil, 1997). Theoretical values were calculated at 5 m intervals up to 100 meters water depth, and below 100 meters water depth at larger intervals, constrained by available data.

This method is sensitive to the choice of equation used for calculating $\delta^{18}O_{calcite}$ and to the availability of representative $\delta^{18}O_{sw}$ data. We utilize a different $\delta^{18}O_{calcite}$ equation than with Method 2 to explore this source of uncertainty. Uncertainties in the measured $\delta^{18}O_{calcite}$ are used

to estimate minimum and maximum calcification depths and the range of seasonal WOA temperature and errors are shown as this range and treated as absolute errors. An estimated uncertainty of 0.2‰ for seawater $\delta^{18}O$ (Peral et al., 2018) was propagated through the calculation of assumed calcification depths. Following Meinicke et al. (2020), in cases where the measured sample $\delta^{18}O_{calcite}$ represented a temperature warmer or colder than those available in the appropriate seasonal WOA data for a given site, the WOA temperature for 0 m or deepest available temperature, respectively, was used.

S4. Comparison of calcification temperatures

Several studies have compared calibrations derived using different methods for estimating foraminiferal calcification temperatures. These studies each concluded that similar results are obtained for Δ_{47}-calibrations, irrespective of method used (Tripati et al., 2010; Meinecke et al., 2019). Here, we probe the impact of using different methods more rigorously using much larger sample sizes and find similar results.

Isotopic data including $\delta^{13}C$, $\delta^{18}O$, and Δ_{47}, along with $\delta^{18}O_{sw}$, calcification depth and calcification temperature estimates using all three methods described in section 3 are listed in Table 1.S.1. Table 1.S.2 lists temperature estimates for all samples using different methods. Method 1 yields calcification temperatures for mixed-layer planktonic foraminifera that range from -1.5 to 29.6 ℃, thermocline planktonics that range from 14.1 to 28.6 ℃, and benthic foraminifera that range from -0.9 to 19.9 ℃. Method 2 yields temperatures for mixed-layer planktonic foraminifera that range from 2.0 to 28.7 ℃, thermocline planktonics that range from 14.3 to 22.3 ℃, and benthic foraminifera that range from -2.5 to 21.9 ℃. Method 3 yields temperatures for mixed-layer planktonic foraminifera that range from -1.7 to 28.4 ℃, thermocline planktonics that range from 12.6 to 21.7 ℃, and benthic foraminifera that range from -0.92 to 19.9 ℃.

Δ_{47} measurements range from 0.552-0.697 ‰ with an average value of 0.624 ‰ and an average standard error of 0.009 ‰. For Δ_{47} thermometry, typically a linear relationship is described between Δ_{47} and independent estimates of T (in Kelvin) using the following equation:

$$\Delta_{47\ (I-CDES\ 90℃)} = m \times \frac{10^6}{T^2} + y \qquad \text{(Equation S2)}$$

Regressions between calcification temperature and Δ_{47} (Fig. S8) yield the following equations:

Method 1: $\Delta_{47\ (I-CDES\ 90℃)} = 0.0315 \times \frac{10^6}{T^2} + 0.2477$ (Equation S3)

Method 2: $\Delta_{47\ (I-CDES\ 90℃)} = 0.0374 \times \frac{10^6}{T^2} + 0.1744$ (Equation S4)

Method 3: $\Delta_{47\ (I-CDES\ 90℃)} = 0.0363 \times \frac{10^6}{T^2} + 0.1853$ (Equation S5)

Pearson's correlation results indicate a strong correlation between these two variables using all methods (method 1: r = 0.822, t = 23.2, $p < 0.001$; method 2: r = 0.873, t = 28.7, $p < 0.001$; method 3: r = 0.869, t = 28.2, $p < 0.001$), consistent with prior work (Ghosh et al., 2006; Schauble et al., 2014; hill et al., 2014; Tripati et al., 2015) including previous studies on core-top foraminifera (e.g., Tripati et al., 2010; Meinecke et al., 2019) that used relatively small sample sizes (n = 13 to 43).

We note that the correlation coefficients for each method are relatively similar. For planktonics, method 1 yields a correlation coefficient of 0.721 compared to 0.821 using method 2 and 0.818 using method 3. For benthics, method 1 yields a correlation coefficient of 0.784 compared to 0.794 using method 2 and 0.782 using method 3.

Average differences between Methods 1 and 2 are 0.7 ± 3.5 ℃ (all foraminiferal data), 0.8 ± 3.5 ℃ (planktonics), and 0.5 ± 2.2 ℃ (benthics). Average differences between Methods 1 and 3 are 1.5 ± 3.1 ℃ (all foraminiferal data), 2.0 ± 3.5 ℃ (planktonics), and 0.1 ± 0.5 ℃

(benthics). Average differences between Methods 2 and 3 are 0.8 ± 1.8 ℃ (all foraminiferal data), 1.2 ± 1.4 ℃ (planktonics), 0.5 ± 2.3 ℃ (benthics).

Though the Pearson's correlation coefficient between Δ_{47} and temperature is high, there is scatter in the data. This scatter is to be expected in natural systems and could reflect the presence of non-thermal effects. In the meta-analysis, the largest range in foraminiferal Δ_{47} is at higher temperatures, similar to what was reported by Meinicke et al. (2019). This was also observed in the dataset measured at UCLA.

We also explored the impact of removing individual taxa on calculated regression parameters. Removing *N. pachyderma* from the foraminiferal calibration yields a reduced slope of 0.0373 ±0.0013 instead of 0.0374 ± 0.0013 and a modified intercept of 0.1753 ± 0.0158 instead of 0.1748 ± 0.0153 .The largest change in slope and intercept comes from the removal of mixed benthic samples resulting in a slope of 0.0392 ± 0.0014 and an intercept of 0.1522 ± 0.0163, followed by *T. sacculifer* with a slope of 0.0365 ± 0.0013 and an intercept of 0.1855 ± 0.0159.

S5. R-based model selection

To quantify the potential impacts of specific non-thermal factors on Δ_{47}, we employ a model selection-based approach in R. Deming regression is a strictly univariate procedure, so multivariate linear regression (OLS) models were substituted. Linear models were fit with a variety of interactive and additive variables (temperature, carbonate ion saturation, depth, dataset, genus, general habitat – benthic or planktonic, specific habitat – mixed-layer or thermocline etc., ocean, region, salinity, and symbiont presence/absence), and tested for variable selection. Numerical data were z-scored prior to model selection owing to the suite of variables having different units. We report coefficients from linear models fit to z-scored data, which provides an estimate of the per mil change in Δ_{47} for each 1 standard deviation (1 σ) increase in

the predictor variable(s) of interest. Uncertainty around coefficients is given in standard error in permil units. The effect size, partial eta squared (η^2), is used to evaluate how much variation in foraminiferal Δ_{47} is explained by each model component (fit to z-scored data) and determine whether those effects are small (partial $\eta^2 = 0.01$), medium (partial $\eta^2 = 0.06$), or large (partial $\eta^2 >= 0.14$) when all other variables in the model are held constant. The calculation for η^2 is mathematically similar to the calculation for R^2 and may therefore be interpreted in a similar manner for individual model components. Note that we report effect sizes calculated using Type II (non-sequential) sums-of-squares as implemented in the *car* package for R (Fox and Weisberg 2019). This means that the impact of each predictor variable on foraminiferal Δ_{47} is evaluated individually in turn, while all other predictor variables are held constant. Effect sizes may therefore add up to >1. As η^2 is calculated using a one-sided hypothesis, we report one-sided 95% confidence intervals. Where final models include only a single predictor variable (temperature), partial η^2 is equivalent to η^2, and so η^2 is reported. Linear model F-statistics are reported with the numerator and denominator degrees of freedom listed as subscripts in that order. Incomplete observations, i.e., those with one or more non-thermal variables unavailable/unreported, cannot be included in model selection procedures, so we report a smaller subset of the data in this section (n = 260).

Supplemental Figures

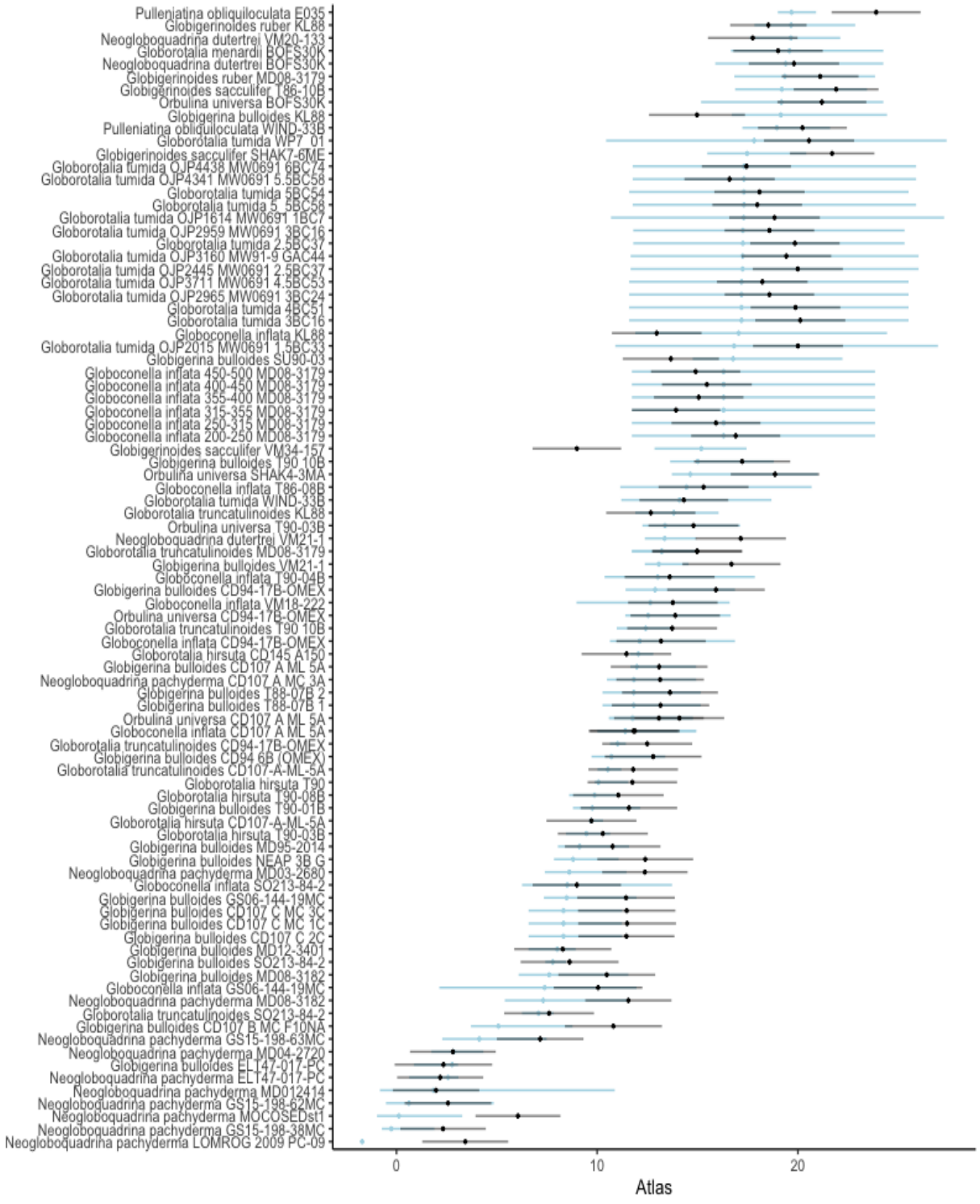

Figure 1.S.1a: Part 1 of comparison of calcification temperatures calculated for planktonic foraminiferal samples in this study using Method 1 (Atlas temperatures – black) and Method 2 (Isotopic temperatures – Malevich et al., 2019). Data utilized are in Tables 1.S.1 and 1.S.2.

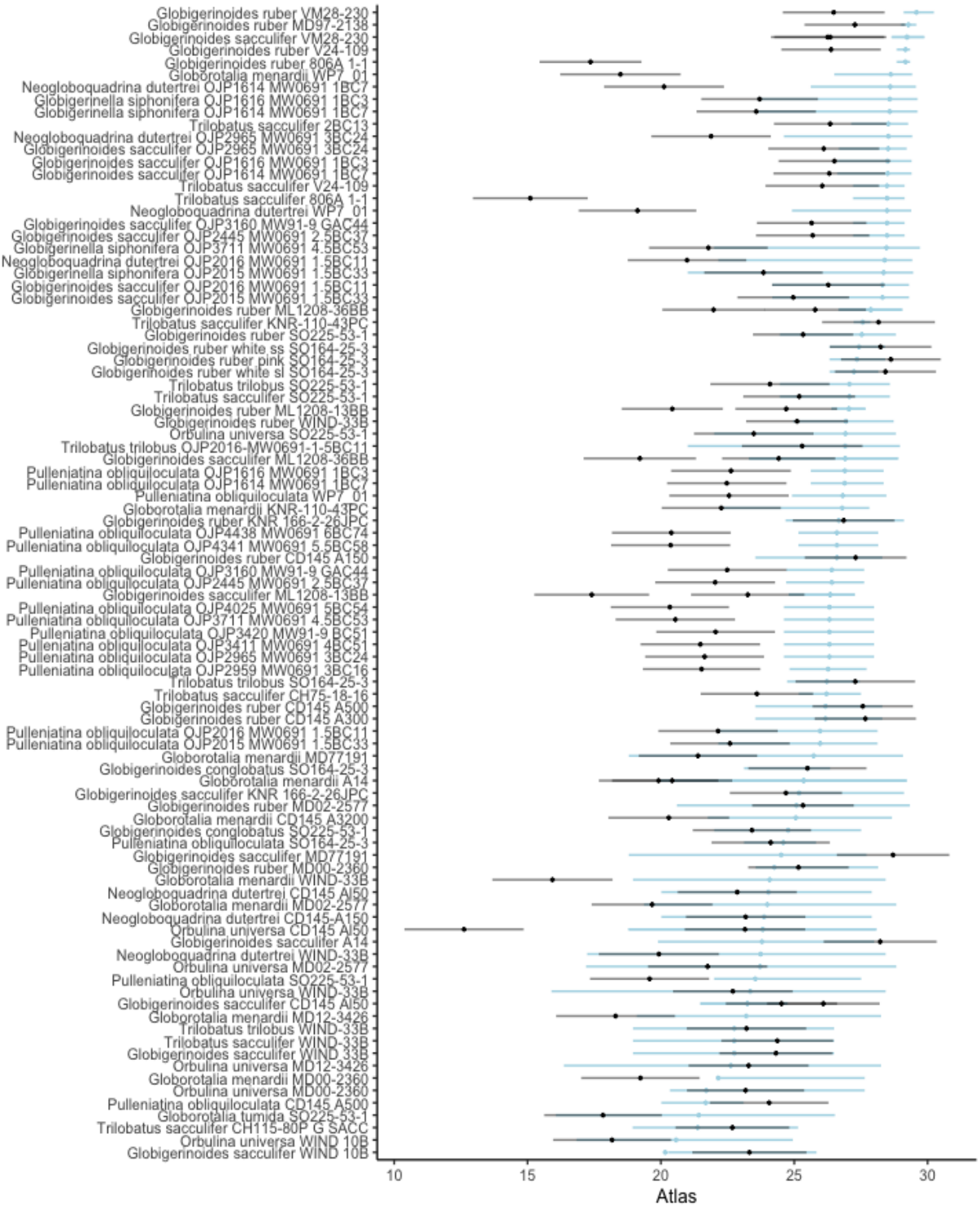

Figure 1.S.1b: Part 2 of comparison of calcification temperatures calculated for planktonic foraminiferal samples in this study using Method 1 (Atlas temperatures – black) and Method 2 (Isotopic temperatures – Malevich et al., 2019). Data utilized are in Tables 1.S.1 and 1.S.2.

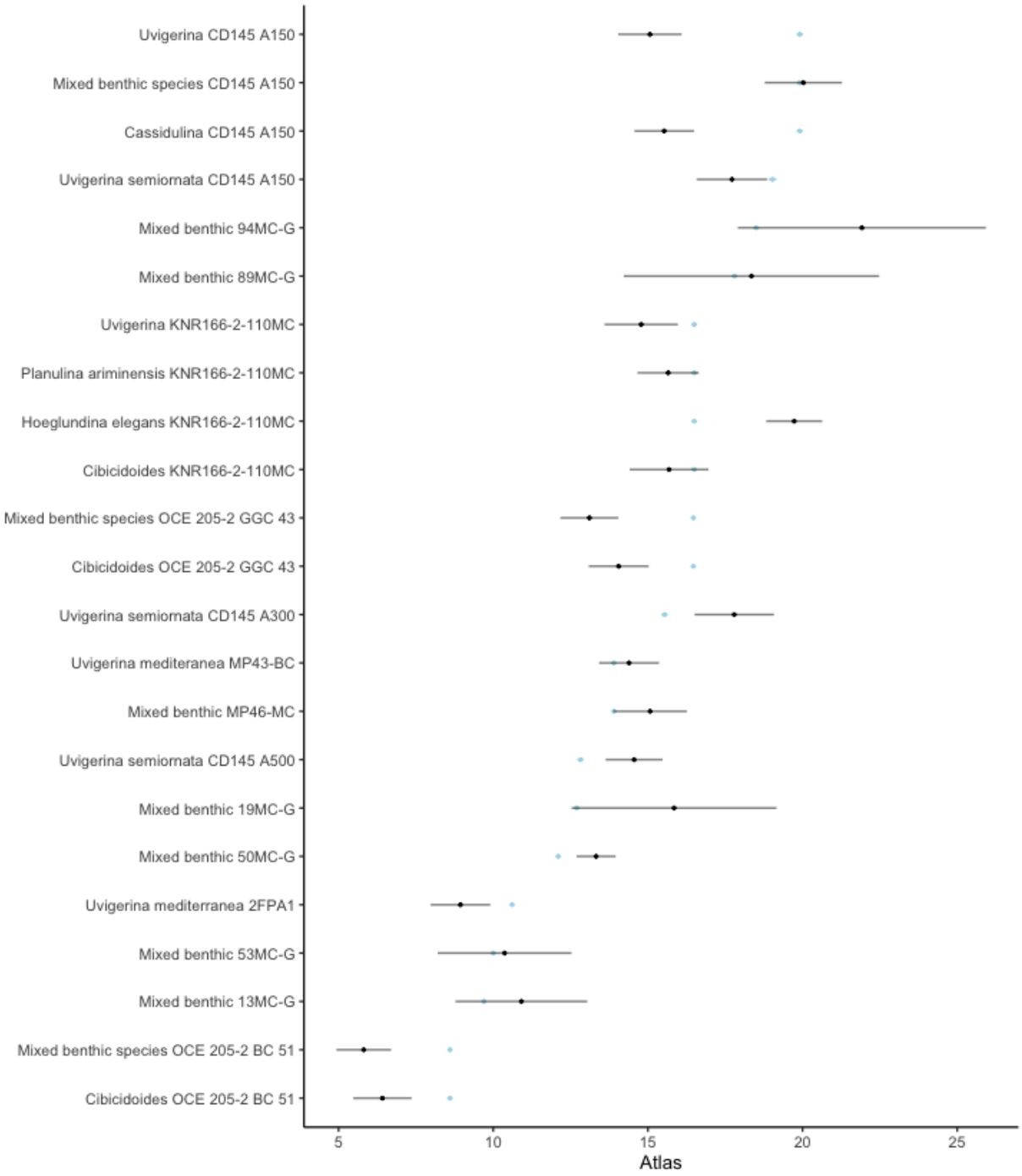

Figure 1.S.2a: Part 1 of comparison of calcification temperatures calculated for benthic foraminiferal samples in this study using Method 1 (Atlas temperatures – black) and Method 2 (Isotopic temperatures – Marchitto et al., 2014). Data utilized are in Tables 1.S.1 and 1.S.2.

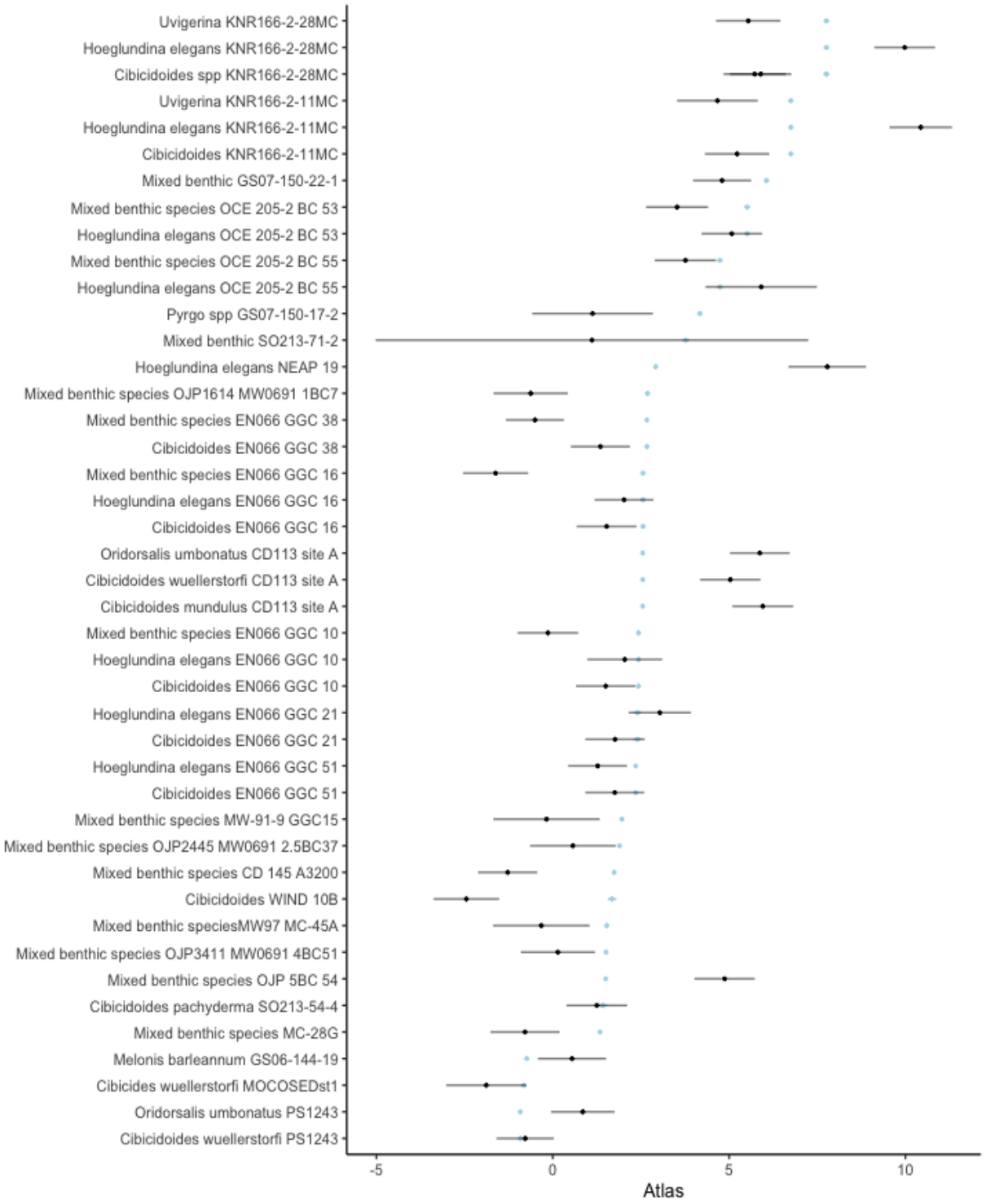

Figure 1.S.2b: Part 2 of comparison of calcification temperatures calculated for benthic foraminiferal samples in this study using Method 1 (Atlas temperatures – black) and Method 2 (Isotopic temperatures – Marchitto et al., 2014). Data utilized are in Tables 1.S.1 and 1.S.2.

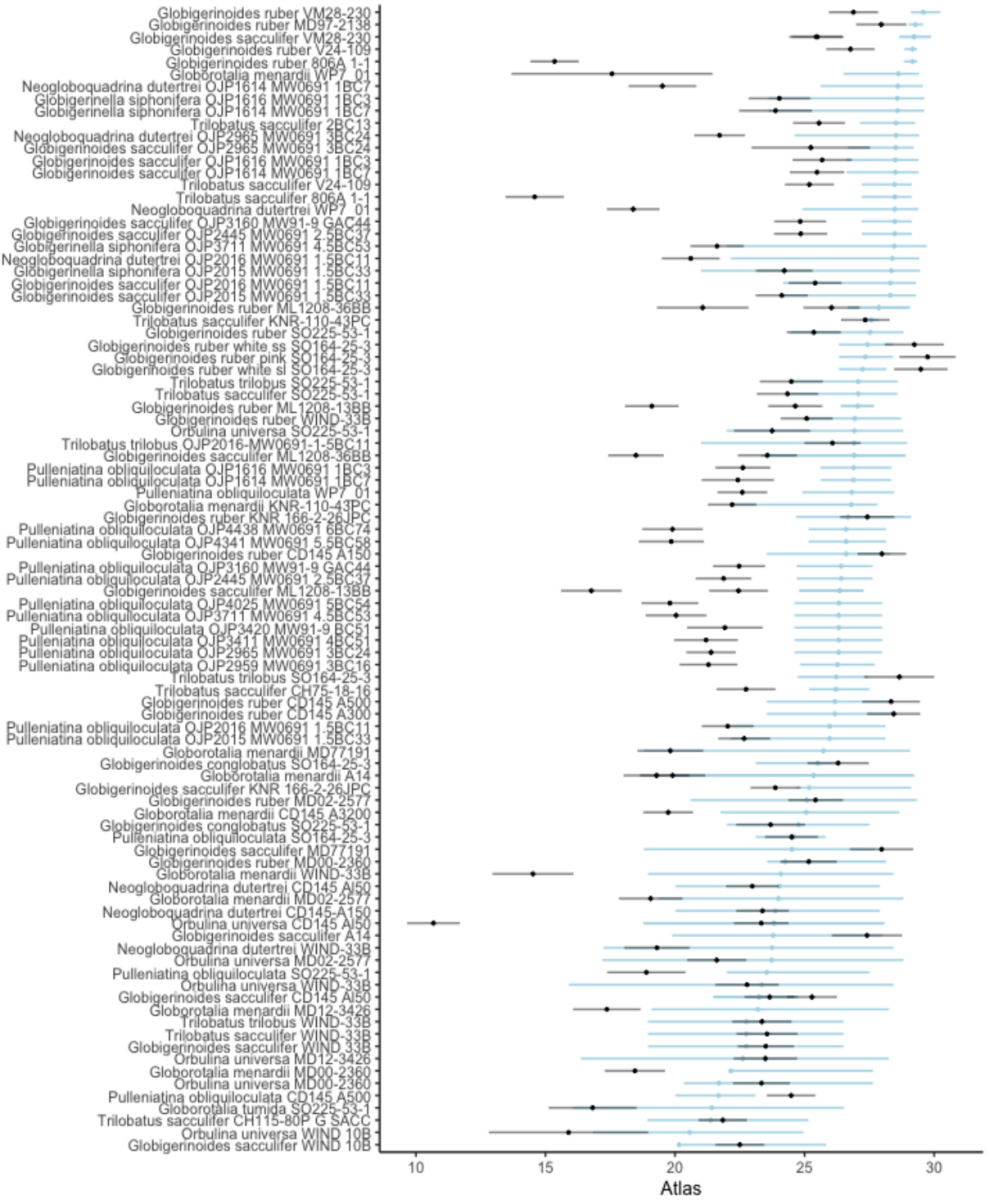

Figure 1.S.3a: Part 1 of comparison of calcification temperatures calculated for planktonic foraminiferal samples in this study using Method 1 (Atlas temperatures – black) and Method 2 (Isotopic temperatures – Kim and O'Neil, 1997). Data utilized are in Tables 1.S.1 and 1.S.2.

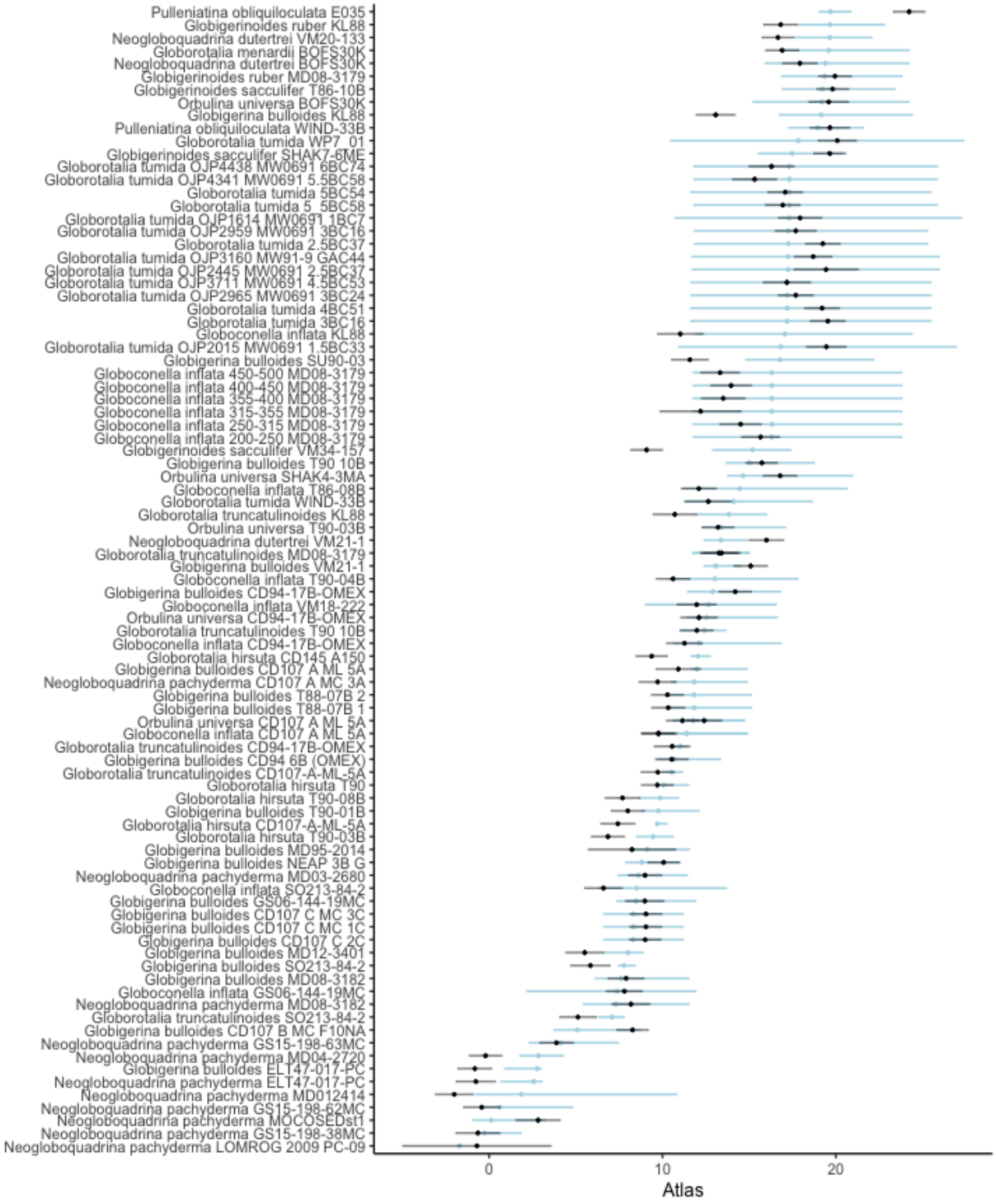

Figure 1.S.3b: Part 2 of comparison of calcification temperatures calculated for planktonic foraminiferal samples in this study using Method 1 (Atlas temperatures – black) and Method 2 (Isotopic temperatures – Kim and O'Neil, 1997). Data utilized are in Tables 1.S.1 and 1.S.2.

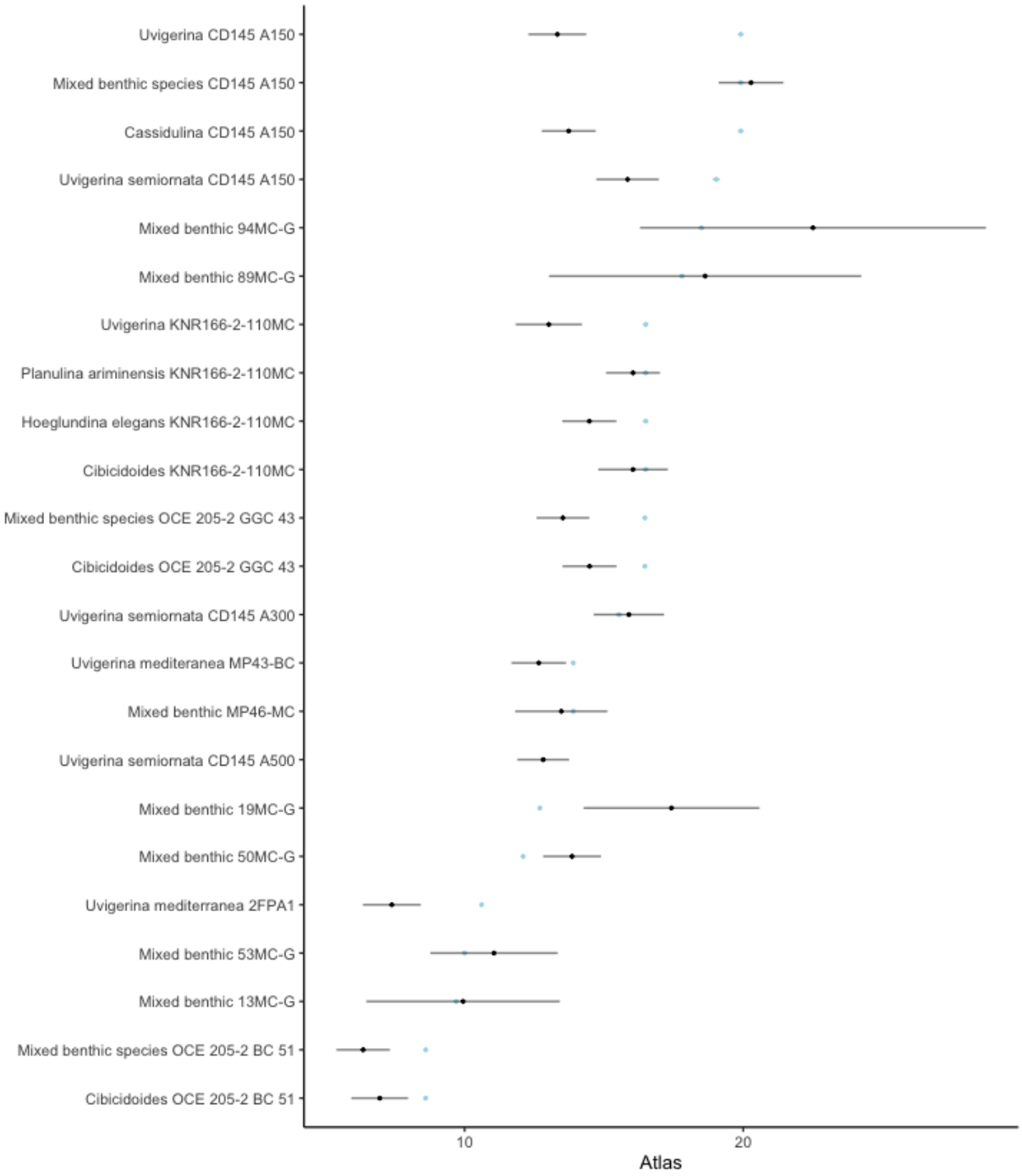

Figure 1.S.4a: Part 1 of comparison of calcification temperatures calculated for benthic foraminiferal samples in this study using Method 1 (Atlas temperatures – black) and Method 2 (Isotopic temperatures – Kim and O'Neil, 1997). Data utilized are in Tables 1.S.1 and 1.S.2.

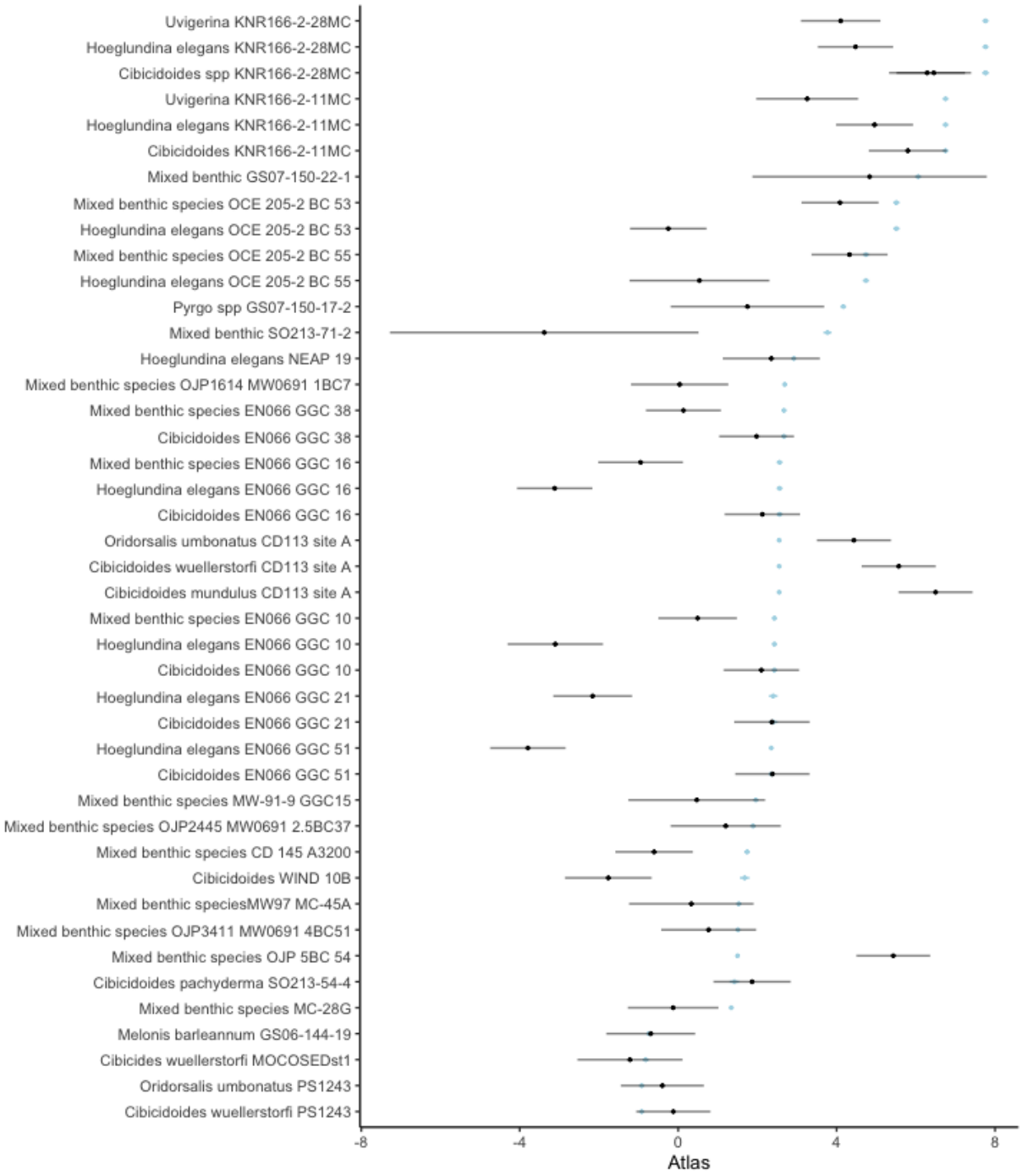

Figure 1.S.4a: Part 2 of comparison of calcification temperatures calculated for benthic foraminiferal samples in this study using Method 1 (Atlas temperatures – black) and Method 2 (Isotopic temperatures – Kim and O'Neil, 1997). Data utilized are in Tables 1.S.1 and 1.S.2.

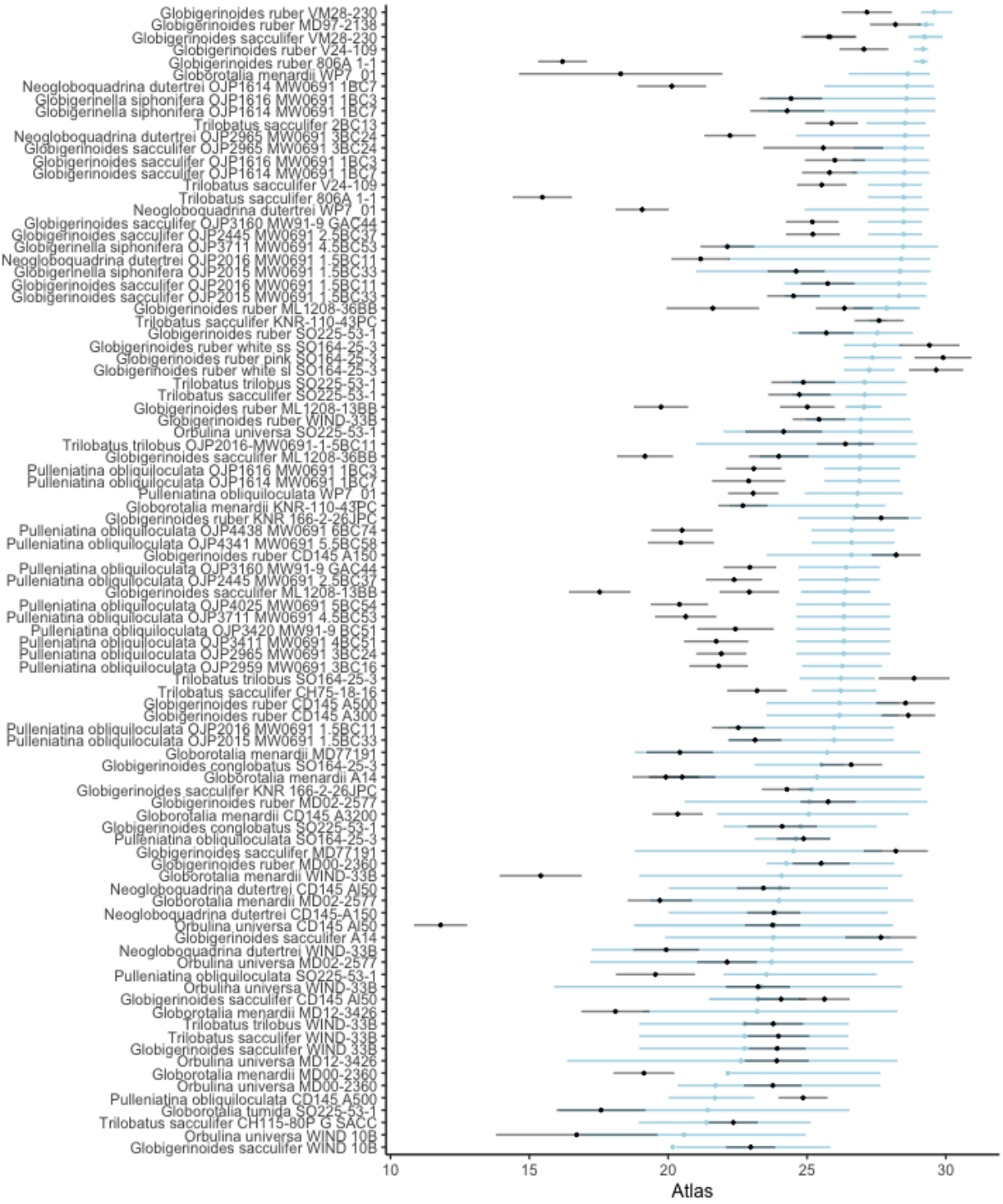

Figure 1.S.5a: Part 1 of comparison of calcification temperatures calculated for planktonic foraminiferal samples in this study using Method 1 (Atlas temperatures – black) and Method 2 (Isotopic temperatures – Shackleton, 1974). Data utilized are in Tables 1.S.1 and 1.S.2.

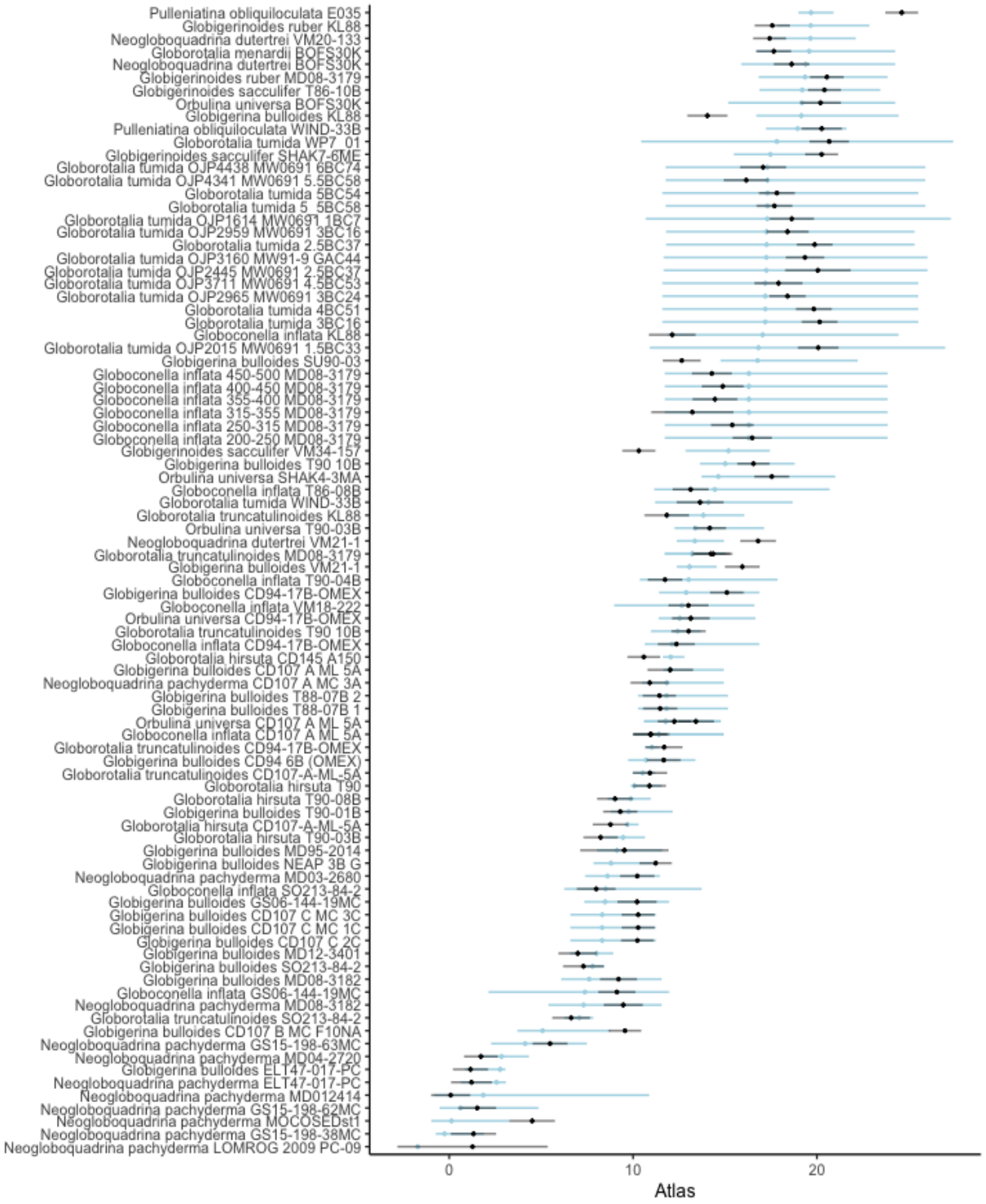

Figure 1.S.5b: Part 2 of comparison of calcification temperatures calculated for planktonic foraminiferal samples in this study using Method 1 (Atlas temperatures – black) and Method 2 (Isotopic temperatures – Shackleton, 1974). Data utilized are in Tables 1.S.1 and 1.S.2.

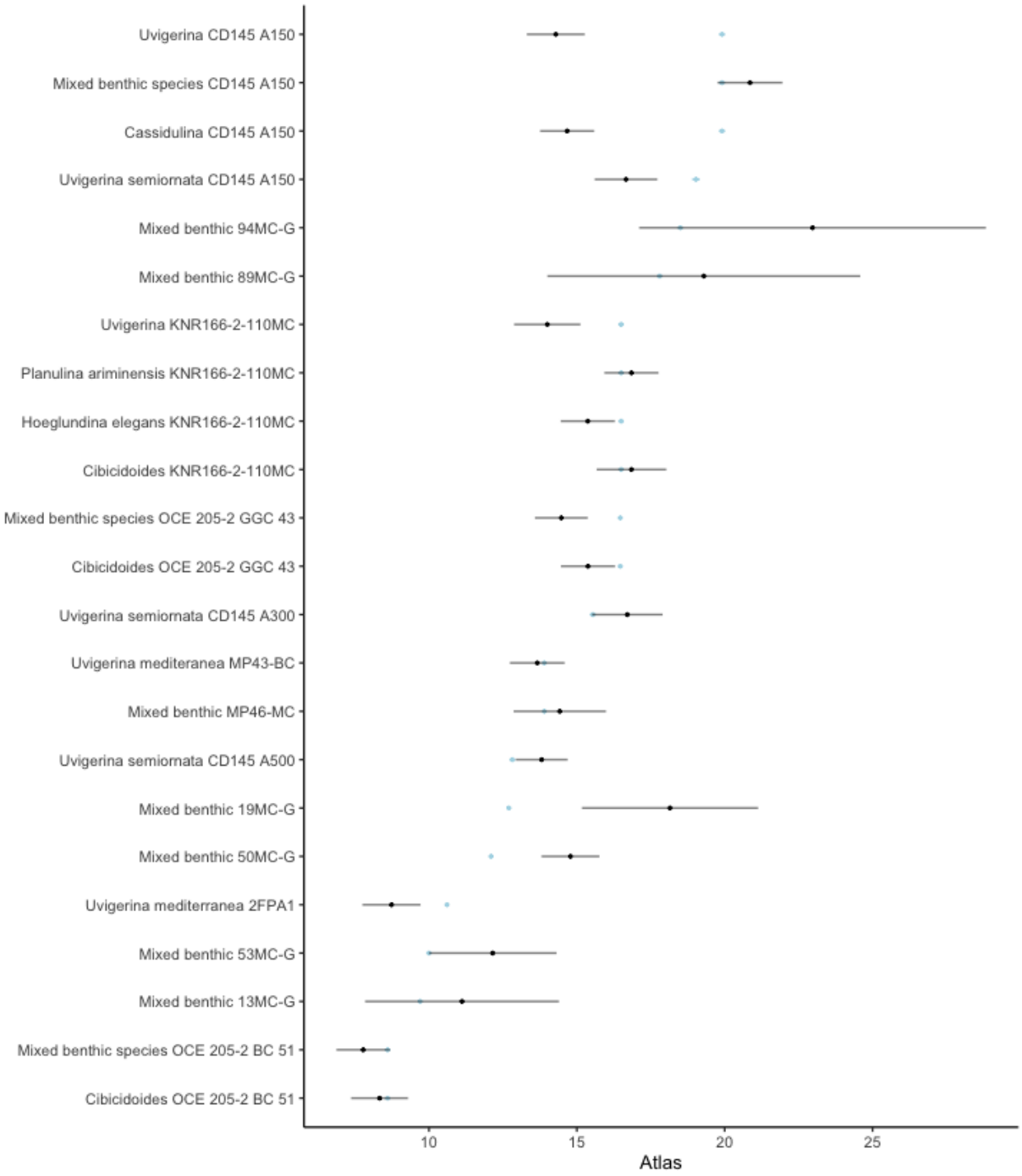

Figure 1.S.6a: Part 1 of comparison of calcification temperatures calculated for benthic foraminiferal samples in this study using Method 1 (Atlas temperatures – black) and Method 2 (Isotopic temperatures – Shackleton, 1974). Data utilized are in Tables 1.S.1 and 1.S.2.

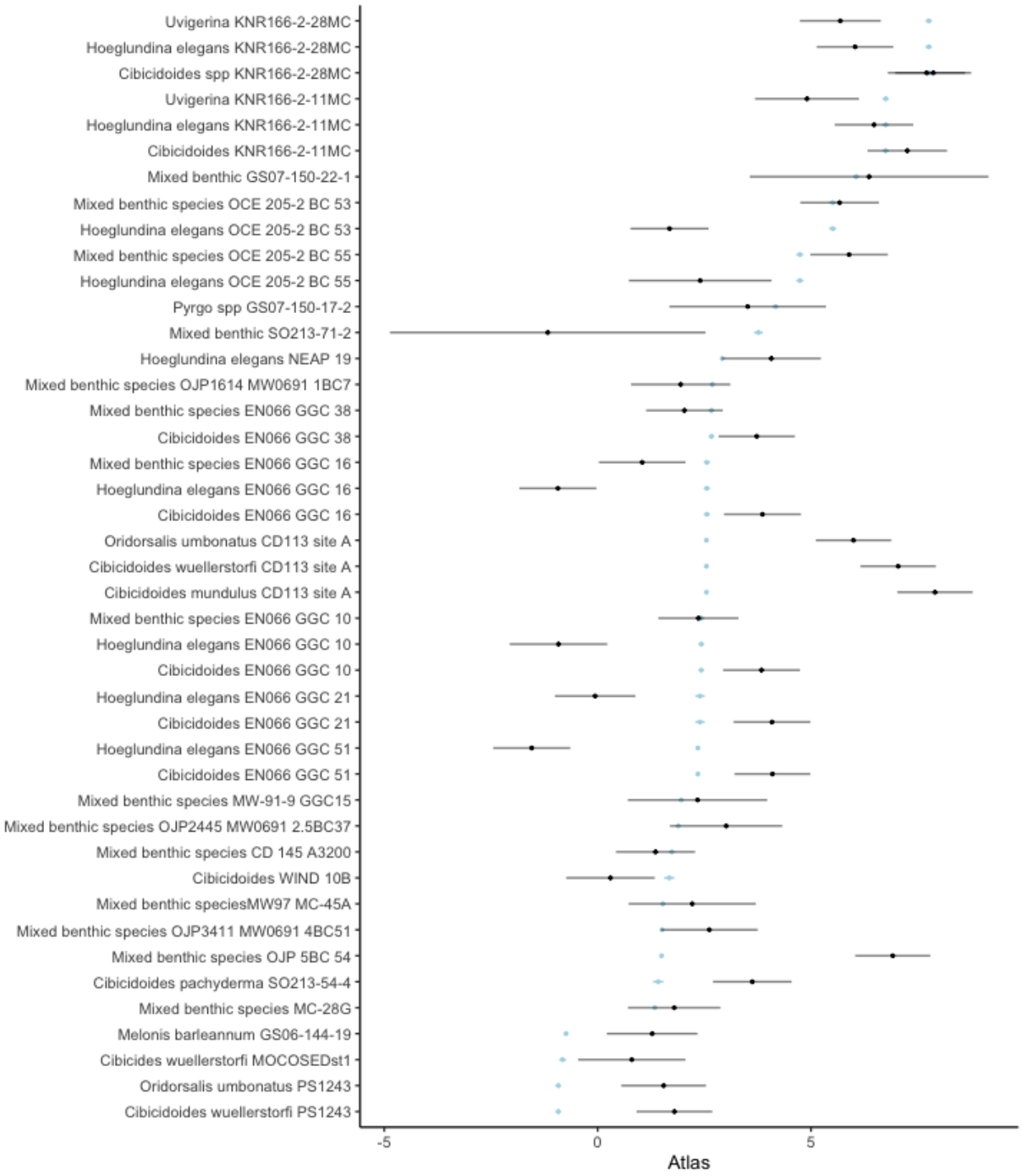

Figure 1.S.6b: Part 2 of comparison of calcification temperatures calculated for benthic foraminiferal samples in this study using Method 1 (Atlas temperatures – black) and Method 2 (Isotopic temperatures – Shackleton, 1974). Data utilized are in Tables 1.S.1 and 1.S.2.

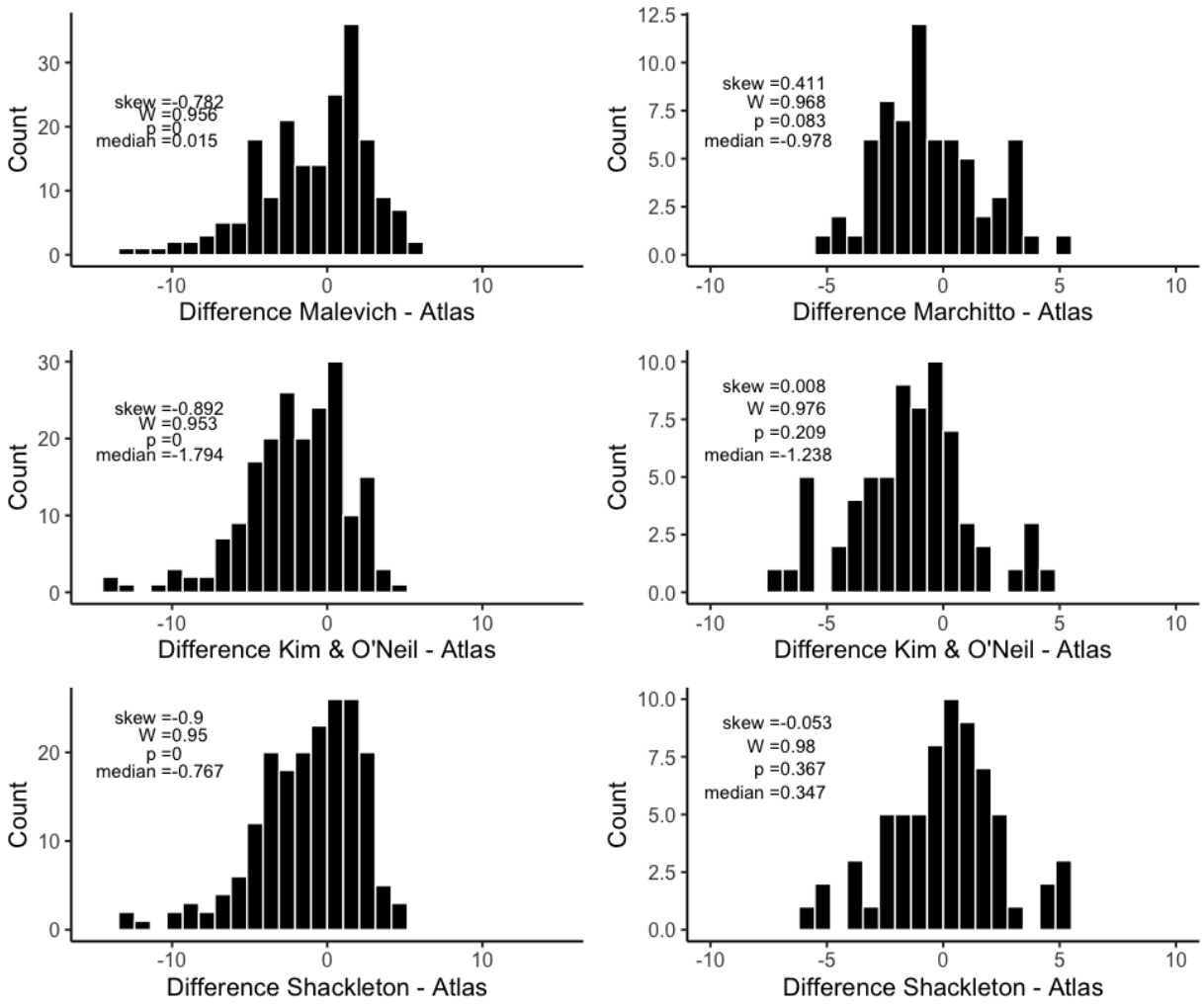

Figure 1.S.7: Histogram of differences between calcification temperatures calculated using Method 2 (Isotopic temperatures from Marchitto et al., 2014 and Malevich et al., 2019) and Method 1 (Atlas temperatures)

.

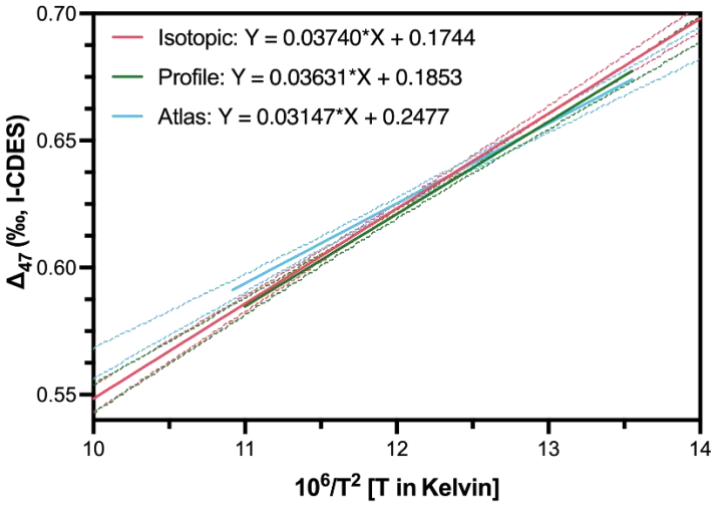

Figure 1.S.8: Comparison of regression parameters derived using different methods for estimating calcification temperatures.

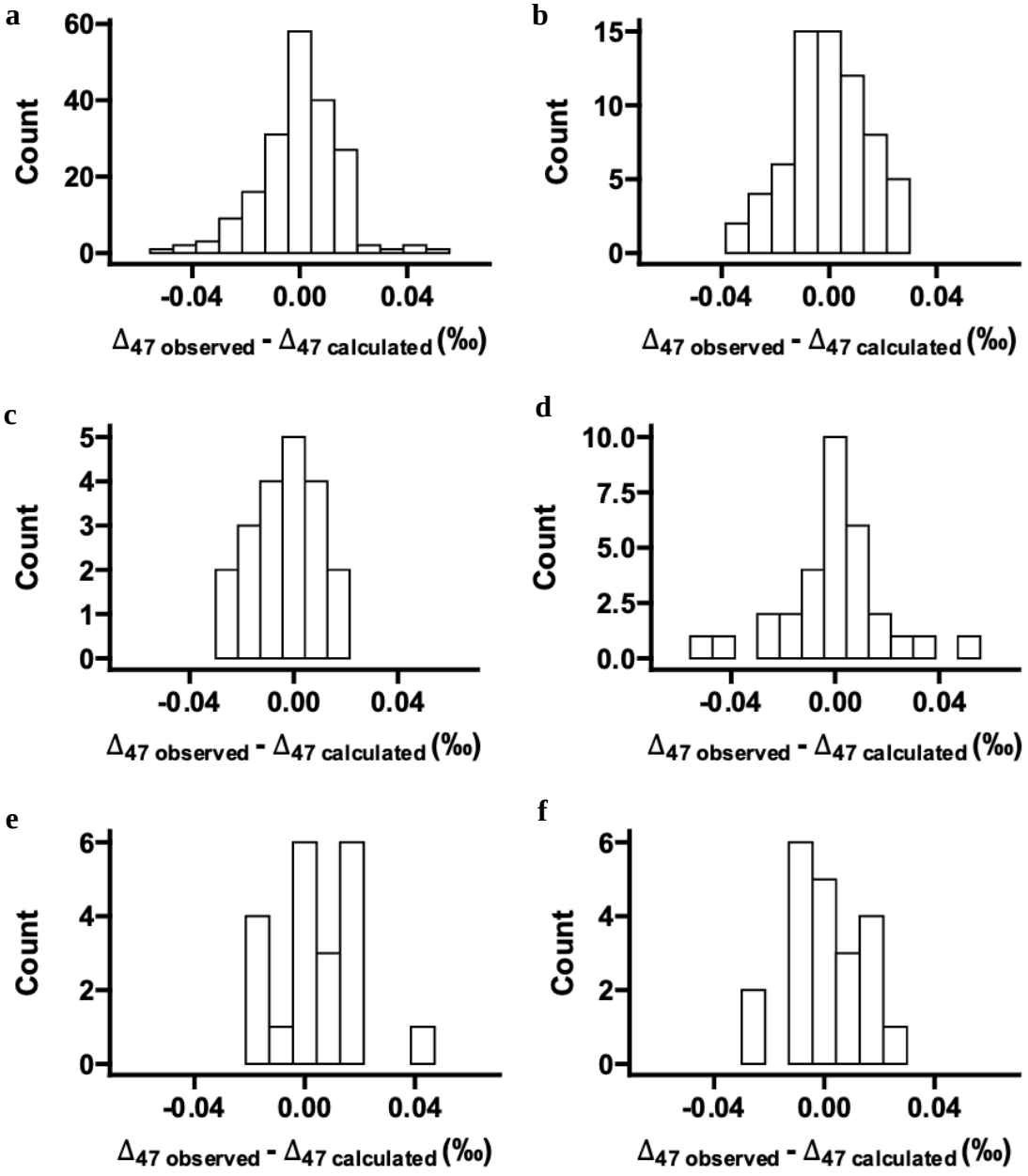

Figure 1.S.9: Histogram and Shaprio-Wilk test statistics of calculated Δ_{47} residuals using the regression through the compiled foraminifera data. Results are for A) planktonics B) benthics and n > 20 species C*) P. obliquiloculata* D) *T. sacculifer* E*) G. ruber* and F) *G. bulloides*. Δ_{47} residuals for different taxa calculated as $\Delta_{47observed}$ minus $\Delta_{47calculated}$ using the foraminiferal calibration equation from our meta-analysis. Shapiro-Wilk test entire dataset, W = 0.981, p <0.01, skewness = -0.16).

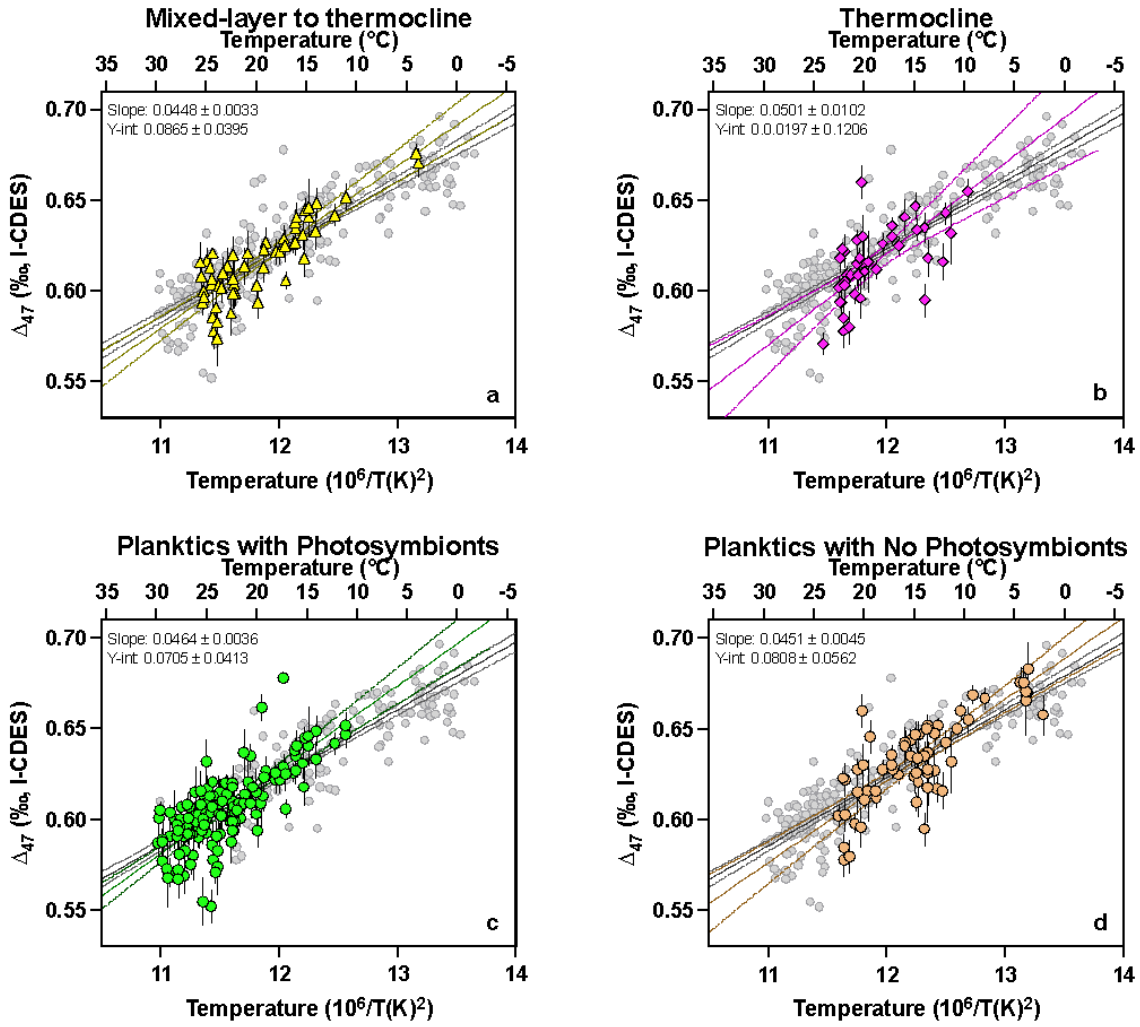

Figure 1.S.10: Regressions for subsets of planktonic foraminiferal core-top data. 95% confidence interval shown. Grey symbols are for the entire foraminiferal dataset and colored symbols are data for individual populations. Errors for individual points in SE.

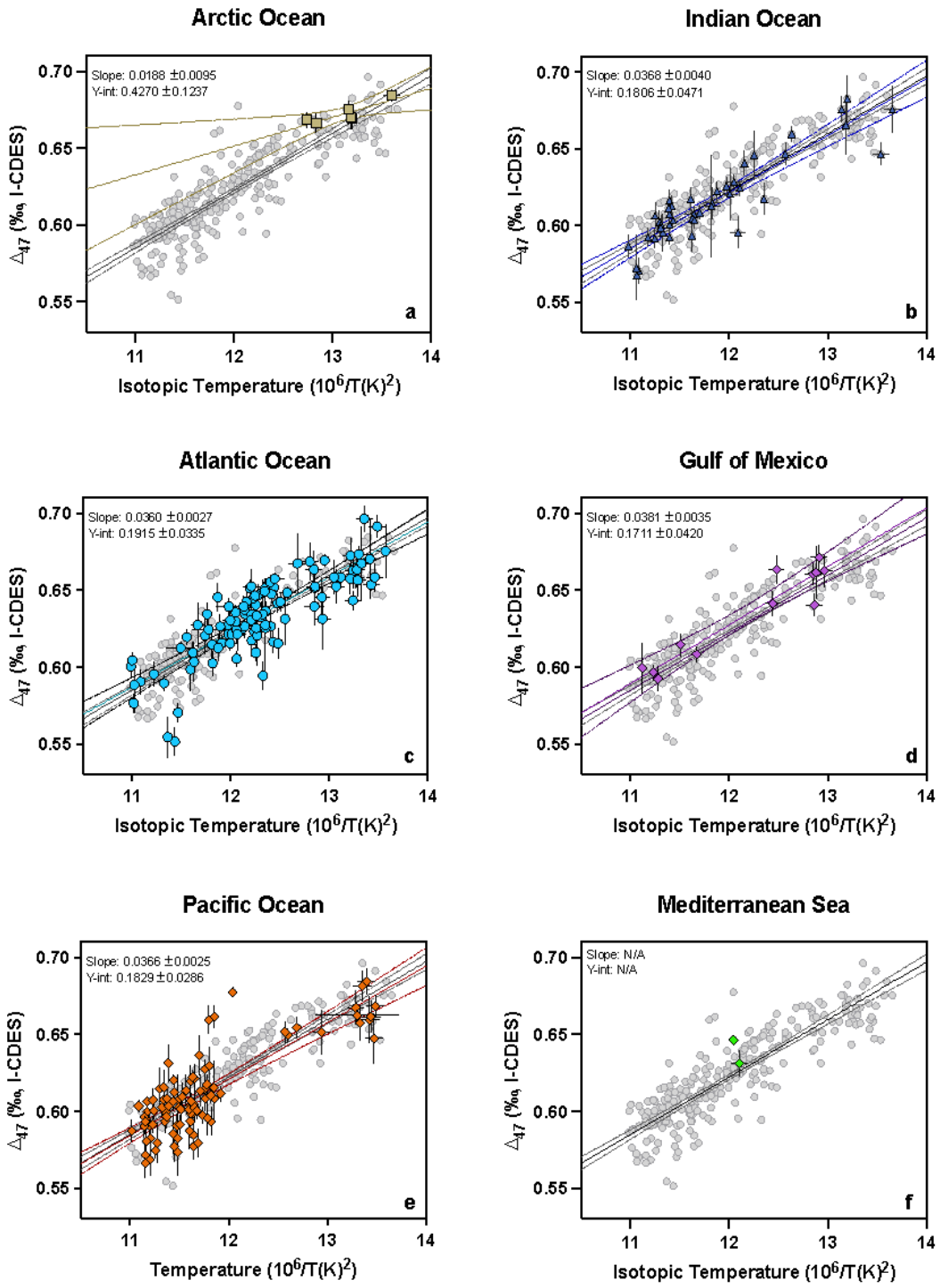

Figure 1.S.11: Regressions for subsets of foraminiferal core-top data by ocean region. 95% confidence interval shown. Grey symbols are for the entire foraminiferal dataset and colored symbols are data for a specific region. Errors for individual points in SE.

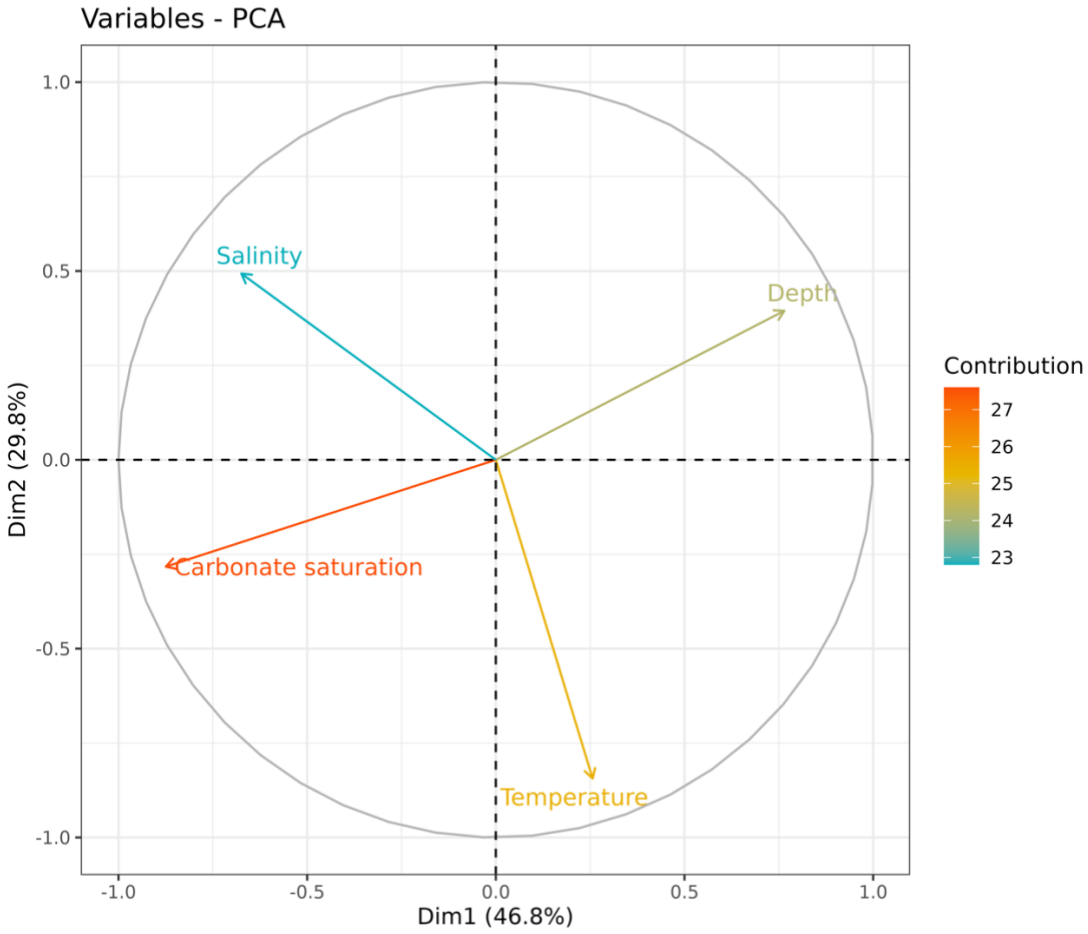

Figure 1.S.12: PCA analysis of hydrographic parameters: temperature, salinity, carbonate saturation, and depth.

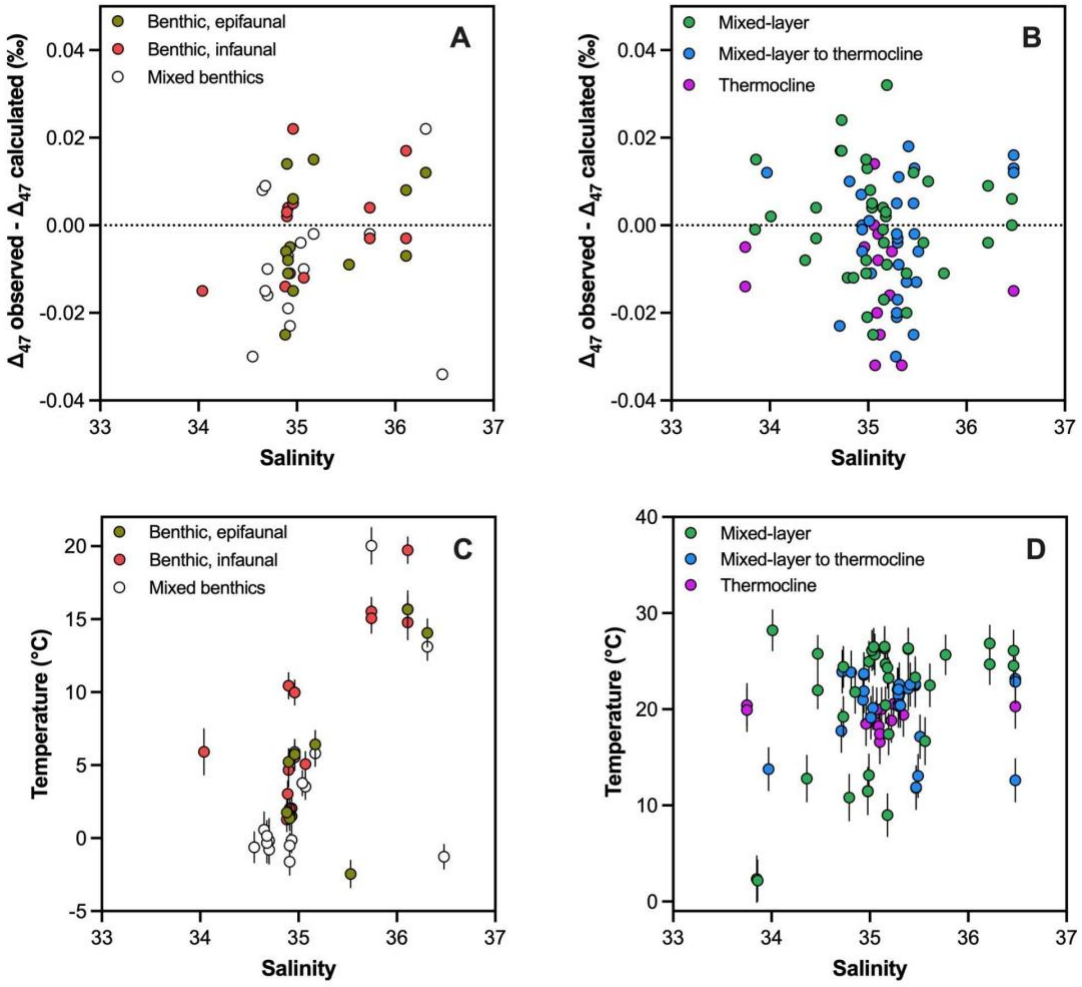

Figure 1.S.13: Δ_{47} residuals vs salinity (A, C) and temperature vs. salinity (B, D) for benthic (left) and planktonic (right) foraminifera. Δ_{47} residuals for different taxa calculated as $\Delta_{47observed}$ minus $\Delta_{47calculated}$ using the foraminiferal calibration equation from our meta-analysis.

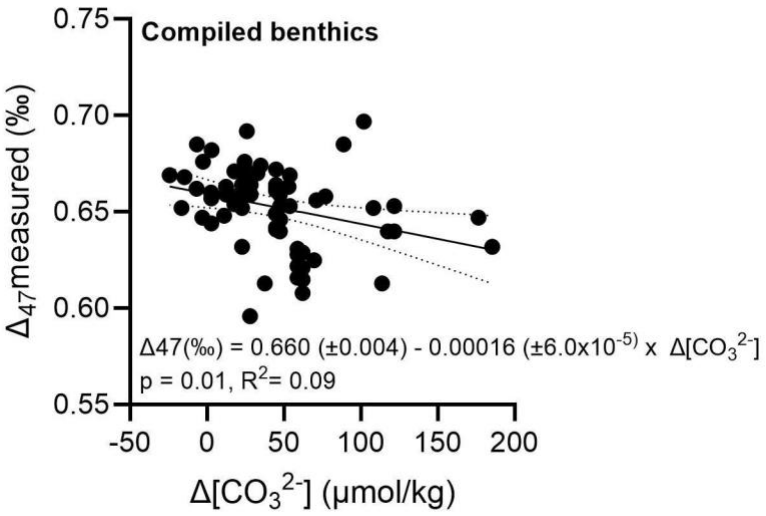

Figure 1.S.14: Linear regression between benthic foraminiferal Δ_{47} and $\Delta[CO_3^{2-}]$. There is a weak but significant linear relationship consistent with a potential carbonate ion effect.

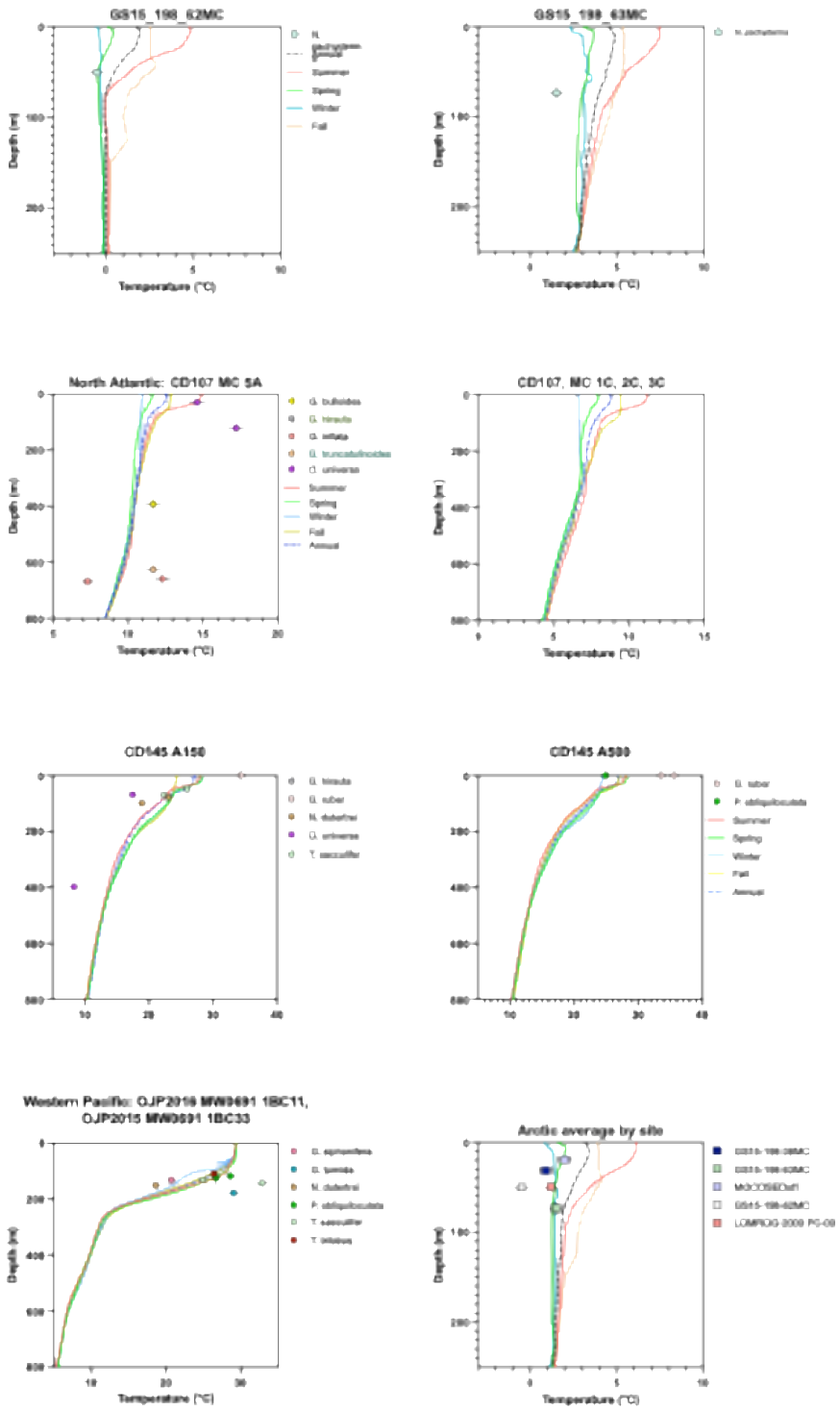

Figure 1.S.15a: Part 1 of Δ_{47}-T reconstructed for each species and seasonal and annual temperature profiles for each of the sites (World Ocean Atlas, 2013). Calcification depth for each species was determined following method 3; see also Section S3.

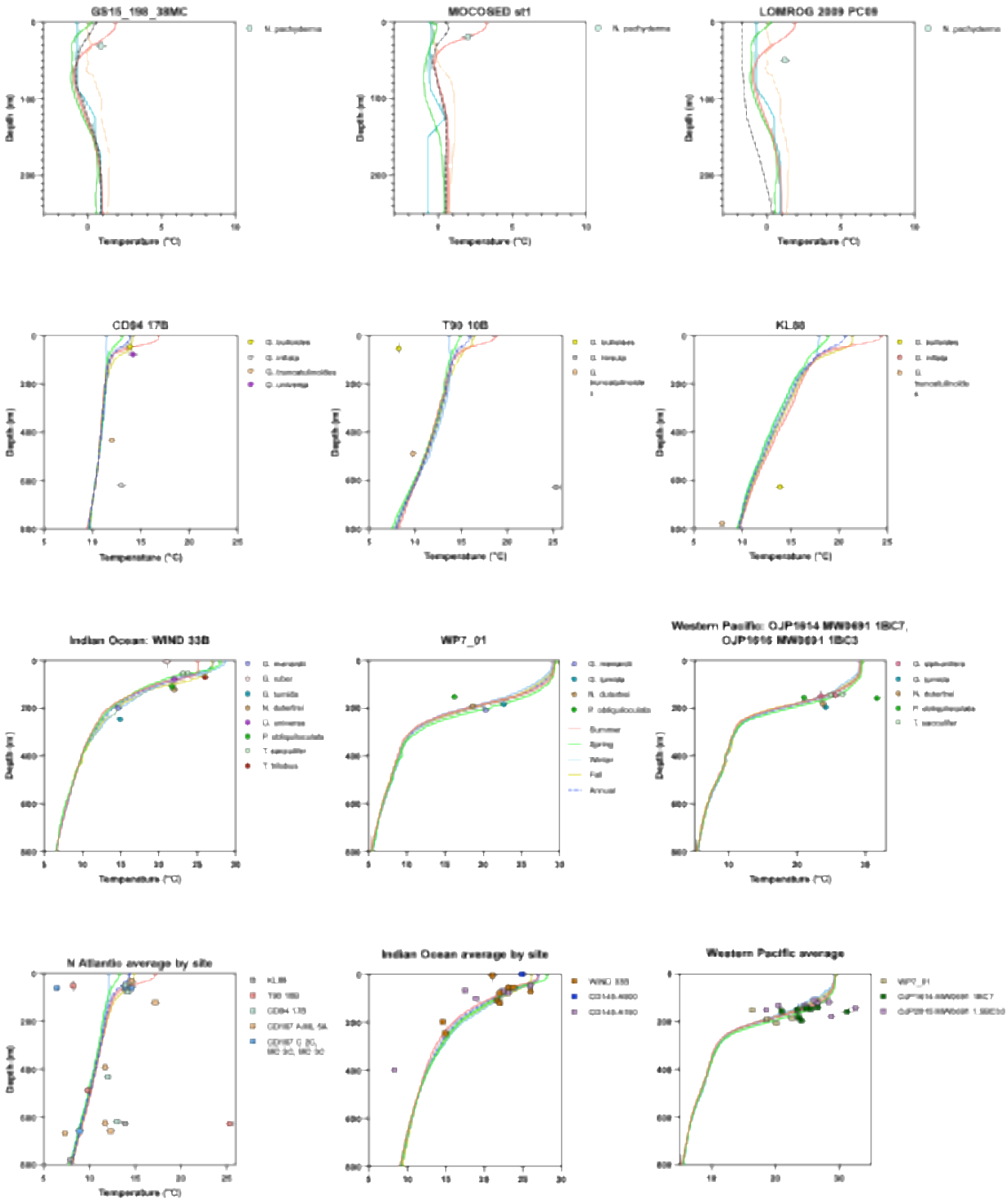

Figure 1.S.15b: Part 2 of Δ_{47}-T reconstructed for each species and seasonal and annual temperature profiles for each of the sites (World Ocean Atlas, 2013). Calcification depth for each species was determined following method 3; see also Section S3.

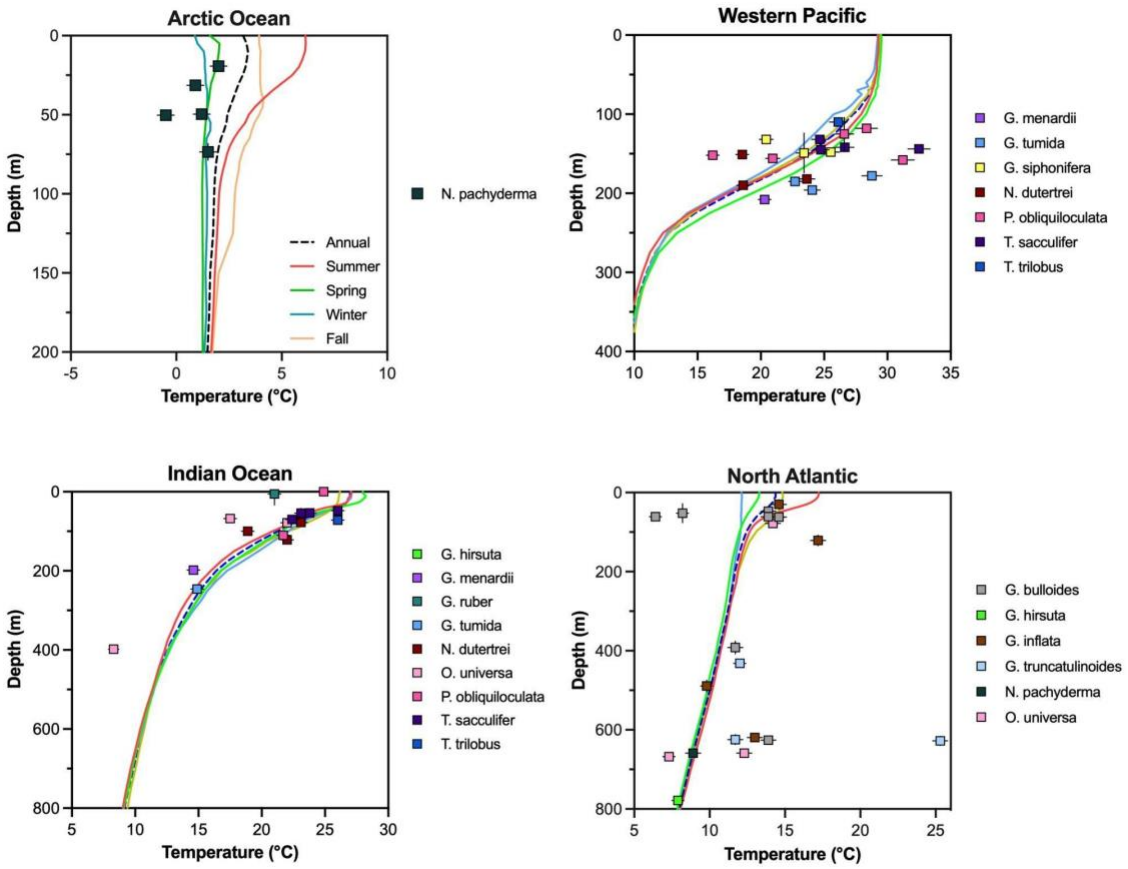

Figure 1.S.16: Composite figure showing Δ_{47}-T reconstructed for each basin using data from multiple sites compared to seasonal and annual temperature profiles for the different basins (World Ocean Atlas, 2013). Calcification depth for each species was determined following method 3; see also Section S3.

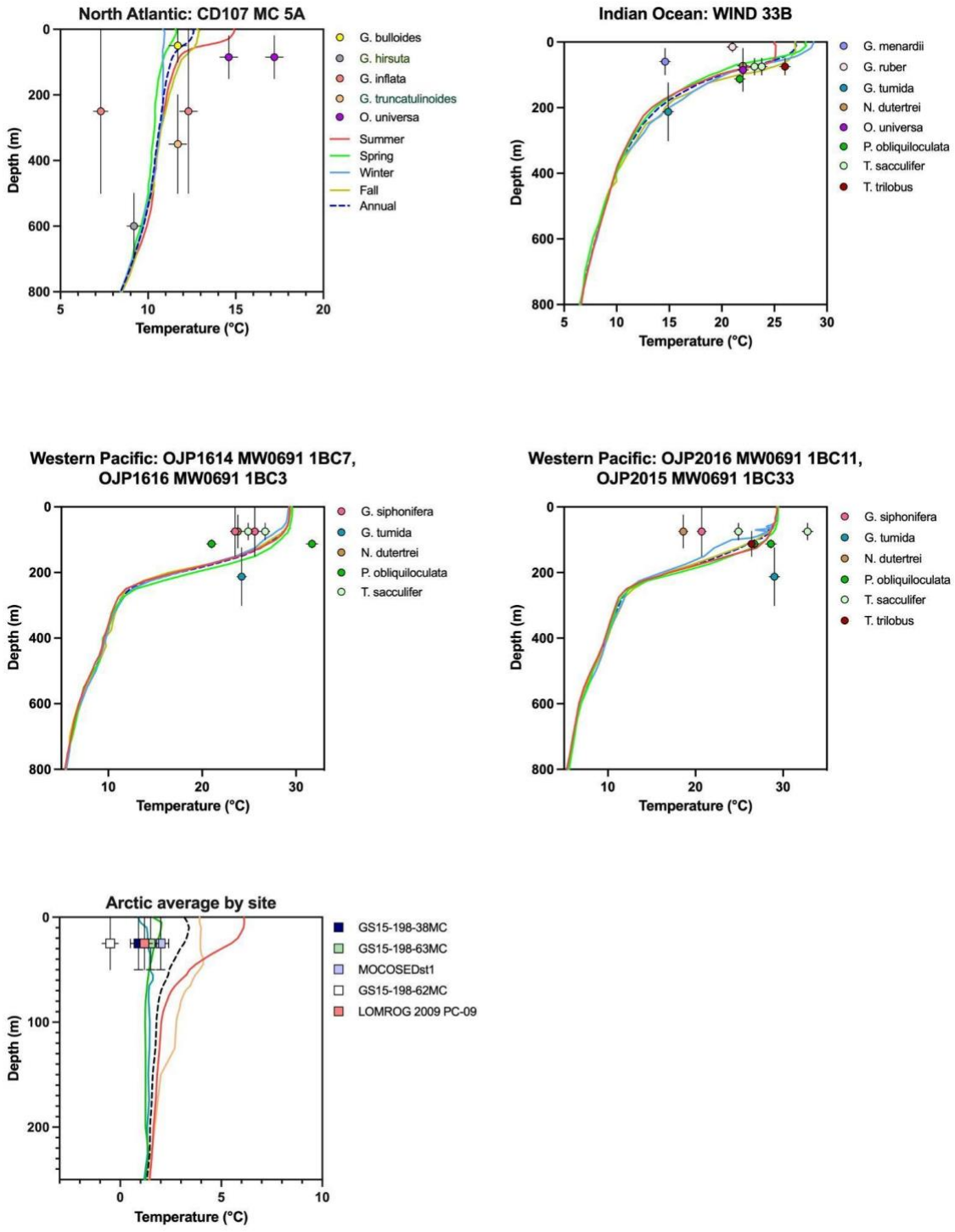

Figure 1.S.17: Δ_{47}-T reconstructed for different species compared to seasonal and annual vertical temperature profiles (World Ocean Atlas, 2013) for the Arctic, North Atlantic, Indian, and Western Pacific Oceans.

References

Agterhuis, T., Ziegler, M., de Winter, N. J., and Lourens, L. J. (2022). Warm deep-sea temperatures across Eocene Thermal Maximum 2 from clumped isotope thermometry. *Communications Earth and Environment*, *3*(1), 1–9. https://doi.org/10.1038/s43247-022-00350-8

Anand, P., Elderfield, H., and Conte, M. H. (2003). Calibration of Mg/Ca thermometry in planktic foraminifera from a sediment trap time series. *Paleoceanography*, *18*(2). https://doi.org/10.1029/2002PA000846

Anderson, N. T., Kelson, J. R., Kele, S., Daëron, M., Bonifacie, M., Horita, J., et al. (2021). A Unified Clumped Isotope Thermometer Calibration (0.5–1,100°C) Using Carbonate-Based Standardization. *Geophysical Research Letters*, *48*(7), e2020GL092069. https://doi.org/10.1029/2020GL092069

Bard, E. (2000). Hydrological Impact of Heinrich Events in the Subtropical Northeast Atlantic. *Science*, *289*(5483), 1321–1324. https://doi.org/10.1126/science.289.5483.1321

Bard, E., Rostek, F., and Sonzogni, C. (1997). Interhemispheric synchrony of the last deglaciation inferred from alkenone palaeothermometry. *Nature*, *385*(6618), 707–710. https://doi.org/10.1038/385707a0

Barker, S., Greaves, M., and Elderfield, H. (2003). A study of cleaning procedures used for foraminiferal Mg/Ca paleothermometry. *Geochemistry, Geophysics, Geosystems*, *4*(9). https://doi.org/10.1029/2003GC000559

Barker, S., Cacho, I., Benway, H., and Tachikawa, K. (2005). Planktic foraminiferal Mg/Ca as a proxy for past oceanic temperatures: a methodological overview and data compilation for the Last Glacial Maximum. *Quaternary Science Reviews*, *24*(7), 821–834. https://doi.org/10.1016/j.quascirev.2004.07.016

Bartoń, K. (2022). MuMIn: Multi-model inference (2020). [R package version 1.5].

Bemis, B. E., Spero, H. J., Bijma, J., and Lea, D. W. (1998). Reevaluation of the oxygen isotopic composition of planktic foraminifera: Experimental results and revised paleotemperature equations. *Paleoceanography*, *13*(2), 150–160. https://doi.org/10.1029/98PA00070

Bernasconi, S. M., Müller, I. A., Bergmann, K. D., Breitenbach, S. F. M., Fernandez, A., Hodell, D. A., et al. (2018). Reducing Uncertainties in Carbonate Clumped Isotope Analysis Through Consistent Carbonate-Based Standardization. *Geochemistry, Geophysics, Geosystems*, *19*(9), 2895–2914. https://doi.org/10.1029/2017GC007385

Bernasconi, S. M., Daëron, M., Bergmann, K. D., Bonifacie, M., Meckler, A. N., Affek, H. P., et al. (2021). InterCarb: A Community Effort to Improve Interlaboratory Standardization of the Carbonate Clumped Isotope Thermometer Using Carbonate Standards. *Geochemistry, Geophysics, Geosystems*, *22*(5), e2020GC009588. https://doi.org/10.1029/2020GC009588

Bian, N., and Martin, P. A. (2010). Investigating the fidelity of Mg/Ca and other elemental data from reductively cleaned planktic foraminifera. *Paleoceanography*, *25*(2). https://doi.org/10.1029/2009PA001796

Breitenbach, S. F. M., Mleneck-Vautravers, M. J., Grauel, A.-L., Lo, L., Bernasconi, S. M., Müller, I. A., et al. (2018). Coupled Mg/Ca and clumped isotope analyses of foraminifera provide consistent water temperatures. *Geochimica et Cosmochimica Acta*, *236*, 283–296. https://doi.org/10.1016/j.gca.2018.03.010

Came, R. E., Oppo, D. W., and McManus, J. F. (2007). Amplitude and timing of temperature and salinity variability in the subpolar North Atlantic over the past 10 k.y. *Geology*, *35*(4), 315–318. https://doi.org/10.1130/G23455A.1

Conte, M. H., Weber, J. C., King, L. L., and Wakeham, S. G. (2001). The alkenone temperature signal in western North Atlantic surface waters. *Geochimica et Cosmochimica Acta*, *65*(23), 4275–4287. https://doi.org/10.1016/S0016-7037(01)00718-9

Conte, M. H., Sicre, M.-A., Rühlemann, C., Weber, J. C., Schulte, S., Schulz-Bull, D., and Blanz, T. (2006). Global temperature calibration of the alkenone unsaturation index (UK′37) in surface waters and comparison with surface sediments. *Geochemistry, Geophysics, Geosystems*, *7*(2). https://doi.org/10.1029/2005GC001054

Coxall, H. K., Wilson, P. A., Pälike, H., Lear, C. H., and Backman, J. (2005). Rapid stepwise onset of Antarctic glaciation and deeper calcite compensation in the Pacific Ocean. *Nature*, *433*(7021), 53–57. https://doi.org/10.1038/nature03135

Cramer, B. S., Miller, K. G., Barrett, P. J., and Wright, J. D. (2011). Late Cretaceous–Neogene trends in deep ocean temperature and continental ice volume: Reconciling records of benthic foraminiferal geochemistry (δ18O and Mg/Ca) with sea level history. *Journal of Geophysical Research: Oceans*, *116*(C12). https://doi.org/10.1029/2011JC007255

Daëron, M., and Gray, W. R. (2023). Revisiting Oxygen-18 and Clumped Isotopes in Planktic and Benthic Foraminifera. *Paleoceanography and Paleoclimatology*, *38*(10), e2023PA004660. https://doi.org/10.1029/2023PA004660

Daëron, M., Blamart, D., Peral, M., and Affek, H. P. (2016). Absolute isotopic abundance ratios and the accuracy of Δ47 measurements. *Chemical Geology*, *442*, 83–96. https://doi.org/10.1016/j.chemgeo.2016.08.014

Darling, K. F., Wade, C. M., Siccha, M., Trommer, G., Schulz, H., Abdolalipour, S., and Kurasawa, A. (2017). Genetic diversity and ecology of the planktic foraminifers Globigerina bulloides, Turborotalita quinqueloba and Neogloboquadrina pachyderma off

the Oman margin during the late SW Monsoon. *Marine Micropaleontology*, *137*, 64–77. https://doi.org/10.1016/j.marmicro.2017.10.006

Dawber, C. F., and Tripati, A. (2012). Relationships between bottom water carbonate saturation and element/Ca ratios in core-top samples of the benthic foraminifera *Oridorsalis umbonatus*. *Biogeosciences*, *9*(8), 3029–3045. https://doi.org/10.5194/bg-9-3029-2012

Defliese, W. F., and Lohmann, K. C. (2015). Non-linear mixing effects on mass-47 CO2 clumped isotope thermometry: Patterns and implications. *Rapid Communications in Mass Spectrometry*, *29*(9), 901–909. https://doi.org/10.1002/rcm.7175

Defliese, W. F., and Tripati, A. (2020). Analytical effects on clumped isotope thermometry: Comparison of a common sample set analyzed using multiple instruments, types of standards, and standardization windows. *Rapid Communications in Mass Spectrometry*, *34*(8), e8666. https://doi.org/10.1002/rcm.8666

Dennis, K. J., Affek, H. P., Passey, B. H., Schrag, D. P., and Eiler, J. M. (2011). Defining an absolute reference frame for 'clumped' isotope studies of CO2. *Geochimica et Cosmochimica Acta*, *75*(22), 7117–7131. https://doi.org/10.1016/j.gca.2011.09.025

Dickson, A. G., Sabine, C. L., Christian, J. R., Bargeron, C. P., and North Pacific Marine Science Organization (Eds.). (2007). *Guide to best practices for ocean CO2 measurements*. Sidney, BC: North Pacific Marine Science Organization.

Elderfield, H., and Ganssen, G. (2000). Past temperature and δ18O of surface ocean waters inferred from foraminiferal Mg/Ca ratios. *Nature*, *405*(6785), 442–445. https://doi.org/10.1038/35013033

Elderfield, H., Yu, J., Anand, P., Kiefer, T., and Nyland, B. (2006). Calibrations for benthic foraminiferal Mg/Ca paleothermometry and the carbonate ion hypothesis. *Earth and Planetary Science Letters*, *250*(3), 633–649. https://doi.org/10.1016/j.epsl.2006.07.041

Evans, D., Sagoo, N., Renema, W., Cotton, L. J., Müller, W., Todd, J. A., et al. (2018). Eocene greenhouse climate revealed by coupled clumped isotope-Mg/Ca thermometry. *Proceedings of the National Academy of Sciences*, *115*(6), 1174–1179. https://doi.org/10.1073/pnas.1714744115

Ferguson, J. E., Henderson, G. M., Kucera, M., and Rickaby, R. E. M. (2008). Systematic change of foraminiferal Mg/Ca ratios across a strong salinity gradient. *Earth and Planetary Science Letters*, *265*(1), 153–166. https://doi.org/10.1016/j.epsl.2007.10.011

Fox, J., and Weisberg, S. (2019). Using car functions in other functions. [CRAN R].

de Garidel-Thoron, T., Rosenthal, Y., Bassinot, F., and Beaufort, L. (2005). Stable sea surface temperatures in the western Pacific warm pool over the past 1.75 million years. *Nature*, *433*(7023), 294–298. https://doi.org/10.1038/nature03189

Ghosh, P., Adkins, J., Affek, H., Balta, B., Guo, W., Schauble, E. A., et al. (2006). 13C–18O bonds in carbonate minerals: A new kind of paleothermometer. *Geochimica et Cosmochimica Acta*, *70*(6), 1439–1456. https://doi.org/10.1016/j.gca.2005.11.014

de Goeyse, S., Webb, A. E., Reichart, G.-J., and de Nooijer, L. J. (2021). Carbonic anhydrase is involved in calcification by the benthic foraminifer *Amphistegina lessonii*. *Biogeosciences*, *18*(2), 393–401. https://doi.org/10.5194/bg-18-393-2021

Grauel, A.-L., Schmid, T. W., Hu, B., Bergami, C., Capotondi, L., Zhou, L., and Bernasconi, S. M. (2013). Calibration and application of the 'clumped isotope' thermometer to foraminifera for high-resolution climate reconstructions. *Geochimica et Cosmochimica Acta*, *108*, 125–140. https://doi.org/10.1016/j.gca.2012.12.049

Gray, W. R., and Evans, D. (2019). Nonthermal Influences on Mg/Ca in Planktic Foraminifera: A Review of Culture Studies and Application to the Last Glacial Maximum.

Paleoceanography and Paleoclimatology, *34*(3), 306–315. https://doi.org/10.1029/2018PA003517

Greaves, M., Caillon, N., Rebaubier, H., Bartoli, G., Bohaty, S., Cacho, I., et al. (2008). Interlaboratory comparison study of calibration standards for foraminiferal Mg/Ca thermometry. *Geochemistry, Geophysics, Geosystems*, *9*(8). https://doi.org/10.1029/2008GC001974

Guo, W. (2020). Kinetic clumped isotope fractionation in the DIC-H2O-CO2 system: Patterns, controls, and implications. *Geochimica et Cosmochimica Acta*, *268*, 230–257. https://doi.org/10.1016/j.gca.2019.07.055

Hill, P. S., Tripati, A. K., and Schauble, E. A. (2014). Theoretical constraints on the effects of pH, salinity, and temperature on clumped isotope signatures of dissolved inorganic carbon species and precipitating carbonate minerals. *Geochimica et Cosmochimica Acta*, *125*, 610–652. https://doi.org/10.1016/j.gca.2013.06.018

Hönisch, B., Allen, K. A., Lea, D. W., Spero, H. J., Eggins, S. M., Arbuszewski, J., et al. (2013). The influence of salinity on Mg/Ca in planktic foraminifers – Evidence from cultures, core-top sediments and complementary δ18O. *Geochimica et Cosmochimica Acta*, *121*, 196–213. https://doi.org/10.1016/j.gca.2013.07.028

Hoogakker, B. A. A., Klinkhammer, G. P., Elderfield, H., Rohling, E. J., and Hayward, C. (2009). Mg/Ca paleothermometry in high salinity environments. *Earth and Planetary Science Letters*, *284*(3), 583–589. https://doi.org/10.1016/j.epsl.2009.05.027

Ishimura, T., Tsunogai, U., Hasegawa, S., Nakagawa, F., Oi, T., Kitazato, H., et al. (2012). Variation in stable carbon and oxygen isotopes of individual benthic foraminifera: tracers for quantifying the magnitude of isotopic disequilibrium. *Biogeosciences*, *9*(11), 4353–4367. https://doi.org/10.5194/bg-9-4353-2012

Jautzy, J. J., Savard, M. M., Dhillon, R. S., Bernasconi, S. M., and Smirnoff, A. (2020). Clumped isotope temperature calibration for calcite: Bridging theory and experimentation. *Geochemical Perspectives Letters*, *14*, 36–41. https://doi.org/10.7185/geochemlet.2021

Jentzen, A., Nürnberg, D., Hathorne, E. C., and Schönfeld, J. (2018). Mgandthinsp;/andthinsp;Ca and δ^{18}O in living planktic foraminifers from the Caribbean, Gulf of Mexico and Florida Straits. *Biogeosciences*, *15*(23), 7077–7095. https://doi.org/10.5194/bg-15-7077-2018

John, C. M., and Bowen, D. (2016). Community software for challenging isotope analysis: First applications of 'Easotope' to clumped isotopes. *Rapid Communications in Mass Spectrometry*, *30*(21), 2285–2300. https://doi.org/10.1002/rcm.7720

Kelson, J. R., Huntington, K. W., Schauer, A. J., Saenger, C., and Lechler, A. R. (2017). Toward a universal carbonate clumped isotope calibration: Diverse synthesis and preparatory methods suggest a single temperature relationship. *Geochimica et Cosmochimica Acta*, *197*, 104–131. https://doi.org/10.1016/j.gca.2016.10.010

Kim, J.-H., Schouten, S., Hopmans, E. C., Donner, B., and Sinninghe Damsté, J. S. (2008). Global sediment core-top calibration of the TEX86 paleothermometer in the ocean. *Geochimica et Cosmochimica Acta*, *72*(4), 1154–1173. https://doi.org/10.1016/j.gca.2007.12.010

Kim, S.-T., and O'Neil, J. R. (1997). Equilibrium and nonequilibrium oxygen isotope effects in synthetic carbonates. *Geochimica et Cosmochimica Acta*, *61*(16), 3461–3475. https://doi.org/10.1016/S0016-7037(97)00169-5

Kluge, T., John, C. M., Jourdan, A.-L., Davis, S., and Crawshaw, J. (2015). Laboratory calibration of the calcium carbonate clumped isotope thermometer in the 25–250 °C

temperature range. *Geochimica et Cosmochimica Acta*, *157*, 213–227. https://doi.org/10.1016/j.gca.2015.02.028

Koutavas, A. (2002). El Nino-Like Pattern in Ice Age Tropical Pacific Sea Surface Temperature. *Science*, *297*(5579), 226–230. https://doi.org/10.1126/science.1072376

Lea, D. W., Mashiotta, T. A., and Spero, H. J. (1999). Controls on magnesium and strontium uptake in planktic foraminifera determined by live culturing. *Geochimica et Cosmochimica Acta*, *63*(16), 2369–2379. https://doi.org/10.1016/S0016-7037(99)00197-0

Lea, D. W., Martin, P. A., Pak, D. K., and Spero, H. J. (2002). Reconstructing a 350ky history of sea level using planktic Mg/Ca and oxygen isotope records from a Cocos Ridge core. *Quaternary Science Reviews*, *21*(1), 283–293. https://doi.org/10.1016/S0277-3791(01)00081-6

Lear, C. H., and Rosenthal, Y. (2006). Benthic foraminiferal Li/Ca: Insights into Cenozoic seawater carbonate saturation state. *Geology*, *34*(11), 985–988. https://doi.org/10.1130/G22792A.1

Lear, C. H., Mawbey, E. M., and Rosenthal, Y. (2010). Cenozoic benthic foraminiferal Mg/Ca and Li/Ca records: toward unlocking temperatures and saturation states. *Paleoceanography*, *25*(4). https://doi.org/10.1029/2009PA001880

LeGrande, A. N., and Schmidt, G. A. (2006). Global gridded data set of the oxygen isotopic composition in seawater. *Geophysical Research Letters*, *33*(12). https://doi.org/10.1029/2006GL026011

Leider, A., Hinrichs, K.-U., Mollenhauer, G., and Versteegh, G. J. M. (2010). Core-top calibration of the lipid-based U37K′ and TEX86 temperature proxies on the southern

Italian shelf (SW Adriatic Sea, Gulf of Taranto). *Earth and Planetary Science Letters*, *300*(1), 112–124. https://doi.org/10.1016/j.epsl.2010.09.042

Leutert, T. J., Sexton, P. F., Tripati, A., Piasecki, A., Ho, S. L., and Meckler, A. N. (2019). Sensitivity of clumped isotope temperatures in fossil benthic and planktic foraminifera to diagenetic alteration. *Geochimica et Cosmochimica Acta*, *257*, 354–372. https://doi.org/10.1016/j.gca.2019.05.005

Leutert, T. J., Auderset, A., Martínez-García, A., Modestou, S., and Meckler, A. N. (2020). Coupled Southern Ocean cooling and Antarctic ice sheet expansion during the middle Miocene. *Nature Geoscience*, *13*(9), 634–639. https://doi.org/10.1038/s41561-020-0623-0

Levitus, S., Locarnini, R. A., Boyer, T. P., Mishonov, A. V., Antonov, J. I., Garcia, H. E., et al. (2010). World ocean atlas 2009. Retrieved from https://repository.library.noaa.gov/view/noaa/1259

Lucarelli, J. K., Carroll, H. M., Ulrich, R. N., Elliott, B. M., Coplen, T. B., Eagle, R. A., and Tripati, A. (2023). Equilibrated Gas and Carbonate Standard-Derived Dual (Δ47 and Δ48) Clumped Isotope Values. *Geochemistry, Geophysics, Geosystems*, *24*(2), e2022GC010458. https://doi.org/10.1029/2022GC010458

Lucarelli, J. K., Purgstaller, B., Parven, Z., Watkins, J. M., Eagle, R., Dietzel, M., and Tripati, A. (2022). Paired Δ47 and Δ48 analyses and model calculations constrain equilibrium, experimentally-manipulated kinetic isotope effects, and mixing effects in calcite. Retrieved from https://eartharxiv.org/repository/view/3039/

Malevich, S. B., Vetter, L., and Tierney, J. E. (2019). Global Core Top Calibration of δ18O in Planktic Foraminifera to Sea Surface Temperature. *Paleoceanography and Paleoclimatology*, *34*(8), 1292–1315. https://doi.org/10.1029/2019PA003576

Marchitto, T. M., Curry, W. B., Lynch-Stieglitz, J., Bryan, S. P., Cobb, K. M., and Lund, D. C. (2014). Improved oxygen isotope temperature calibrations for cosmopolitan benthic foraminifera. *Geochimica et Cosmochimica Acta*, *130*, 1–11. https://doi.org/10.1016/j.gca.2013.12.034

Martin, P. A., and Lea, D. W. (2002). A simple evaluation of cleaning procedures on fossil benthic foraminiferal Mg/Ca. *Geochemistry, Geophysics, Geosystems*, *3*(10), 1–8. https://doi.org/10.1029/2001GC000280

Mashiotta, T. A., Lea, D. W., and Spero, H. J. (1999). Glacial–interglacial changes in Subantarctic sea surface temperature and δ18O-water using foraminiferal Mg. *Earth and Planetary Science Letters*, *170*(4), 417–432. https://doi.org/10.1016/S0012-821X(99)00116-8

Meckler, A. N., Sexton, P. F., Piasecki, A. M., Leutert, T. J., Marquardt, J., Ziegler, M., et al. (2022). Cenozoic evolution of deep ocean temperature from clumped isotope thermometry. *Science*, *377*(6601), 86–90. https://doi.org/10.1126/science.abk0604

Meinicke, N., Ho, S. L., Hannisdal, B., Nürnberg, D., Tripati, A., Schiebel, R., and Meckler, A. N. (2020). A robust calibration of the clumped isotopes to temperature relationship for foraminifers. *Geochimica et Cosmochimica Acta*, *270*, 160–183. https://doi.org/10.1016/j.gca.2019.11.022

Müller, P. J., Kirst, G., Ruhland, G., von Storch, I., and Rosell-Melé, A. (1998). Calibration of the alkenone paleotemperature index U37K′ based on core-tops from the eastern South Atlantic and the global ocean (60°N-60°S). *Geochimica et Cosmochimica Acta*, *62*(10), 1757–1772. https://doi.org/10.1016/S0016-7037(98)00097-0

de Nooijer, L. J., Spero, H. J., Erez, J., Bijma, J., and Reichart, G. J. (2014). Biomineralization in perforate foraminifera. *Earth-Science Reviews*, *135*, 48–58. https://doi.org/10.1016/j.earscirev.2014.03.013

Nürnberg, D., Buma, J., and Hemleben, C. (1996). Assessing the reliability of magnesium in foraminiferal calcite as a proxy for water mass temperatures. *Geochimica et Cosmochimica Acta*, *60*(5), 803–814.

Olsen, A., Lange, N., Key, R. M., Tanhua, T., Álvarez, M., Becker, S., et al. (2019). GLODAPv2.2019 – an update of GLODAPv2. *Earth System Science Data*, *11*(3), 1437–1461. https://doi.org/10.5194/essd-11-1437-2019

Pak, D. K., Lea, D. W., and Kennett, J. P. (2004). Seasonal and interannual variation in Santa Barbara Basin water temperatures observed in sediment trap foraminiferal Mg/Ca. *Geochemistry, Geophysics, Geosystems*, *5*(12). https://doi.org/10.1029/2004GC000760

Parvez, Z., Lucarelli, J., Matamoros, I. W., Rubi, J., Miguel, K., Elliott, B., et al. (2023). Dual carbonate clumped isotopes (Δ47-Δ48) constrains kinetic effects and timescales in peridotite-associated springs at the Cedars, Northern California. *Geochimica et Cosmochimica Acta*, *358*, 77–92.

Peck, V. L., Yu, J., Kender, S., and Riesselman, C. R. (2010). Shifting ocean carbonate chemistry during the Eocene-Oligocene climate transition: Implications for deep-ocean Mg/Ca paleothermometry. *Paleoceanography*, *25*(4). https://doi.org/10.1029/2009PA001906

Peral, M., Daëron, M., Blamart, D., Bassinot, F., Dewilde, F., Smialkowski, N., et al. (2018). Updated calibration of the clumped isotope thermometer in planktic and benthic foraminifera. *Geochimica et Cosmochimica Acta*, *239*, 1–16. https://doi.org/10.1016/j.gca.2018.07.016

Petersen, S. V., Defliese, W. F., Saenger, C., Daëron, M., Huntington, K. W., John, C. M., et al. (2019). Effects of Improved 17O Correction on Interlaboratory Agreement in Clumped Isotope Calibrations, Estimates of Mineral-Specific Offsets, and Temperature Dependence of Acid Digestion Fractionation. *Geochemistry, Geophysics, Geosystems*, *20*(7), 3495–3519. https://doi.org/10.1029/2018GC008127

Piasecki, A., Bernasconi, S. M., Grauel, A.-L., Hannisdal, B., Ho, S. L., Leutert, T. J., et al. (2019). Application of Clumped Isotope Thermometry to Benthic Foraminifera. *Geochemistry, Geophysics, Geosystems*, *20*(4), 2082–2090. https://doi.org/10.1029/2018GC007961

Powers, L., Werne, J. P., Vanderwoude, A. J., Sinninghe Damsté, J. S., Hopmans, E. C., and Schouten, S. (2010). Applicability and calibration of the TEX86 paleothermometer in lakes. *Organic Geochemistry*, *41*(4), 404–413. https://doi.org/10.1016/j.orggeochem.2009.11.009

Pusz, A. E., Thunell, R. C., and Miller, K. G. (2011). Deep water temperature, carbonate ion, and ice volume changes across the Eocene-Oligocene climate transition. *Paleoceanography*, *26*(2). https://doi.org/10.1029/2010PA001950

R Core Team. (2022). R: A language and environment for statistical computing. (Version 4.2.1). Vienna, Austria: R Foundation for Statistical Computing. Retrieved from https://www.R-project.org/

Rathman, S., and Kuhnert, H. (2008). Carbonate ion effect on Mg/Ca, Sr/Ca and stable isotopes on the benthic foraminifera Oridorsalis umbonatus off Namibia. *Marine Micropaleontology*, *66*(2), 120–133.

Regenberg, M., Steph, S., Nürnberg, D., Tiedemann, R., and Garbe-Schönberg, D. (2009). Calibrating Mg/Ca ratios of multiple planktic foraminiferal species with δ18O-

calcification temperatures: Paleothermometry for the upper water column. *Earth and Planetary Science Letters*, *278*(3), 324–336. https://doi.org/10.1016/j.epsl.2008.12.019

Rippert, N., Nürnberg, D., Raddatz, J., Maier, E., Hathorne, E., Bijma, J., and Tiedemann, R. (2016). Constraining foraminiferal calcification depths in the western Pacific warm pool. *Marine Micropaleontology*, *128*, 14–27. https://doi.org/10.1016/j.marmicro.2016.08.004

Rohling, E.J., Gernon, T.M., Heslop, D., Reichart, G.J., Roberts, A.P. and Yu, J. (2024). Reconciling the apparent discrepancy between Cenozoic deep-sea temperatures from proxies and from benthic oxygen isotope deconvolution. *Paleoceanography and Paleoclimatology*, *39*(11), p.e2024PA004872.

Román-Palacios, C., Carroll, H., Arnold, A., Flores, R., Petersen, S., McKinnon, K., and Tripati, A. (2021). BayClump: Bayesian Calibration and Temperature Reconstructions for Clumped Isotope Thermometry. *Earth and Space Science Open Archive*. https://doi.org/10.1002/essoar.10507995.1

Rosenthal, Y., Perron-Cashman, S., Lear, C. H., Bard, E., Barker, S., Billups, K., et al. (2004). Interlaboratory comparison study of Mg/Ca and Sr/Ca measurements in planktic foraminifera for paleoceanographic research. *Geochemistry, Geophysics, Geosystems*, *5*(4). https://doi.org/10.1029/2003GC000650

Russell, A. D., Hönisch, B., Spero, H. J., and Lea, D. W. (2004). Effects of seawater carbonate ion concentration and temperature on shell U, Mg, and Sr in cultured planktic foraminifera. *Geochimica et Cosmochimica Acta*, *68*(21), 4347–4361. https://doi.org/10.1016/j.gca.2004.03.013

Sachs, J. P., Schneider, R. R., Eglinton, T. I., Freeman, K. H., Ganssen, G., McManus, J. F., and Oppo, D. W. (2000). Alkenones as paleoceanographic proxies. *Geochemistry, Geophysics, Geosystems*, *1*(11). https://doi.org/10.1029/2000GC000059

Sadekov, A. Yu., Darling, K. F., Ishimura, T., Wade, C. M., Kimoto, K., Singh, A. D., et al. (2016). Geochemical imprints of genotypic variants of Globigerina bulloides in the Arabian Sea. *Paleoceanography*, *31*(10), 1440–1452. https://doi.org/10.1002/2016PA002947

Schauble, E. A., Ghosh, P., and Eiler, J. M. (2006). Preferential formation of 13C–18O bonds in carbonate minerals, estimated using first-principles lattice dynamics. *Geochimica et Cosmochimica Acta*, *70*(10), 2510–2529. https://doi.org/10.1016/j.gca.2006.02.011

Schiebel, R., and Hemleben, C. (2017). *Planktic Foraminifers in the Modern Ocean*. Berlin, Heidelberg: Springer Berlin Heidelberg. https://doi.org/10.1007/978-3-662-50297-6

Schouten, S., Huguet, C., Hopmans, E. C., Kienhuis, M. V. M., and Sinninghe Damsté, J. S. (2007). Analytical Methodology for TEX $_{86}$ Paleothermometry by High-Performance Liquid Chromatography/Atmospheric Pressure Chemical Ionization-Mass Spectrometry. *Analytical Chemistry*, *79*(7), 2940–2944. https://doi.org/10.1021/ac062339v

Shackleton, N. J. (1974). Attainment of isotopic equilibrium between ocean water and the benthonic foraminifera genus Uvigerina: isotopic changes in the ocean during the last glacial. *Cent. Nat. Rech. Schi. Colloq. Int.*, *219*, 203–209.

Shackleton, Nicholas John, and Opdyke, N. D. (1973). Oxygen Isotope and Palaeomagnetic Stratigraphy of Equatorial Pacific Core V28-238: Oxygen Isotope Temperatures and Ice Volumes on a 10 ^{5} Year and 10 ^{6} Year Scale. *Quaternary Research*, *3*(1), 39–55. https://doi.org/10.1016/0033-5894(73)90052-5

Skinner, L. C., and Elderfield, H. (2005). Constraining ecological and biological bias in planktic foraminiferal Mg/Ca and δ18Occ: A multispecies approach to proxy calibration testing. *Paleoceanography*, *20*(1). https://doi.org/10.1029/2004PA001058

Skinner, L. C., Elderfield, H., and Hall, M. (2007). Phasing of millennial climate events and Northeast Atlantic deep-water temperature change since 50 ka BP. *Ocean Circulation: Mechanisms and Impacts—Past and Future Changes of Meridional Overturning*, *173*, 197–208.

Spero, H. J., Bijma, J., Lea, D. W., and Bemis, B. E. (1997). Effect of seawater carbonate concentration on foraminiferal carbon and oxygen isotopes. *Nature*, *390*(6659), 497–500. https://doi.org/10.1038/37333

Stirpe, C. R., Allen, K. A., Sikes, E. L., Zhou, X., Rosenthal, Y., Cruz-Uribe, A. M., and Brooks, H. L. (2021). The Mg/Ca proxy for temperature: A Uvigerina core-top study in the Southwest Pacific. *Geochimica et Cosmochimica Acta*, *309*, 299–312. https://doi.org/10.1016/j.gca.2021.06.015

Swart, P. K., Lu, C., Moore, E. W., Smith, M. E., Murray, S. T., and Staudigel, P. T. (2021). A calibration equation between Δ48 values of carbonate and temperature. *Rapid Communications in Mass Spectrometry*, *35*(17), e9147. https://doi.org/10.1002/rcm.9147

Tang, J., Dietzel, M., Fernandez, A., Tripati, A. K., and Rosenheim, B. E. (2014). Evaluation of kinetic effects on clumped isotope fractionation (Δ47) during inorganic calcite precipitation. *Geochimica et Cosmochimica Acta*, *134*, 120–136. https://doi.org/10.1016/j.gca.2014.03.005

Taylor, V. E., Wilson, P. A., Bohaty, S. M., and Meckler, A. N. (2023). Transient Deep Ocean Cooling in the Eastern Equatorial Pacific Ocean at the Eocene-Oligocene Transition. *Paleoceanography and Paleoclimatology*, *38*(8), e2023PA004650. https://doi.org/10.1029/2023PA004650

Thiagarajan, N., Adkins, J., and Eiler, J. (2011). Carbonate clumped isotope thermometry of deep-sea corals and implications for vital effects. *Geochimica et Cosmochimica Acta*, *75*(16), 4416–4425. https://doi.org/10.1016/j.gca.2011.05.004

Tierney, J. E., and Tingley, M. P. (2014). A Bayesian, spatially-varying calibration model for the TEX86 proxy. *Geochimica et Cosmochimica Acta*, *127*, 83–106. https://doi.org/10.1016/j.gca.2013.11.026

Tripati, A. K., Backman, J., Elderfield, H., and Ferretti, P. (2005). Eocene bipolar glaciation associated with global carbon cycle changes. *Nature*, *436*(7049), 341–346. https://doi.org/10.1038/nature03874

Tripati, A. K., Eagle, R. A., Thiagarajan, N., Gagnon, A. C., Bauch, H., Halloran, P. R., and Eiler, J. M. (2010). 13C–18O isotope signatures and 'clumped isotope' thermometry in foraminifera and coccoliths. *Geochimica et Cosmochimica Acta*, *74*(20), 5697–5717. https://doi.org/10.1016/j.gca.2010.07.006

Tripati, A. K., Sahany, S., Pittman, D., Eagle, R. A., Neelin, J. D., Mitchell, J. L., and Beaufort, L. (2014). Modern and glacial tropical snowlines controlled by sea surface temperature and atmospheric mixing. *Nature Geoscience*, *7*(3), 205–209. https://doi.org/10.1038/ngeo2082

Tripati, A. K., Hill, P. S., Eagle, R. A., Mosenfelder, J. L., Tang, J., Schauble, E. A., et al. (2015). Beyond temperature: Clumped isotope signatures in dissolved inorganic carbon species and the influence of solution chemistry on carbonate mineral composition. *Geochimica et Cosmochimica Acta*, *166*, 344–371. https://doi.org/10.1016/j.gca.2015.06.021

Upadhyay, D., Lucarelli, J., Arnold, A., Flores, R., Bricker, H., Ulrich, R. N., et al. (2021). Carbonate clumped isotope analysis (Δ47) of 21 carbonate standards determined via gas-

source isotope-ratio mass spectrometry on four instrumental configurations using carbonate-based standardization and multiyear data sets. *Rapid Communications in Mass Spectrometry*, *35*(17), e9143. https://doi.org/10.1002/rcm.9143

Yu, J., and Elderfield, H. (2008). Mg/Ca in the benthic foraminifera Cibicidoides wuellerstorfi and Cibicidoides mundulus: Temperature versus carbonate ion saturation. *Earth and Planetary Science Letters*, *276*(1), 129–139. https://doi.org/10.1016/j.epsl.2008.09.015

Zachos, J., Stott, L. D., and Lohmann, K. C. (1994). Evolution of Early Cenozoic marine temperatures. *Paleoceanography*, *9*(2), 353–387. https://doi.org/10.1029/93PA03266

Zachos, J., Pagani, M., Sloan, L., Thomas, E., and Billups, K. (2001). Trends, Rhythms, and Aberrations in Global Climate 65 Ma to Present. *Science*, *292*(5517), 686–693. https://doi.org/10.1126/science.1059412

Zachos, J., Dickens, G. R., and Zeebe, R. E. (2008). An early Cenozoic perspective on greenhouse warming and carbon-cycle dynamics. *Nature*, *451*(7176), 279–283. https://doi.org/10.1038/nature06588

Zeebe, R. E. (1999). An explanation of the effect of seawater carbonate concentration on foraminiferal oxygen isotopes. *Geochimica et Cosmochimica Acta*, *63*(13), 2001–2007. https://doi.org/10.1016/S0016-7037(99)00091-5

Zeebe, R. E., and Zachos, J. C. (2007). Reversed deep-sea carbonate ion basin gradient during Paleocene-Eocene thermal maximum. *Paleoceanography*, *22*(3). https://doi.org/10.1029/2006PA001395

Zweng, M. M., Reagan, J. R., Seidov, D., Boyer, T. P., Locarnini, R. A., Garcia, H. E., et al. (2019). *World Ocean Atlas 2018 Volume 2: Salinity*. (A. V. Mishonov, Ed.). NOAA Atlas NESDIS 82.

Chapter 2: Dissolution effects on clumped isotope signatures in planktic foraminifera

Hannah Tandy, Randon J. Flores, Adam V. Subhas, Daniela N. Schmidt, Khushboo Tanya Khan, Soyoun Gwak, Lina Savage, Robert A. Eagle, Aradhna Tripati

Key points

- In multiple species surveyed from core-tops on the Ontong Java Plateau, Δ_{47} values increase by ~0.01 ‰ below the carbonate saturation horizon
- In dissolution experiments, some species show evidence for an increase in Δ_{47} with mass loss, while no change was resolved in others
- Multiple mechanisms for dissolution impacts on Δ_{47} and correction methods are explored

Abstract

The carbonate clumped isotope paleothermometer is becoming more widely used in the geosciences because it is less sensitive to solution $\delta^{18}O$ and Mg/Ca than other carbonate-based temperature proxies. Here, we examine the impacts of dissolution on foraminiferal clumped isotope records (Δ_{47}). Dissolution is known to impact carbonate minerals in ocean sediments near and below the carbonate saturation horizon. The effects of dissolution on foraminiferal mass, $\delta^{18}O$, and Mg/Ca have been the subject of prior work but have not yet been reported for the carbonate clumped isotope paleothermometer. We examine six planktic foraminiferal species from core-tops collected at different water depths on the Ontong Java Plateau. Below the carbonate saturation horizon, multiple species exhibit higher Δ_{47} values, likely due to dissolution, biasing Δ_{47} to cooler temperatures. The largest effects are observed in *G. siphonifera, P.*

obliquiloculata, and *G. tumida* with an ~0.01 ‰ difference from above to below the saturation horizon; $p < 0.01$ corresponding to a temperature bias of ~4 °C at a measured temperature of 28 °C and of ~3 °C at a measured temperature of 18 °C. Normalizing data for different species yields a pooled slope of -0.0006 ‰/µmol/kg $\Delta[CO_3^{2-}]$ ($p < 0.01$). Dissolution experiments show that for two species, *T. sacculifer* and *G. tumida*, Δ_{47} increased with mass loss. We propose multiple mechanisms by which dissolution may impact Δ_{47} including intra-test heterogeneous dissolution, which provide context to enable corrections for the impacts of dissolution on clumped isotope-based paleo-records.

Plain Language Summary

Carbonate clumped isotopes (Δ_{47}) are becoming more widely used as a proxy for temperature, including in foraminifera. To date, no studies have examined the impact of dissolution on Δ_{47}, a process that is known to bias several other carbonate-hosted proxies. We report data for multiple species of foraminifera from core-tops in the Western Equatorial Pacific, and from laboratory experiments. We show that some taxa exhibit higher Δ_{47} with increasing levels of dissolution. Dissolution may bias reconstructions of temperature from Δ_{47} and should be factored into interpretations of proxy data.

1. Introduction

Robust paleoclimate data is fundamental to our understanding of the sensitivity of Earth system processes and feedbacks to climate forcing. Most quantitative paleoclimate reconstructions of ocean temperature and ice volume are based on the oxygen isotope ($\delta^{18}O$) and minor element (Mg/Ca) composition of fossil planktic and benthic foraminiferal shells which have increased our understanding of past climate states (Epstein et al., 1953; Lea et al., 2002; Rosenthal et al., 1997; Shackleton and Opdyke, 1973; Urey, 1947). Studies based on these

proxies have been limited by their sensitivity to seawater chemistry, including primary effects (e.g., seawater $\delta^{18}O$ and Mg/Ca ratios; carbonate ion effects during mineral formation, organismal physiology) on carbonate mineral chemistry, and secondary effects (e.g., dissolution and recrystallization) that can alter the composition of the carbonate after it forms.

Clumped isotope thermometry is a paleoclimate proxy that can be used to calculate temperatures independent of seawater chemistry (Meinicke et al., 2020; Schauble et al., 2006; Tripati et al., 2010). The clumped isotope composition of carbonate minerals is reported as Δ_{47} and has been shown to be independent of seawater $\delta^{18}O$ in foraminifera (Breitenbach et al., 2018; Daëron and Gray, 2023; Meinicke et al., 2020; Peral et al., 2018; Piasecki et al., 2019; Tripati et al., 2010). Despite nearly 20 years of research though, the potential scope of dissolution on field-collected samples, such as foraminifera, has not yet been explored for Δ_{47}.

To address this knowledge gap, we conducted a study to examine and quantify the impact of dissolution on the carbonate clumped isotope paleothermometer. We utilize a classical approach for this work by examining planktic foraminifera in core-top sediments from a depth transect at the Ontong Java Plateau in the Western Tropical Pacific Ocean. Due to its location, the samples contain a large number of different taxa and very limited seasonal temperature variability.

Prior work has shown that measurements of planktic foraminiferal species from in-situ ocean sediments, such as shell weight, $\delta^{18}O$, and Mg/Ca ratios, can be significantly correlated with carbonate ion saturation and degree of dissolution (e.g. Bonneau et al., 1980; Brown and Elderfield, 1996; Johnstone et al., 2010). We identify that dissolution influences foraminiferal clumped isotope signatures, which represents a new isotope effect that should be considered in reconstructions. The measurements allow for the determination of first-order effects of dissolution on Δ_{47} and provide a means by which dissolution impacts can be quantified and

potentially corrected for. We also explore the mechanics of carbonate mineral dissolution in foraminifera. We hypothesize that Δ_{47} values may shift towards colder estimates with increased dissolution, as inner test layers precipitated earlier in the life cycle, in warmer habitats and at shallower depths, tend to dissolve preferentially. Thus, it is possible that foraminiferal species with larger depth habitat ranges and additional calcite layers (gametogenic, cortex or crustal calcite) will exhibit stronger signals.

1.1 Background

Dissolution of foraminiferal tests begins in the water column driven by microbial decay of organic matter and decreased calcite saturation, which accelerates below the foraminiferal lysocline towards the carbonate compensation depth (Regenberg et al., 2014; Rosenthal et al., 2000; Schiebel and Hemleben, 2017). By analyzing core-top sediments from depth transects (e.g. Brown and Elderfield, 1996; Dekens et al., 2002; McCorkle et al., 1995; Mekik and Raterink, 2008; Regenberg et al., 2014; Rosenthal et al., 2000; Rosenthal and Lohmann, 2002), multiple studies have quantified the impact of dissolution on the total mass of calcium carbonate in ocean sediments, and have provided evidence of progressive dissolution of biogenic carbonate phases (e.g. Cubillas et al., 2005; Regenberg et al., 2006; Rosenthal et al., 2000; Subhas et al., 2018). Studies have used various methods to quantify dissolution impacts on foraminifera, including measurements of test mass, test fragmentation, and x-ray micro-computed tomography (CT) (e.g. Broecker and Clark, 2001, 1999; Johnstone et al., 2011, 2010; Mekik and François, 2006).

Dissolution impacts on geochemical proxies in planktic foraminifera from the Ontong-Java Plateau and other regions have also been reported in multiple studies, with tests from sediment core-tops recovered from increased water depths that exhibit lower shell weights also yielding higher $\delta^{18}O$, and lower Mg/Ca values (Bonneau et al., 1980; Brown and Elderfield,

1996; Dekens et al., 2002; Fehrenbacher and Martin, 2014; Johnstone et al., 2010; McCorkle et al., 1995; Regenberg et al., 2014, 2006; Rosenthal et al., 2000; Rosenthal and Lohmann, 2002). This body of work has shown that dissolution can affect foraminiferal species differently, likely linked to ecology, test structure and composition.

Variations in biological processes, including proteins associated with biomineralization, calcification pH, metabolic activity, and symbiont activity, as well as environmental conditions including growth temperature and environmental chemistry, are associated with species-level differences in test structure and chemical composition variations within foraminiferal layers (e.g. Schiebel and Hemleben, 2017). For example, the symbiont-bearing species *T. sacculifer* precipitates a thin final gametogenic calcite layer in deeper colder waters at the end of its life cycle, thus recording a heavier $\delta^{18}O$ signal than the rest of the test (Duplessy et al., 1981; Wycech et al., 2018). The cortex and crustal calcite present in other species such as *P. obliquiloculata* and *G. tumida*, also grown in colder depth habitats in late life stages, are typically much thicker than the gametogenic calcite and also impact the bulk whole shell $\delta^{18}O$ (e.g. Duplessy et al., 1981; Jentzen et al., 2018). Strong differences in Mg/Ca ratios between inner chamber calcite and cortex or crustal calcite in these two taxa are also observed (Branson et al., 2015; Brown and Elderfield, 1996; Schmidt et al., 2008; Steinhardt et al., 2015).

Compositional differences between foraminifera, such as amount of organic material within the calcite wall, Mg-content, the occurrence of crystal defects, crystallinity, and microstructure have all been proposed as mechanisms for dissolution effects (Bischoff et al., 1985; Keir, 1980; Mucci and Morse, 1984; Naviaux et al., 2019; Paquette and Reeder, 1990; Schott et al., 1989; Subhas et al., 2018; Walter and Morse, 1985). Johnstone et al. (2010) observed that inner chambers and layers near the primary organic membrane of certain species tended to thin and dissolve before other layers using CT scanning. This approach has revealed

dissolution effects on the inner walls of the test, even when changes are not visible on the surface (Foster et al., 2013; Iwasaki et al., 2023; Johnstone et al., 2010; Zarkogiannis et al., 2022).

A common explanation for dissolution effects on carbonates is that Mg and other non-Ca cations in calcite and aragonite slightly disrupt the mineral lattice (Bischoff et al., 1985; Mucci and Morse, 1984; Paquette and Reeder, 1990; Subhas et al., 2018; Walter and Morse, 1985). These point defects could serve as nuclei for dissolution and may be preferentially removed at lower carbonate saturation states, causing further disruption to the mineral surface. Consequently, high-Mg calcite is much more soluble than low-Mg calcite. Additionally, microstructure features such as rough surfaces and smaller crystal sizes, common during early chamber formation, have been shown to dissolve more easily than smooth mineral surfaces or large crystals (Keir, 1980; Lastam et al., 2023; Naviaux et al., 2019; Schott et al., 1989; Walter and Morse, 1985). Recent work has begun to examine microcrystalline structures in foraminifera and found different crystal microstructures both among species and within individual tests (Lastam et al., 2023).

Despite the clear impact of dissolution on temperature proxies derived from foraminiferal carbonate, to date no paper has quantified the influence of dissolution on foraminiferal Δ_{47}. In principle, because foraminifera migrate in the water column and calcify at different depths and temperatures throughout their life cycle, dissolution effects on bulk isotopic composition ($\delta^{18}O$, $\delta^{13}C$) and/or selective dissolution of Mg-rich portions of tests or higher Mg-content individual specimens could bias the Δ_{47} temperature recorded in the preserved calcite. Despite this possibility, Breitenbach et al. (2018) hypothesized that removal of high-Mg sections of individual tests would not result in a measurable signal in Δ_{47}. They suggested that in a mono-specific picked samples of foraminifera, individual tests would contain variable amounts of Mg, depending on the mean calcification temperature of each individual, and that the selective

dissolution of tests that contained more Mg due to growth at higher temperatures, would result in a bias in Δ_{47} to colder temperature estimates (i.e., to higher Δ_{47} values). Additionally, recent work on foraminiferal non-thermal effects on clumped isotopes identified through model selection that carbonate ion saturation of bottom waters is a significant predictor of planktic Δ_{47} (Chapter 1). In this study, we examine the impact of dissolution on the carbonate clumped isotope paleothermometer and investigate possible mechanisms for Δ_{47} changes.

2. Methods:

Foraminifera from a core-top depth transect at the Ontong Java Plateau were measured to examine effects of dissolution on six foraminiferal species (Table 2.1). Core tops from the Ontong Java Plateau have been used to study the effect of post-depositional dissolution on the veracity of foraminifera-based proxies for decades (e.g. Berger et al., 1982; Brown and Elderfield, 1996; Dekens et al., 2002; McCorkle et al., 1995; Mekik and François, 2006; Rosenthal et al., 2000). Sea surface temperatures over this tropical region vary by < 0.5 °C annually (Huang et al., 2021).

2.1 Samples:

We studied six planktic foraminiferal species (*Globigerinoides ruber, Trilobus sacculifer* - without final sac-like chamber, *Globigerinella siphonifera, Neogloboquadrina dutertrei, Pulleniatina obliquiloculata,* and *Globorotalia tumida)* from a series of core-tops from the Ontong Java Plateau that span a range of depths and calcite saturations (Figure 2.1, Table 2.1). The foraminiferal species chosen for this study exhibit variable dissolution susceptibility, with certain species fragmenting faster than others. *G. tumida* is the most resistant to dissolution of the species examined, followed by *P. obliquiloculata, N. dutertrei, G. siphonifera, T. sacculifer,*

and *G. ruber* (Berger, 1970; Berger et al., 1982). *G. ruber* is the least resistant to dissolution and therefore at deeper sites abundance decreased in core-tops (Berger, 1970; Berger et al., 1982). We do not have samples of *G. ruber* in core-tops from below the carbonate saturation horizon. *G. ruber* loses up to ~30 % of its mass before fragmentation, while other species maintain their structure at higher mass losses and lose up to ~40-50 % on deposition at the deepest sites of the transect (Johnstone et al. 2010). Assumed calcification depths for each species of foraminifera are from (Rippert et al., 2016; Schiebel and Hemleben, 2017) and references therein and temperature ranges for these depths are from the World Ocean Atlas 2018 dataset (Table 2.2) (Garcia et al., 2019). All cores were dated to be Holocene in age (Barker et al., 2003; Berger, 1970; Dekens et al., 2002).

Water depths span the carbonate saturation horizon from 10.3 to -30.2 [μmol/kg] $\Delta[CO_3^{2-}]$ (Table 2.1). Calcite saturation ($\Delta[CO_3^{2-}]$) is calculated as the difference between the *in situ* carbonate ion concentration ($[CO_3^{2-}]$) and the carbonate ion concentration at saturation ($[CO_3^{2-}]_{sat}$). Carbon system data was obtained from the nearby station 78 (B) cruise P13_3220CGC92_2 located at 0.02 °N, 164.91 °E from the World Ocean Circulation Experiment and the Global Ocean Data Analysis Project (Olsen et al., 2019) and carbonate ion concentration was calculated via Ocean Data Viewer (http://woce.nodc.noaa.gov/wdiu) using best practices by Dickson et al. (2007).

The calcite saturation horizon is defined as the depth at which $\Delta[CO_3^{2-}] = 0$, and we define the foraminiferal lysocline as the depth separating well-preserved from poorly preserved foraminiferal assemblages in the sediment as described by Berger et al. (1982).

2.2 Sample Preparation:

Sediment samples were sieved and foraminifera picked from the 355 μm to 425 μm size fraction. Over 600 individuals of each species were picked from each core-top sample, where available. The foraminiferal samples were cleaned for clays by sonication with water and methanol using published procedures (Meinicke et al., 2020; Chapter 1).

2.3 CT Scanning:

CT scanning was used to image foraminiferal tests. Dissolution impacts on some species (*N. dutertrei*, *P. obliquiloculata*, *G. sacculifer*, and *G. ruber*) from this study have previously been examined using CT-scanning (Johnstone et al., 2010), while *G. tumida* and *G. siphonifera* were not previously characterized in this context. To prepare samples for imaging, individual foraminifera were cleaned to remove clays and infill by sonication with methanol and deionized water. Around 2 ml of methanol was added to a 5 ml plastic vial and sonicated for 3 bursts of 5 seconds each followed by the same steps repeated with DI water three times. Samples were left to dry overnight in a 40 ℃ oven. Samples were then mounted via double-sided tape on a pipette tip cut at a 45° angle to minimize specimen overlap (Vanadzina and Schmidt, 2022).

MicroCT scans were acquired using a Nikon XT H 225ST CT scanner with a 225 kV reflection target, a 88 μA current and a 708 exposure time at the University of Bristol (Schmidt et al., 2018). X-ray projections from a 360° scan of the samples were stored in a TIFF format and images were processed using the "Dragonfly" software, Version 2022.2 for Windows. Comet Technologies Canada Inc., Montreal, Canada. Software available at https://www.theobjects.com/dragonfly was used to investigate whether there was any indication of internal dissolution, loss in carbonate density, and if there was evidence it progressed at sites

with bottom waters that had a lower carbonate ion concentration. Lighter grey values on the scans indicate a relatively lower density than darker values (Iwasaki et al., 2023).

2.4 Isotopic Measurements:

Samples were powdered with a pestle and weighed between 0.35-0.52 mg for each replicate. The samples were reacted in a common acid bath with phosphoric acid at a temperature of 90 °C to produce CO_2 (Upadhyay et al., 2021). Measurements of the isotopic composition of CO_2 were made on Nu Perspective mass spectrometers at UCLA to simultaneously determine Δ_{47}, $\delta^{18}O$, and $\delta^{13}C$. Instrumental configurations 2 and 3B as described in Upadhyay et al. (2021) were used, with 1200 s of integration time per replicate. Published carbonate standards ETH-1, ETH-2, ETH-3, ETH-4, CM Tile, Carmel Chalk, and Veinstrom were run alongside the samples to correct for instrument drift (Lucarelli et al., 2023; Upadhyay et al., 2021). Additional carbonate standards TV_BT and TV_ST were also used for developing empirical transfer functions and are defined in the supplementary information. Samples and standards were input into the Easotope software (John and Bowen, 2016) to calculate $\delta^{18}O$, $\delta^{13}C$, and Δ_{47}, with final bulk isotope data reported relative to the V-PDB standard, and Δ_{47} reported on the I-CDES reference frame. Several replicates per species per sample were analyzed (Supporting Information Table 2.1) (Lucarelli et al., 2023; Upadhyay et al., 2021).

Data quality control followed procedures described in Parvez et al. (2023). Samples were screened based on Δ_{48} or Δ_{49} values that were indicative of high organic content, but all samples reported for this study fell within initial screening bounds, so no replicates were excluded based on this criteria. Replicates with incomplete gas transfer and Δ_{47}, $\delta^{13}C$, and $\delta^{18}O$ values that fall outside of a SD range of ±0.5‰ for $\delta^{13}C$ and $\delta^{18}O$ and ±0.05‰ for Δ_{47} were flagged. Data were also screened based on instrument source stability, pump-down times and leaks in the acid

digestion system, and standard data quality during correction intervals. In total, 778 replicates were included from transect samples, and 29 replicates were excluded. 182 replicates were run from dissolution experiments and 0 replicates were excluded. Some data used in this study were first published in *Chapter 1*, and are included in this study to specifically examine dissolution effects (Supporting Information Table *2.*1)

2.5 Dissolution Experiments

We conducted experiments to examine four species in a controlled environment and manually dissolved the tests with undersaturated seawater and monitored dissolution: *G. ruber*, *T. sacculifer, P. obliquiloculata,* and *G. tumida*. Three sets of experimental methods were used and are detailed in the supplement. One set of results is shown in the main text (for experimental design 3) and the remainder are in the supplement.

Briefly, four species were each picked from core MW91-9 1BC3 (1616 m depth) above the saturation horizon ($\Delta[CO_3^{2-}]$ = 10.2 µmol/kg) at the 355 - 425 µm size fraction. The samples were weighed with ~6 - 12 mg of material per experiment and heat-sealed into polycarbonate filter paper pouches, which were then placed into gas-impermeable foil bags, heat-sealed shut, and evacuated (Supporting Information Table 2.S.7) (Naviaux, Subhas, Dong, et al., 2019; Subhas et al., 2015). A known mass of undersaturated seawater solution was siphoned into the experimental bags, and the bags were then transferred to a shaker table to maintain the flow of the solution over the particles. Measured changes in solution total alkalinity were used to calculate percent dissolution. Foraminiferal samples were then collected and run for clumped isotopes.

3. Results:

3.1 CT Scans

Results from CT scans of four species of foraminifera are shown in Figure 2.1 alongside CT scans of *G. ruber* and *T. sacculifer* from Johnstone et al. (2010). Species without secondary calcite layers exhibit uniform dissolution starting in the earlier chambers (*G. ruber* and *G. siphonifera*) while those with a lower Mg outer thick calcite layer show preferential dissolution of inner test layers (*T. sacculifer, N dutertrei, P. obliquiloculata,* and *G. tumida*) (Figure 2.1). The innermost chambers dissolve first , likely due to their higher Mg values and small carbonate crystals (Figure 2.1). *G. tumida* displays significant dissolution of the inner walls of the chambers, indicated by the change from dark to lighter grey values on the scans, similar to what is observed in *P. obliquiloculata* and *N. dutertrei* (Figure 2.1) (Johnstone et al. 2010).

3.2 $\delta^{18}O$ and $\delta^{13}C$

Data from core-tops are shown in Figures 2.3 and 2.S.1. $\delta^{18}O$ and $\delta^{13}C$ values for all species from this study show trends with depth that are consistent with prior work (Figures 2.3, 2.S.1, Supporting Information Table 2.1, 2.4). For *T. sacculifer, G. siphonifera, N. dutertrei, P. obliquiloculata,* and *G. tumida*, near the carbonate saturation horizon, test $\delta^{18}O$ values increase with depth (Figure 2.3, Table 2.3). For *N. dutertrei*, test $\delta^{18}O$ values exhibit a significant decrease above the carbonate saturation horizon.

N. dutertrei, T. sacculifer, P. obliquiloculata, and *G. tumida* exhibit significant differences in $\delta^{13}C$ from above and below the carbonate saturation horizon (Supporting Information Figure 2.S.1). Depth-dependent trends in $\delta^{13}C$ are observed in *T. sacculifer, P. obliquiloculata,* and *G. tumida* (Supporting Information Figure 2.S.1, Table 2.3). No trends were discerned in other species (Supporting Information Figure 2.S.1, Table 2.3).

We note that the size fraction we examined and the sample preparation methods used likely contribute to the offsets observed between publications. For example, we used foraminifera from the 355-425 μm size fraction, compared to 250-350 μm in Dekens et al. (2002), 250-315 or >400 μm in Bonneau et al. (1980), and 350-500 μm in Russell et al. (1994). Bonneau et al. (1980) do not report a clay removal step unlike other more recent studies including this study. $\delta^{18}O$ values from this study are slightly higher than those from Dekens et al. (2002) (Figure 2.3), potentially reflecting that in the larger size fractions that we used. This might be linked to the higher number of symbionts in larger taxa impacting the carbonate ion effect symbiont activity (e.g. Bouvier-Soumagnac and Duplessy, 1985; Duplessy et al., 1981; Zeebe, 1999). $\delta^{13}C$ values show more scatter in symbiont-bearing species (*G. ruber, T. sacculifer* and *G. siphonifera*, Supporting Information Figure 2.S.1) than in asymbiotic taxa. *P. obliquiloculata* and *G. tumida* $\delta^{13}C$ values are slightly higher than those reported by Bonneau et al. (1980) despite the overlap in size fraction, though both records exhibit an increase in values (Supporting Information Figure 2.S.1). This offset could be due to differences in cleaning procedures.

3.3 Δ_{47}

Δ_{47} results are presented in Figure 2.4 (Supporting Information Table 2.S.1). *G. siphonifera, P. obliquiloculata,* and *G. tumida* exhibit significant differences above and below the carbonate saturation horizon (Table 2.2) and the Δ_{47} values are correlated with water depth (Table 2.3). The variance between samples changes slightly above and below the saturation horizon, decreasing in three species (*T. sacculifer*, *N. dutertrei*, and *P. obliquiloculata*) but increasing in two species (*T. sacculifer* and *G. tumida*) (Supporting Information Table 2.S.2). However, these differences are not significant at the 95% confidence level.

The Δ_{47} values of five of the six different foraminiferal species from the shallowest core-tops (<1700 m) are consistent with published calcification depth ranges (black horizontal bar in Figure 2.4). *N. dutertrei* may be an exception; two core-tops at 1614 m and 1616 m are within the calcification temperatures estimated based on assumed water depths, while a third core-top at 1598 m is slightly outside of the range, even with uncertainties associated with shot noise limits of the mass spectrometers (grey bar in Figure 2.4; 0.008‰; Lucarelli et al., 2023). There is some uncertainty in the assumed calcification depth range for this species in the Equatorial Pacific, which varies from 30 to 200 m depth depending on the publication (e.g. Dekens et al., 2002; Nürnberg et al., 1996; Rippert et al., 2016). Given this, it may also be that the assumed calcification depth range we chose may be too shallow (Rippert et al., 2016). If the species calcifies in the deeper range up to 200 m, this would extend the black bar in Figure 2.4 to 0.617 ‰ which would make all Δ_{47} values consistent with the assumed water depth. The mean Δ_{47} of *N. dutertrei* is at the highest end of values associated with temperatures from the assumed calcification depth range of Rippert et al. (2016), which was used here (0.587-0.603 ‰, Figure 2.4, Table 2.2).

Samples above and below the saturation horizon fall into two groups, with respect to showing evidence for dissolution impacts on Δ_{47}. Some species do not exhibit a shift in Δ_{47} values, while others do show a statistically significant increase in Δ_{47} (and a bias to cooler Δ_{47}-temperatures) (Figure 2.4).

For *G. ruber*, the average value of samples from above the carbonate saturation horizon (0.590 ‰) are near the center of the assumed calcification depth range (0.582-0.599 ‰) highlighting the fidelity of this mixed layer species without secondary calcite layers in recording surface conditions. No trend with water depth is discernible, and there are no samples measured here from below the saturation horizon. For *T. sacculifer*, average Δ_{47} values are similar to mid-

range assumed calcification depth temperatures above the saturation horizon, while below the horizon values are slightly elevated. However, this difference is not significant at the 95% confidence level (Figure 2.4, Table 2.2). The mean Δ_{47} of *N. dutertrei* samples from above and below the carbonate saturation horizon (0.603 ‰ and 0.602 ‰, respectively; vertical grey bars) are similar, while the mean below the foraminiferal lysocline is 0.608 (vertical dark grey dashed line). A significant shift to higher Δ_{47} values is observed in *G. siphonifera* ($p = 0.02$), *P. obliquiloculata* ($p = 0.02$) and *G. tumida* ($p = 0.04$) (Figure 2.4, Table 2.2). Thus, these data would yield colder reconstructed temperatures if dissolution was not taken into account, with an offset of 0.011 ‰ and bias of 3.9 °C for *G. siphonifera,* 0.013 ‰ and bias of 4.5 °C for *P. obliquiloculata,* and 0.008 ‰ and bias of 2.8 °C for *G. tumida.* The shift in *N. dutertrei* below the foraminiferal lysocline is 0.007 ‰ and corresponds to a bias of 2.3 °C.

3.4 Dissolution Experiments

Due to bacterial contamination of a subset of dissolution experiments (see Supporting Information information S2.2.3), we were only able to progress dissolution levels to <25% in most species (33% in *G. ruber*), which is less than what is associated with a change in Δ_{47} in some of the species in the core-top transect (Supporting Information Table 2.S.3). However, for the experiments that did occur, $\delta^{18}O$ and $\delta^{13}C$ values align with field transect results (Figure 2.5; Supporting Information Figure 2.S.3). No shifts in Δ_{47} were discernible in *P. obliquiloculata* when comparing the undissolved sample with the sample that had dissolved by 16 % (Figure 2.6), or in *G. ruber* when comparing the undissolved sample with one that had dissolved by 33 % (Figure 2.6).

However, with increased dissolution, elevated Δ_{47} values were observed in both *G. sacculifer* and *G. tumida* (Figure 2.6). In *G. sacculifer,* a significant correlation between Δ_{47} and

percent dissolution was calculated ($p = 0.05$) and an increase of 0.018 ‰ was observed when comparing the undissolved experimental sample with the most dissolved (24%, Figure 2.6). A similar correlation is associated with dissolution in *G. tumida* ($p = 0.06$), with values increasing 0.018 ‰ from 0 % to 19 % dissolution (Figure 2.6). The magnitudes of change found in both *T. sacculifer* and *G. tumida* in the experiments are larger than those changes estimated by the transect data (0.005 ‰ and 0.008 ‰ respectively). The measurement variance on these samples could contribute to the larger offsets we are measuring compared to the transect samples, especially as the 95 % CIs overlap between the non-dissolved and most-dissolved samples from the experiments (Figure 2.6).

4. Discussion:

Both core-top samples from the Ontong-Java Plateau and manual experiments show evidence that Δ_{47} values in some species may be affected at dissolution intensities similar to those which occur at or below the calcite saturation horizon. *G. siphonifera, P. obliquiloculata,* and *G. tumida* are species that do show evidence for a dissolution effect in the core-tops, with a ~0.01 ‰ difference above and below the saturation horizon ($p < 0.01$) (Figure 2.4). In the dissolution experiments, we also see that *G. sacculifer* and *G. tumida* exhibited a positive shift in values (Figure 2.6).

However, these two independent types of data also show that some species do not exhibit evidence for dissolution impacts on Δ_{47}. Some species do not show detectable changes in Δ_{47} above and below the carbonate saturation horizon, or significant trends with depth. *T. sacculifer* and *N. dutertrei* do not show significant changes at the 95% confidence level in the core-top data (Figure 2.4), and species *P. obliquiloculata* and *G. ruber* do not show significant changes in the dissolution experiments. The signal-to-noise ratio in these data may simply be too large to

discern any significant trend, while *G. ruber* are not present in the deepest samples and thus no data are available to analyze.

Thus, we suggest the effects of dissolution on Δ_{47} are relatively small and difficult to detect, but can be oceanographically significant. Notably, Δ_{47} averages for all species remain within error of assumed calcification depth bounds throughout the transect (Figure 2.4). However, for *G. siphonifera, P. obliquiloculata* and *G. tumida,* below the carbonate saturation horizon, there is evidence that dissolution does shift Δ_{47} towards higher values towards the colder limit of the assumed calcification depth temperatures. The same may be true for *N. dutertrei* below the foraminiferal lysocline, though for this species, the data are more uncertain given low sample density.

It is possible a dissolution effect could be present in the broader suite of core-top data, but that it is not detected. In Chapter 1, non-thermal effects on clumped isotopes were statistically investigated using model selection and revealed that carbonate ion saturation of bottom waters is a significant predictor of planktic Δ_{47}. Given that Mg- and ^{16}O-rich parts of tests are known to be more susceptible to dissolution (Bonneau et al., 1980; Brown and Elderfield, 1996; Dekens et al., 2002; Fehrenbacher and Martin, 2014; Johnstone et al., 2010; McCorkle et al., 1995; Regenberg et al., 2014, 2006; Rosenthal et al., 2000; Rosenthal and Lohmann, 2002), it is possible that this mechanism could drive discernible effects on Δ_{47} below the carbonate saturation horizon, that in turn could impact proxy reconstructions of temperature.

4.1 Mechanisms for dissolution effects on Δ_{47}

Figure 2.7 shows a schematic proposing different hypotheses that may explain the results. There are a few key elements to these mechanisms. The primary factor relates to whether the species calcifies over a narrow depth range or a broad depth range and the corresponding

calcification temperatures, as that influences Mg and $\delta^{18}O$ content and variability within the test, and also is linked to shell ultrastructure. Many planktic species will migrate deeper in the water column during their life cycle and produce test features associated with late ontogenetic stages such as cortex and crustal layers (e.g. *N. dutertrei, P. obliquiloculata, G. tumida*) (Schiebel and Hemleben, 2017) or other forms of secondary calcite. Species with secondary calcite are thick-walled and hence often dissolution resistant. These taxa have higher Mg content in the primary calcite that is often also more poorly crystallized and less ordered, making it more prone to dissolution.

Mg and other elements do not uniformly get incorporated into foraminiferal tests (e.g. Lea et al., 1999; Russell et al., 2004; Sadekov et al., 2005; van Dijk et al., 2019) and Mg/Ca concentrations can vary outside of values expected from the given precipitation temperatures due to changes in metabolic uptake or exclusion of Mg (Eggins et al., 2003; Fehrenbacher et al., 2017; Spero et al., 2015). The higher solubility of calcite with elevated Mg levels is well established though at higher concentrations than typically found in foraminifera (Bischoff et al., 1985; Mucci and Morse, 1984; Paquette and Reeder, 1990; Subhas et al., 2018; Walter and Morse, 1985), and has been proposed as a driver of dissolution effects on foraminiferal Mg/Ca and $\delta^{18}O$ (Bonneau et al., 1980; Brown and Elderfield, 1996; Dekens et al., 2002; Fehrenbacher and Martin, 2014; Johnstone et al., 2010; McCorkle et al., 1995; Regenberg et al., 2014, 2006; Rosenthal et al., 2000; Rosenthal and Lohmann, 2002).

Other factors, including microcrystalline structure, crystallinity, crystal defects, and organic content may also influence dissolution susceptibility. For example, microcrystalline structures precipitate based on species-specific inner structures (Lastam et al., 2023). An additional possibility is that lighter isotopologues of calcite are preferentially removed during

dissolution due to kinetic effects. Experiments with doped calcite crystals could potentially be used to test this hypothesis.

Within this framework, we describe the patterns in each species, going from most dissolution-prone, to least. *G. ruber* is the most sensitive to dissolution of all of the species we examined. This mixed-layer dwelling species is often used for paleoceanographic reconstructions in the tropics (Meinicke et al., 2021; Tripati et al., 2014). It calcifies at warm temperatures and has a high Mg content, and a narrow calcification depth range in the water column (Birch et al., 2013; Rippert et al., 2016) though there is evidence for Mg heterogeneity in tests (Gray et al., 2023; Sadekov et al., 2009, 2005). The species is not thought to precipitate secondary calcite (Caron et al., 1990; Schiebel and Hemleben, 2017).

For *G. ruber,* tests thin relatively homogeneously (Figure 2.2) (Johnstone et al., 2010) and consequently $\delta^{18}O$ does not vary with water depth (Dekens et al., 2002). However, Mg/Ca ratios do decrease which contributes to reduced Mg/Ca heterogeneity with increased dissolution (Fehrenbacher and Martin, 2014; Rosenthal and Lohmann, 2002). The Δ_{47} data do not resolve any significant depth-dependent trends (Figures 2.3-2.4). While we do not have data for below the carbonate saturation horizon, we note that this taxa shows a predilection to fragmentation with dissolution. If whole specimens from large size fractions are used for paleoceanographic work, then dissolution biases are likely to be weak to non-existent (Figure 2.7).

T. sacculifer is a tropical spinose species living in the lower parts of the mixed layer, especially during the end of the life cycle, and is also widely used for tropical sea surface temperature reconstructions (De Vleeschouwer et al., 2022; Meinicke et al., 2021). Like *G. ruber,* it calcifies at warm temperatures resulting in a high Mg content (e.g. Anand et al., 2003; Schmuker and Schiebel, 2002). To begin gametogenesis, the species is known to migrate deeper

in the water column, form a thin crustal layer, and then may develop a gametogenic sac (Bijma et al., 1990).

For *T. sacculifer*, both carbonate $\delta^{18}O$ and Mg/Ca exhibit depth-dependent trends that are linked to dissolution effects supported by CT-scanning (Figures 2.2-2.4, Supporting Information Figure 2.S.4) (Bonneau et al., 1980; Brown and Elderfield, 1996; Dekens et al., 2002; Johnstone et al., 2010; Russell et al., 1994). The lack of significance in core-top data with depth in Δ_{47} for *T. sacculifer* may be attributable to scatter in the data and limitations in the number of specimens available from the deepest sites, as with *G. ruber* (Figure 2.7). This observation is supported by the dissolution experiment data raising caution in using the taxon for paleoceanographic reconstructions (Figure 2.5).

G. siphonifera is thin-walled species prone to dissolution and fragmentation, similar to *G. ruber* and *T. sacculifer*. The mixed-layer dwelling taxa also calcifies at warm temperatures and migrates to deeper depths prior to gametogenesis, but does not produce secondary or crustal calcite (Bijma et al., 1998; Hemleben et al., 1989). CT-scanning shows thinning of the full test with increased dissolution similar to *G. ruber* with loss of the smallest chambers at the deepest depths (Figure 2.2). Mg/Ca shows depth-dependent trends (Supporting Information Figure 2.S.4) (Elderfield and Ganssen, 2000) and the carbonate $\delta^{18}O$ results show evidence for depth-dependent enrichment following the carbonate saturation horizon, consistent with dissolution (Figure 2.3).

The significant increase across the carbonate saturation horizon in *G. siphonifera* despite not having crustal calcite may be attributed to the same processes that cause a shift in shell $\delta^{18}O$ and Mg/Ca. There are three possible explanations. First, potential differences in $\delta^{18}O$ and Δ_{47} with dissolution may potentially be due to the dissolution of high-Mg (and/or ^{16}O-containing) portions of the shell and associated thinning, as the latter is seen in CT scanning (Figure 2.2). A

second possibility is the preferential loss of the smallest chambers of the test, as observed in CT scanning (Figure 2.2), that may have lower $\delta^{18}O$ and Δ_{47} values (Figure 2.7). A third possibility is the occurrence of different ontogenetic stages and/or genotypes in *G. siphonifera* with different dissolution susceptibilities leading to population shifts, though this has not been observed in other taxa (Figure 2.7) (Rongstad et al., 2017).

N. dutertrei is a mixed-layer to thermocline dweller known to produce a thick layer of secondary crustal calcite (Eggins et al., 2003; Steinhardt et al., 2015). CT-scanning shows thinning of the inner layers of the test with increased dissolution until the complete loss of inner calcite leaves only crustal calcite at the deepest depths (Figure 2.2) (Johnstone et al., 2010). Mg/Ca shows depth-dependent trends (Supporting Information Figure 2.S.4) (Dekens et al., 2002; Mekik and François, 2006; Russell et al., 1994). Core-top data for $\delta^{18}O$ in *N. dutertrei* show evidence for depth-dependent trends that differ from other taxa above the carbonate saturation horizon where $\delta^{18}O$ decreases by 0.6 ‰ in this study and by 0.3 ‰ in Dekens et al. (2002) (Figure 2.3), while Mg/Ca may increase (Supporting Information Figure 2.S.4).

The core-top data in Δ_{47} does not exhibit systematic changes above or below the carbonate saturation horizon though the two deepest samples, that are below the foraminiferal lysocline, do yield higher values. This pattern may be attributable to differences in dissolution susceptibility of various aspects of the test, with an “early” and “late” phase of dissolution, which has not been described for *N. dutertrei* previously (Figure 2.7). It is possible that in an early phase of dissolution, there may be small portions of the test where factors such as Mg/Ca heterogeneity and/or or microcrystalline structure promote higher solubility, such that while it may potentially have precipitated in colder water, selective dissolution of these regions could alter shell $\delta^{18}O$ towards lower values and reduce Mg/Ca (Figure 2.7). However, it may not be substantial enough to impact Δ_{47}. This early dissolution phase could then be followed by a later

phase of dissolution that yields the more typical pattern in $\delta^{18}O$ and Mg/Ca seen in other species. It is only following this second stage, when dissolution is extreme below the foraminiferal lysocline, that a signal may be present in Δ_{47} (Figure 2.4).

The second-most dissolution-resistant taxa that we examined is *P. obliquiloculata. P. obliquiloculata* is a thick-walled species and thermocline dweller that produces a smooth layer of secondary cortex calcite (Steinhardt et al., 2015). Mg/Ca shows depth-dependent trends (Supporting Information Figure 2.S.4) (Mekik and François, 2006), carbonate $\delta^{18}O$ results show evidence for depth-dependent enrichment (Bonneau et al., 1980), and CT-scanning shows thinning of the inner layers (Johnstone et al., 2010), all consistent with dissolution (Figures 2.2, 2.3, Supporting Information Figure 2.S.4).

We hypothesize the increase in Δ_{47} for *P. obliquiloculata* with depth (0.008 ‰/km), similar to what is observed in $\delta^{18}O$, is due to the preferred preservation of the low-Mg cortex calcite over the high-Mg inner chamber calcite in *P. obliquiloculata* (Kunioka et al., 2006; Steinhardt et al., 2015) reflective of lower temperature crystal formation in deeper depths of the species' assumed calcification range (Figure 2.7).

The most dissolution-resistant species we measured is *G. tumida,* which is a thermocline dweller known to produce a thick layer of secondary cortex calcite and also has an outer keel (Hemleben et al., 1989). CT-scanning shows patterns similar to *P. obliquiloculata* with thinning of the inner layers of the test with increased dissolution until only crustal calcite is left at the deepest depths (Figure 2.2). Mg/Ca shows depth-dependent trends (Supporting Information Figure 2.S.4) (Brown and Elderfield, 1996; Mekik and François, 2006; Russell et al., 1994) and carbonate $\delta^{18}O$ results show evidence for depth-dependent enrichment, consistent with dissolution (Figure 2.3) (Bonneau et al., 1980; Russell et al., 1994).

In *G. tumida,* the increase in Δ_{47} with depth (0.005 ‰/km) parallels the observed trend in $\delta^{18}O$, just as with *P. obliquiloculata.* The increase in $\delta^{18}O$ has also been linked to the dissolution of inner chamber calcite (Brown and Elderfield, 1996), with a similar mass loss evident in CT scans (Figure 2.2) (Johnstone et al., 2010). Thus, we hypothesize the same mechanisms are driving the observed patterns in both species (Figure 2.7).

4.2 Potential dissolution biases on temperatures

It is well-established that the dissolution of foraminiferal carbonates and impacts on test geochemistry can affect their reliability as recorders of past environments and climates (Berger et al., 1982; Brown and Elderfield, 1996; McCorkle et al., 1995; Mekik and François, 2006; Rosenthal et al., 2000). Unless discerned, dissolution effects can limit the accurate assessment of past climate variability, often coupled with changes in the carbonate system impacting the carbonate saturation horizon and carbonate compensation depth. In downcore studies, as with other isotopic and elemental proxy systems, dissolution could bias reconstructed temperatures to cooler values. Temperature amplitudes therefore could be inaccurately assessed if dissolution is not taken into account. Below, we compare the potential impacts of dissolution biases on temperatures estimated from Δ_{47}, Mg/Ca, and $\delta^{18}O$.

If Mg/Ca data from core-top samples are compared from the shallowest and deepest sites on the Ontong-Java Plateau, then a potential dissolution cold bias of ~5 °C is calculated for *P. obliquiloculata* and ~8 °C for *G. tumida,* associated with about a 50% mass loss (Johnstone et al., 2010). This corresponds to a reduction in Mg/Ca of ~1.11 mmol/mol for *P. obliquiloculata* and ~1.37 mmol/mol for *G. tumida* (Supporting Information Figure 2.S.4) (Brown and Elderfield, 1996; Mekik and François, 2006), with temperatures calculated using the Anand et al. (2003) multispecies calibration. Mg/Ca data for *T. sacculifer* and *N. dutertrei,* with a reduction of

0.52 mmol/mol and 0.88 mmol/mol, respectively, associated with approximately 40 % mass loss (Johnstone et al., 2010), results in an estimated cold bias of ~2 °C and ~6 °C (Supporting Information Figure 2.S.4) (Dekens et al., 2002).

A shift in foraminiferal $\delta^{18}O$ due to dissolution, if not factored in, could bias estimated temperatures by about 4 °C for both *P. obliquiloculata* and *G. tumida*. These calculations use the modified equation from Bemis et al. (1998) and assume a 0.82 ‰ increase in $\delta^{18}O$ for the first species, and a 0.58 ‰ increase for the second species from our transect data (Figure 2.3). If a similar magnitude change in $\delta^{18}O$ was driven by dissolution in *T. sacculifer* and *N. dutertrei*, this would bias temperatures by about 1 °C.

The Δ_{47} of sample populations above and below the carbonate saturation horizon can similarly be used to estimate potential dissolution biases for the different species we examined here (or foraminiferal lysocline for *N. dutertrei*). We report $\Delta\Delta_{47\text{-dissolution}}$ as the mean Δ_{47} above the carbonate saturation horizon minus the mean Δ_{47} below the carbonate saturation horizon. A caveat is that for *T. sacculifer* and *N. dutertrei*, these differences are not significant at the 95% confidence level. A $\Delta\Delta_{47\text{-dissolution}}$ for *T. sacculifer* of 0.005 ‰ yields a cold temperature bias of 2 °C, while a $\Delta\Delta_{47\text{-dissolution}}$ for *G. siphonifera* of 0.011 ‰ yields a cold temperature bias of 4 °C °C (Figure 2.4). A $\Delta\Delta_{47\text{-dissolution}}$ of 0.013 ‰ for *P. obliquloculata* and 0.008 ‰ for *G. tumida,* yield cold temperature biases of 4 °C and 3 °C, respectively (Figure 2.4). For *N. dutertrei,* differences from samples above the foraminiferal lysocline and below the foraminiferal lysocline yield a $\Delta\Delta_{47\text{-dissolution}}$ of 0.003 ‰ and 1 °C (Figure 2.4).

4.3 Correcting for potential dissolution effects

We explore the potential use of different corrections for possible dissolution effects on Δ_{47} using constraints from core-top data, as these results most likely best reflect processes

relevant to down-core records. One type of correction that could be used is a fixed correction (i.e., $\Delta\Delta_{47\text{-dissolution}}$), depending on if a site is known to have been above or below the carbonate saturation horizon. In this case, the average pooled offset between taxa shift Δ_{47} of 0.010 ‰ (all species) could be applied (Figure 2.8D), or of 0.012 ‰ (all species exhibiting a significant effect; Figure 2.8A), or a taxon-specific effect $\Delta\Delta_{47\text{-dissolution}}$ as described in the section above.

An alternative approach is to utilize the change associated with bottom water carbonate saturation (or water depth) (Figures 2.8B-C and E-F, 2.S.5, Tables 2.2-2.3), that could be constrained using a proxy such as benthic Li/Ca, B/Ca, $d^{11}B$, and/or modeling. For example, over a carbonate ion saturation range from approximately 10.3 to -30.2 umol/kg across the transect, with around 40-50 % dissolution in the deepest core tops (Johnstone et al., 2010), there is a change in Δ_{47} per kilometer of depth of 0.007 ± 0.003, 0.008 ± 0.002, and 0.005 ± 0.002 ‰ for *G. siphonifera*, *P. obliquiloculata,* and *G. tumida* (Table 2.3). Using these slopes to calculate predicted temperature for Δ_{47} at 4.4 km we find that for *P. obliquiloculata* and *G. siphonifera* temperatures decrease by approximately 7 °C and for *G. tumida* by approximately 5 °C.

4.4 Implications

Our findings indicate that dissolution could have a significant effect on estimated clumped-isotope derived temperatures when there is high mass loss with the largest effects in species that do not fragment quickly such as those with late ontogenetic stage calcite.

Because the signals are small compared to the uncertainties in measurements, we suggest only utilizing a correction in cases when there is evidence for substantial dissolution such as times of extreme environmental change. The possible scope of such effects is shown in Figure 2.9, which uses the pooled slope for all species that show a dissolution signal (-0.0006 ‰ / µmol/kg $\Delta[CO_3^{2-}]$). Overall, estimated Δ_{47}-temperatures increase the most when correcting for

high levels of dissolution in warm samples, such as during the Paleocene-Eocene Thermal Maximum.

5. Conclusions:

To test for dissolution effects on Δ_{47}, we examined core-top samples of six species of planktic foraminifera from the Ontong Java Plateau. Data for three species shows evidence for small, statistically significant increases of approximately 0.01 ‰ in Δ_{47} when there is ~40-50% mass loss. Results for *G. siphonifera, P. obliquiloculata,* and *G. tumida* show evidence for a pooled trend of -0.0006 ‰ / μmol/kg $\Delta[CO_3^{2-}]$. Although small increases were observed in *T. sacculifer* and *N. dutertrei*, they were not significant at the 95% confidence level. No significant shift was observed in *G. ruber,* although there were insufficient specimens from the deeper sites. Lab experiments for two species, *G. sacculifer* and *G. tumida,* support an increase in Δ_{47} with enhanced dissolution, with up to ~20% mass loss. However, no change was detected for *G. ruber* or *P. obliquiloculata* corresponding to ~20% mass loss.

Areas we recommend for further investigation include examining Δ_{47} in additional core-tops, and manual dissolution experiments at higher intensity. Future studies could also examine coupling Δ_{47} with CT-imaging to map microstructure in tandem with Mg/Ca mapping of tests, and SIMS analysis for $\delta^{18}O$. Coupling these approaches in downcore studies could also constrain the potential scope of dissolution biases in paleo-records.

We suggest that the preference for dissolution of poorly-crystallized higher-Mg calcite will affect Δ_{47}-based paleoclimatic reconstructions, especially in thick-walled, dissolution-resistant species with secondary calcite growth. The magnitude of changes in core-top samples facilitates potential upper temperature limits for intervals such as the Paleocene-Eocene Thermal Maximum. Ultimately, this work helps to identify additional sources of isotopic variability in

Δ_{47}, and to develop more accurate interpretations of clumped isotope temperature proxy signals and reconstructed water $\delta^{18}O$ for paleoclimatic reconstruction.

Acknowledgements

This work was supported by Heising-Simons Foundation grant 2022-3314, DOE BES grant DE-FG02-83613ER16402, the Packard Foundation, and by NSF grants EAR-0949191, EAR-1352212, and RISE-228198. It was also supported by a Royal Society Wolfson Visiting Research Fellowship. We thank B. Elliot, L. Martin-Silverstone, H. Taylor, K. Miguel, and J. Rubi for lab support.

Open Research

All data are in the Supplementary information associated with this paper. In addition, on publication, all data will be archived in Pangaea and EarthChem.

6 Figures

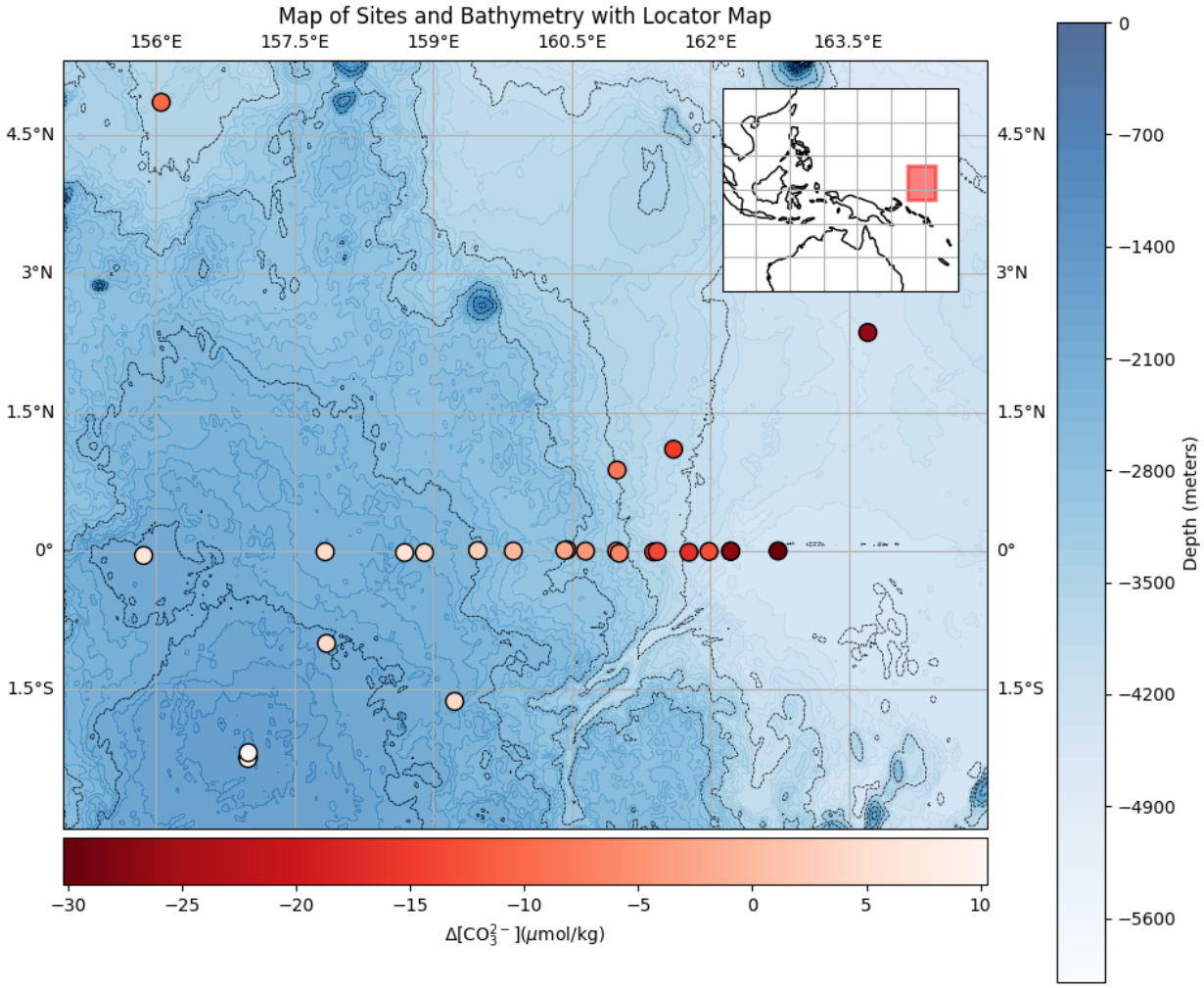

Figure 2.1 Map of sites on the Ontong Java Plateau used in this study to examine dissolution impacts of planktic foraminiferal Δ_{47}, and corresponding bottom water carbonate saturations ($\Delta[CO_3^{2-}]$). At the shallowest site (water depth of 1598 m), bottom water $\Delta[CO_3^{2-}]$ is 10.3 µmol/kg, while at the deepest site (water depth of 4438 m), bottom water $\Delta[CO_3^{2-}]$ is -30.2 µmol/kg. Bathymetric data is from NOAA's ETOPO1 1 arc-minute global relief model (Amante and Eakins, 2009). Blue contours are every 100 m depth and black are every 500 m. Sea surface temperatures over this tropical region vary by < 0.5 °C annually and are ~ 29 °C (Huang et al., 2021). The mixed layer depth is ~ 100 m and the thermocline depth is ~ 130-230 m (Rippert et al., 2016).

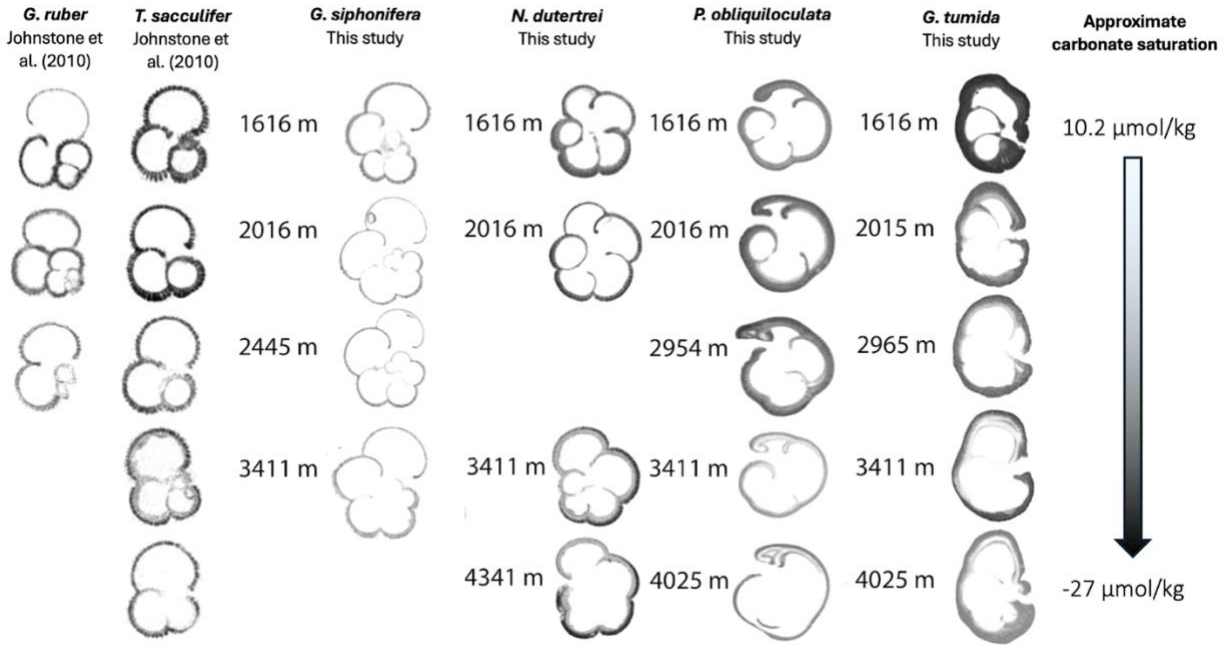

Figure 2.2. MicroCT scans for 6 species of planktic foraminifera in core-tops from the Ontong-Java Plateau, ordered from least to most resistant to dissolution. Images are from this work and from Johnstone et al. (2010). In species without a thick outer calcite layer, the key feature of dissolution is the progressive loss of the earlier chambers (*G. ruber* and *G. siphonifera*) resulting in uniform dissolution. Specimens with outer calcite layers show preferential dissolution of inner test layers (*T. sacculifer, N dutertrei, P. obliquiloculata*, and *G. tumida*). *G. ruber* and *T. sacculifer* images are from Johnstone et al. (2010) and *G. siphonifera, N. dutertrei, P. obliquiloculata*, and *G. tumida* are from this study. Results for *N. dutertrei* and *P. obliquiloculata* from this work are highly comparable to results from Johnstone et al. (2010).

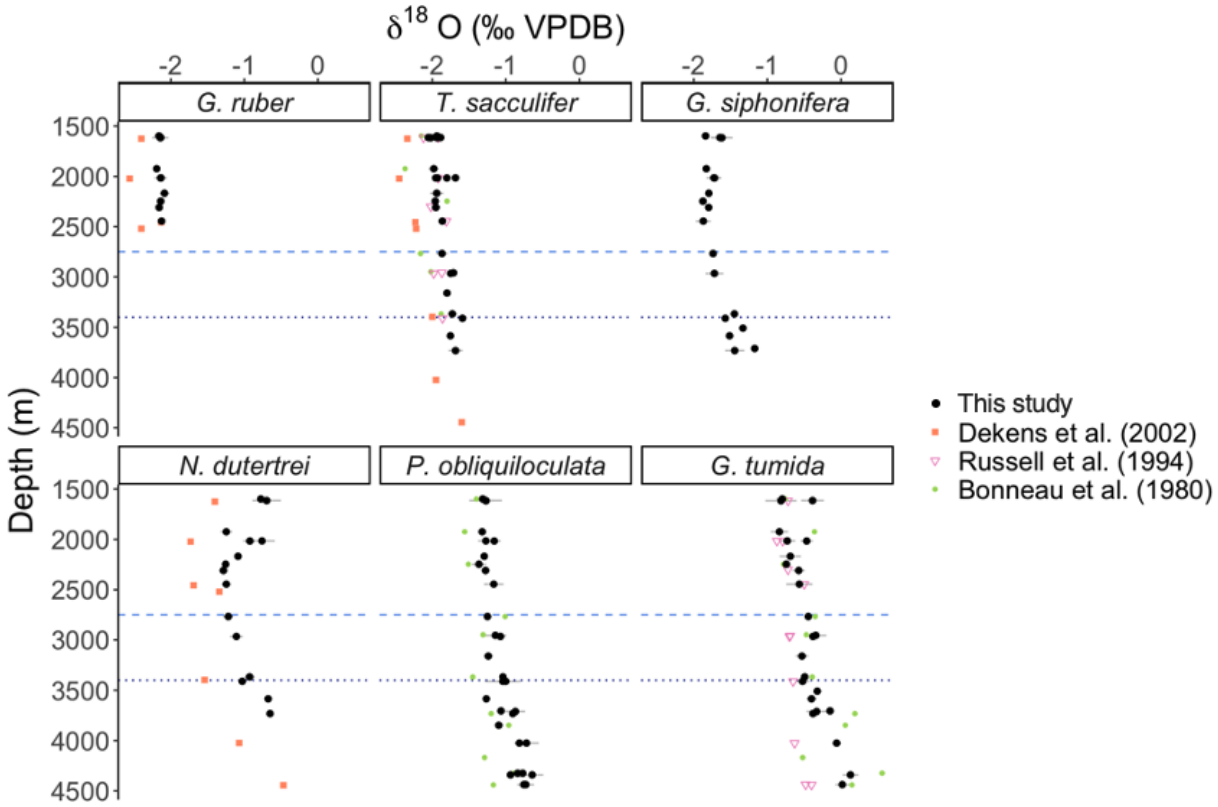

Figure 2.3. Foraminifera $\delta^{18}O$ (VPDB) for six species in core-tops from the Ontong Java Plateau. *G,. ruber* is only found fragmented below the saturation horizon in the region (Dekens et al., 2002; Johnstone et al., 2010; this study). All species show a shift to more positive values below the carbonate saturation horizon. The horizontal dashed blue line represents the carbonate saturation horizon and the dark blue dotted line represents the foraminiferal lysocline (Berger et al., 1982).

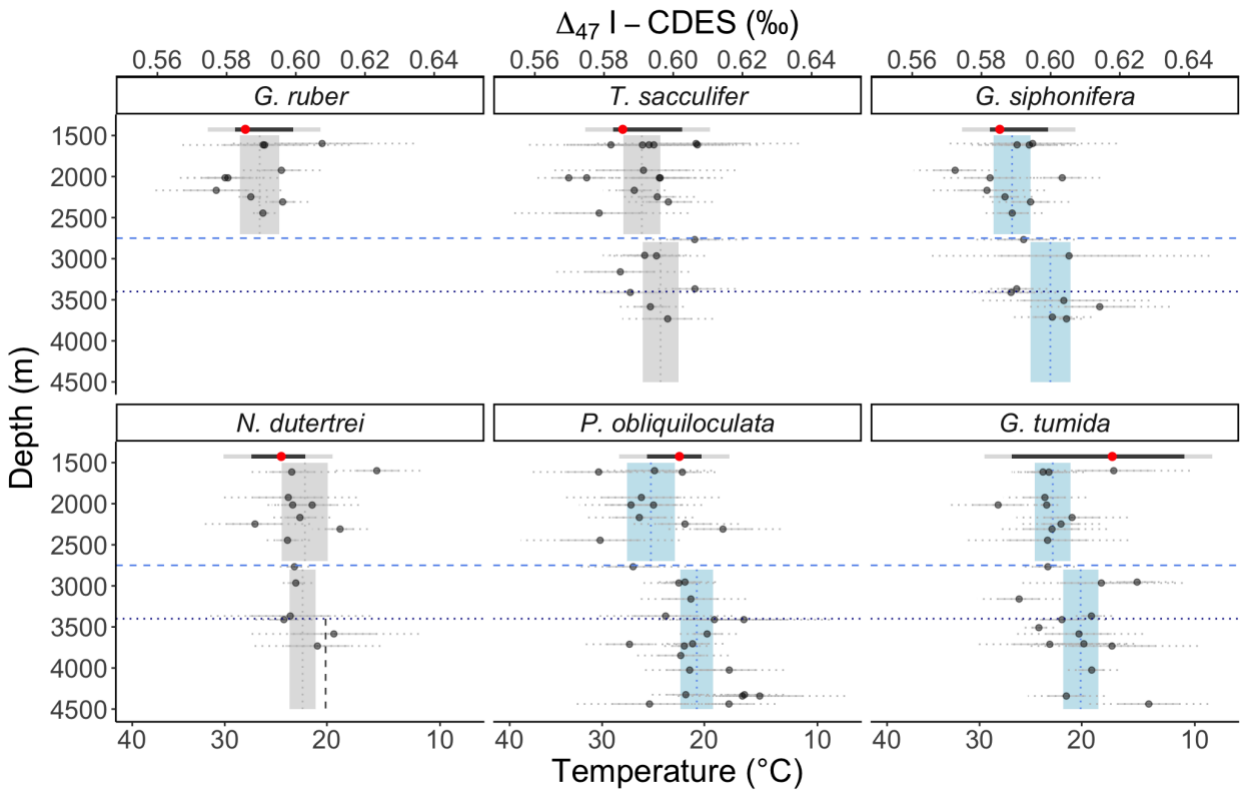

Figure 2.4: Δ_{47} values measured on core-top planktic foraminifera from the Ontong Java Plateau as a function of water depth. Δ_{47}-temperature scale shown as a second x-axis. Species are ordered by dissolution resistance (least to greatest from top left to lower right). Errors are 1SE (solid) and 95% CI (dotted). Vertical bands show mean sample Δ_{47} values - blue bands indicate species that show significant differences (at the 95% confidence level) above and below the carbonate saturation horizon, while gray bands do not. The grey vertical dashed line for *N. dutertrei* is the mean of the samples below the foraminiferal lysocline. The horizontal dashed light blue line represents the calcite saturation horizon and the dotted dark blue line represents the foraminiferal lysocline or the depth separating well-preserved from poorly preserved foraminiferal assemblages in the sediment (Berger et al., 1982). The horizontal black bar at the top of each panel represents the temperature range of the assumed calcification depth of the species in the region (Table 2.2) (Rippert et al., 2016; Schiebel and Hemleben, 2017), with an additional 0.008‰ error indicated in gray that reflects shot noise limits of the mass spectrometers (Lucarelli et al., 2023). The red point is the average temperature within the calcification depth range. For all species, samples above the saturation horizon are within error of the SST (with one sample of *N. dutertrei* just outside of the limits). For several species, samples below the saturation horizon exhibit higher Δ_{47} values (and a bias to cooler Δ_{47}-temperatures). Figure 2.8 and Supporting Information Figure 2.S.2 show Δ_{47} data for individual species as a function of bottom water carbonate saturation.

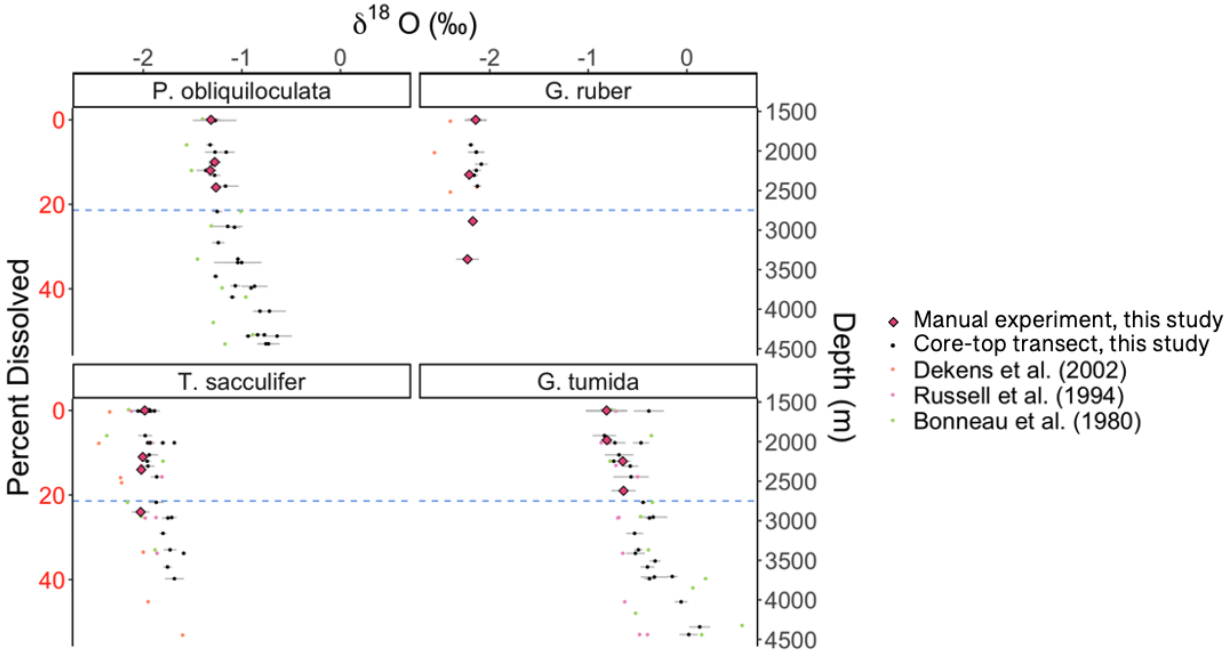

Figure 2.5: Comparison of manual dissolution experimental results (diamonds) to core-top $\delta^{18}O$ data from Ontong Java Plateau (black circles) for four species as a function of percent dissolved (left y-axis). Right y-axis shows water depth for core-top samples. Axes are aligned based on Johnstone et al. (2010) estimates of dissolution. The horizontal blue line is the carbonate saturation horizon.

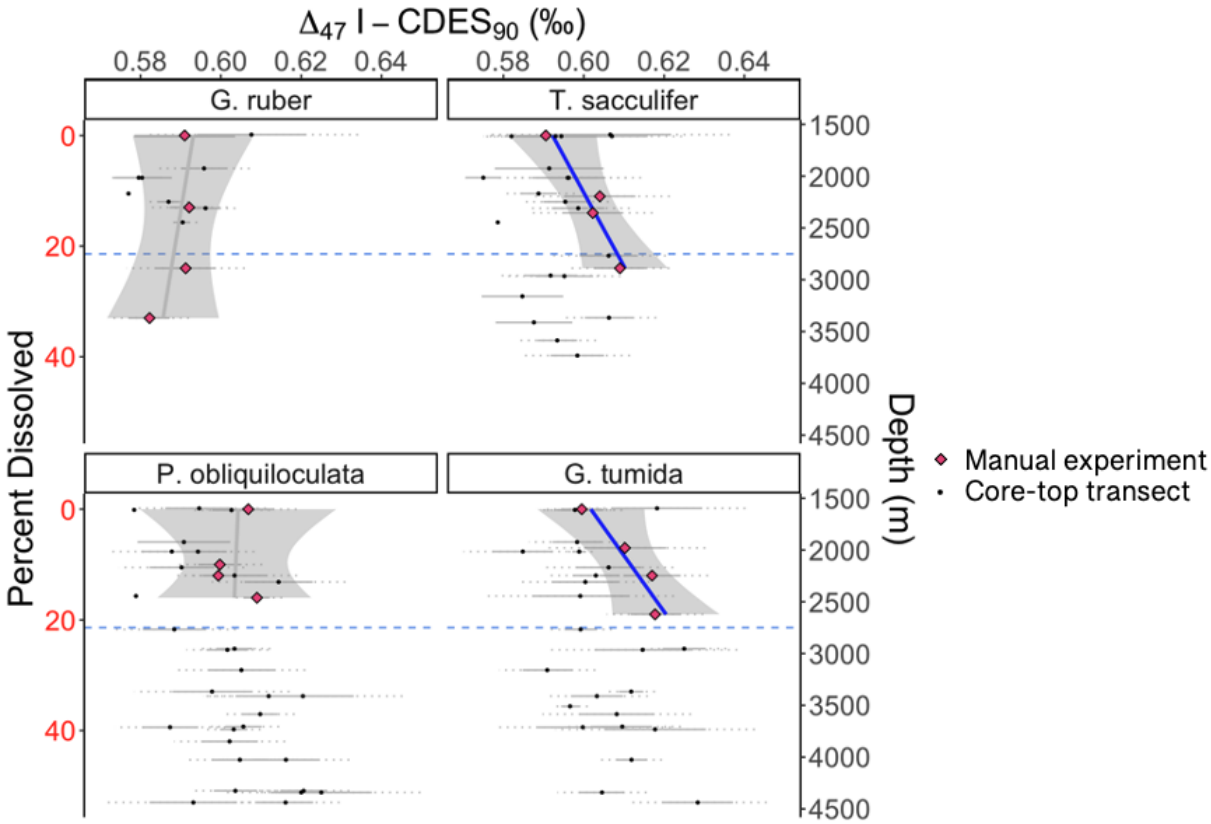

Figure 2.6: Comparison of manual dissolution experimental results (diamonds) to core-top Δ_{47} data from Ontong Java Plateau (black circles) for four species as a function of percent dissolved (left y-axis). Axes are aligned based on Johnstone et al. (2010) estimates of dissolution. The horizontal blue line is the carbonate saturation horizon. Regressions through the experimental data for *G. ruber* and *P. obliquiloculata* do not show significant trends (grey line; $p > 0.1$), while regressions through data for *T. sacculifer* and *G. tumida* do show significant increases with dissolution (blue line; $p < 0.1$). 95% confidence intervals are also shown for regressions.

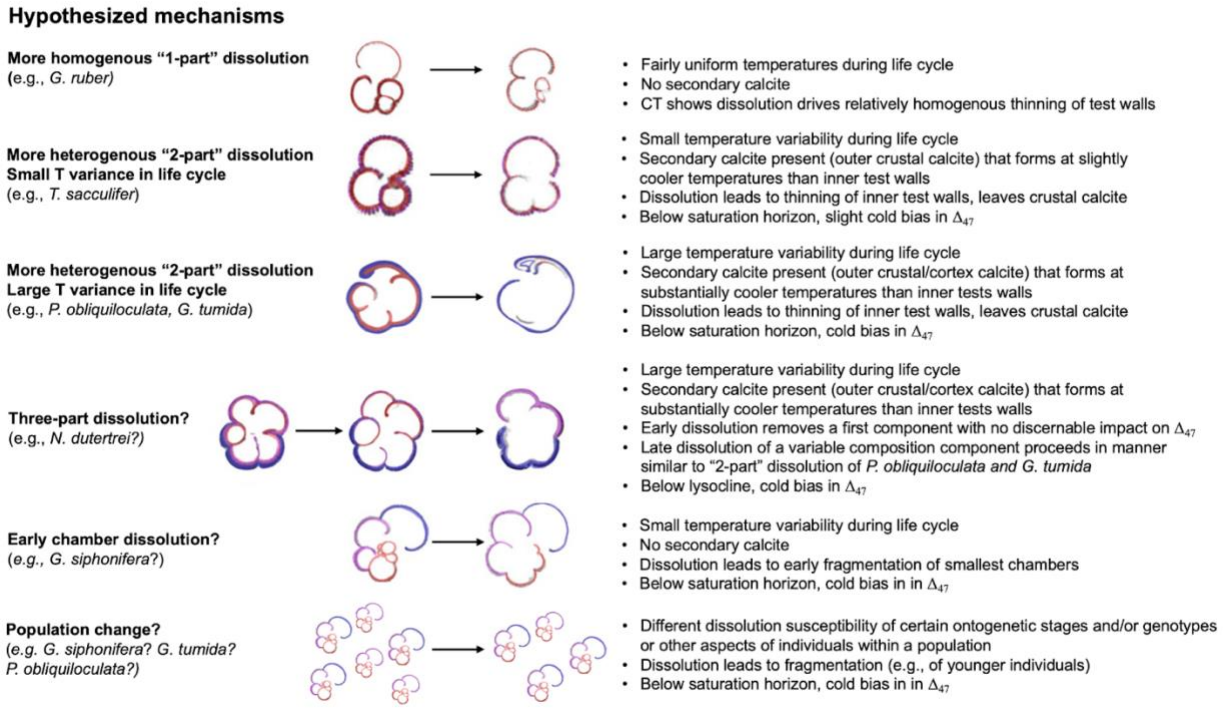

Figure 2.7: Hypothesized mechanisms for dissolution and potential effects on Δ_{47}. Images are modified from CT scans (this study, Johnstone et al., 2010), with red color illustrating warmer calcification temperatures, and blue color indicating cooler calcification temperatures.

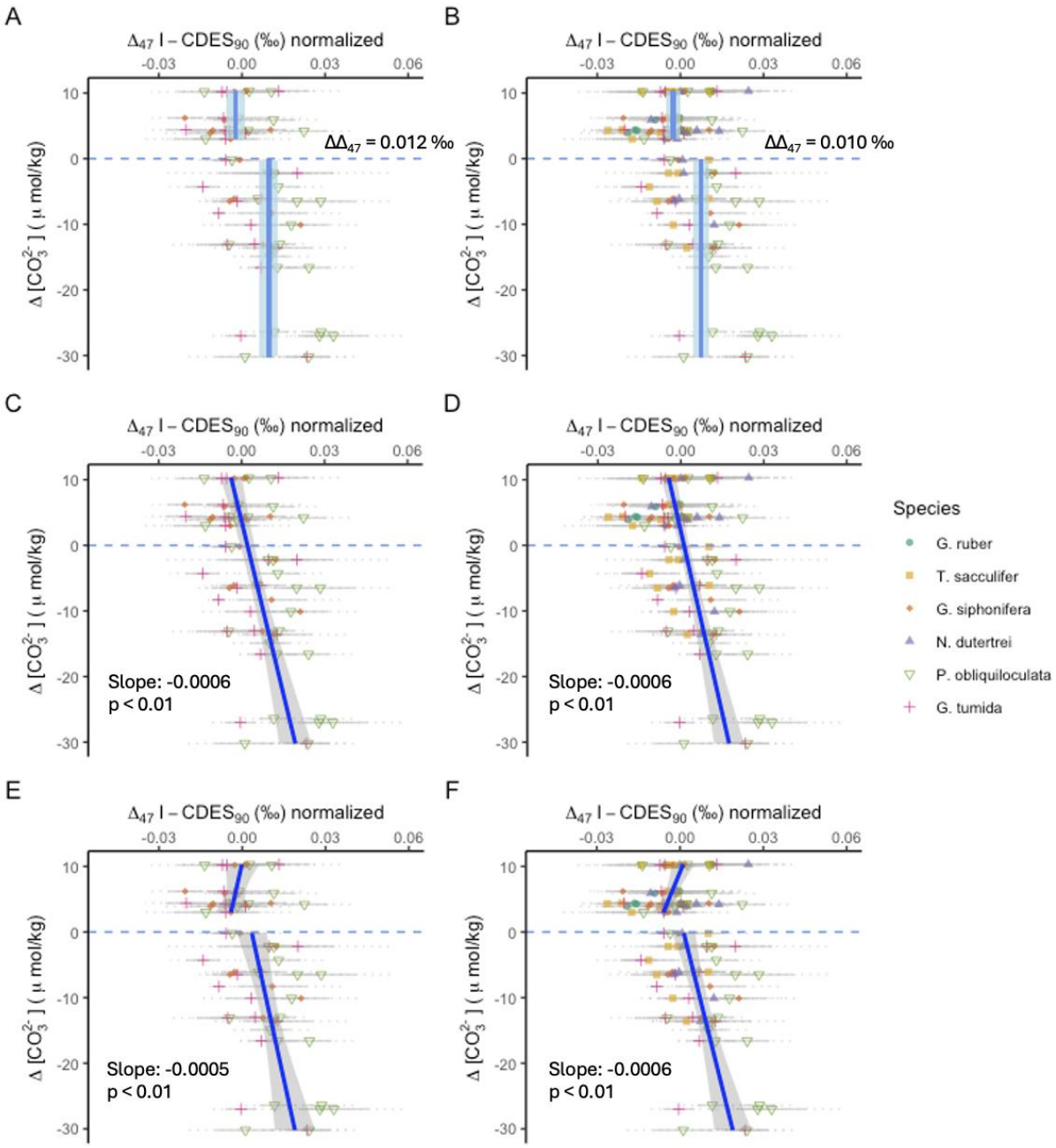

Figure 2.8: Dissolution impacts on Δ_{47} shown as normalized and pooled offsets in species with $\Delta[CO_3^{2-}]$. Supporting Information Figure 2.S.6 shows the same data as a function of water depth. Δ_{47} data are normalized to the average or each species' shallowest samples (>10 (µmol/kg) $\Delta[CO_3^{2-}]$). Panels A, C, E show results for species that show significant correlations with depth (Species *G. siphonifera*, *P. obliquiloculata*, and *G. tumida*). Panels B, D, and F show data for all species. The dashed blue line is the carbonate saturation horizon. Panels A and B show means of populations above and below the carbonate saturation horizon. In A, the mean offset of the pooled species is 0.012 ‰, and in B, 0.010 ‰. Panels C and D show linear regressions through all of the data with 95% CI, with both yielding a pooled slope of -0.0006 ‰ / µmol/kg $\Delta[CO_3^{2-}]$. Panels E and F show linear regressions calculated separately for the data above and below the carbonate saturation horizon, with the data in Panel E yielding a slope of -0.0005 ‰ / µmol/kg, $p < 0.01$ below the carbonate saturation horizon, and the results in Panel F yielding a slope of -

0.0006 ‰ / μmol/kg, $p < 0.01$. The slope on the regression through the data above the saturation horizon in panel E is not significant at the 95% confidence level (0.0005 ‰ / μmol/kg, $p = 0.4$), while the results in panel F yield a slope of 0.0009 ‰ / μmol/kg, $p = 0.03$; if the outlier *N. dutertrei* point is removed, the slope is 0.0008, $p=0.08$.

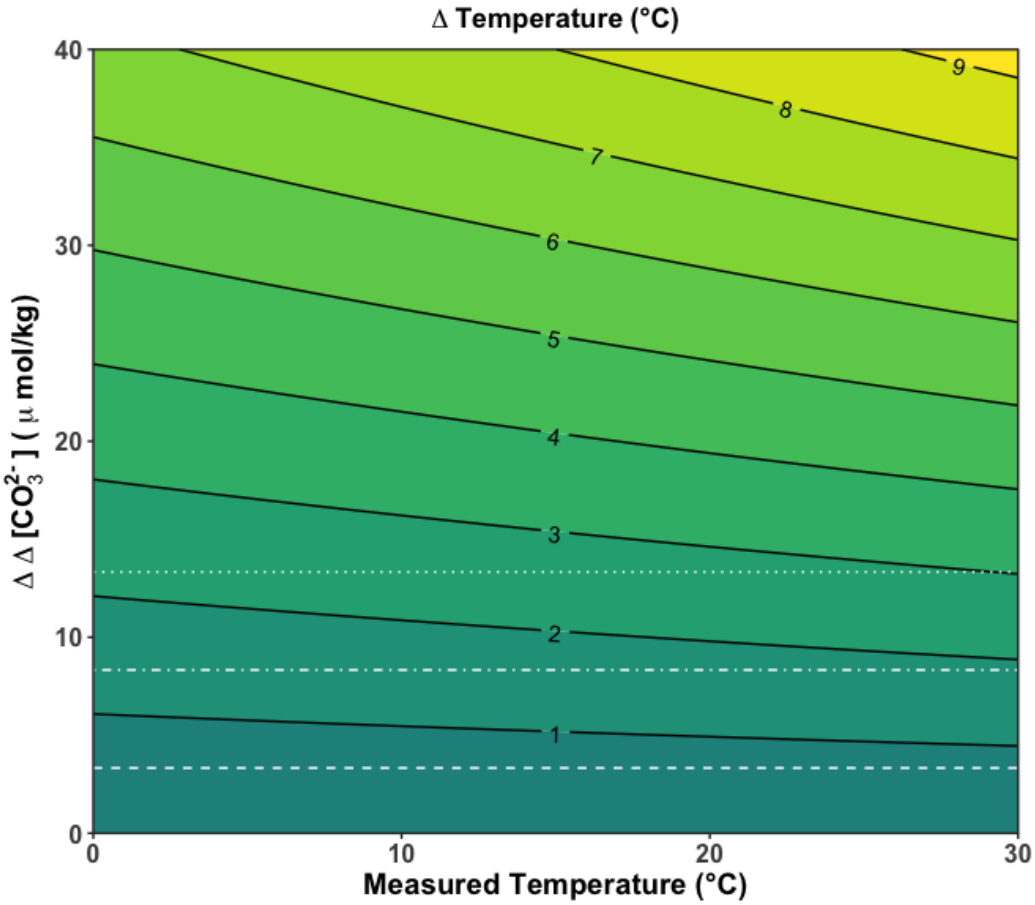

Figure 2.9: Change in estimated temperature with a pooled dissolution correction of -0.0006 ‰ / μmol/kg $\Delta[CO_3^{2-}]$. The contours show the increase in temperature calculated given a range of measured Δ_{47} temperatures and carbonate saturation changes. The horizontal lines represent generalized temperature error for Δ_{47}. The dotted line represents the shot noise limit of 0.008 ‰, and the dot-dash line represents the average SE of standards of 0.005 ‰ both defined in Lucarelli et al. (2023). The dashed line is a hypothetical value of what may be possible with higher ohm resistors or laser spectroscopy of 0.002 ‰.

7 Tables

Core	Latitude	Longitude	Water Depth, [m]	$\Delta[CO_3^{2-}]$ [µmol/kg]
ERDC 92BX	2°13.5'S	156°59.88'E	1598	10.3
MW91-9 1BC3	2°14.56'S	156°59.87'E	1616	10.2
MW91-9 1BC7	2°10.75'S	157°00.08'E	1614	10.2
ERDC 88BX	0°02.88'S	155°52.08'E	1924	6.2
MW91-9 1.5BC11	0°00.48'S	157°50.00'E	2016	4.3
MW91-9 1.5BC33	0°59.86'S	157°50.92'E	2015	4.4
ERDC 112BX	1°37.50'S	159°14.10'E	2168	3.9
ERDC 120BX	0°01.02'S	158°41.58'E	2247	5.9
MW97-20 MC-17F	0°00.01'S	158°54.46'E	2309	4.2
MW91-9 2.5BC37	0°00.28'N	159°29.03'E	2445	3
MW97-20 MC-55B	0°00.25'S	159°52.16'E	2767	-0.2
MW91-9 3BC16	0°00.83'N	160°27.10'E	2954	-2.2
MW91-9 3BC24	0°00.47'N	160°25.52'E	2965	-2.2
MW91-9 GAC44	0°00.04'S	160°39.11'E	3160	-4.3
MW97-20 MC-45A	0°00.22'S	160°59.31'E	3367	-6.1
MW91-9 4BC51	0°01.41'S	161°00.99'E	3411	-6.5
ERDC 135BX	0°52.50'N	160°59.58'N	3509	-8.3
ERDC 77BX	4°51.0'N	156°03.48'E	3585	-10.1
MW97-20 MC-39A	0°0.28'S	161°59.31'E	3705	-13
MW91-9 4.5BC53	0°00.53'S	161°23.32'E	3711	-13.1
ERDC 128BX	0°00.30'S	161°25.62'E	3732	-13.6
ERDC 136BX	1°06.0'N	161°36.30'E	3848	-14.9
MW91-9 5BC54	0°00.80'S	161°46.21'E	4025	-16.6
MW97-20 MC-28G	0°00.22'S	162°13.28'E	4325	-26.4
ERDC 141BX	2°21.72'N	163°42.42'E	4325	-26.4
MW91-9 5.5BC58	0°00.08'S	162°13.41'E	4341	-27
MW91-9 6BC74	0°00.04'N	162°44.08'E	4438	-30.2

Table 2.1: Site locations on the Ontong Java Plateau with depth (m) and $\Delta[CO_3^{2-}]$ [µmol/kg].

Species	Assumed calcification depth (m)	Assumed calcification temperature range (°C)	ACD Δ_{47} range*	Δ_{47} avg above carbonate saturation horizon (‰)	95% CI	Δ_{47} avg below carbonate saturation horizon (‰)	95% CI	Welch's 2 sample t-test p-value
G. ruber	5-150	23.6-29.6	0.582-0.599	0.59	0.584-0.596	NA	NA	NA
T. sacculifer	5-160	22.4-29.6	0.582-0.602	0.591	0.586-0.596	0.596	0.591-0.601	0.248
G. siphonifera	0-150	23.6-29.6	0.582-0.599	0.589	0.584-0.594	0.6	0.594-0.606	**0.018**
N. dutertrei	110-160	22.4-27.9	0.587-0.602	0.603	0.596-0.610	0.602	0.599-0.606	0.873
P. obliquiloculata	145-175	20.5-26.0	0.592-0.608	0.594	0.587-0.601	0.607	0.602-0.612	**0.018**
G. tumida	125-300	10.7-27.3	0.589-0.639	0.601	0.596-0.606	0.609	0.604-0.614	**0.04**

***** Calculated using Δ_{47}-temperature equation (Chapter 1)

Table 2.2: Species assumed calcification depth range and averages above and below the carbonate saturation horizon.

Species	Pearson's correlation Δ_{47} with $\Delta[CO_3^{2-}]$	*p*	Slope of Δ_{47} with $\Delta[CO_3^{2-}]$ (‰/µmol/kg)	SE	*p*	Slope of $\delta^{18}O$ with $\Delta[CO_3^{2-}]$ (‰/µmol/kg)	SE	*p*	Slope of $\delta^{13}C$ with $\Delta[CO_3^{2-}]$ (‰/µmol/kg)	SE	*p*
*G. ruber**	*0.554*	*0.1*	*0.002*	*0.0009*	*0.1*	*-0.003*	*0.003*	*0.4*	*0.019*	*0.019*	*0.4*
T. sacculifer	-0.054	0.81	-0.00008	0.0003	0.81	**-0.014**	**0.002**	**< 0.01**	**0.021**	**0.005**	**< 0.01**
G. siphonifera	**-0.55**	**0.02**	**-0.0007**	**0.0003**	**0.02**	**-0.02**	**0.004**	**< 0.01**	0.004	0.005	0.3
N. dutertrei	0.021	0.94	0.00002	0.0003	0.9	-0.009	0.009	0.3	0.005	0.003	0.07
P. obliquiloculata	**-0.565**	**<0.01**	**-0.0005**	**0.0001**	**< 0.01**	**-0.015**	**0.002**	**< 0.01**	**-0.008**	**0.001**	**< 0.01**
G. tumida	**-0.428**	**0.04**	**-0.0004**	**0.0002**	**0.04**	**-0.02**	**0.002**	**< 0.01**	**-0.011**	**0.002**	**< 0.01**
Pooled normalized species[a]	**-0.55**	**<0.01**	**-0.0006**	**0.0001**	**< 0.01**						

Species	Pearson's correlation Δ_{47} with depth	*p*	Slope of Δ_{47} with depth (‰/km)	SE	*p*	Slope of $\delta^{18}O$ with depth (‰/km)	SE	*p*	Slope of $\delta^{13}C$ with depth (‰/km)	SE	*p*
*G. ruber**	*-0.364*	*0.3*	*-0.011*	*0.01*	*0.3*	*0.027*	*0.03*	*0.39*	*-0.312*	*0.15*	*0.08*
T. sacculifer	0.095	0.67	0.001	0.003	0.67	**0.135**	**0.024**	**< 0.01**	**-0.209**	**0.046**	**< 0.01**
G. siphonifera	**0.536**	**0.02**	**0.007**	**0.003**	**0.02**	**0.19**	**0.043**	**< 0.01**	-0.044	0.05	0.36
N. dutertrei	-0.083	0.77	-0.001	0.003	0.77	0.054	0.09	0.56	-0.05	0.025	0.07
P. obliquiloculata	**0.557**	**<0.01**	**0.008**	**0.002**	**< 0.01**	**0.197**	**0.021**	**< 0.01**	**0.108**	**0.018**	**< 0.01**
G. tumida	**0.406**	**0.05**	**0.005**	**0.002**	**0.05**	**0.243**	**0.034**	**< 0.01**	**0.139**	**0.019**	**< 0.01**
Pooled normalized species[a]	**0.549**	**< 0.01**	**0.007**	**0.001**	**< 0.01**						

*No samples below the carbonate saturation horizon

[a]Normalized species with significant trends: *G. siphonifera, P. obliquiloculata, and G tumida*

Table 2.3: Correlations and slopes with depth.

Supporting Information for

Dissolution effects on clumped isotope signatures in foraminifera

Additional Supporting Information (Files uploaded separately)

Tables 2.S.1-2.S.8

S1. Clumped isotope standards TV_ST and TV_BT

Travertine tiles were then crushed and homogenized by mortar and pestle. 23 replicates of TV_BT and 29 replicates of TV_ST were measured. Values are reported in the were defined based on conversion into I-CDES reference frame as described in the methods section. Data were analyzed to test for normality (Table 2.S.5) and passed all normality tests. Standard values conform to predictions for equilibrium in a paired Δ_{47}-Δ_{48} space (Figure 2.S.7). Mean values were then used to develop empirical transfer functions (Table 2.S.6).

S2. Dissolution Experiments:

Dissolution experiments in filtered seawater were conducted for a preliminary investigation into the precise quantification of dissolution percentage and relationships to clumped isotopes. Different experimental methods were iteratively utilized with the goal of simulating patterns in $\delta^{13}C$ and $\delta^{18}O$ with respect to percent dissolution that are reminiscent of core-top data from *in-situ* environments with similar mass losses. Three sets of experiments are detailed below. The final version (Experimental Set 3) is discussed in the main text.

S2.1 Methods:

S2.1.1 Sample and solution preparation:

Samples were manually dissolved from additional cleaned planktic specimens picked from core MW91-9 1BC3 (1616m), well above the calcite lysocline in this region (3400m). In this study we adapt protocols from previous dissolution studies to precisely quantify dissolution

percentages (Naviaux, Subhas, Dong, et al., 2019; Naviaux, Subhas, Rollins, et al., 2019; Subhas et al., 2015, 2018).

First, ESL-filtered seawater was collected and weighed into gas-impermeable foil bags. Alkalinity was measured on the non-acidified seawater. The water is UV-treated, 0.2 µm filtered, and $HgCl_2$ poisoned to discourage bacterial respiration to maintain control over alkalinity and DIC. We prepare undersaturated seawater by adjusting its alkalinity using 0.1 N HCl.

S2.1.2 Experimental Set 1:

P. obliquiloculata samples were separated into 4 sub-samples. One was not dissolved and the other three were weighed into small glass vials to be run in batches. Samples were weighed into glass vials with masses from 4.048-5.102 mg. The alkalinity of the solution was dropped to a calcite saturation of approximately 0.2 or lower. 120ml glass jars were weighed and then filled with the acidified seawater and the jar was overflowed for 5 seconds and then slightly emptied to the shoulder of the bottle to leave room for the foraminifera to be added. The samples were immediately poured into the jar and sealed closed. The bottles were then weighed again to measure water mass. Blanks of just seawater were additionally added to the run to measure drift in alkalinity over the course of the experiment. The experiments were placed on a shaker table and left for 4-5 days to vary the amount of dissolution in the samples.

Water samples were extracted by opening the jar and sampling 20 ml of solution. Foraminifera samples were then extracted by pouring the rest of the water and picking up the remaining calcite with a syringe. Alkalinity measurements were run in triplicate, and DIC with single replicates to determine the carbon system.

S2.1.3 Experimental Set 2:

P. obliquiloculata samples were first cracked between glass plates with DI water and left to dry overnight in an oven (< 50 °C). The samples were then weighed at different masses into

glass vials with lowest values around 7 mg and highest masses around 13 mg to attempt to vary final dissolution percentages. The alkalinity of the solution was dropped further to a saturation of 0.05. The solution was added to 120 ml jars and samples were immediately poured into the jar and sealed closed. The experiments were placed on a shaker table and left for 5 days.

Water samples were extracted by opening the jar and quickly sampling 20 ml of solution. Foraminifera samples were then extracted by pouring the rest of the water and picking up the remaining calcite with a syringe. Alkalinity measurements were run in triplicate, and DIC with single replicates to determine the carbon system.

S2.1.4 Experimental Set 3:

Foraminiferal calcite from *P. obliquiloculata*, *G. tumida*, *T. sacculifer*, and *G. ruber* was weighed and heat sealed into polycarbonate filter paper pouches with masses from approximately 5.6 to 12.0 mg, which were then placed into gas-impermeable foil bags, heat-sealed shut and evacuated. A measured mass of solution with a calcite saturation of approximately 0.8 was siphoned into the experimental bags ranging from around 0.350 L to 3.0 L to vary dissolution percentage. The bags were then transferred to a shaker table to maintain the flow of the solution over the particles.

Alkalinity and DIC are checked three times throughout the experiment: once on the first day, then halfway through, and then one final time at the end of the experiment, with the full experiment lasting two months. Following the final alkalinity and DIC measurements, the water is drained, and samples are extracted by cutting open the bags and removing the pouches. Pouches are rinsed three times with milli-Q water and dried overnight in an oven held at approximately 40 °C (<50 °C). The pouches were then cut open and the sample was weighed to verify the dissolution percentage.

S2.1.5 Alkalinity and DIC measurements:

Alkalinity and DIC were measured on each experiments' solution water. These parameters are then used to calculate all carbonate system parameters, including the saturation state. Alkalinity-DIC pairs are used as inputs variables to CO2SYS v1.1 (Van Heuven et al., 2011) run in Excel with the calcite K_{sp}^* of Mucci (1983). Measured changes in the alkalinity of the solution are used to calculate percent dissolution.

S2.1.6 Stable and clumped isotopes:

Stable and clumped isotopes were measured using the same procedures outlined in the primary text and presented in Figures 2.S.3, 2.S.8 and 2.S.9.

S2.2 Results and Discussion

S2.2.1 Experimental Set 1:

Dissolution percentages attained through this method ranged from 6 - 21% in *P. obliquiloculata,* with lowest alkalinity and longest experimental time samples having the highest level of dissolution. Experimental results from stable isotopes show negative shifts in $\delta^{18}O$, or lighter isotopes being preserved in the remaining calcite. This is the opposite signal from what is expected from transect studies, which all suggest that the stable isotope values should increase with increased dissolution (Figure 2.S.8). The shift in an unexpected direction could be due to the dissolution of different portions of the test in an experimental setup compared to natural environments, resulting in different trends. We hypothesized that the shift we observe in this experiment may be due to the outer portion of the test being preferentially dissolved.

S2.2.2 Experimental Set 2:

We did not reach the expected dissolution percentages calculated from equilibrium with the masses added to the solution. The final dissolution percentages from the experiment ranged by ~5% despite the large spread in sample mass each container started with. Dissolution

percentages in *P. obliquiloculata* ranged from approximately 27 to 33%. $\delta^{18}O$ in this experiment did not show the negative shift visible in the first version, however, the $\delta^{18}O$ still did not move towards a more positive value and instead seemed not to change at all with the new access to the inside of the chamber provided in this version of the experiment (Figure 2.S.8). This result could signify uniform dissolution across the whole of the test potentially resulting from the extremely low alkalinity and the more rapid rate of dissolution in this experiment.

S2.2.3 Experimental Set 3:

Dissolution percentages in this experiment ranged from 12 - 16 % for *P. obliquiloculata,* with the largest degree of dissolution exhibited in G. *ruber* (33%). For this experiment, rates of dissolution decreased after the first month, given that the alkalinity and DIC measurements did not continue to increase following our second sampling point (Table 2.S.7). This experiment did result in the expected trends in $\delta^{18}O$ with increased dissolution (Figure 2.S.8). Using this experiment as a benchmark for Δ_{47} given its agreement with other stable isotopes shows potential slight increases in Δ_{47} in *T. sacculifer* and *G. tumida* and no increase in the other species. However, these results are difficult to compare to transect studies as the signal in Δ_{47} from these archives is only visible at higher dissolution percentages than what is captured by this experiment (Figure 2.3, 2.4, 2.S.9). Future experiments should aim for higher dissolution percentages than gathered here and potentially look into organic blockage of dissolution in natural seawater with no microbial activity as a potential hindrance towards these higher levels of dissolution.

Attempts to increase the range in dissolution percentages were unsuccessful due to contamination by mercury-resistant bacteria and time constraints. Specifically, additional samples were set up following the same procedure as this experiment, however at later sampling stages total alkalinity and DIC measurements became decoupled. Total alkalinity began to

decrease while DIC increased drastically which is an indicator of respiration rather than dissolution (Zeebe & Wolf-Gladrow, 2001). For this reason, we were unable to rely on total alkalinity and DIC measurements for estimates of dissolution.

S3 Additional Statistics

Multivariate linear regressions were also performed on the whole of the dataset. No interactive effect between species type and depth or carbonate saturation were found to be significant. However, the additive effects of depth and species were found to be significant (ANOVA p <0.01). Regression analysis results are presented in Supplemental Table 2.S.8. Slopes from these regressions could also be used to correct for dissolution with a smaller effect on Δ_{47} values when the species is unknown. These multivariate regressions could also be used in place of individual species slopes (Table 2.S.8).

Supplementary Figures

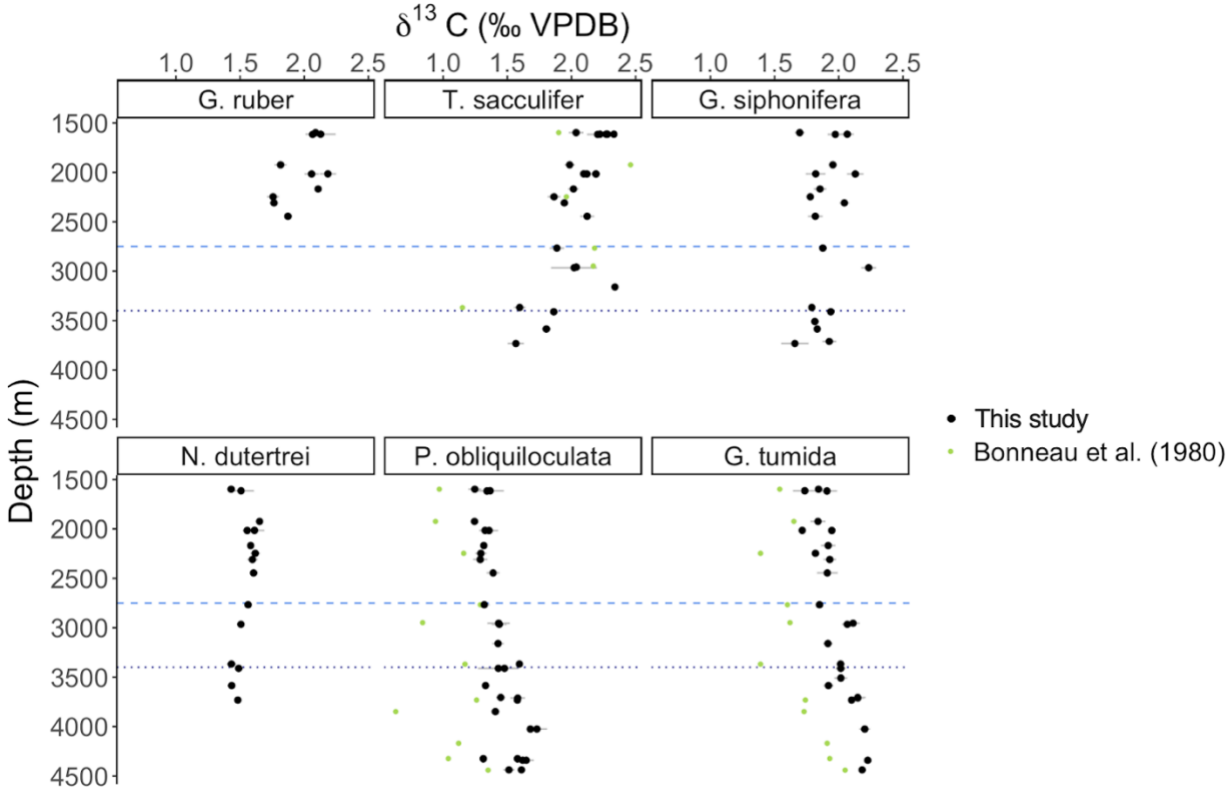

Figure 2.S.1. Foraminifera $\delta^{13}C$ (VPDB) for six species in core-tops from the Ontong Java Plateau. The horizontal dashed blue line represents the carbonate saturation horizon and the dark blue dotted line represents the lysocline (Berger et al., 1982).

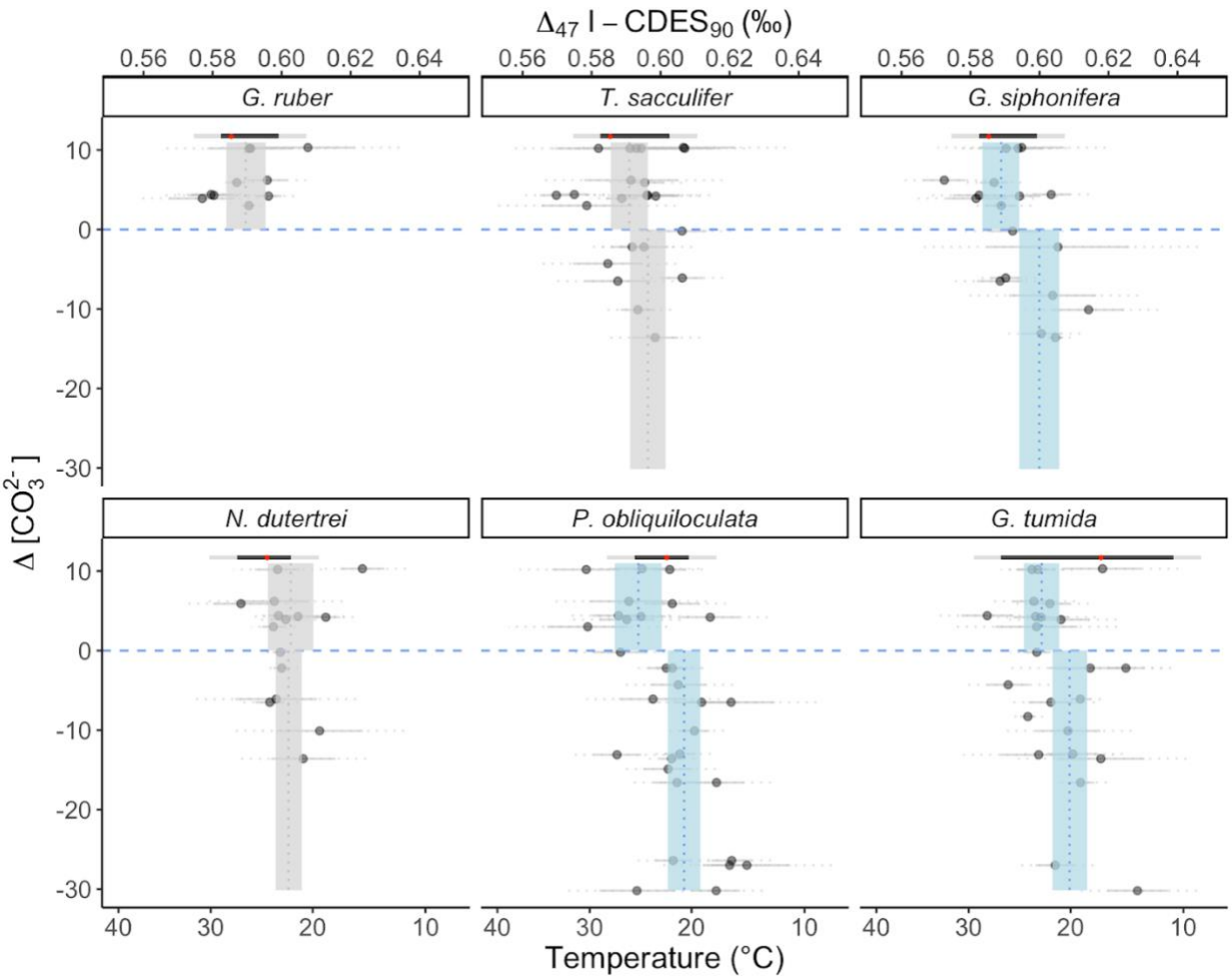

Figure 2.S.2: Δ_{47} values measured on core-top planktic foraminifera from the Ontong Java Plateau as a function of $\Delta[CO_3^{2-}]$. Δ_{47}-temperature scale shown as a second x-axis. Species are ordered by dissolution resistance (least to greatest from top left to lower right). Errors are 1SE (solid) and 95% CI (dotted). Vertical bands show mean sample Δ_{47} values - blue bands indicate species that show significant differences (at the 95% confidence level) above and below the carbonate saturation horizon, while gray bands do not. The grey vertical dashed line for *N. dutertrei* is the mean of the samples below the lysocline. The horizontal dashed light blue line represents the calcite saturation horizon and the dotted dark blue line represents the foraminiferal lysocline (Berger et al., 1982). The horizontal black bar at the top of each panel represents the temperature range of the assumed calcification depth of the species in the region, with an additional 0.008‰ error indicated in gray that reflects shot noise limits of the mass spectrometers (Lucarelli et al., 2023). The red point is the average temperature within the calcification depth range. For all species, samples above the saturation horizon are within error of the SST (with one sample of *N. dutertrei* just outside of the limits). For several species, samples below the saturation horizon exhibit higher Δ_{47} values (and a bias to cooler Δ_{47}-temperatures).

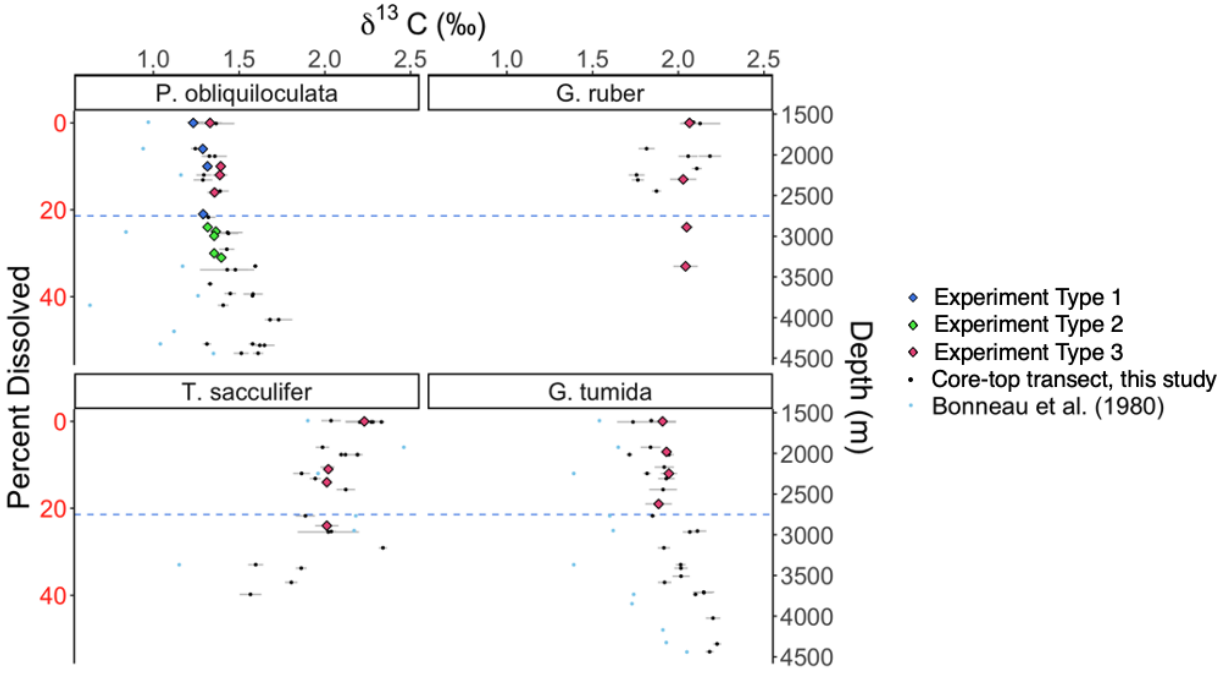

Figure 2.S.3: Ontong Java Plateau $\delta^{13}C$ depth transects (circles, left axis) and manual dissolution results (red, right axis) for four species. The horizontal blue line is the calcite saturation horizon. Axes are aligned based on Johnstone et al. (2010) estimates of dissolution. Experiment type 3 is the experiment discussed in the main text.

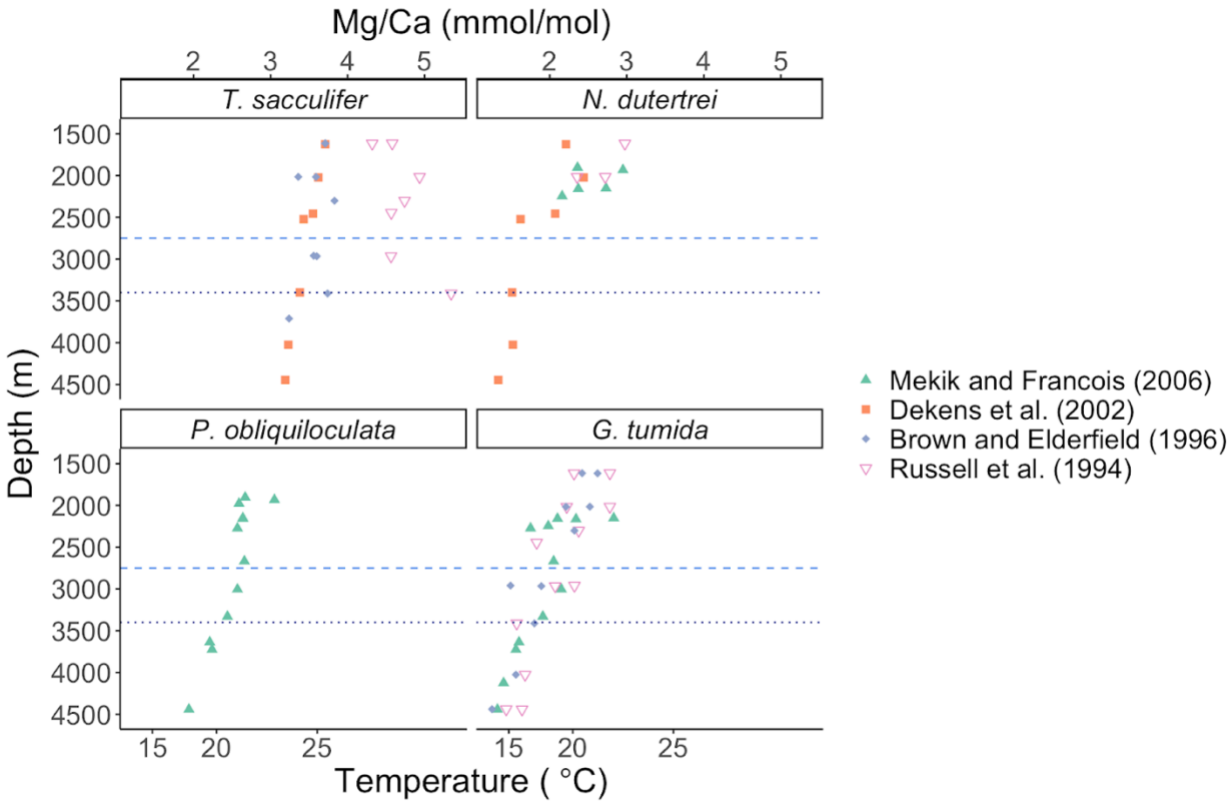

Figure 2.S.4: Mg/Ca data compiled from previous studies on the Ontong Java Plateau. The temperature axis is calculated from the Mg/Ca regression from Anand et al. (2003).

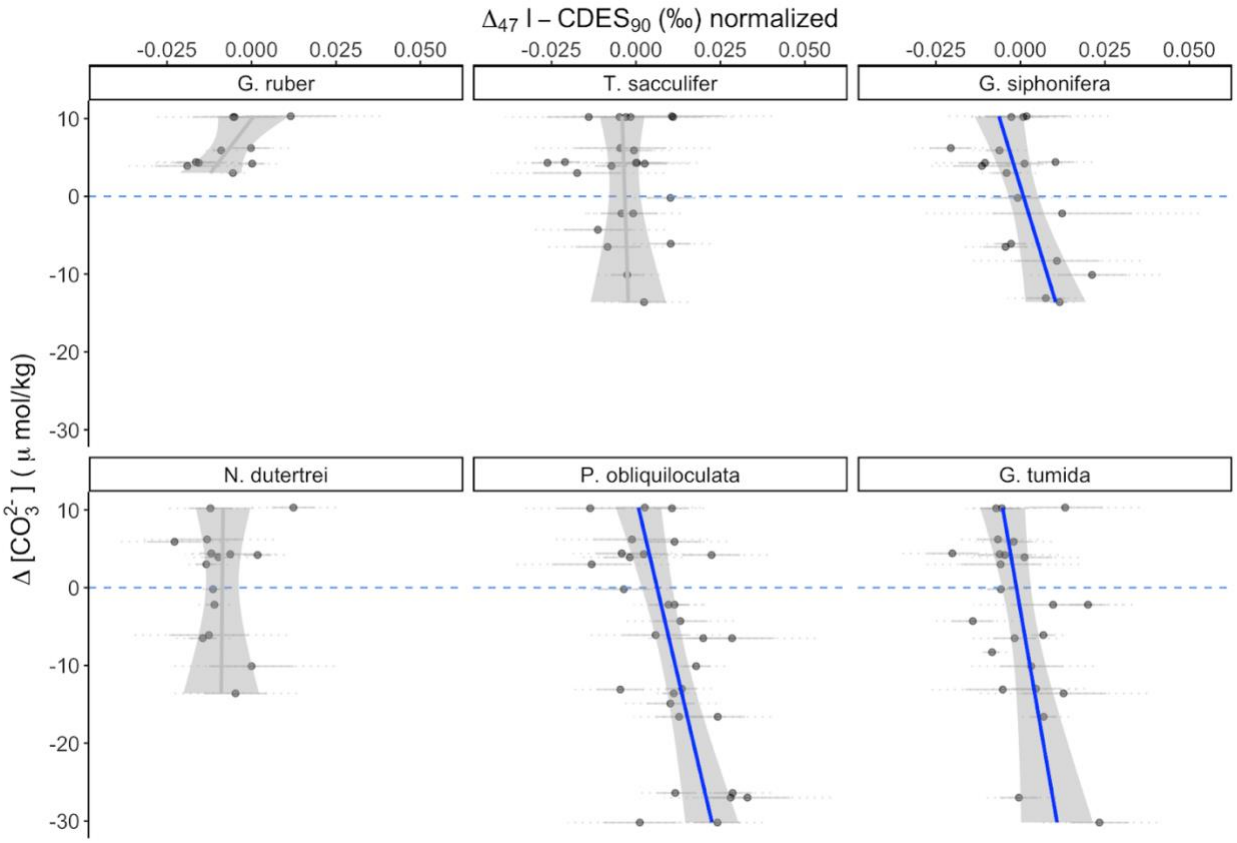

Figure 2.S.5: Normalized Δ_{47} values to the top Δ_{47} values of each species transect against $\Delta[CO_3^{2-}]$. Blue lines are linear regressions taken through each species. Only *G. siphonifera*, *P obliquiloculata* and *G. tumida* are significant. Data is normalized to the average of each species' topmost samples (<2 km depth).

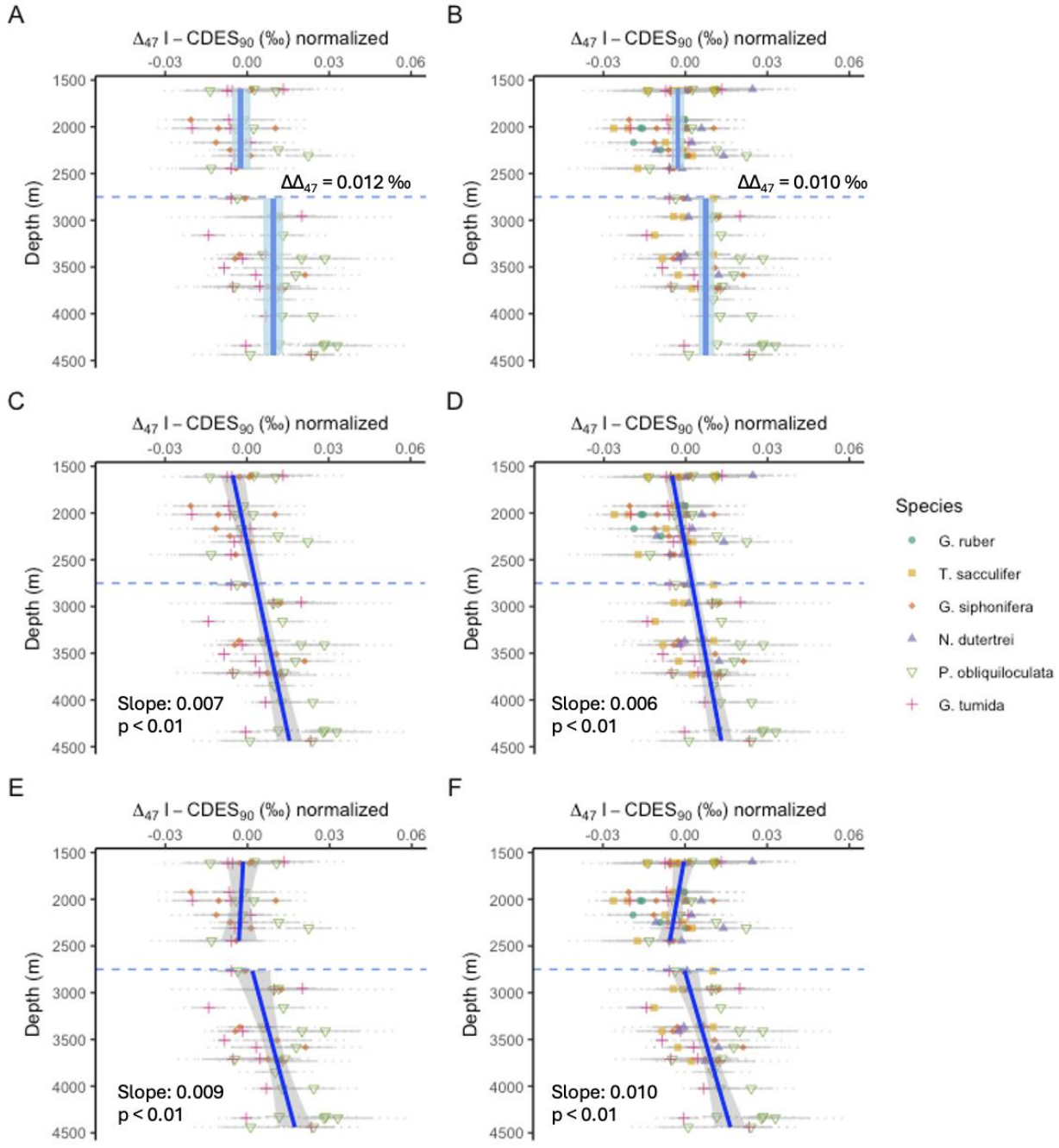

Figure 2.S.6: Dissolution impacts on Δ_{47} shown as normalized and pooled offsets in species with depth. Δ_{47} data are normalized to the average or each species' shallowest samples (>10 (µmol/kg) $\Delta[CO_3^{2-}]$). Panels A, C, E show results for species that show significant correlations with depth (Species *G. siphonifera*, *P. obliquiloculata*, and *G. tumida*). Panels B, D, F show data for all species. The dashed blue line is the carbonate saturation horizon. Panels A and B show means of populations above and below the carbonate saturation horizon. In A, the mean offset of the pooled species is 0.012 ‰, and in D, 0.010 ‰. Panels C and D show linear regressions through all of the data with 95% CI, with the data in Panel C yielding a pooled slope of 0.007 ‰ / km and Panel D yielding slope of 0.006 ‰ / km. Panels E and F show linear regressions calculated separately for the data above and below the calcite saturation horizon, with the data in Panel E yielding a slope of 0.009 ‰ / km, $p < 0.01$ below the carbonate saturation

horizon, and the results in Panel F yielding a slope of 0.010 ‰ / km, $p < 0.01$. The slope on the regression through the data above the saturation horizon in panel E is not significant at the 95% confidence level (-0.002 ‰ / km, $p = 0.8$), while the results in panel F yield a slope of -0.006 ‰ / km, $p = 0.12$; if the outlier *N. dutertrei* point is removed, the slope is -0.004, $p=0.33$.

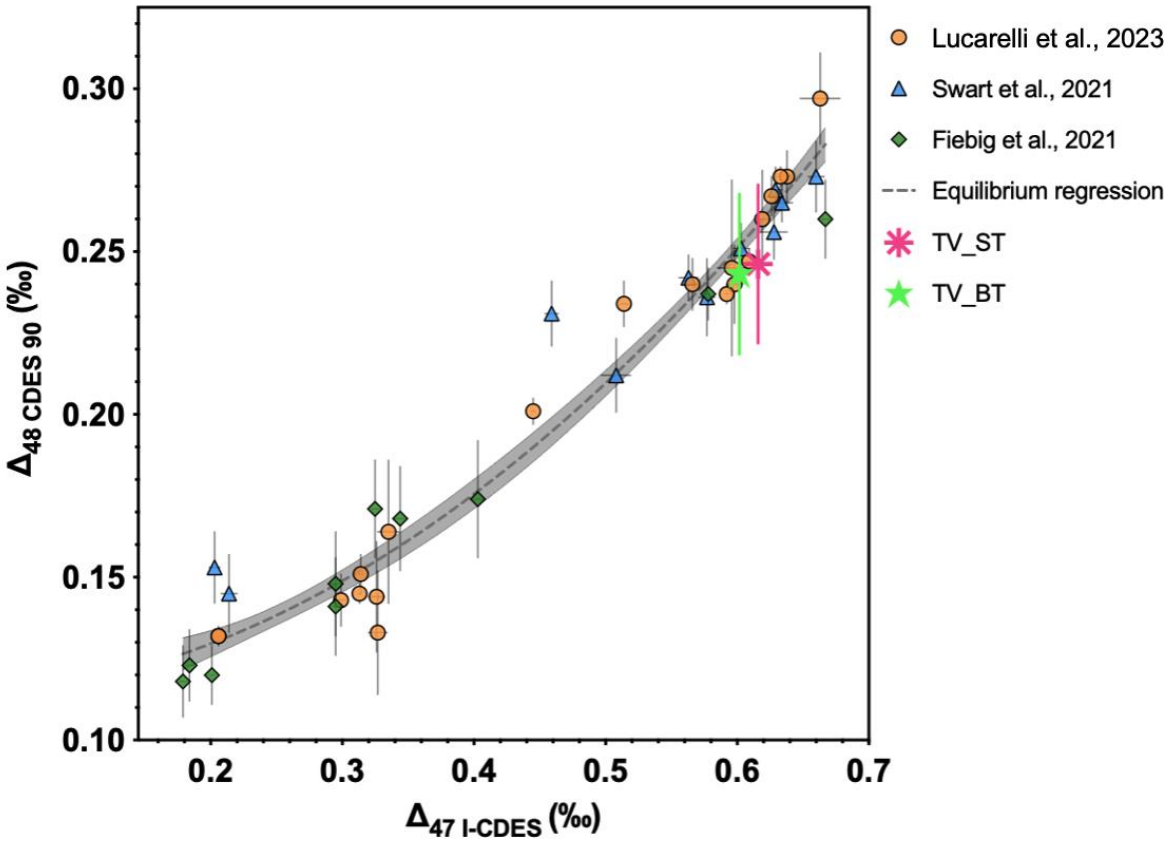

Figure 2.S.7: Description of TV_ST and TV_BT in-house standard values.

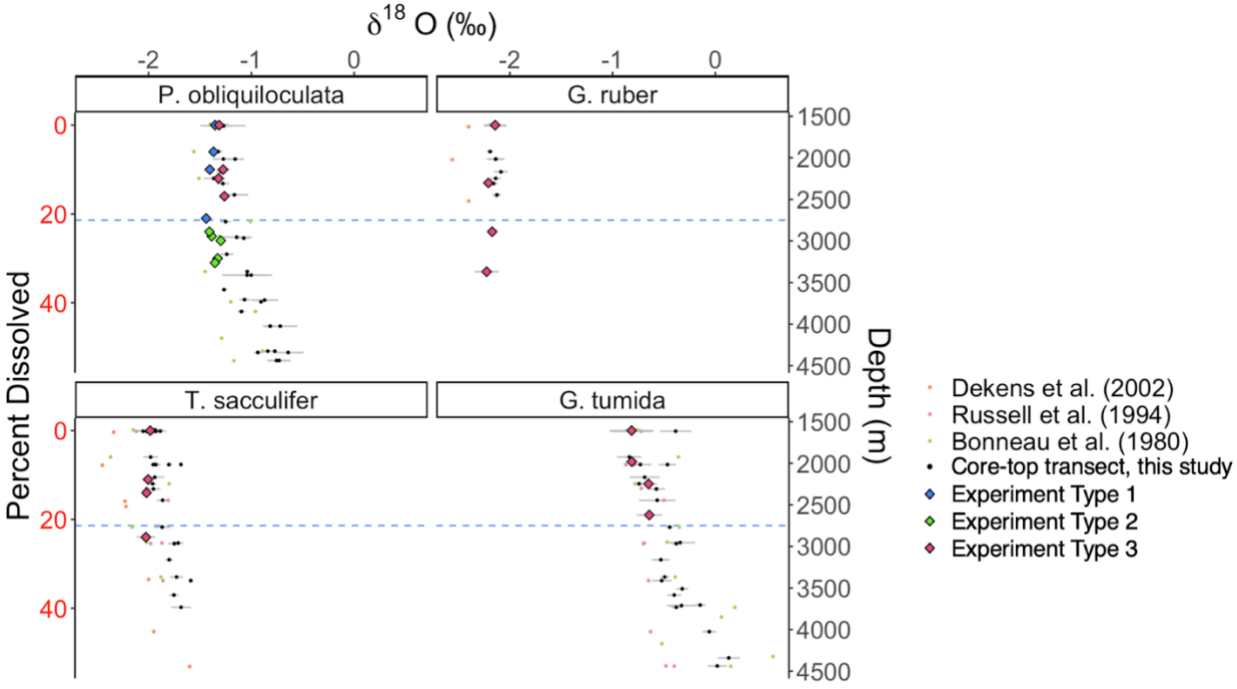

Figure 2.S.8: Ontong Java Plateau $\delta^{18}O$ depth transects (circles, right axis) and manual dissolution results (diamonds, left axis) for four species. The horizontal blue line is the calcite saturation horizon. Axes are aligned based on Johnstone et al. (2010) estimates of dissolution.

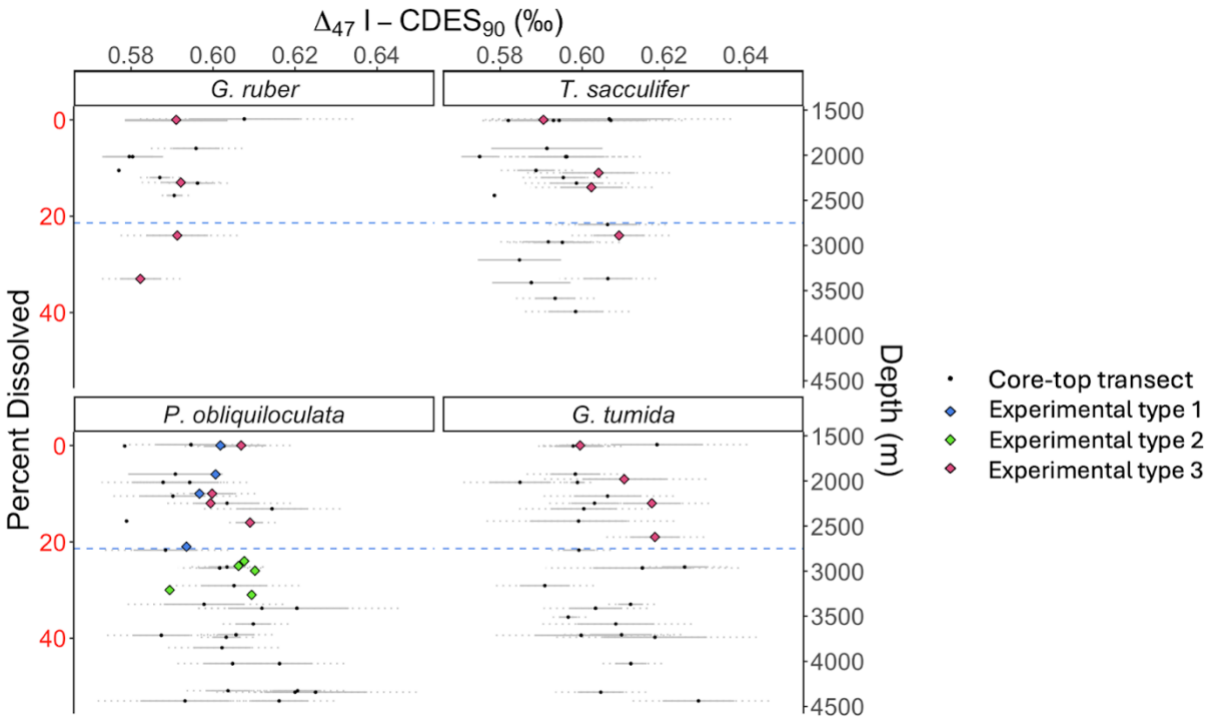

Figure 2.S.9: Comparison of manual dissolution experimental results (diamonds) to core-top Δ_{47} data from Ontong Java Plateau (black circles) for four species as a function of percent dissolved (left y-axis). Right y-axis shows water depth for core-top samples. The horizontal blue line represents the carbonate saturation horizon for core-top samples. Y-axes are aligned based on Johnstone et al. (2010) estimates of dissolution. Three types of manual dissolution experiments were done (blue, green, and red symbols). No significant changes in dissolution were observed in *G. ruber* with the manual dissolution experiments. For P. *obliquiloculata*, the sample with 16% dissolution shows no significant change in Δ_{47} compared to the undissolved sample. In contrast, for *T. sacculifer*, the sample with >20% dissolution is 0.018 ‰ elevated in Δ_{47} compared to the undissolved sample. For *G. tumida*, the sample with 19% dissolution is 0.018 ‰ elevated compared to the least dissolved sample.

References

2022.2 [Computer software]. Comet Technologies Canada Inc., Montreal, Canada; software available at https://www.theobjects.com/dragonfly.

Amante, C., Eakins, B.W., 2009. ETOPO1 1 Arc-Minute Global Relief Model: Procedures, Data Sources and Analysis.

Anand, P., Elderfield, H., Conte, M.H., 2003. Calibration of Mg/Ca thermometry in planktonic foraminifera from a sediment trap time series. Paleoceanography 18. https://doi.org/10.1029/2002PA000846

Aze, T., Ezard, T.H.G., Purvis, A., Coxall, H.K., Stewart, D.R.M., Wade, B.S., Pearson, P.N., 2011. A phylogeny of Cenozoic macroperforate planktonic foraminifera from fossil data. Biol. Rev. 86, 900–927. https://doi.org/10.1111/j.1469-185X.2011.00178.x

Barker, S., Greaves, M., Elderfield, H., 2003. A study of cleaning procedures used for foraminiferal Mg/Ca paleothermometry. Geochem. Geophys. Geosystems 4. https://doi.org/10.1029/2003GC000559

Bemis, B.E., Spero, H.J., Bijma, J., Lea, D.W., 1998. Reevaluation of the oxygen isotopic composition of planktonic foraminifera: Experimental results and revised paleotemperature equations. Paleoceanography 13, 150–160. https://doi.org/10.1029/98PA00070

Berger, W.H., 1970. Planktonic Foraminifer: Selective Solution and the Lysocline. Mar. Geol. 8, 111–138. https://doi.org/10.1016/0025-3227(70)90001-0

Berger, W.H., Bonneau, M.C., Parker, F.L., 1982. Foraminifera on the deep-sea floor: lysocline and dissolution rate. Oceanol. Acta 5, 249–258.

Bijma, J., Erez, J., Hemleben, C., 1990. Lunar and semi-lunar reproductive cycles in some

spinose planktonic foraminifers. J. Foraminifer. Res. 20, 117–127. https://doi.org/10.2113/gsjfr.20.2.117

Bijma, J., Hemleben, C., Huber, B.T., Erlenkeuser, H., Kroon, D., 1998. Experimental determination of the ontogenetic stable isotope variability in two morphotypes of *Globigerinella siphonifera* (d'Orbigny). Mar. Micropaleontol. 35, 141–160. https://doi.org/10.1016/S0377-8398(98)00017-6

Birch, H., Coxall, H.K., Pearson, P.N., Kroon, D., O'Regan, M., 2013. Planktonic foraminifera stable isotopes and water column structure: Disentangling ecological signals. Mar. Micropaleontol. 101, 127–145. https://doi.org/10.1016/j.marmicro.2013.02.002

Bischoff, W.D., Sharma, S.K., MacKenzie, F.T., 1985. Carbonate ion disorder in synthetic and biogenic magnesian calcites: a Raman spectral study. Am. Mineral. 70, 581–589.

Bonneau, M.C., Vergnaud-Grazzini, C., Berger, W.H., 1980. Stable isotope fractionation and differential dissolution in recent planktonic foraminifera from Pacific box-cores. Oceanol. Acta 3, 377–382.

Bouvier-Soumagnac, Y., Duplessy, J.-C., 1985. Carbon and oxygen isotopic composition of planktonic foraminifera from laboratory culture, plankton tows and Recent sediment; implications for the reconstruction of paleoclimatic conditions and of the global carbon cycle. J. Foraminifer. Res. 15, 302–320. https://doi.org/10.2113/gsjfr.15.4.302

Branson, O., Read, E., Redfern, S.A.T., Rau, C., Elderfield, H., 2015. Revisiting diagenesis on the Ontong Java Plateau: Evidence for authigenic crust precipitation in Globorotalia tumida. Paleoceanography 30, 1490–1502. https://doi.org/10.1002/2014PA002759

Breitenbach, S.F.M., Mleneck-Vautravers, M.J., Grauel, A.-L., Lo, L., Bernasconi, S.M., Müller, I.A., Rolfe, J., Gázquez, F., Greaves, M., Hodell, D.A., 2018. Coupled Mg/Ca and clumped isotope analyses of foraminifera provide consistent water temperatures.

Geochim. Cosmochim. Acta, Chemistry of oceans past and present: A Special Issue in tribute to Harry Elderfield 236, 283–296. https://doi.org/10.1016/j.gca.2018.03.010

Broecker, W., Clark, E., 2001. An evaluation of Lohmann's foraminifera weight dissolution index. Paleoceanography 16, 531–534. https://doi.org/10.1029/2000PA000600

Broecker, W.S., Clark, E., 1999. CaCO3 size distribution: A paleocarbonate ion proxy? Paleoceanography 14, 596–604. https://doi.org/10.1029/1999PA900016

Brown, S.J., Elderfield, H., 1996. Variations in Mg/Ca and Sr/Ca ratios of planktonic foraminifera caused by postdepositional dissolution: Evidence of shallow Mg-dependent dissolution. Paleoceanography 11, 543–551. https://doi.org/10.1029/96PA01491

Caron, D.A., Roger Anderson, O., Lindsey, J.L., Faber, W.W., Lin Lim, E.E., 1990. Effects of gametogenesis on test structure and dissolution of some spinose planktonic foraminifera and implications for test preservation. Mar. Micropaleontol. 16, 93–116. https://doi.org/10.1016/0377-8398(90)90031-G

Cubillas, P., Köhler, S., Prieto, M., Chaïrat, C., Oelkers, E.H., 2005. Experimental determination of the dissolution rates of calcite, aragonite, and bivalves. Chem. Geol. 216, 59–77. https://doi.org/10.1016/j.chemgeo.2004.11.009

Daëron, M., Gray, W.R., 2023. Revisiting Oxygen-18 and Clumped Isotopes in Planktic and Benthic Foraminifera. Paleoceanogr. Paleoclimatology 38, e2023PA004660. https://doi.org/10.1029/2023PA004660

Davis, C.V., Thunell, R., Astor, Y.M., 2017. Seasonal Trends and Inter-Individual Heterogeneity: A multi-species record of Mg, Sr, Ba, & Mn in Planktic Foraminifera from the Modern Cariaco Basin.

De Vleeschouwer, D., Peral, M., Marchegiano, M., Füllberg, A., Meinicke, N., Pälike, H., Auer, G., Petrick, B., Snoeck, C., Goderis, S., Claeys, P., 2022. Plio-Pleistocene Perth Basin

water temperatures and Leeuwin Current dynamics (Indian Ocean) derived from oxygen and clumped-isotope paleothermometry. Clim. Past 18, 1231–1253. https://doi.org/10.5194/cp-18-1231-2022

Dekens, P.S., Lea, D.W., Pak, D.K., Spero, H.J., 2002. Core top calibration of Mg/Ca in tropical foraminifera: Refining paleotemperature estimation. Geochem. Geophys. Geosystems 3, 1–29. https://doi.org/10.1029/2001GC000200

Dickson, A.G., Sabine, C.L., Christian, J.R., Bargeron, C.P., North Pacific Marine Science Organization (Eds.), 2007. Guide to best practices for ocean CO2 measurements, PICES special publication. North Pacific Marine Science Organization, Sidney, BC.

Dragonfly, 2022.

Duplessy, J.C., Bé, A.W.H., Blanc, P.L., 1981. Oxygen and carbon isotopic composition and biogeographic distribution of planktonic foraminifera in the Indian Ocean. Palaeogeogr. Palaeoclimatol. Palaeoecol., Oxygen and Carbon Isotopes in Foraminifera 33, 9–46. https://doi.org/10.1016/0031-0182(81)90031-6

Eggins, S., De Deckker, P., Marshall, J., 2003. Mg/Ca variation in planktonic foraminifera tests: implications for reconstructing palaeo-seawater temperature and habitat migration. Earth Planet. Sci. Lett. 212, 291–306. https://doi.org/10.1016/S0012-821X(03)00283-8

Elderfield, H., Ganssen, G., 2000. Past temperature and δ18O of surface ocean waters inferred from foraminiferal Mg/Ca ratios. Nature 405, 442–445. https://doi.org/10.1038/35013033

Epstein, S., Buchsbaum, R., Lowenstam, A., Urey, H.C., 1953. Revised Carbonate-Water Isotopic Temperature Scale. Bull. Geol. Soc. Am. 64, 1315–1326.

Fehrenbacher, J.S., Martin, P.A., 2014. Exploring the dissolution effect on the intrashell Mg/Ca variability of the planktic foraminifer Globigerinoides ruber. Paleoceanography 29, 854–868. https://doi.org/10.1002/2013PA002571

Fehrenbacher, J.S., Russell, A.D., Davis, C.V., Gagnon, A.C., Spero, H.J., Cliff, J.B., Zhu, Z., Martin, P., 2017. Link between light-triggered Mg-banding and chamber formation in the planktic foraminifera Neogloboquadrina dutertrei. Nat. Commun. 8, 15441. https://doi.org/10.1038/ncomms15441

Garcia, H.E., Boyer, T.P., Baranova, O.K., Locarnini, R.A., Mishonov, A.V., Grodsky, A., Paver, C.R., Weathers, K.W., Smolyar, I.V., Reagan, J.R., Seidov, D., Zweng, M.M., 2019. WOA 2018.

Gray, W.R., Evans, D., Henehan, M., Weldeab, S., Lea, D.W., Müller, W., Rosenthal, Y., 2023. Sodium incorporation in foraminiferal calcite: An evaluation of the Na/Ca salinity proxy and evidence for multiple Na-bearing phases. Geochim. Cosmochim. Acta 348, 152–164. https://doi.org/10.1016/j.gca.2023.03.011

Hemleben, C., Spindler, M., Anderson, O.R., 1989. Taxonomy and Species Features, in: Hemleben, C., Spindler, M., Anderson, O.R. (Eds.), Modern Planktonic Foraminifera. Springer, New York, NY, pp. 8–32. https://doi.org/10.1007/978-1-4612-3544-6_2

Huang, B., Liu, C., Banzon, V., Freeman, E., Graham, G., Hankins, B., Smith, T., Zhang, H.-M., 2021. Improvements of the Daily Optimum Interpolation Sea Surface Temperature (DOISST) Version 2.1 in: Journal of Climate Volume 34 Issue 8 (2021). Am. Meteorol. Soc. 34, 2923–2939.

Iwasaki, S., Kimoto, K., Kucera, M., 2023. Development of a Deep-Water Carbonate Ion Concentration Proxy Based on Preservation of Planktonic Foraminifera Shells Quantified by X-Ray CT Scanning. Paleoceanogr. Paleoclimatology 38, e2022PA004601. https://doi.org/10.1029/2022PA004601

Jentzen, A., Nürnberg, D., Hathorne, E.C., Schönfeld, J., 2018. Mg / Ca and δ^{18}O in living planktic foraminifers from the

Caribbean, Gulf of Mexico and Florida Straits. Biogeosciences 15, 7077–7095. https://doi.org/10.5194/bg-15-7077-2018

John, C.M., Bowen, D., 2016. Community software for challenging isotope analysis: First applications of 'Easotope' to clumped isotopes. Rapid Commun. Mass Spectrom. 30, 2285–2300. https://doi.org/10.1002/rcm.7720

Johnstone, H.J.H., Schulz, M., Barker, S., Elderfield, H., 2010. Inside story: An X-ray computed tomography method for assessing dissolution in the tests of planktonic foraminifera. Mar. Micropaleontol. 77, 58–70. https://doi.org/10.1016/j.marmicro.2010.07.004

Johnstone, H.J.H., Yu, J., Elderfield, H., Schulz, M., 2011. Improving temperature estimates derived from Mg/Ca of planktonic foraminifera using X-ray computed tomography–based dissolution index, XDX. Paleoceanography 26. https://doi.org/10.1029/2009PA001902

Keir, R.S., 1980. The dissolution kinetics of biogenic calcium carbonates in seawater. Geochim. Cosmochim. Acta 44, 241–252. https://doi.org/10.1016/0016-7037(80)90135-0

Lastam, J., Griesshaber, E., Yin, X., Rupp, U., Sánchez-Almazo, I., Heß, M., Walther, P., Checa, A., Schmahl, W.W., 2023. Patterns of crystal organization and calcite twin formation in planktonic, rotaliid, foraminifera shells and spines. J. Struct. Biol. 215, 107898. https://doi.org/10.1016/j.jsb.2022.107898

Lea, D.W., Martin, P.A., Pak, D.K., Spero, H.J., 2002. Reconstructing a 350ky history of sea level using planktonic Mg/Ca and oxygen isotope records from a Cocos Ridge core. Quat. Sci. Rev., EPILOG 21, 283–293. https://doi.org/10.1016/S0277-3791(01)00081-6

Lea, D.W., Mashiotta, T.A., Spero, H.J., 1999. Controls on magnesium and strontium uptake in planktonic foraminifera determined by live culturing. Geochim. Cosmochim. Acta 63, 2369–2379. https://doi.org/10.1016/S0016-7037(99)00197-0

Lucarelli, J.K., Carroll, H.M., Ulrich, R.N., Elliott, B.M., Coplen, T.B., Eagle, R.A., Tripati, A., 2023. Equilibrated Gas and Carbonate Standard-Derived Dual (Δ47 and Δ48) Clumped Isotope Values. Geochem. Geophys. Geosystems 24, e2022GC010458. https://doi.org/10.1029/2022GC010458

McCorkle, D.C., Martin, P.A., Lea, D.W., Klinkhammer, G.P., 1995. Evidence of a dissolution effect on benthic foraminiferal shell chemistry: d13C, Cd/Ca, Ba/Ca, and Sr/Ca results from the Ontong Java Plateau. Paleoceanography 10, 699–714.

Meinicke, N., Ho, S.L., Hannisdal, B., Nürnberg, D., Tripati, A., Schiebel, R., Meckler, A.N., 2020. A robust calibration of the clumped isotopes to temperature relationship for foraminifers. Geochim. Cosmochim. Acta 270, 160–183. https://doi.org/10.1016/j.gca.2019.11.022

Meinicke, N., Reimi, M.A., Ravelo, A.C., Meckler, A.N., 2021. Coupled Mg/Ca and Clumped Isotope Measurements Indicate Lack of Substantial Mixed Layer Cooling in the Western Pacific Warm Pool During the Last ∼5 Million Years. Paleoceanogr. Paleoclimatology 36, e2020PA004115. https://doi.org/10.1029/2020PA004115

Mekik, F., François, R., 2006. Tracing deep-sea calcite dissolution: Agreement between the Globorotalia menardii fragmentation index and elemental ratios (Mg/Ca and Mg/Sr) in planktonic foraminifers. Paleoceanography 21. https://doi.org/10.1029/2006PA001296

Mekik, F., Raterink, L., 2008. Effects of surface ocean conditions on deep-sea calcite dissolution proxies in the tropical Pacific. Paleoceanography 23. https://doi.org/10.1029/2007PA001433

Mucci, A. (1983). The solubility of calcite and aragonite in seawater at various salinities, temperatures, and one atmosphere total pressure. *American Journal of Science*, *283*(7), 780–799. https://doi.org/10.2475/ajs.283.7.780

Mucci, A., Morse, J.W., 1984. The solubility of calcite in seawater solutions of various magnesium concentration, It = 0.697 m at 25 °C and one atmosphere total pressure. Geochim. Cosmochim. Acta 48, 815–822. https://doi.org/10.1016/0016-7037(84)90103-0

Naviaux, J.D., Subhas, A.V., Dong, S., Rollins, N.E., Liu, X., Byrne, R.H., Berelson, W.M., Adkins, J.F., 2019. Calcite dissolution rates in seawater: Lab vs. in-situ measurements and inhibition by organic matter. Mar. Chem. 215, 103684. https://doi.org/10.1016/j.marchem.2019.103684

Naviaux, J. D., Subhas, A. V., Rollins, N. E., Dong, S., Berelson, W. M., & Adkins, J. F. (2019). Temperature dependence of calcite dissolution kinetics in seawater. *Geochimica et Cosmochimica Acta*, *246*, 363–384. https://doi.org/10.1016/j.gca.2018.11.037

Nouet, J., Bassinot, F., 2007. Dissolution effects on the crystallography and Mg/Ca content of planktonic foraminifera Globorotalia tumida (Rotaliina) revealed by X-ray diffractometry. Geochem. Geophys. Geosystems 8. https://doi.org/10.1029/2007GC001647

Olsen, A., Lange, N., Key, R.M., Tanhua, T., Álvarez, M., Becker, S., Bittig, H.C., Carter, B.R., Cotrim da Cunha, L., Feely, R.A., van Heuven, S., Hoppema, M., Ishii, M., Jeansson, E., Jones, S.D., Jutterström, S., Karlsen, M.K., Kozyr, A., Lauvset, S.K., Lo Monaco, C., Murata, A., Pérez, F.F., Pfeil, B., Schirnick, C., Steinfeldt, R., Suzuki, T., Telszewski, M., Tilbrook, B., Velo, A., Wanninkhof, R., 2019. GLODAPv2.2019 – an update of GLODAPv2. Earth Syst. Sci. Data 11, 1437–1461. https://doi.org/10.5194/essd-11-1437-2019

Paquette, J., Reeder, R.J., 1990. New type of compositional zoning in calcite: Insights into crystal-growth mechanisms. Geology 18, 1244–1247.

Peral, M., Daëron, M., Blamart, D., Bassinot, F., Dewilde, F., Smialkowski, N., Isguder, G.,

Bonnin, J., Jorissen, F., Kissel, C., Michel, E., Vázquez Riveiros, N., Waelbroeck, C., 2018. Updated calibration of the clumped isotope thermometer in planktonic and benthic foraminifera. Geochim. Cosmochim. Acta 239, 1–16. https://doi.org/10.1016/j.gca.2018.07.016

Piasecki, A., Bernasconi, S.M., Grauel, A.-L., Hannisdal, B., Ho, S.L., Leutert, T.J., Marchitto, T.M., Meinicke, N., Tisserand, A., Meckler, N., 2019. Application of Clumped Isotope Thermometry to Benthic Foraminifera. Geochem. Geophys. Geosystems 20, 2082–2090. https://doi.org/10.1029/2018GC007961

Procter, F.A., Piazolo, S., John, E.H., Walshaw, R., Pearson, P.N., Lear, C.H., Aze, T., 2024. Electron backscatter diffraction analysis unveils foraminiferal calcite microstructure and processes of diagenetic alteration. Biogeosciences 21, 1213–1233. https://doi.org/10.5194/bg-21-1213-2024

Regenberg, M., Nürnberg, D., Steph, S., Groeneveld, J., Garbe-Schönberg, D., Tiedemann, R., Dullo, W.-C., 2006. Assessing the effect of dissolution on planktonic foraminiferal Mg/Ca ratios: Evidence from Caribbean core tops. Geochem. Geophys. Geosystems 7. https://doi.org/10.1029/2005GC001019

Regenberg, M., Regenberg, A., Garbe-Schönberg, D., Lea, D.W., 2014. Global dissolution effects on planktonic foraminiferal Mg/Ca ratios controlled by the calcite-saturation state of bottom waters. Paleoceanography 29, 127–142. https://doi.org/10.1002/2013PA002492

Rippert, N., Nürnberg, D., Raddatz, J., Maier, E., Hathorne, E., Bijma, J., Tiedemann, R., 2016. Constraining foraminiferal calcification depths in the western Pacific warm pool. Mar. Micropaleontol. 128, 14–27. https://doi.org/10.1016/j.marmicro.2016.08.004

Rosenthal, Y., Boyle, E.A., Slowey, N., 1997. Temperature control on the incorporation of

magnesium, strontium, fluorine, and cadmium into benthis foraminifera shells from Little Bahama Bank: Prospects for thermocline paleoceanography. Geochim. Cosmochim. Acta 61, 3633–3643.

Rosenthal, Y., Lohmann, G.P., 2002. Accurate estimation of sea surface temperatures using dissolution-corrected calibrations for Mg/Ca paleothermometry. Paleoceanography 17, 16-1-16–6. https://doi.org/10.1029/2001PA000749

Rosenthal, Y., Lohmann, G.P., Lohmann, K.C., Sherrell, R.M., 2000. Incorporation and preservation of Mg in Globigerinoides sacculifer: implications for reconstructing the temperature and 18O/16O of seawater. Paleoceanography 15, 135–145. https://doi.org/10.1029/1999PA000415

Russell, A.D., Emerson, S., Nelson, B.K., Erez, J., Lea, D.W., 1994. Uranium in foraminiferal calcite as a recorder of seawater uranium concentrations. Geochim. Cosmochim. Acta 58, 671–681. https://doi.org/10.1016/0016-7037(94)90497-9

Russell, A.D., Hönisch, B., Spero, H.J., Lea, D.W., 2004. Effects of seawater carbonate ion concentration and temperature on shell U, Mg, and Sr in cultured planktonic foraminifera. Geochim. Cosmochim. Acta 68, 4347–4361. https://doi.org/10.1016/j.gca.2004.03.013

Sadekov, A., Eggins, S.M., Deckker, P.D., Ninnemann, U., Kuhnt, W., Bassinot, F., 2009. Surface and subsurface seawater temperature reconstruction using Mg/Ca microanalysis of planktonic foraminifera Globigerinoides ruber, Globigerinoides sacculifer, and Pulleniatina obliquiloculata. Paleoceanography 24. https://doi.org/10.1029/2008PA001664

Sadekov, A.Yu., Eggins, S.M., De Deckker, P., 2005. Characterization of Mg/Ca distributions in planktonic foraminifera species by electron microprobe mapping. Geochem. Geophys.

Geosystems 6. https://doi.org/10.1029/2005GC000973

Sadekov, A.Yu., Eggins, S.M., Klinkhammer, G.P., Rosenthal, Y., 2010. Effects of seafloor and laboratory dissolution on the Mg/Ca composition of *Globigerinoides sacculifer* and *Orbulina universa* tests — A laser ablation ICPMS microanalysis perspective. Earth Planet. Sci. Lett. 292, 312–324. https://doi.org/10.1016/j.epsl.2010.01.039

Schauble, E.A., Ghosh, P., Eiler, J.M., 2006. Preferential formation of 13C–18O bonds in carbonate minerals, estimated using first-principles lattice dynamics. Geochim. Cosmochim. Acta 70, 2510–2529. https://doi.org/10.1016/j.gca.2006.02.011

Schiebel, R., Hemleben, C., 2017. Planktic Foraminifers in the Modern Ocean. Springer Berlin Heidelberg, Berlin, Heidelberg. https://doi.org/10.1007/978-3-662-50297-6

Schmidt, D.N., Thomas, E., Authier, E., Saunders, D., Ridgwell, A., 2018. Strategies in times of crisis—insights into the benthic foraminiferal record of the Palaeocene–Eocene Thermal Maximum. Philos. Trans. R. Soc. Math. Phys. Eng. Sci. 376, 20170328. https://doi.org/10.1098/rsta.2017.0328

Schmuker, B., Schiebel, R., 2002. Planktic foraminifers and hydrography of the eastern and northern Caribbean Sea. Mar. Micropaleontol. 46, 387–403. https://doi.org/10.1016/S0377-8398(02)00082-8

Schott, J., Brantley, S., Crerar, D., Guy, C., Borcsik, M., Willaime, C., 1989. Dissolution kinetics of strained calcite. Geochim. Cosmochim. Acta 53, 373–382. https://doi.org/10.1016/0016-7037(89)90389-X

Shackleton, N.J., Opdyke, N.D., 1973. Oxygen Isotope and Palaeomagnetic Stratigraphy of Equatorial Pacific Core V28-238: Oxygen Isotope Temperatures and Ice Volumes on a 10^5 Year and 10^6 Year Scale. Quat. Res. 3, 39–55. https://doi.org/10.1016/0033-5894(73)90052-5

Spero, H.J., Eggins, S.M., Russell, A.D., Vetter, L., Kilburn, M.R., Hönisch, B., 2015. Timing and mechanism for intratest Mg/Ca variability in a living planktic foraminifer. https://doi.org/10.1016/j.epsl.2014.10.030

Steinhardt, J., de Nooijer, L.L.J., Brummer, G.-J., Reichart, G.-J., 2015. Profiling planktonic foraminiferal crust formation. Geochem. Geophys. Geosystems 16, 2409–2430. https://doi.org/10.1002/2015GC005752

Subhas, A. V., Rollins, N. E., Berelson, W. M., Dong, S., Erez, J., & Adkins, J. F. (2015). A novel determination of calcite dissolution kinetics in seawater. *Geochimica et Cosmochimica Acta*, *170*, 51–68. https://doi.org/10.1016/j.gca.2015.08.011

Subhas, A.V., Rollins, N.E., Berelson, W.M., Erez, J., Ziveri, P., Langer, G., Adkins, J.F., 2018. The dissolution behavior of biogenic calcites in seawater and a possible role for magnesium and organic carbon. Mar. Chem. 205, 100–112. https://doi.org/10.1016/j.marchem.2018.08.001

Tripati, A.K., Eagle, R.A., Thiagarajan, N., Gagnon, A.C., Bauch, H., Halloran, P.R., Eiler, J.M., 2010. 13C–18O isotope signatures and 'clumped isotope' thermometry in foraminifera and coccoliths. Geochim. Cosmochim. Acta 74, 5697–5717. https://doi.org/10.1016/j.gca.2010.07.006

Tripati, A.K., Sahany, S., Pittman, D., Eagle, R.A., Neelin, J.D., Mitchell, J.L., Beaufort, L., 2014. Modern and glacial tropical snowlines controlled by sea surface temperature and atmospheric mixing. Nat. Geosci. 7, 205–209. https://doi.org/10.1038/ngeo2082

Upadhyay, D., Lucarelli, J., Arnold, A., Flores, R., Bricker, H., Ulrich, R.N., Jesmok, G., Santi, L., Defliese, W., Eagle, R.A., Carroll, H.M., Bateman, J.B., Petryshyn, V., Loyd, S.J., Tang, J., Priyadarshi, A., Elliott, B., Tripati, A., 2021. Carbonate clumped isotope analysis (Δ47) of 21 carbonate standards determined via gas-source isotope-ratio mass

spectrometry on four instrumental configurations using carbonate-based standardization and multiyear data sets. Rapid Commun. Mass Spectrom. 35, e9143. https://doi.org/10.1002/rcm.9143

Urey, H.C., 1947. The thermodynamic properties of isotopic substances. J Chem Soc 562–581. https://doi.org/10.1039/JR9470000562

van Dijk, I., Mouret, A., Cotte, M., Le Houedec, S., Oron, S., Reichart, G.-J., Reyes-Herrera, J., Filipsson, H.L., Barras, C., 2019. Chemical Heterogeneity of Mg, Mn, Na, S, and Sr in Benthic Foraminiferal Calcite. Front. Earth Sci. 7. https://doi.org/10.3389/feart.2019.00281

Van Heuven, S., Pierrot, D., Rae, J. W. B., Lewis, E., & Wallace, D. W. R. (2011, September). CO2SYS v 1.1, MATLAB program developed for CO2 system calculations (Version 1.1). U.S. Department of Energy, Oak Ridge, Tennessee.: Carbon Dioxide Information Analysis Center, Oak Ridge National Laboratory.

Vanadzina, K., Schmidt, D.N., 2022. Developmental change during a speciation event: evidence from planktic foraminifera. Paleobiology 48, 120–136. https://doi.org/10.1017/pab.2021.26

Walter, L.M., Morse, J.W., 1985. The dissolution kinetics of shallow marine carbonates in seawater: A laboratory study. Geochim. Cosmochim. Acta 49, 1503–1513. https://doi.org/10.1016/0016-7037(85)90255-8

Weiner, A.K.M., Weinkauf, M.F.G., Kurasawa, A., Darling, K.F., Kucera, M., 2015. Genetic and morphometric evidence for parallel evolution of the *Globigerinella calida* morphotype. Mar. Micropaleontol. 114, 19–35. https://doi.org/10.1016/j.marmicro.2014.10.003

Wycech, J.B., Kelly, D.C., Kitajima, K., Kozdon, R., Orland, I.J., Valley, J.W., 2018. Combined

Effects of Gametogenic Calcification and Dissolution on δO Measurements of the Planktic Foraminifer. Geochem. Geophys. Geosystems 19, 4487–4501. https://doi.org/10.1029/2018GC007908

Zarkogiannis, S.D., Iwasaki, S., Rae, J.W.B., Schmidt, M.W., Mortyn, P.G., Kontakiotis, G., Hertzberg, J.E., Rickaby, R.E.M., 2022. Calcification, Dissolution and Test Properties of Modern Planktonic Foraminifera From the Central Atlantic Ocean. Front. Mar. Sci. 9. https://doi.org/10.3389/fmars.2022.864801

Zeebe, R.E., 1999. An explanation of the effect of seawater carbonate concentration on foraminiferal oxygen isotopes. Geochim. Cosmochim. Acta 63, 2001–2007. https://doi.org/10.1016/S0016-7037(99)00091-5

Chapter 3: Clumped Isotope Constraints on Subtropical Atlantic Ocean Warming, Hydrology, and Proxy Bias at the Paleocene-Eocene Thermal Maximum

H. Tandy, M. Guillermic, M. Tharpe, S. Zheng, G. Toranzo, S. Nguyen, L. Avila, C. Ulloa, R. Eagle, J. Zachos, C. Kelly, A. Tripati

Abstract

The Paleocene-Eocene Thermal Maximum (PETM) is associated with a large carbon input into the ocean-atmosphere system and geologically rapid temperature rise, making this interval of interest as an analogue for anthropogenic climate change. However, temperature estimates from proxies such as $\delta^{18}O$ and Mg/Ca are confounded by uncertainties relating to seawater composition and impacts of secondary effects and diagenesis. We apply the clumped isotope proxy (Δ_{47}) to samples from Site 1263 on Walvis Ridge (ODP Leg 208) in the subtropical Atlantic Ocean and reconstruct PETM sea surface temperatures (SSTs) and seawater $\delta^{18}O$. Δ_{47} data support Late Paleocene SSTs of ~18.8 °C and a minimum warming of 3-4 °C. If secondary effects are considered (e.g., recrystallization, dissolution), then baseline SSTs increase to ~20.5 °C with a PETM warming of ~7 °C. Absolute SSTs are intermediate to published estimates from Mg/Ca and foraminiferal $\delta^{18}O$, and the Δ_{47}-temperature anomalies are larger than other proxies. These differences can largely be reconciled if non-thermal effects on Mg/Ca and $\delta^{18}O$ are considered. We also show that at Site 1263, estimates of SSTs and warming derived from Δ_{47} and from multi-proxy averages (ΔT = 5.9 °C) are in broad agreement with climate model predictions for $3xCO_2$ and $6xCO_2$, if non-thermal effects are included.

1. Introduction:

Climate proxies indicate the late Paleocene and Early Eocene were the warmest times of the past 66 Ma. Global temperatures were ~13 °C warmer than pre-industrial conditions in the late Paleocene (Tierney et al., 2022), while greenhouse gas concentrations have been estimated to be 650 and 850 ppmv, 2.3-3 times pre-industrial concentrations (CenCO2PIP, 2023). Within this greenhouse interval, the Paleocene-Eocene Thermal Maximum (PETM) was a hyperthermal characterized by geologically rapid warming resulting from major changes in the carbon cycle ~55.8 million years ago (CenCO2PIP, 2023; Zachos et al., 2001). The PETM is defined by a negative carbon isotope excursion (CIE) in sedimentary records (Zachos et al., 2003), indicating large fluxes of ^{12}C-enriched carbon into the atmosphere and oceans, most likely in the form of methane and/or carbon dioxide, over a period of about 10,000 years (Gutjahr et al., 2017; Zachos et al., 2003; Zeebe et al., 2009). The hypothesized source(s) of carbon include volcanism, methane hydrates, and/or other reduced reservoirs (DeConto et al., 2012; Dickens et al., 1995; Gutjahr et al., 2017; Higgins and Schrag, 2006). Due to the pace and probable cause of the warming, the PETM has been often cited as the closest historical analogue to modern-day climate change (Gingerich, 2019; Meissner et al., 2014; Ridgwell and Schmidt, 2010; Zeebe and Zachos, 2013).

For this reason, model-proxy data comparisons for the late Paleocene and early Eocene have become increasingly relevant as a tool for assessing the ability of climate models to accurately simulate responses to elevated greenhouse conditions (Hollis et al., 2019; Huber and Sloan, 2001; Lunt et al., 2017; Pagani et al., 2013; Tierney et al., 2022) and for model parameterization (Sagoo et al., 2013; Zhu et al., 2019). However, there are discrepancies between model-proxy comparisons for the PETM (e.g. Huber and Caballero, 2011; Lunt et al., 2021, 2017), and between existing proxy reconstructions for the PETM (Dunkley Jones et al., 2013;

Hollis et al., 2019). The extent to which deep-time proxy reconstructions are impacted by variations in seawater chemistry, vital effects, and diagenetic processes, is also unclear (e.g., Zeebe, 2001; Uchikawa and Zeebe, 2010; Hollis et al., 2019).

Thus, this study utilizes a novel temperature proxy, clumped isotopes (Δ_{47}), in a combination of planktic foraminiferal and coccolith-dominated calcite at Ocean Drilling Program (ODP) Site 1263 on Walvis Ridge in the South Atlantic to develop reconstructions of sea surface temperatures (SSTs) for the PETM. While the Δ_{47}-proxy for temperature also has sources of uncertainty (Tripati et al., 2010, 2015; Bernasconi et al., 2021; Clark et al., 2024; Daëron and Gray, 2023; Chapter 1, 2), it is independent from changes in seawater Mg/Ca and $\delta^{18}O$, and there is no evidence for species specificity in foraminifera (Meinicke et al., 2020; Tripati et al., 2010). As such, the proxy is being increasingly used for temperature reconstructions for past time periods (e.g. Anagnostou et al., 2020; Drury and John, 2016; Leutert et al., 2019; Meckler et al., 2022). Sample size requirements, however, have restricted foraminiferal-based SST reconstructions using clumped isotopes (Tripati et al., 2014; Anagnostou et al., 2020; Evans et al., 2018; Leutert et al., 2019). For this reason, some studies have begun to examine coccolith-derived calcite for temperature reconstructions (Clark et al., 2024; Drury and John, 2016; Katz et al., 2017).

PETM sections from Walvis Ridge that were recovered during DSDP Leg 74 have been examined using other proxies to estimate SSTs. Previously, estimates of SST for DSDP Site 527 were derived from planktic $\delta^{18}O$ (Thomas et al., 1999), and Mg/Ca (Tripati and Elderfield, 2004). While absolute SSTs from $\delta^{18}O$ are cooler than those from Mg/Ca, PETM temperature anomalies are similar (~3.2 °C for $\delta^{18}O$ and ~3 °C for Mg/Ca) (Dunkley Jones et al., 2013; Thomas et al., 1999; Tripati and Elderfield, 2004). However, changes in the calibrations used and

assumptions within the calculations alter both the absolute SSTs and PETM anomalies that are calculated, for each of these proxy systems. For example, the $\delta^{18}O$ temperature estimates at Site 527 originally published by Thomas et al. (1999) assume higher $\delta^{18}O_{sw}$ at this site than more recent studies that have reprocessed this data. Thomas et al. (1999) used a $\delta^{18}O_{sw}$ of -0.2 ‰ VSMOW that was based on using the modern offset of 0.8 ‰ from mean ocean values, while Hollis et al. (2019) used a $\delta^{18}O_{sw}$ of -0.53 ‰ VSMOW, which in turn reduces $\delta^{18}O$-temperature by ~ 1°C. pH effects can influence planktic $\delta^{18}O$ (Spero et al., 1997; Bijma et al., 1998, 1999; Zeebe, 1999) and are hypothesized to impact $\delta^{18}O$ temperatures from planktic foraminifera by up to 3°C the PETM (Uchikawa and Zeebe, 2010) and 2-4 °C in the Cretaceous (Zeebe et al., 2001). Similarly, for Mg/Ca, early Cenozoic paleotemperature estimates will be sensitive to assumptions about Mg/Ca_{sw} (e.g. Hines et al., 2017; Lear et al., 2000), and to pH changes (Evans et al., 2016; Lea et al., 1999; Russell et al., 2004). Dunkley-Jones et al. (2013) used Mg/Ca data from Tripati and Elderfield (2004) and estimated a PETM warming of 3.0 °C. However, Hollis et al. (2019) calculated a warming of 0.7 °C, using the same primary data but also accounting for pH change across the event.

To independently assess SSTs at Walvis Ridge, we determined Δ_{47} in planktic foraminifera, and in fine-fraction (coccolith-dominated) carbonate. We calculated temperatures and assessed the potential impacts of material type, recrystallization, and dissolution, and reported a reconstruction that factors in these potential sources of uncertainty. We compared Δ_{47}-temperatures to other proxy data and tested for systematic biases in each. We compared the results to Deep-Time Model Intercomparison Project (DeepMIP) ensemble runs for three times and six times pre-industrial CO_2 concentrations with early Eocene topography, which are available for the CESM1.2 CAM5 and GFDL CM2.1 models (Lunt et al., 2021). To facilitate

comparison with models and other DeepMIP data (Hollis et al., 2019), data were grouped into different intervals (Late Paleocene - 55.93 - 56.05 Ma; peak-PETM - 55.82- 55.89 Ma; Post-PETM - 55.50 - 55.82 Ma; EECO - 51 - 53 Ma).

2. Methods:

2.1 Site Description:

Site 1263 has an estimated paleodepth of 1500 m (Zachos et al., 2004). Changes in dissolution are well-constrained at the site, with evidence that it was below the carbonate lysocline during the Late Paleocene and just below the carbonate compensation depth during the initial portion of the PETM (Zachos et al., 2005, 2004). The 2 km shoaling of the carbonate compensation depth along Walvis Ridge is marked by reductions in carbonate percentages in the clay layer of the PETM onset at this site and other sites in the region (Zachos et al., 2005).

The section contains an expanded (>1 m) PETM interval, with the onset marked by a 5 cm clay layer (Zachos et al., 2004). A higher clay content during the PETM and lower porosity should be more conducive to lower rates of recrystallization compared to other deep-sea sections (Zachos et al., 2004), though foraminiferal tests are still frosty in texture suggesting some recrystallization has occurred (Leutert et al., 2019).

The paleolatitude of Site 1263 is estimated at 41.0937 °S (Hinsbergen et al., 2015; paleolatitude.org), based on the paleomagnetic reference frame of Vaes et al. (2023) (Figure 1). The paleodepth of this site is estimated at 1500 m for the early Eocene (Zachos et al., 2005). The CENOGRID age model for the Cenozoic was used (Westerhold et al., 2020).

2.2 Sample types:

64 samples of planktic foraminifera and 53 samples of fine fraction from ODP Site 1263 that span the late Paleocene through early Eocene were prepared and analyzed for clumped isotopes. Sediment samples were wet sieved with deionized water to 63 µm. Coarse fractions sediment (>63 µm) was then further sieved to 125 µm and 212 µm.

Planktic foraminifera from the genus *Morozovella,* and *Acarinina* were picked from each sample. 300 specimens per genus from the >212 µm size fraction were picked, when available, so several replicates could be measured for Δ_{47}. If the sample lacked sufficient specimens from the larger size fractions, specimens from smaller size fractions (>125 and >63 µm) were also picked for clumped isotope analysis. An additional ~ 100 specimens of the species *Acarinina soldadoensis* were picked for Mg/Ca.

Fine fraction sediment (<63 µm) is primarily composed of coccolith plates (See Supplemental Figures 3.S.1-3.S.3), and can also contain foraminiferal fragments, clays, and siliceous material at various percentages depending on the samples (Supplemental Figures 3.S.1-3.S.3) (Zachos et al, 2005).

2.3 Sample Preparation for Δ_{47}:

For planktic foraminiferal samples, specimens were cleaned to remove potential contaminants. Specimens were placed in 1.5 ml vials and ultrasonicated with deionized water for 3 intervals of 5 seconds. After sonication the supernatant was removed and samples were dried overnight at 40 °C (< 50 °C). Specimens were then powdered by gently crushing the foraminifera within weigh paper with a pestle and placed back into the vials until they were ready to be weighed and run.

For fine fraction sediment, approximately 20 mg of sample were cleaned for organics by adding dilute (3%) H_2O_2 to the sediment for ~3 hours. The sediment was then rinsed three times with deionized water and left to dry overnight at 40 °C (< 50 °C). Samples were then powdered with a mortar and pestle and collected for weighing.

2.4 Measurement Procedure for Δ_{47}:

This study reports 687 analyses of 140 samples on multiple clumped isotope instruments in the Eagle-Tripati Lab at UCLA. Machine configurations are described in detail in Lucarelli et al. (2023). All data is reported in the I-CDES reference frame (Bernasconi et al., 2021) and was processed using the software Easotope (John and Bowen, 2016).

Briefly, most samples were run on one of three Nu Perspective Dual inlet mass spectrometers with secondary electron suppression (described in Lucarelli et al., 2023; Upadhyay et al., 2021). These instruments were run under Nu Perspective configuration 1a, with a minimum of 5 replicates at 0.35 – 0.48 mg (or equivalent carbonate percentage) analyzed, if sufficient material was present. With this configuration, samples are digested through custom-built common acid bath systems with 105% phosphoric acid held at 90 °C. Carbonate standards ETH-1 and ETH-2 were used for a non-linearity correction. ETH-1, ETH-2, ETH-3, CMTile, Carmel Chalk, Veinstrom, TV_ST and TV_BT were run as standards for the Empirical Transfer Function (ETF) (Chapter 2, Lucarelli et al., 2023; Upadhyay et al., 2021).

A small number of samples were run on a Thermo MAT 253 configuration described in prior publications (Lucarelli et al., 2023; Upadhyay et al., 2021). Samples weighing 5-6 mg were digested in a custom-built common acid bath system with 105% phosphoric acid held at 90 °C. Carbonate standards ETH-1 and ETH-2 and heated and non-heated gas standards with varying

composition were used for non-linearity corrections (Lucarelli et al., 2023). ETH-1, ETH-2, ETH-3, ETH-4, CMTile, Carmel Chalk, TV_ST, TV_BT, and Veinstrom were used for the ETF (Chapter 2; Lucarelli et al., 2023; Upadhyay et al., 2021).

2.5 Quality control for Δ_{47}:

Data quality control criteria are similar to what was reported by Lucarelli et al. (2023), Meinicke et al. (2020), Parvez et al. (2023), Upadhyay et al. (2021). Briefly, data are screened based on instrument source stability, leaks in the acid digestion system, and data quality of standards during correction intervals as described in Parvez et al. (2023). Replicates with incomplete gas transfer and Δ_{47}, $\delta^{13}C$, and $\delta^{18}O$ values that fall outside of a SD range of ±0.5‰ for $\delta^{13}C$ and $\delta^{18}O$ and ±0.05‰ for Δ_{47} were flagged. Of analyses conducted for this study, 687 replicates were included, and 27 flagged replicates excluded.

2.6 Mg/Ca analyses:

Mg/Ca analysis was performed on eight samples from Site 1263 on the species *A. soldadoensis*. Approximately 100 individuals of *A. soldadoensis* were picked in the >212 um size fraction for analysis. Samples were cleaned using published procedures (Barker et al., 2003). Briefly, samples were gently cracked open between two glass plates and rinsed with MQ water and methanol for clays. An oxidative step was performed followed by dilute acid leach before full sample dissolution into solution for measuring. Samples were measured on the Quadrupole ICP-MS (Agilent 8900) at the University of Southern California Dornsife PLASMA Facility.

2.7 Temperature reconstructions

2.7.1 Clumped Isotopes

Δ_{47} averages for samples were calculated and converted to temperature using the calibration of Anderson et al. (2021), that is similar to the all foraminifera calibration from Chapter 1. The equation used is:

$$\Delta_{47(ICDES)} = 0.0391 \pm 0.0004 \times 10^6/T^2 + 0.154 \pm 0.004 \quad \text{Equation 1}$$

where T is the temperature in K and $\Delta_{47(ICDES)}$ is the clumped isotope value in the I-CDES reference frame (Anderson et al., 2021; Bernasconi et al., 2021). The standard error of the mean is calculated using replicate averages and the uncertainty in the regression is propagated to report an error in reconstructed temperatures (Equation 1) (Supplemental Table 3.S.1). We note that other calibrations including those reported in Chapter 1 result in similar results (Supplemental Table 3.S.2).

2.7.2 $\delta^{18}O$

Carbonate $\delta^{18}O$ values ($\delta^{18}O_{carb}$) are simultaneously determined with Δ_{47}. We use $\delta^{18}O_{carb}$ to estimate temperatures and compare values with Δ_{47}-temperatures. We also combine $\delta^{18}O_{carb}$ with Δ_{47}-temperatures to estimate $\delta^{18}O_{SW}$. The modified equation of Kim and O'Neil (1997) from Bemis et al. (1998) is used for these calculations.

$$T = 16.1\text{-}4.64(\delta^{18}O_{carb}\text{-}\delta^{18}O_{SW}) + 0.09(\delta^{18}O_{carb}\text{-}\delta^{18}O_{SW})^2 \quad \text{Equation 2}$$

Where T is the temperature in Celsius, $\delta^{18}O_{carb}$ is the measured value from the carbonate (VPDB) and $\delta^{18}O_{SW}$ is the estimated value in seawater (VPDB). Values were converted from VPDB to

VSMOW by adding 0.27 ‰. Values for $\delta^{18}O_{SW}$ for Site 1263 that were initially used are from Hollis et al. (2019), with an estimated ice-free global $\delta^{18}O_{SW}$ of -0.89 ‰ (VSMOW) from Cramer et al. (2011).

2.7.3 Mg/Ca

Temperatures from Mg/Ca analyses were calculated using the equation of Hines et al. (2017).

$$T = \ln\left(\frac{\left[Mg/Ca_{shell}\right] \times \left[Mg/Ca_{sw}^{t=0}\right]^{H}}{B \times \left[Mg/Ca_{sw}^{t=1}\right]^{H}}\right) \times \frac{1}{A}$$

Equation 3

Mg/Ca_{shell} is the measured ratio in mmol/mol, $Mg/Ca_{sw}^{t=0}$ is the modern Mg/Ca of seawater at 5.17 mol/mol and $Mg/Ca_{sw}^{t=1}$ is the Mg/Ca of seawater in the Early Eocene, which is estimated at 2.24 mol/mol (Evans et al., 2018). *A* and *B* are calibration constants (*A*=0.09, *B*= 0.38) from Anand et al. (2003). We use an *H*-factor of 0.42 based on modern culture studies of *G. sacculifer* given that no *H*-factor has yet been calculated for the species *A. soldadoensis* (Hasiuk and Lohmann, 2010).

2.8 Non-thermal influences on D47

2.8.1 Taxonomic differences

Recent work indicates that foraminiferal taxa do not exhibit offsets (e.g. Chapter 1; Daëron and Gray, 2023; Meinicke et al., 2020), but that coccoliths and foraminifera may have small but significant offsets in Δ_{47} (Clark et al., 2024). An offset of 0.008 ‰ from experiments has been reported (Clark et al., 2024). An average offset of 0.006 ‰ between fine fraction and

foraminifera that was found in the data from this study for Site 1263 is applied to the data when correcting for non-thermal influences on the reconstruction.

2.8.2 Dissolution effects

There is evidence that intense dissolution can impact the Δ_{47} of planktic foraminifera (Chapter 1, 2). An average offset of 0.010 ‰ is observed in core-top samples from above and below the saturation horizon. Therefore, we apply a dissolution correction of 0.010 ‰ to PETM samples from Site 1263.

2.8.3 Recrystallization effects

A prior study examined the potential impacts of recrystallization on the Δ_{47} of Middle Eocene planktic foraminifera at multiple sites, including Site 1263, and found that for this proxy, similar to $\delta^{18}O$ and Mg/Ca, recrystallization biases temperatures toward colder values (Leutert et al., 2019). Estimates for recrystallization amounts at tropical open ocean sites in the late Paleocene and early Eocene have suggested 5-10 % recrystallization (Site 1209, Pacific, Dutton et al., 2005) and 15-50 % recrystallization (Site 865, Equatorial Pacific, Kozdon et al., 2013, 2011). Given the clay-rich nature of the PETM succession at this site (Zachos et al., 2004; Kelly et al., 2010), and associated better preservation, we assume 10% recrystallization in the main text and use the Leutert et al. (2019) non-linear mixing model for corrections to Δ_{47}. We examine the potential effects of larger amounts of recrystallization in the supplement. For these calculations, we use R version 4.2.1 (R Core Team, 2022).

Briefly, the non-linear mixing model incorporates nonlinear mixing effects on Δ_{47}. In cases where the $\delta^{13}C$ and $\delta^{18}O$ differ between primary calcite and diagenetic calcite by less than

2 ‰, nonlinear mixing effects are unlikely to significantly influence $\Delta_{47;}$ however, $\delta^{13}C$ and $\delta^{18}O$ differences of >2 ‰ would potentially induce non-linearity in calculations (Defliese and Lohmann, 2015). In the case of downcore variability, such as PETM anomalies, non-linear effects could dampen the temperature change during calculations of recrystallization impacts from clumped isotopes (Leutert et al., 2019).

For this work, secondary calcite $\delta^{18}O$ values are assumed to be similar to benthic $\delta^{18}O$, and we use benthic data from Site 1263 from Westerhold et al. (2020). The Δ_{47} composition of the diagenetic endmember calcite used in the mixing model is taken from the average Δ_{47} of benthic foraminifera from Meckler et al. (2022), with late Paleocene and Eocene temperatures updated using the Anderson et al. (2021) calibration (14.6 °C), which is similar to values of early Eocene temperatures from Mg/Ca (Laurenano et al. 2018). Benthic Mg/Ca data suggest that during the PETM, there was ~ 4 °C of warming on Walvis Ridge (Tripati, 2005; Tripati and Elderfield, 2004), which would have also impacted early diagenetic calcites, so we adjust the Meckler et al. (2022) values to account for this. We estimate the $\delta^{13}C$ of secondary calcite using the approach of Leutert et al. (2019), who assume it is the same as the fine fraction composition, with values estimated from a LOESS smoothing regression through the $\delta^{13}C$ of fine fraction data with a span of 0.2.

2.8.4 Carbonate ion effect on calcification

In Chapter 1, a small benthic carbonate ion effect of 0.0001 ‰ / µmol/kg $\Delta[CO_3^{2-}]$ was reported. pH effects are reported in planktic foraminifera on oxygen isotopes and a study on corals suggested that Δ_{47} values could be impacted similarly due to DIC speciation (Spero et al., 1997; Tripati et al., 2015; Zeebe, 1999). The response for Δ_{47} in benthics from Chapter 1,

however, is in the opposite direction of the theorized relationship of Δ_{47} with pH, so it is likely not controlled by the same processes as the pH effect in oxygen isotopes. As a carbonate ion/pH effect on Δ_{47} in planktic foraminifera has not been described, we do not include it in the results and discussion, but we do briefly discuss the possible scope of effects here and in more detail in the supplement.

If such an effect does exist for planktic foraminifera, with a similar sensitivity to benthic foraminifera, then estimates of late Paleocene temperatures for Site 1263 would tend to decrease, and calculated peak PETM temperatures could be an additional ~1 °C degrees cooler than late Paleocene estimates. These calculations assume background values of surface water $\Delta[CO_3^{2-}]$ were lower than today (Anagnostou et al., 2016; Gutjahr et al., 2017; Penman et al., 2014; Uchikawa and Zeebe, 2010), and that PETM values were lowered by ~45 (μmol/kg) $\Delta[CO_3^{2-}]$.

2.9 Non-thermal effects on $\delta^{18}O_{carb}$ and Mg/Ca

Non-thermal effects on $\delta^{18}O$ and Mg/Ca estimates of temperature are discussed in detail in the supplement.

Recrystallization in sediments tends to bias all proxies towards cooler temperatures, however Mg/Ca is thought to be more resilient against recrystallization in semi-closed systems (Staudigal et al., 2022). We therefore apply a recrystallization correction of 10 % similar to Δ_{47} for $\delta^{18}O$ only.

A pH correction to carbonate $\delta^{18}O$ values is explored in the discussion given there have been studies of pH impacts on planktic foraminiferal $\delta^{18}O$ values (Zeebe, 2001, 1999), including for the PETM (Uchikawa and Zeebe, 2010). A 1.42 ‰/unit pH correction is applied where ΔpH

of 0.5 units is assumed in the late Paleocene and early Eocene, and a ΔpH of 0.8 units is assumed for the PETM interval (Anagnostou et al., 2016; Gutjahr et al., 2017; Penman et al., 2014; Uchikawa and Zeebe, 2010). Similar to Δ_{47}, a dissolution correction is applied to $\delta^{18}O$ values during the PETM calculated as the mean offset between samples above and below the carbonate saturation horizon in Chapter 2 of 0.30 ‰.

Mg/Ca ratios in planktic foraminifera have also been found to be sensitive to changes in surface water pH (Evans et al., 2016; Gray et al., 2018; Russell et al., 2004). A correction for pH is explored in the discussion where Mg/Ca has a pH correction where $Mg/Ca_{corrected} = (1 - (8.05 - pH) \times 0.7) \times Mg/Ca_{uncorrected}$ (Evans et al., 2016; Hollis et al., 2019). This leads to estimates of surface water pH of 7.7 for the late Paleocene and early Eocene, and pH values for the PETM of 7.4. A dissolution correction is also applied to Mg/Ca values during the PETM calculated as the mean offset between samples above and below the carbonate saturation horizon in Chapter 2 of -0.54 ‰.

Dissolution corrections are also applied to both $\delta^{18}O$ and Mg/Ca values over the PETM. We subtract 0.30 ‰ from $\delta^{18}O$ and add 0.54 mmol/mol to Mg/Ca values based on anomalies from above to below the carbonate saturation horizon using data from Chapter 2.

2.10 Statistical analyses

Comparisons between sample archives and proxy reconstructions from the same samples are done using paired t-tests. Comparison between means use Welch's t-tests. All statistical analyses were performed in R version 4.2.1 (R Core Team, 2022) except for model skill score performed in Python 3. Skill score is defined as a model's skill in capturing anomalies from a null hypothesis, in our case three times CO_2/late Paleocene temperatures, where a score of 1

reflects a perfect model, a score of 0 that the new model and null hypothesis perform equally well, and a negative score reflects a model error greater than that of the null hypothesis (see Hargreaves et al., 2013; Lora and Ibarra, 2019).

3. Results and Discussion

Figure 3.2 shows the time series of Δ_{47}-temperatures for the PETM at Site 1263 if we assume there are no non-thermal influences on Δ_{47}, and Table 3.1 reports means for different time intervals. The planktic foraminiferal Δ_{47} data for *Morozovella* and *Acarinina* at Site 1263 yield statistically indistinguishable results (paired t-test, n=10, $p = 0.36$), while the fine fraction Δ_{47} data are elevated relative to foraminiferal samples by 0.006 ‰ (n=42, $p < 0.01$), corresponding to a temperature difference that average ~2 °C (Table 3.1). These results are consistent with recently published studies of modern systematics that indicate fractionation factors for different species of mixed-layer foraminifera are not discernibly different (e.g. Chapter 1; Daëron and Gray, 2023; Meinicke et al., 2020), while coccoliths, which make up the majority of carbonate in fine fraction sediment, may be offset by ~0.008 ‰ (Clark et al., 2024). In these samples, $\delta^{18}O_{carb}$ values are higher in fine fraction sediment by an average of 0.32 ‰ (Table 3.1, Supplemental Table 3.S.1).

Taken at face value, the clumped isotope data for Site 1263 would support Late Paleocene SSTs of ~18.8 °C and a minimum warming of 3-4 °C. In Table 3.1 and Figure 3.2, we also show results of temperature calculations that use simple models for interpreting $\delta^{18}O_{carb}$ and Mg/Ca (i.e., that spatial gradients in $\delta^{18}O_{sw}$ have not changed from present, that no proxy is substantively impacted by dissolution or recrystallization). In this scenario, the Δ_{47} data support absolute SSTs that are elevated by about 3 °C compared to $\delta^{18}O$-calcification temperatures, and a

smaller magnitude of warming than inferred from $\delta^{18}O$ (5-7 °C). The absolute SSTs are almost 10 °C cooler than Mg/Ca temperatures, with a similar magnitude of warming estimated using the two proxies (~3-4 °C).

While each of these proxies could be perfect indicators of temperature, it is more likely they each are susceptible to systematic biases. Briefly, we present the impact of three corrections to the Δ_{47}-temperature record that are described in detail in the supplemental information. The first correction is based on the 0.006 ‰ offset between foraminiferal and fine fraction Δ_{47} values. The second correction applied accounts for recrystallization (Luetert et al., 2019). To this end, we assume 10 % recrystallization as a minimum estimate of recrystallization. Finally, the third correction step accounts for increased dissolution across the PETM. This site is thought to have been positioned well above the lysocline, except for during the PETM when the carbonate saturation horizon shoaled by ~2 km (Zachos et al., 2005). We apply the mean correction from Chapter 2 above to below the carbonate saturation horizon of 0.010 ‰ and subtract this value from samples over the PETM. Uncertainties involving these corrections and other impacts to the Δ_{47} are discussed further in the supplementary text.

When non-thermal impacts on Δ_{47} are considered, we reconstruct a baseline Late Paleocene SST of ~20.5 °C and peak PETM SST of ~27 °C. This reconstruction indicates a PETM warming of ~7 °C (Table 3.2; Figure 3.3). The largest effect is from considering the impact of dissolution at the PETM; other non-thermal impacts on the reconstruction are estimated to be minimal (Figure 3.3). In this case, the Δ_{47} data would support a change in temperature that is nearly double most published estimates (Figure 3.3; Table 3.2, Supplemental Table 3.S.4). Figure 3.4 shows that absolute SSTs estimated from Δ_{47}, when factoring in non-

thermal influences, also cannot be reconciled with $\delta^{18}O_{carb}$ and Mg/Ca temperatures (from nearby Site 527), if the latter are interpreted using relatively simple models for proxy systematics.

Prior work on the PETM has reported that discrepancies between $\delta^{18}O$ -based and Mg/Ca based reconstructions occur, even when the effects of pH on Mg/Ca, and changes in seawater $\delta^{18}O$ gradients on carbonate $\delta^{18}O$-based SSTs, are taken into account (Hollis et al., 2019; Figures 3.3, 3.4). The new data from this study for Site 1263 show that for the late Paleocene through the early Eocene, it is difficult to reconcile different carbonate-based proxy reconstructions, unless non-thermal influences are taken into account for each proxy.

If we assume that only Δ_{47}-temperatures are impacted by non-thermal effects, we can not resolve these discrepancies (Figures 3.3, 3.4). For example, Δ_{47}-temperatures increase by 6.7 °C (Figure 3.3). This 6.7 °C PETM temperature anomaly is slightly larger than the 4.7 °C anomaly calculated from $\delta^{18}O$ values from *Acarinina* for Site 1263 or the pooled 6.0 °C anomaly from $\delta^{18}O$ values using all archives when we assume constant $\delta^{18}O_{sw}$ across the PETM and no changes in spatial gradients in $\delta^{18}O_{sw}$ (Figure 3.3). Upper estimates of temperature change for nearby DSDP Site 527 on Walvis Ridge from Mg/Ca also are smaller (3.1 °C for *M. subbotinae*, 2.4 °C for *A. soldadoensis*); the same is true for $\delta^{18}O$ (3.2 °C for *Acarinina spp.*) (Figure 3.4, Dunkley Jones et al., 2013; Hollis et al., 2019). Some differences might be expected between the two sites on Walvis Ridge, as ODP Site 1263 has an expanded record that captures more of the PETM than Site 527, and because it is a shallower site (~1500 m compared to ~3400 m) and should have experienced less dissolution (Zachoes et al., 2004; Thomas et al., 1999).

Absolute SSTs from Δ_{47} also differ from other proxies. Δ_{47}-temperatures that factor into account non-thermal influences are 20.5 °C for the Late Paleocene and 27.3 °C at the PETM (Figure 3.4), both of which are lower than those estimates from Mg/Ca data both at Site 1263

(Figure 3.2, Supplemental Table 3.S.3) and Site 527 recalculated with estimates of Mg/Ca concentrations for the Early Eocene from Cramer et al. (2011) (Figure 3.4) (Cramer et al., 2011; Dunkley Jones et al., 2013; Hollis et al., 2019; Tripati and Elderfield, 2004). Mg/Ca temperatures for the Late Paleocene average 29.4 °C at Site 1263 (Table 3.1) and 28.5 °C at Site 527, which is ~8 °C warmer than Δ_{47}-temperatures (Figure 3.4, Supplemental Tables 3.S.2-3.S.4). The absolute Δ_{47}-temperatures over the study interval are higher than the $\delta^{18}O$-temperatures from site 1263 by an average of 3.3 °C (Figure 3.3, Table 3.1, Supplemental Table 3.S.2, 3.S.4).

3.1 Reconciling carbonate-based proxies for SST for the PETM

If all of the proxy calculations for SSTs on Walvis Ridge assume non-thermal effects were significant for the PETM, both absolute values and temperature anomalies are more readily reconciled (Figure 3.5). Specifically, recrystallization, pH, and dissolution effects on $\delta^{18}O$ and Mg/Ca in planktic foraminifera have been reported (Brown and Elderfield, 1996; Evans et al., 2016; Gray et al., 2018; Gray and Evans, 2019; Rohling et al., 2024; Rosenthal and Lohmann, 2002; Russell et al., 2004; Spero et al., 1997; Staudigel et al., 2022; Zeebe, 2001, 1999). These effects have potentially large impacts on temperature estimates for the PETM (Uchikawa and Zeebe, 2010; Hollis et al., 2019).

A 10 % recrystallization correction is applied to $\delta^{18}O$ similar to Δ_{47} (Section 2.9). The recrystallization correction raises average temperatures ~0.3 °C. This correction is not applied to Mg/Ca estimates as Mg/Ca is thought to be more robust to small recrystallization effects in semi-closed systems (Staudigel et al., 2022).

A pH effect tends to increase $\delta^{18}O$ with decreasing pH, biasing temperature estimates toward colder values due to variations in partitioning of $\delta^{18}O$ in carbonate ion species on water

(Spero et al., 1997; Zeebe et al., 1999, 2001). In foraminifera, this effect has been shown to vary by species but is approximately 1.42 ‰ $\delta^{18}O$ / unit of pH change in planktic foraminifera though it is more uncertain below pH values of 8 (Spero et al., 1997; Uchikawa and Zeebe, 2010; Zeebe et al., 1999, 2001).

For Mg/Ca, reduced pH during the PETM is thought to also result in overestimated temperatures from Mg/Ca, as lab studies have found that for ~0.1 unit decrease in pH is associated with a temperature overestimate of 1 °C (Gray and Evans, 2019). Various Mg/Ca calibrations attempt to correct for this term by having a correction for pH when proxy data for pH is available, but similar to $\delta^{18}O$ this relationship at pHs lower than 7.7 like those estimated across the PETM is uncertain (see discussion in Hollis et al., 2019; Evans et al., 2016; Gray et al., 2018; Russell et al., 2004).

Applying a pH correction increases $\delta^{18}O$-based temperatures (Section 2.9), with an average offset of only 1.6 °C between $\delta^{18}O$-based temperatures and Δ_{47}-temperatures at Site 1263. A pH effect on Mg/Ca-temperatures (Section 2.9) would reduce Mg/Ca temperatures by ~ 5 °C and bring them closer to Δ_{47}-temperatures (Figure 3.6, Table 3.2). Offsets between the two proxy datasets range from 0 to 5 °C.

Dissolution corrections can also be applied to $\delta^{18}O$ and Mg/Ca records over the PETM as dissolution also affects these proxies. The dissolution correction raises temperatures over the PETM by ~1.5 °C for $\delta^{18}O$, and ~ 2.1 °C for Mg/Ca.

Corrected values with the 10 % recrystallization ($\delta^{18}O$ only) and a pH correction and dissolution correction on both $\delta^{18}O$ and Mg/Ca are shown in Figure 3.5.

3.2 Implications of Δ_{47}-temperatures for Paleogene seawater $\delta^{18}O$

With Δ_{47}-temperatures, we can calculate $\delta^{18}O_{sw}$ by combining results with $\delta^{18}O_{carb}$. $\delta^{18}O_{sw}$ estimates that utilize the Δ_{47}-temperatures which factor in non-thermal effects, and consider the impacts of pH on $\delta^{18}O_{carb}$, are shown in Figure 3.5. Uncorrected values are presented in Supplemental Table 3.S.2.

Average $\delta^{18}O_{sw}$ values for the record at Site 1263 are -0.27 ‰ VSMOW. This value is higher than what is estimated assuming the same latitudinal gradients in $\delta^{18}O_{sw}$ existed during the early Cenozoic as at present. A latitudinally-adjusted estimate of $\delta^{18}O_{sw}$ for ice-free conditions in this region would be -0.53 ‰ VSMOW (Hollis et al., 2019), or ~ -1 ‰ VSMOW (Tindall et al., 2010). The $\delta^{18}O_{sw}$ values calculated using Mg/Ca-based temperatures are higher than the ones from Δ_{47} (Figure 3.5B). Higher mean values for Site 1263 than would be otherwise estimated by modern latitudinal gradients could reflect enhanced evaporation rates in the region overall due to **a**n intensified hydrologic cycle, potentially due to increased global temperatures and/or facilitated by paleogeography and broader paleo-atmospheric circulation patterns.

During the PETM, the reconstructed $\delta^{18}O_{sw}$ values for Site 1263 decrease at the onset of the PETM, and then increase to an intermediate level, before recovering to values more similar to the late Paleocene baseline (Figure 3.5B). This initial reduction in $\delta^{18}O_{sw}$ could reflect shifts in the hydrologic cycle over this mid-latitude site with decreased evaporative rates and/or increased precipitation initially during the PETM.

3.3 A closer look at the patterns of warming and seawater $\delta^{18}O$ changes during the PETM at Site 1263

If trends in the Δ_{47}-based reconstructions of temperature and seawater $\delta^{18}O$ in Figure 3.5 are discussed, we would infer that an increase in SSTs of ~ 2.6 °C at the onset of the carbon isotope excursion (~55.93 Ma) was associated with a decrease in subtropical surface water seawater $\delta^{18}O$ of 1.4 ‰. This drop could correspond to a change in salinities of ~ -9.2 ppt if using the modern relationship of 0.15 ‰/ppt salinity (Fairbanks, 1982), which may reflect enhanced subtropical precipitation relative to evaporation. While SSTs continued to rise, reconstructed subtropical surface water $\delta^{18}O$ values increased, implying increased net evaporation. Even as SSTs declined after the recovery from the PETM, net evaporation may have continued to increase slightly. A caveat is that the exact amplitude of changes in $\delta^{18}O_{sw}$ are sensitive to the specific histories of pH and other corrections used for calculations.

3.4 Comparison of warming estimates to climate records

Given that multiple independent proxy estimates for SSTs converge with Δ_{47}-temperatures at Walvis Ridge, we compared Δ_{47}-temperatures and the multi-proxy average to model output from the DeepMIP database. The DeepMIP working group (Lunt et al., 2017) has recommended using DeepMIP standard simulations of $3xCO_2$ (3 times pre-industrial levels; 840 ppmv) for the pre-PETM, and $6xCO_2$ (~1680 ppmv) or $12xCO_2$ (~3360 ppmv) simulations for the PETM. Recently published proxy-based estimates for CO_2 during the Late Paleocene range from 650 to 850 ppmv, which is roughly 2.3-$3xCO_2$, while estimates of CO_2 during the PETM range from ~1500 to ~2800 ppmv, corresponding to 5.4 to $10xCO_2$ (CenCO2PIP, 2023). Thus, we compare results to simulations from DeepMIP that have both $3xCO_2$ and $6xCO_2$ archived,

which at present are from the CESM1.2 CAM5 and GFDL CM2.1 models (Lunt et al., 2021; Zhu et al., 2019).

Overall, changes in SSTs (temperature anomalies) calculated using data for the late Paleocene and PETM at Site 1263 align well with model estimates for the mid-Atlantic (Figures 3.3 and 3.7). Model skill scores evaluated against the Δ_{47}-anomaly of 6.7 °C are positive, with GFDL CM2.1 in slightly better agreement with the data (0.659) than CESM1.2 CAM5 (0.534). If an average temperature anomaly is calculated using all three proxies, with non-thermal effects considered (multi-proxy anomaly = 5.9 °C with the single point Mg/Ca temperature from the end of the excursion included in the PETM mean, or 6.1 °C with it excluded) and used to calculate skill score, both skill scores remain positive. The GFDL CM1.2 model is still in better agreement with the PETM anomaly than CESM2.1 CAM5 (0.734 and 0.599 respectively with the single point Mg/Ca temperature from the end of the excursion included in the PETM mean or 0.709 and 0.578 respectively with it excluded).

Absolute SSTs in the late Paleocene estimated from Δ_{47} are slightly (~3 °C) cooler than estimates from the 3xCO_2 simulations, and the multi-proxy mean about ~2.5 °C cooler (Δ_{47} SST = 20.3 °C; multi-proxy = 21.9 °C; GFDL CM2.1 = 23.5 °C; CESM1.2 CAM5 = 23.8 °C) (Figure 3.7). For the PETM, absolute SSTs match well for both Δ_{47} and the multi-proxy mean with the 6xCO_2 simulations (Δ_{47} = 27.3 °C for; multi-proxy = 27.8 °C; GFDL CM2.1 = 27.7 °C; 27.3 °C for CESM1.2 CAM5).

However, if uncorrected proxy values are used, there are larger disagreements between proxies, and between the proxies and models. PETM anomalies show a large spread for Site 1263 (uncorrected: $\delta^{18}O$ = 15.3 °C, Mg/Ca = 29.4 °C, Δ_{47} = 18.8 °C), similar to what was

previously reported for Site 527 (Hollis et al., 2019) and with a poorer match with the models (GFDL CM2.1 = 23.5 °C; CESM1.2 CAM5 = 23.8 °C). Absolute temperatures for the PETM show a similar pattern (uncorrected: $\delta^{18}O$ = 21.4 °C, Mg/Ca = 32.1 °C, Δ_{47} = 22.5 °C; GFDL CM2.1 = 27.7 °C; 27.3 °C for CESM1.2 CAM5).

4. Conclusion

We reconstruct SSTs and seawater $\delta^{18}O$ for the PETM in the subtropical South Atlantic using clumped isotopes (Δ_{47}). This region is one where prior reconstructions based on different proxies disagree. Here, we show evidence for a PETM warming of ~7 °C from Δ_{47}, and closer agreement with Mg/Ca and $\delta^{18}O$-based SSTs, when non-thermal effects are considered on all proxies, resulting in a multi-proxy estimate of warming of 5.9 °C.

Overall, SSTs for the late Paleocene and PETM at Site 1263 align well with model estimates for the mid-Atlantic (Figures 3.7, 3.8). Model skill scores evaluated against the Δ_{47}-anomalies are positive, with GFDL CM2.1 in slightly better agreement with the data (0.659) than CESM1.2 CAM5 (0.534). If an average temperature anomaly is calculated using all three proxies (Δ T = 6.1 °C) and used to calculate skill score, then the GFDL CM1.2 model is still in better agreement with the PETM anomaly than CESM2.1 CAM5.

Absolute SSTs in the late Paleocene estimated from Δ_{47} are slightly cooler than estimates from the 3xCO2 simulations (Δ_{47} = 20.3 °C for; multi-proxy = 21.9 °C; GFDL CM2.1 = 23.5 °C; CESM1.2 CAM5 = 23.8 °C) (Figure 3.7). Absolute temperatures of PETM are within 1 °C of the 6xCO2 simulations (Δ_{47} = 27.3 °C for; multi-proxy = 27.8 °C; GFDL CM2.1 = 27.7 °C; 27.3 °C for CESM1.2 CAM5).

Acknowledgments

This work was supported by Heising-Simons Foundation grant 2022-3314, DOE BES grant DE-FG02-83613ER16402, the Packard Foundation, and by NSF grants EAR-0949191, EAR-1352212, and RISE-228198. It was also supported by a Royal Society Wolfson Visiting Research Fellowship. We thank B. Elliot, H. Taylor, K. Miguel, and J. Rubi for lab support, and colleague R. Eagle for their support.

Open Research

All data are in the Supplementary information associated with this paper. In addition, on publication, all data will be archived in Pangaea and EarthChem.

5 Figures

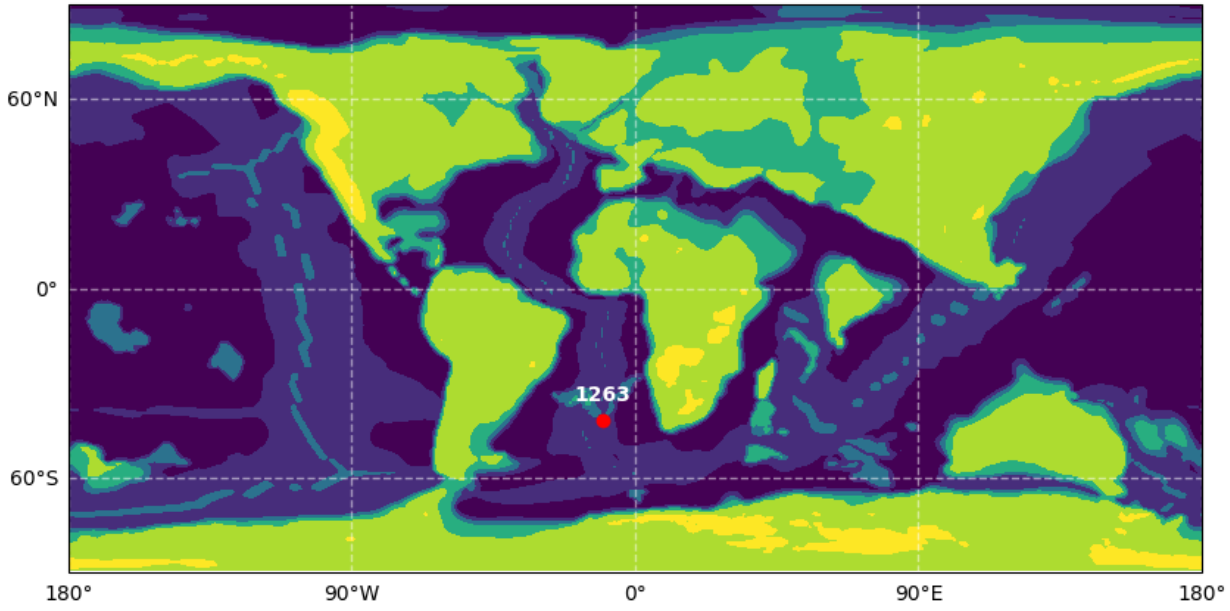

Figure 3.1: Paleogeographic map showing location of ODP Site 1263. The paleolatitude is estimated as 41.1 °S (Hinsbergen et al., 2015). The paleogeographic reconstruction is for the early Eocene and is from Herold et al. (2014).

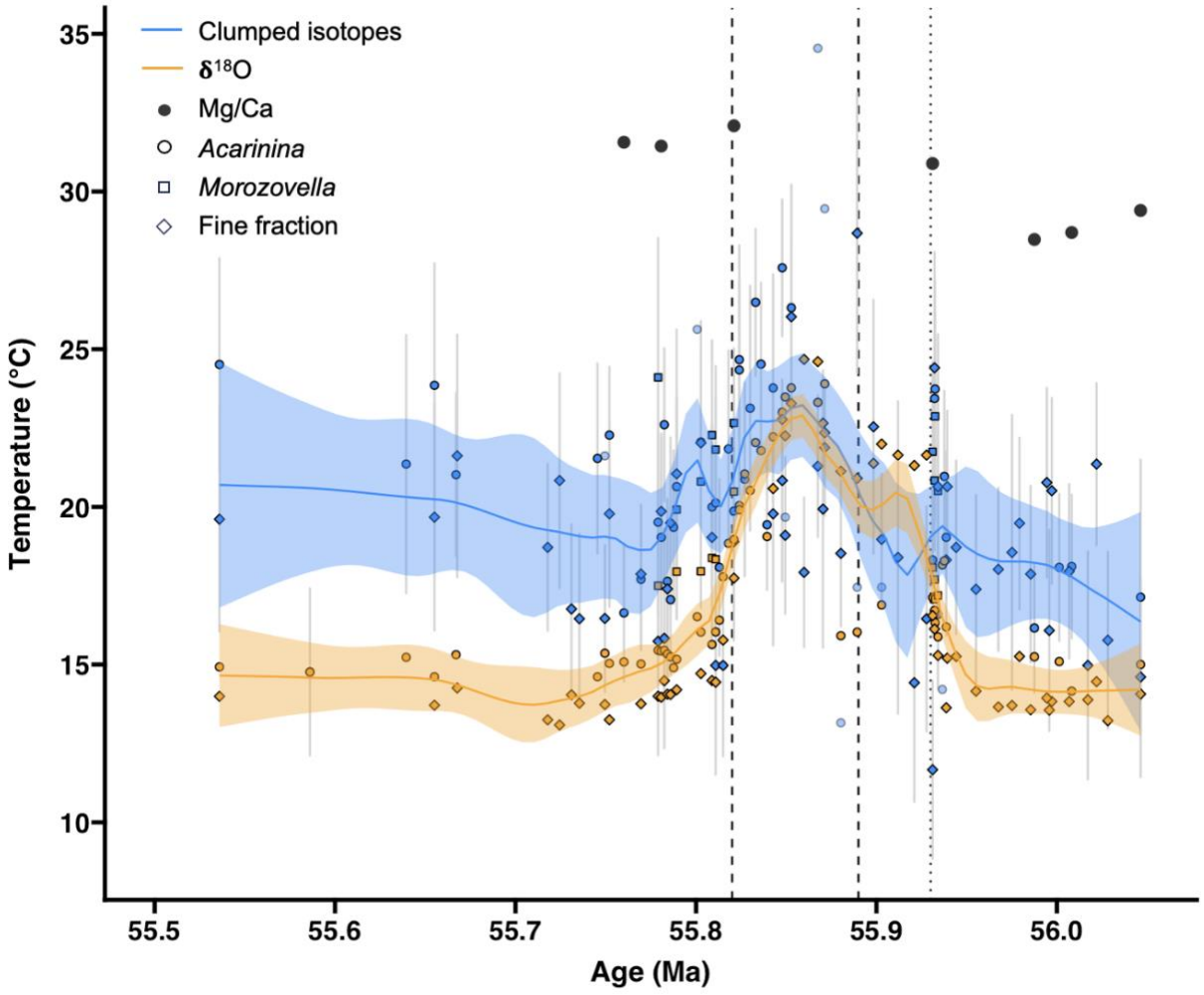

Figure 3.2: Δ_{47}-temperatures for the PETM at Site 1263 compared to temperatures estimated using $\delta^{18}O$ and Mg/Ca data, assuming there are no non-thermal influences on proxies. Dashed vertical lines define the peak of the PETM excursion and the dotted vertical line marks the beginning of the PETM. LOESS regressions through clumped isotope and $\delta^{18}O$ temperature estimates have a span of 0.2 and 95% CI. Points have 1SE error. Δ_{47} data support warmer absolute SSTs and a smaller change during the PETM than inferred from $\delta^{18}O$, based on these assumptions. Faded points are Δ_{47}- temperatures from samples with less than 3 replicates.

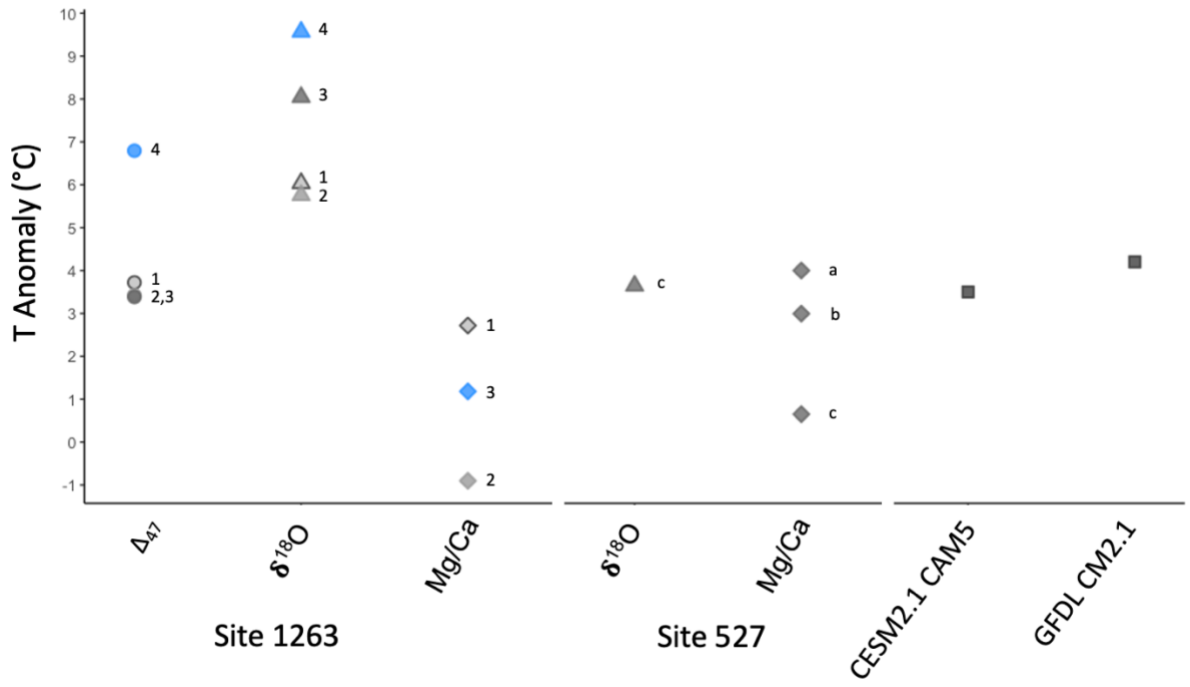

Figure 3.3: PETM warming calculated from different proxies for Walvis Ridge, using different sets of assumptions, and DeepMIP model estimates. Temperature anomalies are defined as PETM minus Late Paleocene values. The numbers next to each symbol reflect the impact of different proxy corrections on reconstructed temperature anomalies. Circles show Δ_{47}-based values with 1) no non-thermal effects considered, 2) fine fraction offset from foraminifera correction 3) same as 2 with a 10 % recrystallization correction, 4) same as 3 with a dissolution correction. Filled blue circle (4) shows the results of assuming there are non-thermal influences on Δ_{47} at Site 1263 and supports a larger amount of warming than other reconstructions. Triangles are $\delta^{18}O$-based values with 1) no non-thermal effects, 2) 10 % recrystallization correction, 3) same as 2 with a pH correction, and 4) same as 3 with a dissolution correction. Diamonds show Mg/Ca-values assuming 1) no non-thermal effects, 2) pH correction, and 3) same as 2 with a dissolution correction. The major non-thermal factor influencing Δ_{47}-temperatures at ODP Site 1263 is the impact of dissolution, as the site was above the lysocline during the Late Paleocene, and near the carbonate compensation depth during the PETM (Zachos et a., 2005). $\delta^{18}O$ as calculated in (a) Hollis et al. (2019), from Thomas et al. (1999) are shown. Warming estimated from Mg/Ca data from (a) Tripati and Elderfield (2004) at DSDP Site 527, (b) recalculated in Dunkley-Jones et al. (2013) (c) and Hollis et al. (2019) are shown. All use the same data but Dunkley-Jones et al. (2013) factors in altered Mg/Ca_{sw} and H-factor, and Hollis et al. (2019) factors in pH effects on Mg/Ca and other non-thermal effects. DeepMIP values are from Lunt et al. (2021) and are based on the difference between $3xCO_2$ and $6xCO_2$ simulations.

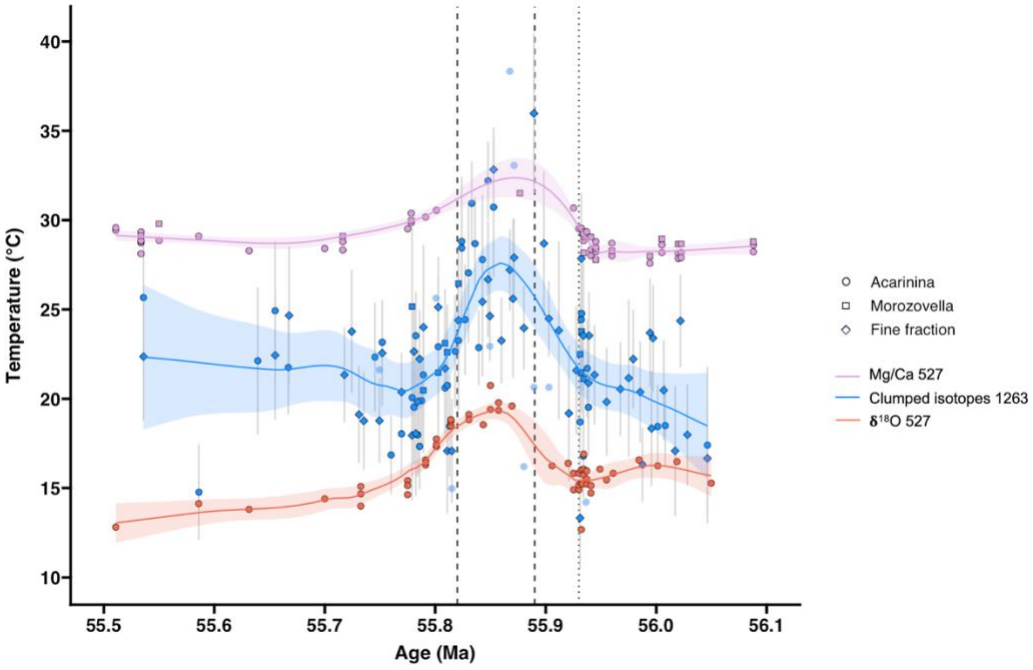

Figure 3.4: Δ_{47}-temperatures for the PETM at ODP Site 1263 that consider non-thermal effects on the reconstruction (blue) compared to published proxy estimates from Mg/Ca (purple) and $\delta^{18}O$ (orange) for nearby Site 527 (Dunkley Jones et al., 2013; Hollis et al., 2019). Δ_{47}-temperature estimates fall between published proxy estimates for absolute temperature on Walvis Ridge. Shapes correspond to sample type (*Acarinina* - circle, *Morozovella* - square, fine fraction - diamond). Faded points represent samples with less than 3 replicates for Δ_{47}. Vertical dashed lines mark the Peak-PETM interval (55.82-55.89 Ma) and the dotted line marks the beginning of the carbon isotope excursion. The lines are LOESS smoothing regressions through all data (span = 0.35, 95% CI error). Errors on points are 1SE.

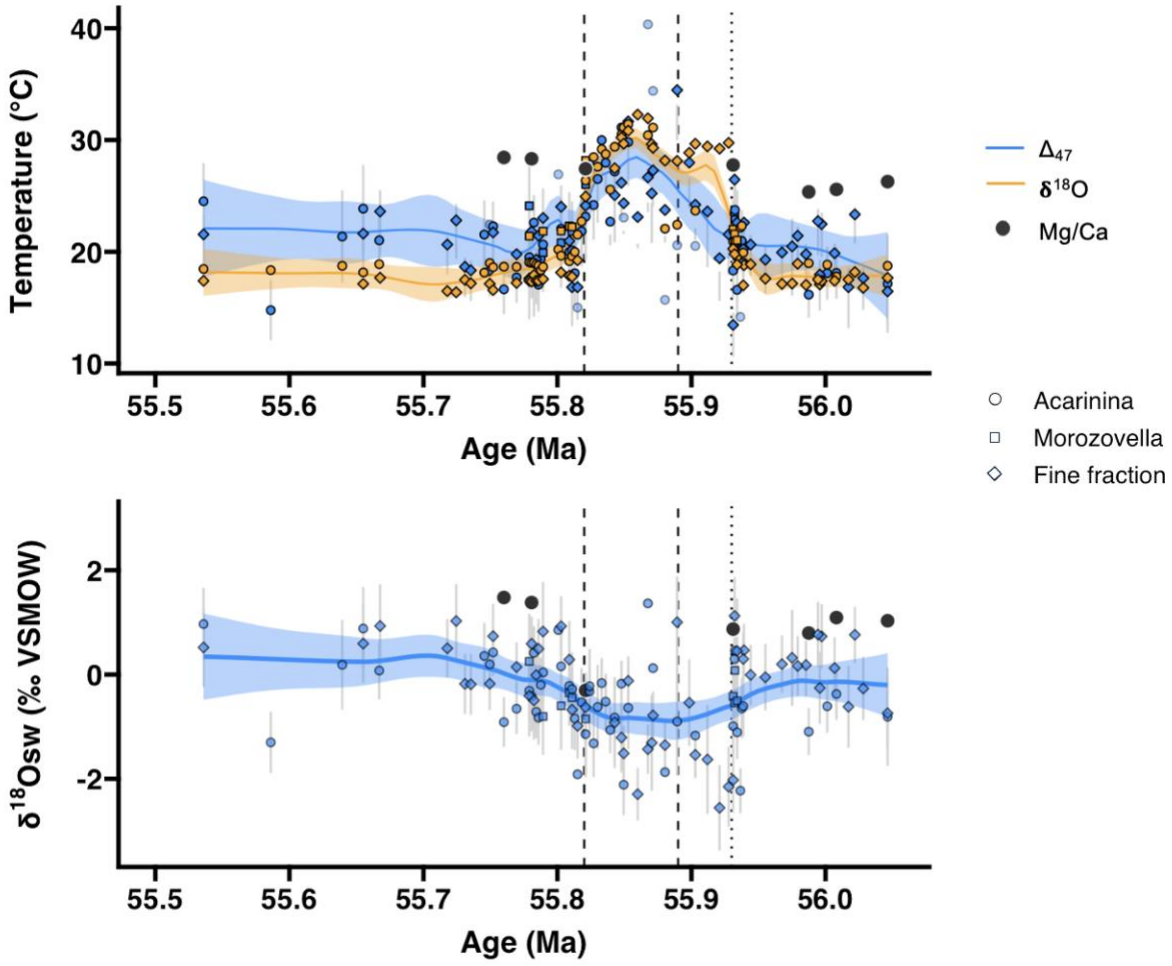

Figure 3.5: Late Paleocene to Early Eocene SSTs and $\delta^{18}O_{sw}$ from Δ_{47}, $\delta^{18}O_{carb}$, and Mg/Ca for Walvis Ridge that show a convergence of values from multiple proxies if non-thermal effects are accounted for. Δ_{47}-temperatures include a 0.006 ‰ correction for offsets between fine fraction and foraminiferal calcite, 10 % recrystallization, and a 0.010 ‰ dissolution correction for the PETM. $\delta^{18}O$-temperatures include the impact of 10 % recrystallization, and both $\delta^{18}O$- and Mg/Ca temperatures factor in a pH correction (pH of 7.4 during the PETM, and 7.7 otherwise). LOESS smoothing with a span of 0.35 and 95% CI shown. Points are for individual samples and show 1SE. Faded circles indicate Δ_{47}-temperatures for samples with less than three replicates.

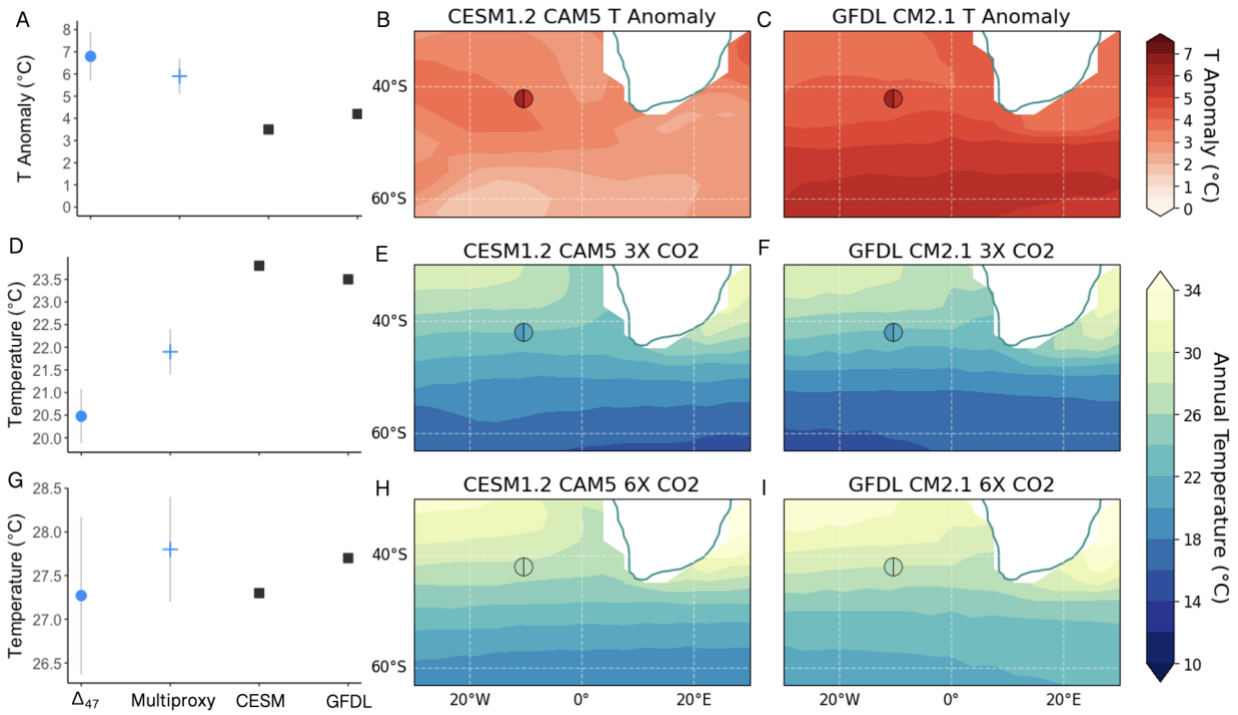

Figure 3.6: Comparison of Δ_{47}-temperatures and multi-proxy averages with DeepMIP model simulations for 3xCO_2 and 6xCO_2. Proxy reconstructions use carbonate-based proxy values from Figure 3.5, with temperatures factoring in non-thermal influences on proxies. A, D, G) show the absolute temperatures or temperature anomalies calculated by different sources with 1 SE error. B, C, E, F, H, I) Left half of the symbol indicates mean Δ_{47}-temperatures for the E, F) Late Paleocene and H, I) PETM or the B, C) temperature anomaly from Δ_{47}-temperatures. The right half of the circles indicates the multiproxy values for the same intervals. 3X simulations are compared to proxy constraints from the late Paleocene, and 6X simulations are compared to PETM values. DeepMIP output is described in Lunt et al. (2021). Model skill score calculated using anomalies are positive in both cases (Δ_{47} only: CESM1.2 CAM5 = 0.534, GFDL CM2.1 = 0.659; multi-proxy: CESM1.2 CAM5 =0.578, GFDL CM2.1 =0.709).

Temperature proxy	Archive	LP (55.93 - 56.05 Ma)				PETM (55.82 - 55.89 Ma)				Post PETM (55.5 - 55.82 Ma)				EECO (51 - 53 Ma)			
		n	analyses	Mean (°C)	SE	n	analyses	Mean (°C)	SE	n	analyses	Mean (°C)	SE	n	analyses	Mean (°C)	SE
Δ_{47}	Foraminifera	15	75	19.4	0.7	17	67	23.4	1.2	29	131	20.3	0.5	3	15	20.8	1.4
	Fine fraction	19	96	18.3	0.7	11	59	21.2	1	21	112	18.5	0.5	2	11	22.2	0.0
$\delta^{18}O$	*Acarinina*	11	53	16.2	0.5	16	61	20.9	0.6	24	108	15.6	0.2	2	9	16.4	0.5
	Morozovella	4	22	17.5	0.2	1	6	20.5		5	23	18	0.2	1	6	15.8	
	Fine fraction	19	96	14.4	0.3	11	59	22.1	0.6	21	112	14.1	0.1	2	14	13.7	0.5
Mg/Ca	*Acarinina soldadoensis*	4	8	29.4	0.3	1	2	32.1		2	4	31.5	0				

Table 3.1: Mean temperatures reconstructed for ODP Site 1263 from different carbonate-based proxies that assume no non-thermal effects and simple models for interpreting $\delta^{18}O_{carb}$ and Mg/Ca (i.e., spatial gradients in $\delta^{18}O_{sw}$ have not changed from present, that no proxy is impacted by dissolution or recrystallization).

Temper-ature proxy	Archive	LP (55.93 - 56.05 Ma)				PETM (55.82 - 55.89 Ma)				Post PETM (55.5 - 55.82 Ma)				EECO (51 - 53 Ma)			
		n	analyses	Mean (°C)	SE	n	analyses	Mean (°C)	SE	n	analyses	Mean (°C)	SE	n	analyses	Mean (°C)	SE
Δ_{47}	*Foraminifera*	15	75	20	0.8	17	67	27.4	1.4	29	131	21.1	0.6	3	15	21.5	1.5
	Fine fraction	19	96	20.9	0.8	11	59	27.1	1.2	21	112	21	0.6	2	11	25.4	0
$\delta^{18}O_{carb}$	*Acarinina*	11	53	21.4	0.4	16	61	26.6	0.7	24	108	19.2	0.2	2	9	20.1	0.6
	Morozovella	4	22	21.4	0.3	1	6	26.6		5	23	21.9	0.2	1	6	19.4	
	Fine fraction	19	96	17.9	0.2	11	59	27.8	0.6	21	112	17.4	0.1	2	14	17	0.6
Mg/Ca	*Acarinina soldadoensis*	4	8	24.4	0.5	1	2	24.1		2	4	26.5	0				

Table 3.2: Mean temperatures reconstructed for ODP Site 1263 from different carbonate-based proxies that assume non-thermal effects on each proxy. Δ_{47} has a 0.006 ‰ correction applied to fine fraction samples, assumes 10 % recrystallization, and a dissolution correction of 0.010 ‰ for the PETM. $\delta^{18}O$ has a 10 % recrystallization correction. Both $\delta^{18}O_{carb}$ and Mg/Ca temperatures have a 1.42 ‰/unit pH correction applied, where ΔpH of 0.5 is assumed outside of the PETM, and a 0.8 pH drop during the PETM. Mg/Ca has a pH correction where $Mg/Ca_{corrected} = (1-(8.05-pH) \times 0.7) \times Mg/Ca_{uncorrected}$ and pH values are defined in the same way as for $\delta^{18}O$. Corrections are described and discussed in Sections 4.1 and 4.2.

Supplemental information

Chapter 3: Clumped Isotope Constraints on Subtropical Atlantic Ocean Warming, Hydrology, and Proxy Bias at the Paleocene-Eocene Thermal Maximum

S1 SEM Methods

Scanning electron microscopy (SEM) was used to image some of the fine fraction sediment from Site 1263. Images were taken at the Ion Microprobe Facility on a Tescan Vega-3 XMU variable-pressure SEM. Samples were poured onto foil sheets and mounted on carbon tape stubs by pressing the tape into the sample on the foil. Samples were then gold coated prior to analysis and imaged at high voltage (20.0 kV) (Figures 3.S.1-3.S.3).

S2 $\delta^{13}C$

Carbon and oxygen isotope results for fine fraction samples composed primarily of coccolith plate and fragmented foraminiferal calcite over our sample interval at Site 1263 align with previous studies (Kelly et al., 2010; Westerhold et al., 2020; Zachos et al., 2004). Comparison with prior study bulk records and global benthic isotope records suggest that our dataset captures the PETM interval and peak $\delta^{13}C$ excursion at this site, as well as a course record over the Early Eocene including the Early Eocene Climatic Optimum (EECO) interval (Figure 3.S.4).

Average Late-Paleocene (LP) $\delta^{13}C$ values (55.93-56.05 Ma) for the genus *Acarinina* are 2.69 ‰ and decrease to a minimum of -0.75 ‰ at the peak of the PETM excursion followed by a recovery to background levels approximately 150,000 years following the peak of the CIE (Figure 3.S.4, Table 3.S.1). Carbon isotopes gradually decrease throughout the Early Eocene reaching an average minimum of 1.65 ‰ around the EECO (averaged between 51-53 Ma). Fine

fraction sediment has an average LP value of 2.15 ‰ and reaches a minimum of -0.93 ‰ over the PETM. $\delta^{13}C$ offsets between the foraminiferal genera and between the foraminifera and the fine fraction are thought to be a result of vital effects such as those associated with photosynthesis (see Schiebel and Hemleben, 2017). The average offset between *Acarinina* and the fine fraction is 0.68 ‰ and between *Acarinina* and *Morozovella* is -0.78 ‰. The largest variability in these offsets are for samples with low replicate counts (< 3 replicates) over the beginning of the PETM interval (Figure 3.S.4, Table 3.S.1).

S3 Discussion of corrections and other uncertainties

S3.1 Archive type

Two distinct carbonate material sample types were used for clumped isotope analysis at Site 1263: foraminiferal calcite from two genera of planktic foraminifera and fine fraction sediment. Differences in isotopic signals could be expected from the different archives given the difference in physical properties of source materials and the mix of carbonate material types in fine fraction sediment. Drury and John (2016) described the potential influence of post depositional non-biogenic calcite on clumped isotope measurements of fine fraction sediments following observations showing that the relative percentage of non-biogenic calcite is likely to increase at smaller size fractions, and may vary by site and time period as carbonate chemistry changes. Furthermore, recent work into coccolith clumped isotope calibrations has indicated that coccolith calcite, a major component of fine fraction sediment, may be offset from foraminiferal and inorganic calcite by approximately 0.008 ‰ (Clark et al., 2024). To include the fine fraction sediment in this study, we first compare the different archives to identify potential differences in calculated Δ_{47}.

At Site 1263, mean differences (0.006 ‰) calculated between the Δ_{47} values of fine fraction sediment and the foraminiferal calcite are 0.002 ‰ smaller than those differences estimated by modern coccolith temperature calibration work (Clark et al., 2024), but this could be a result of the fine fraction sediment not being wholly coccolith in composition. To account for this offset, in the following sections fine fraction sediment samples are corrected by adding 0.006 ‰ to the measured Δ_{47} values. This results in an average temperature increase of 1.9 °C in fine fraction sediment.

S3.2 Recrystallization

The impact of recrystallization on planktic foraminifera in tropical open ocean successions is thought to be significant resulting in a cool-tropics hypothesis early in Paleocene and Eocene temperature reconstruction history, though it remains poorly quantified (Pearson and Burgess, 2008; Schrag et al., 1995). Recrystallization has the potential to affect all three of these temperature estimates though Mg/Ca signatures are thought to potentially be more resilient to recrystallization in closed-systems (Staudigel et al., 2022). Recrystallization at Site 1263 has not been quantified, though tests are frosty in texture (Leutert et al., 2019), so recrystallization most likely does affect these samples (Leutert et al., 2019). A high estimate of 50% recrystallization results in Δ_{47} temperature estimates increasing by an average of 5.6 °C with a largest change of 18.9 °C for the warmest point (Table 3.S.4). The recrystallization correction raises the clumped isotope derived temperatures to agree more with the Mg/Ca estimates. A lower estimate for recrystallization of 10 % raises temperatures on average 0.6 °C (Table 3.S.4). For an initial interpretation of our clumped isotope derived temperatures, we take a lower estimate of recrystallization (10 %) with the acknowledgement that these absolute temperatures can be considered minimum values. Other percentages are presented in Figure 3.S.4 and Table 3.S.4.

Estimates of recrystallization percentages should be conducted in the future to better constrain the increase in absolute temperature from this correction.

S3.3 Dissolution

Another form of diagenetic alteration is dissolution which has been shown to affect Mg/Ca and $\delta^{18}O$ carbonate values in foraminifera and bias temperature reconstructions toward colder values. New work presented in Chapter 2 suggests there is an effect on foraminiferal Δ_{47} that could bias values toward colder temperatures with increasing dissolution. Dissolution can occur at any site and has a higher likelihood of occurring at deeper sites and higher latitudes due to carbonate chemistry changes (Seibold and Berger, 2017 and references therein). Differences in basin chemistry (such as differences between the Atlantic and Pacific oceans) can also affect the amount of dissolution sediments will experience (Seibold and Berger, 2017; Zeebe and Zachos, 2007). Dissolution is difficult to quantify and will affect all carbonate based proxy systems to various extents depending on carbonate source due to preferential changes in Mg/Ca and other elemental variations as well as differences in surface textures and microstructure features (Bonneau et al., 1980; Brown and Elderfield, 1996; Dekens et al., 2002; Fehrenbacher and Martin, 2014; Johnstone et al., 2011; McCorkle et al., 1995; Regenberg et al., 2014, 2006; Rosenthal et al., 2000; Rosenthal and Lohmann, 2002). Given the uncertainties surrounding dissolution even outside the PETM excursion interval, dissolution effects are only considered within this interval where some estimates of shoaling of the carbonate compensation depth have been calculated and are considered as an additional error in the offset between PETM and LP temperatures.

The carbonate saturation horizon shoaled along Walvis Ridge sites by 2 km (Zachos et al., 2005) and foraminiferal fragmentation at Site 1263 increased from ~10 % to ~90% during the

PETM (Kelly et al., 2010). Increased dissolution would impact our Δ_{47} values, as well as the temperature estimates of the other carbonate-based proxies. We apply a dissolution correction of 0.010 ‰ based on the mean offset of the full transect dataset from above and below the carbonate saturation horizon from Chapter 2 to samples over the PETM. Using this offset we estimate an increase in clumped isotope temperature of 3.4 °C over the PETM where the dissolution correction is applied. The PETM temperature anomaly would therefore be of a much larger magnitude (~6.8 °C, Table 3.2).

However, this dissolution correction slope was calculated with foraminiferal species only and not fine fraction coccolith calcite which is known to be more resistant to dissolution than foraminiferal calcite (Schmidt et al., 2006; Subhas et al., 2019). Additionally, a significant correlation with depth and carbonate ion saturation of deposition is only found in specific foraminifera (*G. siphonifera, P. obliquiloculata,* and *G. tumida*). Given that our temperatures are partly constrained by the fine fraction archive and the foraminiferal species included in this study are more similar to those that exhibit minimal dissolution signals (*T. sacculifer*, surface mixed layer dweller with symbionts, Aze et al., 2011), a dissolution signal is likely to be smaller than the value applied.

S3.4 Carbonate ion effect

Here we explore the scope of potential carbonate ion effects on calculated Δ_{47} temperature estimates. To apply the offset in Δ_{47} found in benthic foraminifera from Chapter 1 we first must estimate $\Delta[CO_3^{2-}]$. Estimates of $\Delta[CO_3^{2-}]$ can be made if the temperature and salinity is known and estimates are available for two components of the carbonate system (e.g. pH, $[CO_3^{2-}]$, pCO_2). As we do not know temperatures from this region and must also use estimates of pH and pCO_2 that have large ranges, we supply sensitivity calculations to explore the breadth of the potential scope of this effect. $\Delta[CO_3^{2-}]$ estimates for the late Paleocene range

from 9.7 - 85.2 µmol/kg among estimated temperatures from 15-35 °C and pCO_2 estimates from 650 - 850 ppmv and a pH of 7.7. Estimates from the PETM range from -11.5 - 62.9 µmol/kg among estimated temperatures from 15 - 35 °C and pCO_2 from 1500-2800 ppmv and a pH of 7.4. If we use these values in the multivariate benthic equation from Chapter 1, we can increase temperatures in the late Paleocene by 0.9- 2.8 °C ($\Delta[CO_3^{2-}]$ of 9.7 - 85.2 µmol/kg). For the PETM, we may overestimate the temperature by 2.0 °C (-11.5 µmol/kg) or underestimate them by 1.8 °C (62.9 µmol/kg). Given the uncertainties and the fact that this multivariate equation was based on benthics only, we do not apply a correction related to carbonate saturation on Δ_{47}.

3.5 Uncertainties related to temperature calibrations

There are some uncertainties related to temperature calibrations. Both $\delta^{18}O$ and Mg/Ca in foraminifera are species dependent, with some species fractionating more than others due to various vital effects (Anand et al., 2003; Bemis et al., 1998; Darling et al., 2017; Malevich et al., 2019; Sadekov et al., 2016; Skinner and Elderfield, 2005). Coccolithophore calcite is especially prone to preserving signals associated with vital effects with species specificity contributing up to 5 ‰ offsets in $\delta^{18}O$ between taxa (e.g. Anderson and Steinmetz, 1981; M. Hermoso et al., 2016; Ziveri et al., 2003). Using a different equation for $\delta^{18}O$ temperatures such as the equation of Shackleton et al. (1974) decreases the offset between clumped and $\delta^{18}O$ temperatures by 0.6 °C. Species specificity has not been recorded in Δ_{47} values of planktic foraminifera (Chapter 1, Meinicke et al., 2020; Tripati et al., 2010), but using different calibrations such as the calibration calculated in Chapter 1 increases the reconstructed temperatures by an average of 0.3 °C. These uncertainties related to calibrations are a magnitude smaller than the differences between proxies that we see so are unlikely to fully explain the differences in calculated temperatures.

For Mg/Ca, the H factor in Equation 3 is species specific and sensitive to changes in the incorporation of Mg/Ca with change in Mg/Ca_{sw}. Decreasing the H term to 0.1 which is the

lowest value reported for Eocene planktic foraminifera (Hines et al., 2017), lowers the temperature by ~3 °C, however as this value was calculated based on matching Mg/Ca temperatures to $\delta^{18}O$ temperatures (Hines et al., 2017) for this study we used the H-factor calculated for the modern species *T. sacculifer* as reported in the methods section.

3.6 Uncertainties relating to seawater chemistry

Carbonate $\delta^{18}O$-derived temperature estimates are highly dependent on the $\delta^{18}O$ value of seawater chosen for the calculation (Bemis et al., 1998; Kim and O'Neil, 1997; Urey, 1947). The $\delta^{18}O$ calculation used to estimate the plotted oxygen isotope-based temperatures uses an estimate of $\delta^{18}O_{sw}$ for the Late-Paleocene approximate global ice-free seawater $\delta^{18}O$ of -1.0 ‰ from the mean of -0.89 and -1.11 from Cramer et al. (2011) and L'Homme et al. (2005) as recommended by Hollis et al. (2019). However, seawater $\delta^{18}O$ estimates are highly uncertain due to variability in the cryosphere as well as hydrologic cycle changes on short and long timescales (e.g. Broecker, 1989; Cramer et al., 2009; Zachos et al., 2006). Various efforts have been made to account for these variations including estimates based on the combination of Mg/Ca temperatures and $\delta^{18}O$ measurements, the use of isotope enabled models, and the applications of modern day $\delta^{18}O_{sw}$ gradients (Billups and Schrag, 2003; Tindall et al., 2010; Zachos et al., 1994). Each of these methods carry with them their own uncertainties, such as dependencies on model parameterizations or large assumptions about the stability of $\delta^{18}O_{sw}$ gradients through time (e.g. Hollis et al., 2019; Tindall et al., 2010). Given uncertainties in the $\delta^{18}O_{sw}$ we applied the method described in Hollis et al. (2019) of a global ice-free seawater estimate of -1.00 ‰ with a latitudinal offset from Zachos et al. (1994).

Similarly, reconstructed Mg/Ca temperatures rely on past Mg/Ca values of the seawater. Previous estimates of Mg/Ca_{sw} are thought to be lower than today (~2.24 mol/mol, Coggon et al., 2010; Evans et al., 2018; Horita et al., 2002; Lear et al., 2015). Calculating Mg/Ca based

temperatures with modern Mg/Ca_{sw} values (5.15 mol/mol) decreases the Mg/Ca temperature estimate by approximately 3 °C. As our best estimates of Mg/Ca_{sw} place values at the lower concentration, we assumed the lower concentration of 2.24 mmol/mol in our estimates.

pH effects have been reported on $\delta^{18}O$ incorporation due to DIC speciation (Zeebe 1999, 2001; Spero, 1997). The pH effect on $\delta^{18}O$ tends to increase $\delta^{18}O$ with decreasing pH biasing temperature estimates toward colder values due to variations in partitioning of $\delta^{18}O$ in carbonate ion species on water (Zeebe, 1999, 2001; Spero, 1997). In foraminifera this effect has been shown to vary by species but is approximately 1.42 ‰ $\delta^{18}O$ / unit of pH change in planktic foraminifera (Zeebe, 2001). pH estimates of the surface ocean in the early Eocene from Boron isotopes are around 0.5 units lower than today (7.7 as compared to 8.2) (e.g. Anagnostou et al., 2016,2020; Gutjar et al., 2017; Penman et al., 2014; Rae et al., 2021), which could create a $\delta^{18}O$ bias based on this effect. We take a pH effect into account in our $\delta^{18}O$ measurements.

Lower pH can also cause overestimates of Mg/Ca based temperatures, as lab studies have found that for ~0.1 unit decrease in pH is associated with a temperature overestimate of 1 °C (Gray and Evans, 2019). Various Mg/Ca calibrations attempt to correct for this term by having a correction for pH when proxy data for pH is available, but this data is rare and there are large uncertainties associated with this relationship at pHs lower than 7.7 like those estimated across the PETM (see discussion in Hollis et al., 2019). For our estimates we applied a pH correction as described in Hollis et al. (2019).

3.7 Other Uncertainties

Other sources of uncertainty exist such as sediment mixing processes could affect our records. Post and syn-depositional sediment mixing processes may blend isotopic signals together, resulting in a muted temperature response across periods of abrupt change like the PETM (e.g. Bralower et al, 2014, Kozdon et al. 2013, Kozdon and Kelly, 2020). The

methodology we employ of taking longer time period average intervals to characterize PETM temperatures impose a similar effect that is hard to disentangle from the muting signal of mixing processes, but the high sedimentation rate at this site serves to minimize these effects (Bralower et al., 2014).

Supplementary Figures

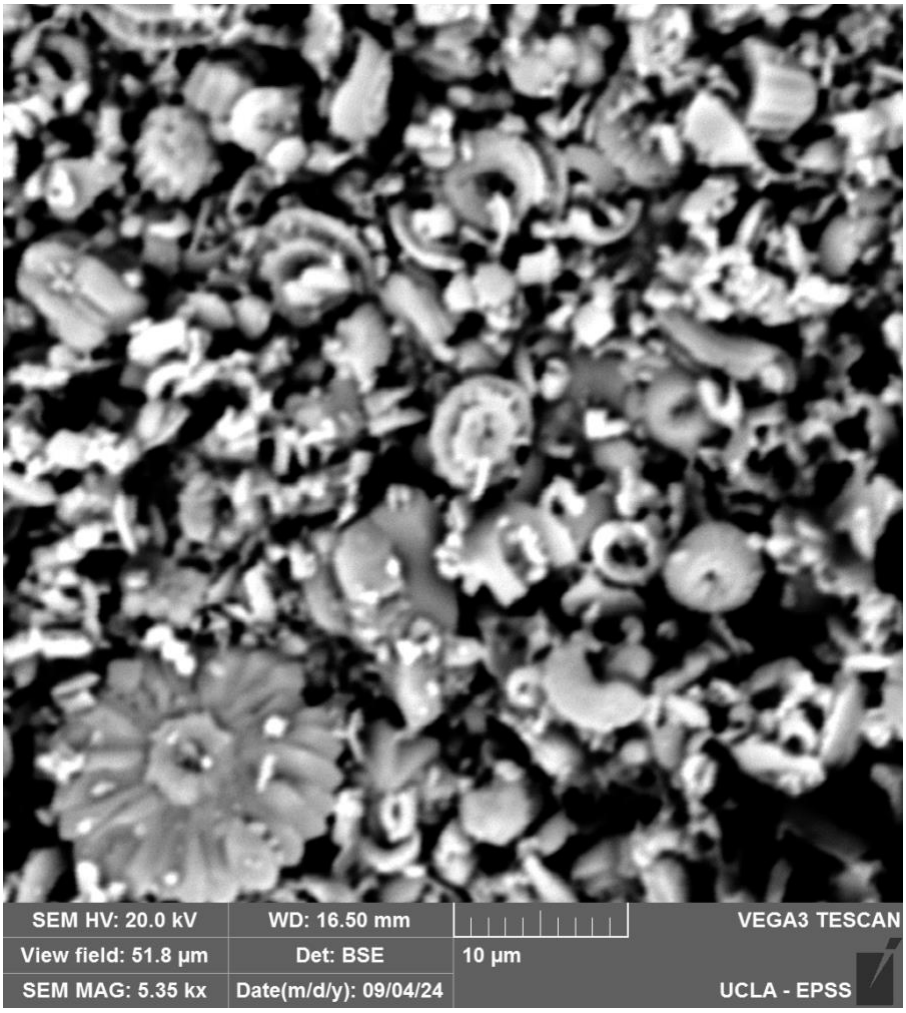

Figure 3.S.1: Fine fraction image from Site 1263C Sample 13-7 50-52. Most of the fine fraction is recognizable as coccolith plates and in line with images from percentages of coccolith calcite recording modern surface temperatures from Drury and John (2016).

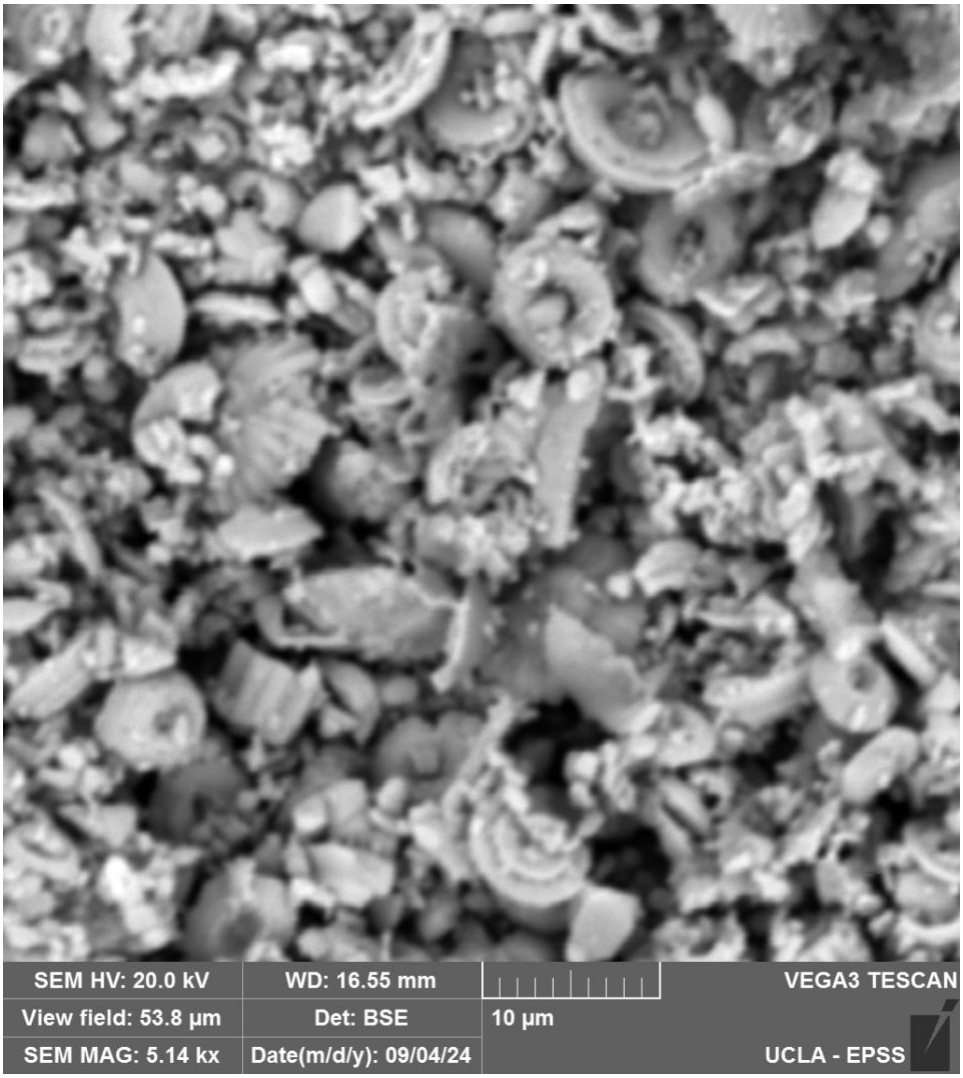

Figure 3.S.2: Fine fraction image from Site 1263C Sample 16-1 30-32. Most of the fine fraction is recognizable as coccolith plates and in line with images from percentages of coccolith calcite recording modern surface temperatures from Drury and John (2016).

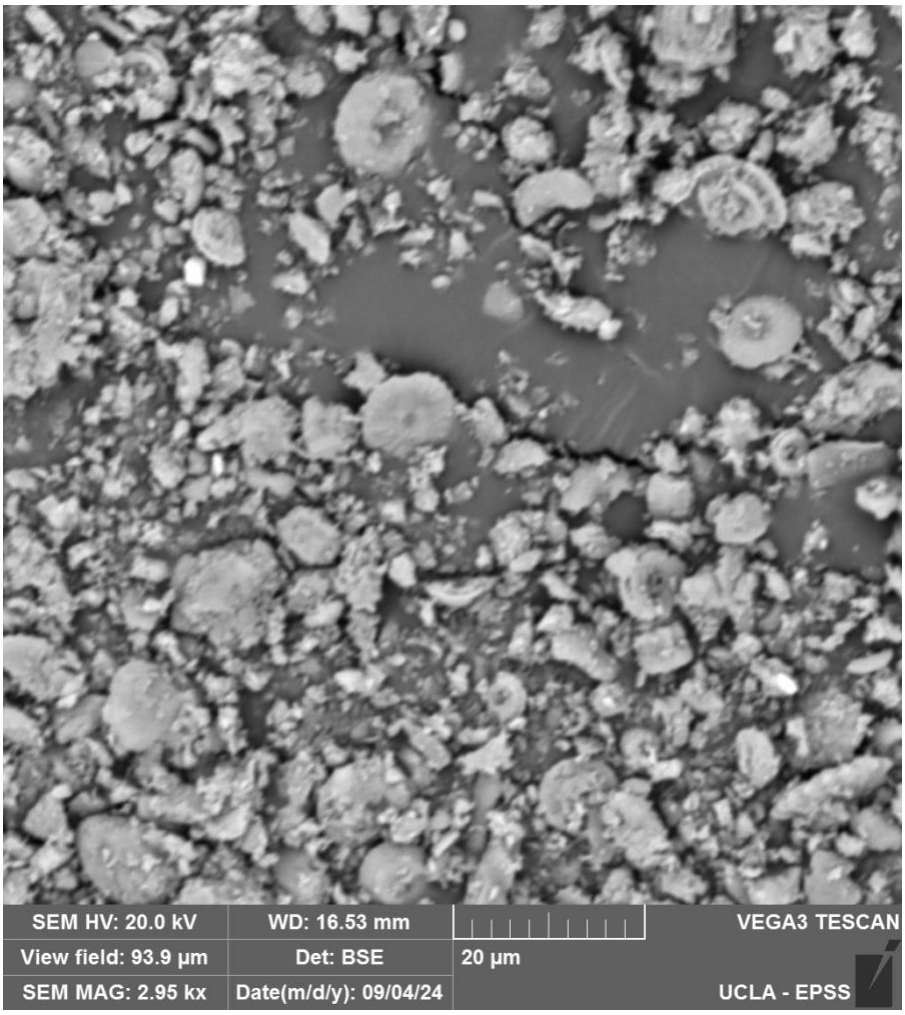

Figure 3.S.3: Fine fraction image from Site 1263C Sample 14-2 112-114 within the PETM. Some of the fine fraction is recognizable as coccolith plates though generally less than percentages of coccolith calcite recording modern surface temperatures from Drury and John (2016).

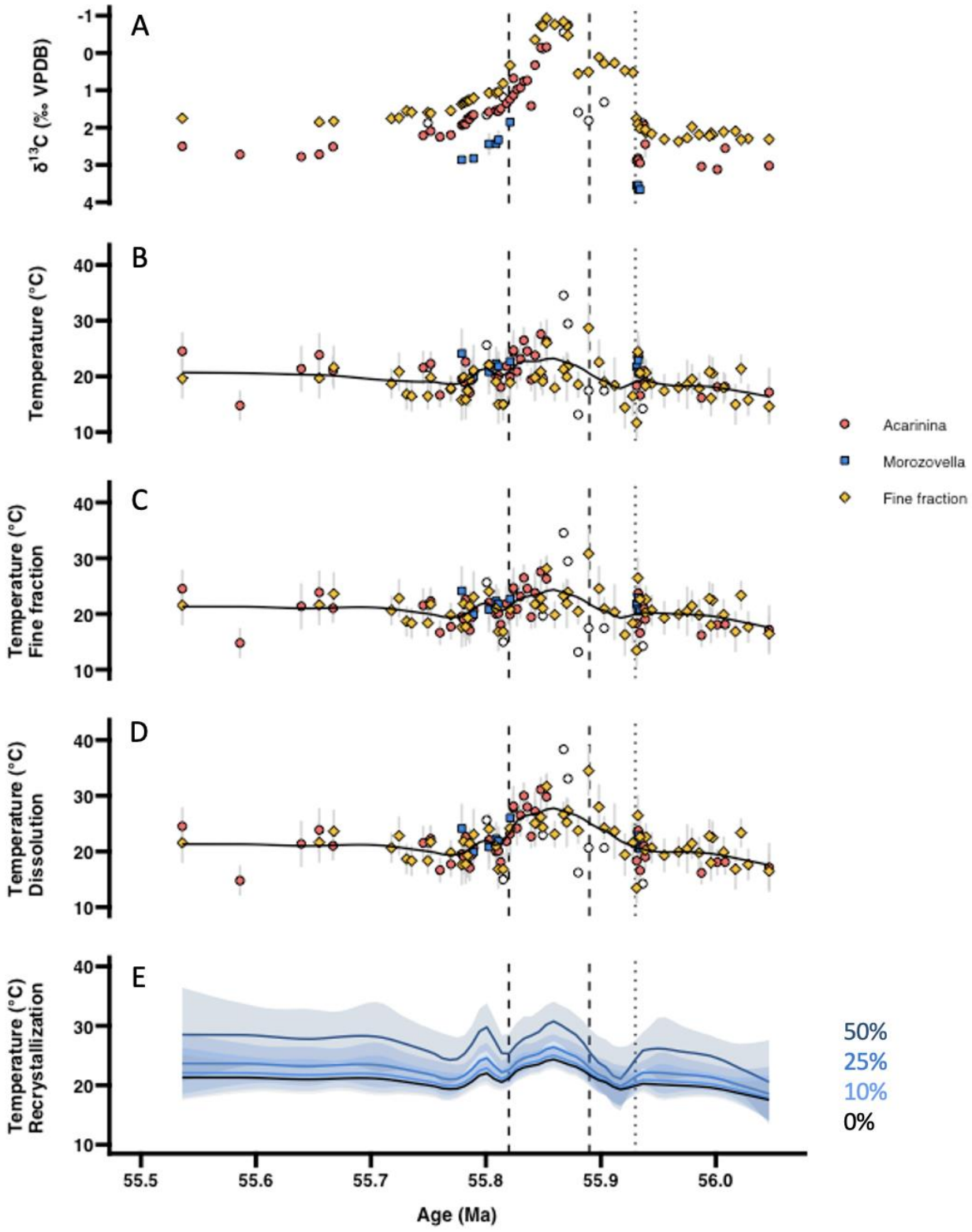

Figure 3.S.4: Data from Site 1263 across the PETM. Smoothed lines are LOESS regressions with a span of 0.2 and 95 % CI. Dashed vertical lines mark the peak of the PETM excursion and the dotted vertical line marks the beginning of the PETM excursion. Empty points are those with fewer than three replicates

per measurement. A) Carbon isotopes (‰ VPDB). B) No corrections are applied to the clumped isotope temperature calculations (Section 3.2). C) Temperatures with a 0.006 ‰ offset applied to the fine fraction clumped isotope values (Section 4.1.1). D) Temperatures with a 0.010 ‰ offset applied to samples over the PETM window to account for increased dissolution (Section 4.1.3). E) Temperatures with various levels of recrystallization applied (Section 4.1.2). With corrections applied absolute temperatures increase in the record at Site 1263. Warming is associated with the carbon excursion at the PETM and increases in magnitude with dissolution and recrystallization corrections.

References

Agterhuis, T., Ziegler, M., de Winter, N.J., Lourens, L.J., 2022. Warm deep-sea temperatures across Eocene Thermal Maximum 2 from clumped isotope thermometry. Commun. Earth Environ. 3, 1–9. https://doi.org/10.1038/s43247-022-00350-8

Anagnostou, E., John, E.H., Babila, T.L., Sexton, P.F., Ridgwell, A., Lunt, D.J., Pearson, P.N., Chalk, T.B., Pancost, R.D., Foster, G.L., 2020. Proxy evidence for state-dependence of climate sensitivity in the Eocene greenhouse. Nat. Commun. 11, 4436. https://doi.org/10.1038/s41467-020-17887-x

Anagnostou, E., John, E.H., Edgar, K.M., Foster, G.L., Ridgwell, A., Inglis, G.N., Pancost, R.D., Lunt, D.J., Pearson, P.N., 2016. Changing atmospheric CO2 concentration was the primary driver of early Cenozoic climate. Nature 533, 380–384. https://doi.org/10.1038/nature17423

Anand, P., Elderfield, H., Conte, M.H., 2003. Calibration of Mg/Ca thermometry in planktonic foraminifera from a sediment trap time series. Paleoceanography 18. https://doi.org/10.1029/2002PA000846

Anderson, N.T., Kelson, J.R., Kele, S., Daëron, M., Bonifacie, M., Horita, J., Mackey, T.J., John, C.M., Kluge, T., Petschnig, P., Jost, A.B., Huntington, K.W., Bernasconi, S.M., Bergmann, K.D., 2021. A Unified Clumped Isotope Thermometer Calibration (0.5–1,100°C) Using Carbonate-Based Standardization. Geophys. Res. Lett. 48, e2020GL092069. https://doi.org/10.1029/2020GL092069

Aze, T., Ezard, T.H.G., Purvis, A., Coxall, H.K., Stewart, D.R.M., Wade, B.S., Pearson, P.N., 2011. A phylogeny of Cenozoic macroperforate planktonic foraminifera from fossil data. Biol. Rev. 86, 900–927. https://doi.org/10.1111/j.1469-185X.2011.00178.x

Barker, S., Greaves, M., Elderfield, H., 2003. A study of cleaning procedures used for foraminiferal Mg/Ca paleothermometry. Geochem. Geophys. Geosystems 4. https://doi.org/10.1029/2003GC000559

Bemis, B.E., Spero, H.J., Bijma, J., Lea, D.W., 1998. Reevaluation of the oxygen isotopic composition of planktonic foraminifera: Experimental results and revised paleotemperature equations. Paleoceanography 13, 150–160. https://doi.org/10.1029/98PA00070

Bernasconi, S.M., Daëron, M., Bergmann, K.D., Bonifacie, M., Meckler, A.N., Affek, H.P., Anderson, N., Bajnai, D., Barkan, E., Beverly, E., Blamart, D., Burgener, L., Calmels, D., Chaduteau, C., Clog, M., Davidheiser-Kroll, B., Davies, A., Dux, F., Eiler, J., Elliott, B., Fetrow, A.C., Fiebig, J., Goldberg, S., Hermoso, M., Huntington, K.W., Hyland, E., Ingalls, M., Jaggi, M., John, C.M., Jost, A.B., Katz, S., Kelson, J., Kluge, T., Kocken, I.J., Laskar, A., Leutert, T.J., Liang, D., Lucarelli, J., Mackey, T.J., Mangenot, X., Meinicke, N., Modestou, S.E., Müller, I.A., Murray, S., Neary, A., Packard, N., Passey, B.H., Pelletier, E., Petersen, S., Piasecki, A., Schauer, A., Snell, K.E., Swart, P.K., Tripati, A., Upadhyay, D., Vennemann, T., Winkelstern, I., Yarian, D., Yoshida, N., Zhang, N., Ziegler, M., 2021. InterCarb: A Community Effort to Improve Interlaboratory Standardization of the Carbonate Clumped Isotope Thermometer Using Carbonate Standards. Geochem. Geophys. Geosystems 22, e2020GC009588. https://doi.org/10.1029/2020GC009588

Bralower, T.J., Kelly, D.C., Gibbs, S., Farley, K., Eccles, L., Lindemann, T.L., Smith, G.J., 2014. Impact of dissolution on the sedimentary record of the Paleocene–Eocene thermal maximum. Earth Planet. Sci. Lett. 401, 70–82. https://doi.org/10.1016/j.epsl.2014.05.055

Broecker, W.S., 1989. The salinity contrast between the Atlantic and Pacific oceans during glacial time. Paleoceanography 4, 207–212. https://doi.org/10.1029/PA004i002p00207

Brown, S.J., Elderfield, H., 1996. Variations in Mg/Ca and Sr/Ca ratios of planktonic foraminifera caused by postdepositional dissolution: Evidence of shallow Mg-dependent dissolution. Paleoceanography 11, 543–551. https://doi.org/10.1029/96PA01491

CenCO2PIP, 2023. Toward a Cenozoic history of atmospheric CO2. Science 382, eadi5177. https://doi.org/10.1126/science.adi5177

Clark, A.J., Torres-Romero, I., Jaggi, M., Bernasconi, S.M., Stoll, H.M., 2024. A clumped isotope calibration of coccoliths at well-constrained culture temperatures for marine temperature reconstructions. Clim. Past 20, 2081–2101. https://doi.org/10.5194/cp-20-2081-2024

Cramer, B.S., Miller, K.G., Barrett, P.J., Wright, J.D., 2011. Late Cretaceous–Neogene trends in deep ocean temperature and continental ice volume: Reconciling records of benthic foraminiferal geochemistry (δ18O and Mg/Ca) with sea level history. J. Geophys. Res. Oceans 116. https://doi.org/10.1029/2011JC007255

Cramer, B.S., Toggweiler, J.R., Wright, J.D., Katz, M.E., Miller, K.G., 2009. Ocean overturning since the Late Cretaceous: Inferences from a new benthic foraminiferal isotope compilation. Paleoceanography 24. https://doi.org/10.1029/2008PA001683

Daëron, M., Gray, W.R., 2023. Revisiting Oxygen-18 and Clumped Isotopes in Planktic and Benthic Foraminifera. Paleoceanogr. Paleoclimatology 38, e2023PA004660. https://doi.org/10.1029/2023PA004660

DeConto, R.M., Galeotti, S., Pagani, M., Tracy, D., Schaefer, K., Zhang, T., Pollard, D., Beerling, D.J., 2012. Past extreme warming events linked to massive carbon release from thawing permafrost. Nature 484, 87–91. https://doi.org/10.1038/nature10929

Defliese, W.F., Lohmann, K.C., 2015. Non-linear mixing effects on mass-47 CO2 clumped isotope thermometry: Patterns and implications. Rapid Commun. Mass Spectrom. 29, 901–909. https://doi.org/10.1002/rcm.7175

Dickens, G.R., O'Neil, J.R., Rea, D.K., Owen, R.M., 1995. Dissociation of oceanic methane hydrate as a cause of the carbon isotope excursion at the end of the Paleocene. Paleoceanography 10, 965–971. https://doi.org/10.1029/95PA02087

Drury, A.J., John, C.M., 2016. Exploring the potential of clumped isotope thermometry on coccolith-rich sediments as a sea surface temperature proxy. Geochem. Geophys. Geosystems 17, 4092–4104. https://doi.org/10.1002/2016GC006459

Dunkley Jones, T., Lunt, D.J., Schmidt, D.N., Ridgwell, A., Sluijs, A., Valdes, P.J., Maslin, M., 2013. Climate model and proxy data constraints on ocean warming across the Paleocene–Eocene Thermal Maximum. Earth-Sci. Rev. 125, 123–145. https://doi.org/10.1016/j.earscirev.2013.07.004

Dutton, A., Lohmann, K.C., Leckie, R.M., 2005. Insights from the Paleogene tropical Pacific: Foraminiferal stable isotope and elemental results from Site 1209, Shatsky Rise. Paleoceanography 20. https://doi.org/10.1029/2004PA001098

Evans, D., Sagoo, N., Renema, W., Cotton, L.J., Müller, W., Todd, J.A., Saraswati, P.K., Stassen, P., Ziegler, M., Pearson, P.N., Valdes, P.J., Affek, H.P., 2018. Eocene greenhouse climate revealed by coupled clumped isotope-Mg/Ca thermometry. Proc. Natl. Acad. Sci. 115, 1174–1179. https://doi.org/10.1073/pnas.1714744115

Evans, D., Wade, B.S., Henenhan, M., Erez, J., Müller, W., 2016. Revisiting carbonate chemistry controls on planktic foraminifera Mg / Ca: implications for sea surface temperature and hydrology shifts over the Paleocene–Eocene Thermal Maximum and Eocene–Oligocene

transition. Climate of the Past, 12 (4), 819-835. (doi:10.5194/cp-12-819-2016 <http://dx.doi.org/10.5194/cp-12-819-2016>).

Fairbanks, R.G., 1982. The origin of continental shelf and slope water in the New York Bight and Gulf of Maine: Evidence from H2 18O/H2 16O ratio measurements. J. Geophys. Res. Oceans 87, 5796–5808. https://doi.org/10.1029/JC087iC08p05796

Gingerich, P.D., 2019. Temporal Scaling of Carbon Emission and Accumulation Rates: Modern Anthropogenic Emissions Compared to Estimates of PETM Onset Accumulation. Paleoceanogr. Paleoclimatology 34, 329–335. https://doi.org/10.1029/2018PA003379

Gray, W.R., Evans, D., 2019. Nonthermal Influences on Mg/Ca in Planktonic Foraminifera: A Review of Culture Studies and Application to the Last Glacial Maximum. Paleoceanogr. Paleoclimatology 34, 306–315. https://doi.org/10.1029/2018PA003517

Gray, W.R., Weldeab, S., Lea, D.W., Rosenthal, Y., Gruber, N., Donner, B., Fischer, G., 2018. The effects of temperature, salinity, and the carbonate system on Mg/Ca in *Globigerinoides ruber* (white): A global sediment trap calibration. Earth Planet. Sci. Lett. 482, 607–620. https://doi.org/10.1016/j.epsl.2017.11.026

Gutjahr, M., Ridgwell, A., Sexton, P.F., Anagnostou, E., Pearson, P.N., Pälike, H., Norris, R.D., Thomas, E., Foster, G.L., 2017. Very large release of mostly volcanic carbon during the Palaeocene–Eocene Thermal Maximum. Nature 548, 573–577. https://doi.org/10.1038/nature23646

Hargreaves, J.C., Annan, J.D., Ohgaito, R., Paul, A., Abe-Ouchi, A., 2013. Skill and reliability of climate model ensembles at the Last Glacial Maximum and mid-Holocene. Clim. Past 9, 811–823. https://doi.org/10.5194/cp-9-811-2013

Harper, D.T., Hönisch, B., Bowen, G.J., Zeebe, R.E., Haynes, L.L., Penman, D.E., Zachos, J.C., 2024. Long- and short-term coupling of sea surface temperature and atmospheric CO2

during the late Paleocene and early Eocene. Proc. Natl. Acad. Sci. 121, e2318779121. https://doi.org/10.1073/pnas.2318779121

Hasiuk, F.J., Lohmann, K.C., 2010. Application of calcite Mg partitioning functions to the reconstruction of paleocean Mg/Ca. Geochim. Cosmochim. Acta 74, 6751–6763. https://doi.org/10.1016/j.gca.2010.07.030

Herold, N., Buzan, J., Seton, M., Goldner, A., Green, J.A.M., Müller, R.D., Markwick, P., Huber, M., 2014. A suite of Early Eocene (~55 Ma) climate model boundary conditions. Geosci. Model Dev. Discuss. 7, 529–562. https://doi.org/10.5194/gmdd-7-529-2014

Higgins, J.A., Schrag, D.P., 2006. Beyond methane: Towards a theory for the Paleocene–Eocene Thermal Maximum. Earth Planet. Sci. Lett. 245, 523–537. https://doi.org/10.1016/j.epsl.2006.03.009

Hines, B.R., Hollis, C.J., Atkins, C.B., Baker, J.A., Morgans, H.E.G., Strong, P.C., 2017. Reduction of oceanic temperature gradients in the early Eocene Southwest Pacific Ocean. Palaeogeogr. Palaeoclimatol. Palaeoecol. 475, 41–54. https://doi.org/10.1016/j.palaeo.2017.02.037

Hinsbergen, D.J.J. van, Groot, L.V. de, Schalk, S.J. van, Spakman, W., Bijl, P.K., Langereis, C.G., Brinkhuis, H., 2015. A Paleolatitude Calculator for Paleoclimate Studies. PLOS ONE 21.

Hollis, C.J., Dunkley Jones, T., Anagnostou, E., Bijl, P.K., Cramwinckel, M.J., Cui, Y., Dickens, G.R., Edgar, K.M., Eley, Y., Evans, D., Foster, G.L., Frieling, J., Inglis, G.N., Kennedy, E.M., Kozdon, R., Lauretano, V., Lear, C.H., Littler, K., Meckler, N., Naafs, B.D.A., Pälike, H., Pancost, R.D., Pearson, P., Royer, D.L., Salzmann, U., Schubert, B., Seebeck, H., Sluijs, A., Speijer, R., Stassen, P., Tierney, J., Tripati, A., Wade, B., Westerhold, T., Witkowski, C., Zachos, J.C., Zhang, Y.G., Huber, M., Lunt, D.J., 2019. The DeepMIP

contribution to PMIP4: methodologies for selection, compilation and analysis of latest Paleocene and early Eocene climate proxy data, incorporating version 0.1 of the DeepMIP database. https://doi.org/10.5194/gmd-2018-309

Huber, M., Caballero, R., 2011. The early Eocene equable climate problem revisited. Clim. Past 7, 603–633. https://doi.org/10.5194/cp-7-603-2011

Huber, M., Sloan, L.C., 2001. Heat transport, deep waters, and thermal gradients: Coupled simulation of an Eocene greenhouse climate. Geophys. Res. Lett. 28, 3481–3484. https://doi.org/10.1029/2001GL012943

John, C.M., Bowen, D., 2016. Community software for challenging isotope analysis: First applications of 'Easotope' to clumped isotopes. Rapid Commun. Mass Spectrom. 30, 2285–2300. https://doi.org/10.1002/rcm.7720

Katz, A., Bonifacie, M., Hermoso, M., Cartigny, P., Calmels, D., 2017. Laboratory-grown coccoliths exhibit no vital effect in clumped isotope (Δ47) composition on a range of geologically relevant temperatures. Geochim. Cosmochim. Acta 208, 335–353. https://doi.org/10.1016/j.gca.2017.02.025

Kelly, D.C., Nielsen, T.M.J., McCarren, H.K., Zachos, J.C., Röhl, U., 2010. Spatiotemporal patterns of carbonate sedimentation in the South Atlantic: Implications for carbon cycling during the Paleocene–Eocene thermal maximum. Palaeogeogr. Palaeoclimatol. Palaeoecol. 293, 30–40. https://doi.org/10.1016/j.palaeo.2010.04.027

Kim, S.-T., O'Neil, J.R., 1997. Equilibrium and nonequilibrium oxygen isotope effects in synthetic carbonates. Geochim. Cosmochim. Acta 61, 3461–3475. https://doi.org/10.1016/S0016-7037(97)00169-5

Kozdon, R., Kelly, D.C., Kita, N.T., Fournelle, J.H., Valley, J.W., 2011. Planktonic foraminiferal oxygen isotope analysis by ion microprobe technique suggests warm tropical sea surface

temperatures during the Early Paleogene. Paleoceanography 26. https://doi.org/10.1029/2010PA002056

Kozdon, R., Kelly, D.C., Kitajima, K., Strickland, A., Fournelle, J.H., Valley, J.W., 2013. In situ δ18O and Mg/Ca analyses of diagenetic and planktic foraminiferal calcite preserved in a deep-sea record of the Paleocene-Eocene thermal maximum. Paleoceanography 28, 517–528. https://doi.org/10.1002/palo.20048

Lea, D.W., Mashiotta, T.A., Spero, H.J., 1999. Controls on magnesium and strontium uptake in planktonic foraminifera determined by live culturing. Geochim. Cosmochim. Acta 63, 2369–2379. https://doi.org/10.1016/S0016-7037(99)00197-0

Lear, C.H., Elderfield, H., Wilson, P.A., 2000. Cenozoic Deep-Sea Temperatures and Global Ice Volumes from Mg/Ca in Benthic Foraminiferal Calcite. Science 287, 269–272. https://doi.org/10.1126/science.287.5451.269

Leutert, T.J., Sexton, P.F., Tripati, A., Piasecki, A., Ho, S.L., Meckler, A.N., 2019. Sensitivity of clumped isotope temperatures in fossil benthic and planktic foraminifera to diagenetic alteration. Geochim. Cosmochim. Acta 257, 354–372. https://doi.org/10.1016/j.gca.2019.05.005

Lora, J.M., Ibarra, D.E., 2019. The North American hydrologic cycle through the last deglaciation. Quat. Sci. Rev. 226, 105991. https://doi.org/10.1016/j.quascirev.2019.105991

Lucarelli, J.K., Carroll, H.M., Ulrich, R.N., Elliott, B.M., Coplen, T.B., Eagle, R.A., Tripati, A., 2023. Equilibrated Gas and Carbonate Standard-Derived Dual (Δ47 and Δ48) Clumped Isotope Values. Geochem. Geophys. Geosystems 24, e2022GC010458. https://doi.org/10.1029/2022GC010458

Lunt, D.J., Bragg, F., Chan, W.-L., Hutchinson, D.K., Ladant, J.-B., Morozova, P., Niezgodzki, I., Steinig, S., Zhang, Z., Zhu, J., Abe-Ouchi, A., Anagnostou, E., de Boer, A.M., Coxall, H.K., Donnadieu, Y., Foster, G., Inglis, G.N., Knorr, G., Langebroek, P.M., Lear, C.H., Lohmann, G., Poulsen, C.J., Sepulchre, P., Tierney, J.E., Valdes, P.J., Volodin, E.M., Dunkley Jones, T., Hollis, C.J., Huber, M., Otto-Bliesner, B.L., 2021. DeepMIP: model intercomparison of early Eocene climatic optimum (EECO) large-scale climate features and comparison with proxy data. Clim. Past 17, 203–227. https://doi.org/10.5194/cp-17-203-2021

Lunt, D.J., Huber, M., Anagnostou, E., Baatsen, M.L.J., Caballero, R., DeConto, R., Dijkstra, H.A., Donnadieu, Y., Evans, D., Feng, R., Foster, G.L., Gasson, E., von der Heydt, A.S., Hollis, C.J., Inglis, G.N., Jones, S.M., Kiehl, J., Kirtland Turner, S., Korty, R.L., Kozdon, R., Krishnan, S., Ladant, J.-B., Langebroek, P., Lear, C.H., LeGrande, A.N., Littler, K., Markwick, P., Otto-Bliesner, B., Pearson, P., Poulsen, C.J., Salzmann, U., Shields, C., Snell, K., Stärz, M., Super, J., Tabor, C., Tierney, J.E., Tourte, G.J.L., Tripati, A., Upchurch, G.R., Wade, B.S., Wing, S.L., Winguth, A.M.E., Wright, N.M., Zachos, J.C., Zeebe, R.E., 2017. The DeepMIP contribution to PMIP4: experimental design for model simulations of the EECO, PETM, and pre-PETM (version 1.0). Geosci. Model Dev. 10, 889–901. https://doi.org/10.5194/gmd-10-889-2017

Meckler, A.N., Sexton, P.F., Piasecki, A.M., Leutert, T.J., Marquardt, J., Ziegler, M., Agterhuis, T., Lourens, L.J., Rae, J.W.B., Barnet, J., Tripati, A., Bernasconi, S.M., 2022. Cenozoic evolution of deep ocean temperature from clumped isotope thermometry. Science 377, 86–90. https://doi.org/10.1126/science.abk0604

Meinicke, N., Ho, S.L., Hannisdal, B., Nürnberg, D., Tripati, A., Schiebel, R., Meckler, A.N., 2020. A robust calibration of the clumped isotopes to temperature relationship for

foraminifers. Geochim. Cosmochim. Acta 270, 160–183. https://doi.org/10.1016/j.gca.2019.11.022

Meissner, K.J., Bralower, T.J., Alexander, K., Jones, T.D., Sijp, W., Ward, M., 2014. The Paleocene-Eocene Thermal Maximum: How much carbon is enough? Paleoceanography 29, 946–963. https://doi.org/10.1002/2014PA002650

Pagani, M., Huber, M., Sageman, B.B., 2013. Greenhouse Climates. Treatise Geochem. Second Ed. 281–304. https://doi.org/10.1016/B978-0-08-095975-7.01314-0

Parvez, Z., Lucarelli, J., Matamoros, I.W., Rubi, J., Miguel, K., Elliott, B., Flores, R., Ulrich, R.N., Eagle, R.A., Watkins, J.M., Christensen, J.N., 2023. Dual carbonate clumped isotopes (Δ47-Δ48) constrains kinetic effects and timescales in peridotite-associated springs at the Cedars, Northern California. Geochim. Cosmochim. Acta 358, 77–92.

Pearson, P.N., Burgess, C.E., 2008. Foraminifer test preservation and diagenesis: comparison of high latitude Eocene sites. Geol. Soc. Lond. Spec. Publ. 303, 59–72. https://doi.org/10.1144/SP303.5

Pearson, P.N., 2012. Oxygen Isotopes in Foraminifera: Overview and Historical Review. Paleontol. Soc. Pap. 18, 1–38. https://doi.org/10.1017/S1089332600002539

Penman, D.E., Hönisch, B., Zeebe, R.E., Thomas, E., Zachos, J.C., 2014. Rapid and sustained surface ocean acidification during the Paleocene-Eocene Thermal Maximum. Paleoceanography 29, 357–369. https://doi.org/10.1002/2014PA002621

R Core Team, 2022. R: A language and environment for statistical computing.

Ridgwell, A., Schmidt, D.N., 2010. Past constraints on the vulnerability of marine calcifiers to massive carbon dioxide release. Nat. Geosci. 3, 196–200. https://doi.org/10.1038/ngeo755

Rohling, E.J., Gernon, T.M., Heslop, D., Reichart, G.J., Roberts, A.P., Yu, J., 2024. Reconciling the Apparent Discrepancy Between Cenozoic Deep-Sea Temperatures From Proxies and From Benthic Oxygen Isotope Deconvolution. Paleoceanogr. Paleoclimatology 39, e2024PA004872. https://doi.org/10.1029/2024PA004872

Rosenthal, Y., Lohmann, G.P., 2002. Accurate estimation of sea surface temperatures using dissolution-corrected calibrations for Mg/Ca paleothermometry. Paleoceanography 17, 16-1-16–6. https://doi.org/10.1029/2001PA000749

Russell, A.D., Hönisch, B., Spero, H.J., Lea, D.W., 2004. Effects of seawater carbonate ion concentration and temperature on shell U, Mg, and Sr in cultured planktonic foraminifera. Geochim. Cosmochim. Acta 68, 4347–4361. https://doi.org/10.1016/j.gca.2004.03.013

Sagoo, N., Valdes, P., Flecker, R., Gregoire, L.J., 2013. The Early Eocene equable climate problem: can perturbations of climate model parameters identify possible solutions? Philos. Trans. R. Soc. Math. Phys. Eng. Sci. 371, 20130123. https://doi.org/10.1098/rsta.2013.0123

Schmidt, D.N., Lazarus, D., Young, J.R., Kucera, M., 2006. Biogeography and evolution of body size in marine plankton. Earth-Sci. Rev. 78, 239–266. https://doi.org/10.1016/j.earscirev.2006.05.004

Schrag, D.P., DePaolo, D.J., Richter, F.M., 1995. Reconstructing past sea surface temperatures: Correcting for diagenesis of bulk marine carbonate. Geochim. Cosmochim. Acta 59, 2265–2278. https://doi.org/10.1016/0016-7037(95)00105-9

Schubert, B.A., Hope Jahren, A., 2013. Reconciliation of marine and terrestrial carbon isotope excursions based on changing atmospheric CO2 levels. Nat. Commun. 4, 1653. https://doi.org/10.1038/ncomms2659

Seibold, E., Berger, W.H., 2017. The sea floor: an introduction to marine geology. Springer.

Spero, H.J., Bijma, J., Lea, D.W., Bemis, B.E., 1997. Effect of seawater carbonate concentration on foraminiferal carbon and oxygen isotopes. Nature 390, 497–500. https://doi.org/10.1038/37333

Staudigel, P.T., John, E.H., Buse, B., Pearson, P.N., Lear, C.H., 2022. Apparent preservation of primary foraminiferal Mg/Ca ratios and Mg-banding in recrystallized foraminifera. Geology 50, 760–764. https://doi.org/10.1130/G49984.1

Subhas, A.V., McCorkle, D.C., Quizon, A., McNichol, A.P., Long, M.H., 2019. Selective Preservation of Coccolith Calcite in Ontong-Java Plateau Sediments. Paleoceanogr. Paleoclimatology 34, 2141–2157. https://doi.org/10.1029/2019PA003731

Thomas, D.J., Bralower, T.J., Zachos, J.C., 1999. New evidence for subtropical warming during the Late Paleocene thermal maximum: Stable isotopes from Deep Sea Drilling Project Site 527, Walvis Ridge. Paleoceanography 14, 561–570. https://doi.org/10.1029/1999PA900031

Tierney, J.E., Zhu, J., Li, M., Ridgwell, A., Hakim, G.J., Poulsen, C.J., Whiteford, R.D.M., Rae, J.W.B., Kump, L.R., 2022. Spatial patterns of climate change across the Paleocene–Eocene Thermal Maximum. Proc. Natl. Acad. Sci. 119, e2205326119. https://doi.org/10.1073/pnas.2205326119

Tindall, J., Flecker, R., Valdes, P., Schmidt, D.N., Markwick, P., Harris, J., 2010. Modelling the oxygen isotope distribution of ancient seawater using a coupled ocean–atmosphere GCM: Implications for reconstructing early Eocene climate. Earth Planet. Sci. Lett. 292, 265–273. https://doi.org/10.1016/j.epsl.2009.12.049

Tripati, A., 2005. Deep-Sea Temperature and Circulation Changes at the Paleocene-Eocene Thermal Maximum. Science 308, 1894–1898. https://doi.org/10.1126/science.1109202

Tripati, A.K., Eagle, R.A., Thiagarajan, N., Gagnon, A.C., Bauch, H., Halloran, P.R., Eiler, J.M., 2010. 13C–18O isotope signatures and 'clumped isotope' thermometry in foraminifera and coccoliths. Geochim. Cosmochim. Acta 74, 5697–5717. https://doi.org/10.1016/j.gca.2010.07.006

Tripati, A.K., Elderfield, H., 2004. Abrupt hydrographic changes in the equatorial Pacific and subtropical Atlantic from foraminiferal Mg/Ca indicate greenhouse origin for the thermal maximum at the Paleocene-Eocene Boundary: Abrupt Hydrographic Changes. Geochem. Geophys. Geosystems 5, n/a-n/a. https://doi.org/10.1029/2003GC000631

Uchikawa, J., Zeebe, R.E., 2010. Examining possible effects of seawater pH decline on foraminiferal stable isotopes during the Paleocene-Eocene Thermal Maximum. Paleoceanography 25. https://doi.org/10.1029/2009PA001864

Upadhyay, D., Lucarelli, J., Arnold, A., Flores, R., Bricker, H., Ulrich, R.N., Jesmok, G., Santi, L., Defliese, W., Eagle, R.A., Carroll, H.M., Bateman, J.B., Petryshyn, V., Loyd, S.J., Tang, J., Priyadarshi, A., Elliott, B., Tripati, A., 2021. Carbonate clumped isotope analysis (Δ47) of 21 carbonate standards determined via gas-source isotope-ratio mass spectrometry on four instrumental configurations using carbonate-based standardization and multiyear data sets. Rapid Commun. Mass Spectrom. 35, e9143. https://doi.org/10.1002/rcm.9143

Urey, H.C., 1947. The thermodynamic properties of isotopic substances. J Chem Soc 562–581. https://doi.org/10.1039/JR9470000562

Vaes, B., van Hinsbergen, D.J.J., van de Lagemaat, S.H.A., van der Wiel, E., Lom, N., Advokaat, E.L., Boschman, L.M., Gallo, L.C., Greve, A., Guilmette, C., Li, S., Lippert, P.C., Montheil, L., Qayyum, A., Langereis, C.G., 2023. A global apparent polar wander

path for the last 320 Ma calculated from site-level paleomagnetic data. Earth-Sci. Rev. 245, 104547. https://doi.org/10.1016/j.earscirev.2023.104547

Westerhold, T., Marwan, N., Drury, A.J., Liebrand, D., Agnini, C., Anagnostou, E., Barnet, J.S.K., Bohaty, S.M., De Vleeschouwer, D., Florindo, F., Frederichs, T., Hodell, D.A., Holbourn, A.E., Kroon, D., Lauretano, V., Littler, K., Lourens, L.J., Lyle, M., Pälike, H., Röhl, U., Tian, J., Wilkens, R.H., Wilson, P.A., Zachos, J.C., 2020. An astronomically dated record of Earth's climate and its predictability over the last 66 million years. Science 369, 1383–1387. https://doi.org/10.1126/science.aba6853

Zachos, J., Kroon, D., Blum, P., Bowles, J., Gaillot, P., Hasegawa, T., Hathorne, E.C., Hodell, D.A., Kelly, D.C., Jung, J.H., Keller, S.M., Lee, Y.S., Leuschner, D.C., Liu, Z., Lohmann, K.C., Lourens, L., Monechi, S., Nicolo, M., Raffi, I., Riesselman, C., Rohl, U., Schellenberg, S.A., Schmidt, D., Sluijs, A., Thomas, D., Vallius, H., 2004. Leg 208, Proceedings of the Ocean Drilling Program, Initial Reports. Ocean Drilling Program, College Station, TX.

Zachos, J., Pagani, M., Sloan, L., Thomas, E., Billups, K., 2001. Trends, Rhythms, and Aberrations in Global Climate 65 Ma to Present. Science 292, 686–693. https://doi.org/10.1126/science.1059412

Zachos, J., Röhl, U., Schellenberg, S.A., Sluijs, A., Hodell, D.A., Kelly, D.C., Thomas, E., Nicolo, M., Raffi, I., Lourens, L.J., McCarren, H., Kroon, D., 2005. Rapid Acidification of the Ocean During the Paleocene-Eocene Thermal Maximum. Science 308, 1611–1615. https://doi.org/10.1126/science.1109004

Zachos, J., Schouten, S., Bohaty, S., Quattlebaum, T., Sluijs, A., Brinkhuis, H., Gibbs, S.J., Bralower, T.J., 2006. Extreme warming of mid-latitude coastal ocean during the

Paleocene-Eocene Thermal Maximum: Inferences from TEX86 and isotope data. Geology 34, 737–740. https://doi.org/10.1130/G22522.1

Zachos, J., Wara, M.W., Bohaty, S., Delaney, M.L., Petrizzo, M.R., Brill, A., Bralower, T.J., Silva, I.P., 2003. A Transient Rise in Tropical Sea Surface Temperature During the Paleocene-Eocene Thermal Maximum. Science 302, 1551–1554. https://doi.org/10.1126/science.1090110

Zeebe, R.E., 2001. Seawater pH and isotopic paleotemperatures of Cretaceous oceans. Palaeogeogr. Palaeoclimatol. Palaeoecol. 170, 49–57. https://doi.org/10.1016/S0031-0182(01)00226-7

Zeebe, R.E., 1999. An explanation of the effect of seawater carbonate concentration on foraminiferal oxygen isotopes. Geochim. Cosmochim. Acta 63, 2001–2007. https://doi.org/10.1016/S0016-7037(99)00091-5

Zeebe, R.E., Zachos, J.C., 2013. Long-term legacy of massive carbon input to the Earth system: Anthropocene versus Eocene. Philos. Trans. R. Soc. Math. Phys. Eng. Sci. 371, 20120006. https://doi.org/10.1098/rsta.2012.0006

Zeebe, R.E., Zachos, J.C., Dickens, G.R., 2009. Carbon dioxide forcing alone insufficient to explain Palaeocene–Eocene Thermal Maximum warming. Nat. Geosci. 2, 576–580. https://doi.org/10.1038/ngeo578

Zeebe, R.E., Zachos, J.C., 2007. Reversed deep-sea carbonate ion basin gradient during Paleocene-Eocene thermal maximum. Paleoceanography 22. https://doi.org/10.1029/2006PA001395

Zhu, J., Poulsen, C.J., Tierney, J.E., 2019. Simulation of Eocene extreme warmth and high climate sensitivity through cloud feedbacks. Sci. Adv. 5, eaax1874. https://doi.org/10.1126/sciadv.aax1874

Chapter 4: Clumped Isotope Sea Surface Temperature and Meridional Temperature Gradient Reconstructions for the Late Paleocene to Early Eocene

H. Tandy, A. Perez-Huerta, R. Kozdon, B. Amato, D. Ramirez, S. Chung, F. Swain, L. Archuleta, N. Rodkin, A. Beck, T. Vollmer, J. Voon, G. Jesmok, R. Eagle, C. Kelly, T. Bralower, J. Zachos, A. Tripati

Abstract

The warmest temperatures and weakest meridional temperature gradients of the past 65 million years occurred during the Late Paleocene and Early Eocene, associated with high levels of greenhouse gases, and multiple hyperthermals associated with carbon release, including the Paleocene-Eocene Thermal Maximum (PETM; ~55.8 Ma). Despite this interval having been the subject of extensive study, there is disagreement between proxy-based reconstructions for warming in different regions, and discrepancies with model simulations. Here, we provide new perspectives on patterns of warming and salinity change by applying the clumped isotope temperature proxy (Δ_{47}) to planktic foraminiferal tests and coccolith dominated fine fraction and reconstruct sea surface temperatures (SSTs) and water $\delta^{18}O$ at five sites that span different latitudes and ocean basins. We consider effects of non-thermal processes, including recrystallization and dissolution, on reconstructions from Δ_{47} and other proxies. Δ_{47} estimates of late Paleocene and PETM SSTs agree with model simulations of meridional temperature gradients at 3 times and 6 times preindustrial CO_2 concentrations, if non-thermal effects are included and corrected for. The data support changes in seawater $\delta^{18}O$ gradients compared to present, with Late Paleocene surface waters more enriched in the subtropics and high latitudes, and further changes associated with PETM and Early Eocene Climatic Optimum warming.

1. Introduction:

The late Paleocene and Early Eocene were the warmest phases of the Cenozoic era (Zachos et al., 2001). Greenhouse gas concentrations during the Late Paleocene were 2.3–3 times those of the pre-industrial era, reaching 650–850 ppmv (CenCO2PIP, 2023), and global temperatures estimated as ~13 °C warmer than pre-industrial levels (Tierney et al., 2022). The Paleocene-Eocene Thermal Maximum (PETM), occurring ~55.8 million years ago, was a hyperthermal due to major disruptions in the carbon cycle, as indicated by a large carbon isotope excursion (CIE) in sedimentary records (Zachos et al., 2003), likely as methane and/or carbon dioxide over about 10,000 years (Gutjahr et al., 2017; Zachos et al., 2003; Zeebe et al., 2009). Estimates of PETM global temperature changes are uncertain, though recent work suggests it may have been ~5-6 °C, higher than previously thought, (Tierney et al., 2022). Both the baseline conditions of the late Paleocene and early Eocene, and changes during the PETM, are of interest as an analogue for understanding greenhouse climate dynamics (Hollis et al., 2019; Lunt et al., 2017, 2021; Tierney et al., 2022).

Climate model simulations show a range of predictions for regional and global temperatures during the Late Paleocene and Early Eocene (Lunt et al., 2017, 2021). A recent study has used data assimilation to combine PETM model simulations with proxy data to re-evaluate equilibrium climate sensitivity and suggested a higher value than previously thought (6.5 °C/doubling of CO_2; Tierney et al., 2022). Other studies that focus on model-proxy comparisons have indicated that poleward temperature gradients may be frequently overestimated in simulations of past warm periods (Hollis et al., 2019; Huber and Caballero, 2011; Huber and Sloan, 2001; Lunt et al., 2021, p. 20, 2017; Sagoo et al., 2013; Zhu et al., 2019). In order to achieve high latitude temperatures 10-25 °C warmer than today, as indicated by proxy reconstructions for the PETM and other greenhouse intervals (Bijl et al., 2009; Hollis et al.,

2019), simply increasing greenhouse gas levels in models would not be sufficient, as simulated tropical temperatures are substantially warmer than proxy data imply (Huber and Caballero, 2011; Lunt et al., 2021, 2012). However, climate models may not accurately represent mechanisms that would reduce the gradient, such as cloud feedbacks that are a large uncertainty in models (Boucher et al., 2013). Recent studies have examined the effects of altering the representation of physical processes in models, model parameterization, to improve model-data agreement (Kiehl and Shields, 2013; Sagoo et al., 2013; Zhu et al., 2019). In particular, model-proxy comparison has been used to update atmospheric processes, specifically the representation of cloud physics, in models (e.g., Sagoo et al., 2013).

However, there remains substantial uncertainty in proxy estimates of temperatures for tropical, subtropical, and polar regions during the early Cenozoic, complicating estimates of regional and global temperatures (e.g., Dunkley-Jones et al., 2013; Hollis et al., 2019; Tierney et al., 2022). For example, carbonate-based proxies for sea surface temperatures (SSTs), such as foraminiferal $\delta^{18}O$ and Mg/Ca ratios, yield conflicting results, potentially due to assumptions used for calculations of SSTs relating to seawater $\delta^{18}O$ (Hollis et al., 2019; Tripati and Elderfield, 2004; Zachos et al., 2003), seawater Mg/Ca (Tripati and Elderfield, 2004; Hollis et al., 2019), seawater pH (Hollis et al., 2019), and variable preservation (Kozdon et al., 2013, 2011; Kozdon and Kelly, 2024). Additionally, species-specific effects can also influence $\delta^{18}O$, Mg/Ca, and TEX_{86} temperature reconstructions, including for the Late Paleocene to Early Eocene (e.g., Hollis et al., 2019 and references therein). These sources of uncertainty in proxies complicate our ability to advance climate theory and to evaluate climate models using data (e.g., Hollis et al., 2019).

Here, we build on an in-depth investigation of PETM samples from Site 1263 (Chapter 3) and utilize the clumped isotope temperature proxy (Δ_{47}) to evaluate SSTs for the Late Paleocene

to Early Eocene at five sites that span a range of latitudes and sediment preservation, and compare results to independent proxy data and simulations. We consider the impact of non-thermal processes on temperatures reconstructed from Δ_{47} and other proxies. Δ_{47} is independent of seawater $\delta^{18}O$ and Mg/Ca, and in foraminifera, species-specific effects have not been detected (Meinicke et al., 2020; Tripati et al., 2010). Some studies have begun to examine in-depth the potential for fine fraction (coccolith-derived) calcite for temperature reconstructions and shown evidence for coccolith offsets from other carbonates from experiments and field sampling (Chapter 3, Clark et al., 2024; Drury and John, 2016; Katz et al., 2017).

Each carbonate-based proxy is susceptible to the impact of dissolution. Dissolution is known to impact $\delta^{18}O$ and Mg/Ca values in foraminifera (e.g. Bonneau et al., 1980; Brown and Elderfield, 1996; Dekens et al., 2002; Fehrenbacher and Martin, 2014; Johnstone et al., 2011; McCorkle et al., 1995; Regenberg et al., 2014, 2006; Rosenthal et al., 2000; Rosenthal and Lohmann, 2002). Recent work suggests that dissolution also has the potential to impact Δ_{47} and bias temperatures to colder values (Chapters 1 and 2).

Recrystallization also has been shown to impact $\delta^{18}O$, Mg/Ca, and Δ_{47} (e.g. Sexton et al., 2006; Leutert et al., 2019; Stolper et al., 2018; Staudigel et al., 2022). The impact of recrystallization on planktic foraminifera in tropical open ocean successions is thought to be the most significant, and difficult to quantify, while the impact of recrystallization in samples from mid- and high-latitudes is thought to be less pronounced (Leutert et al., 2019). To quantify impacts, a few recent studies have used novel approaches. Secondary Ion Mass Spectrometry (SIMS) has been used to determine primary and diagenetic calcite oxygen isotope compositions of foraminifera, and within the framework of a two-component diagenetic model, has been used to infer 15-50% alteration at one site (Kozdon et al., 2013, 2011). Electron Back Scatter Diffraction (EBSD) analysis has shown that recrystallization can be quantified more precisely,

with uncertainties of <5%, with values of 20% +/-10% alteration reported for corals and brachiopods (Cummins et al., 2014; Cusack, 2016), and the potential for use in foraminifera explored (Pabich et al., 2020; Procter et al., 2024).

In this study, we report new Δ_{47} data for planktic foraminiferal and coccolith calcite at Ocean Drilling Program Sites 1409 (North Atlantic), 1209 and 865 (tropical Pacific), and 690 (Southern Ocean), and use results from Site 1263 (subtropical South Atlantic) from Chapter 3. We consider non-thermal effects on reconstructed SSTs and seawater $\delta^{18}O$ from Δ_{47}. We compare results to independent proxy estimates, and model simulations.

2. Methods:

2.1 Site Description:

Samples analyzed are from Southeast Newfoundland Ridge (IODP Site 1409), Maud Rise (ODP Site 690), Shatsky Rise (ODP Site 1209), and Allison Guyot (ODP Site 865). Data from Walvis Ridge (ODP Site 1263) is from Chapter 3. Site locations are listed in Table 4.1 and shown in Figure 4.1. The CENOGRID age model for the Cenozoic is used (Westerhold et al., 2020) based on $\delta^{13}C$ tie-points to Site 1263 (Supplemental Text 1, Supplemental Table 4.S.1).

2.2 Sample Types

2.2.1 Planktic foraminifera from the genera *Morozovella* and *Acarinina* were picked from each sample. Specimens from the >212 µm size fraction were picked to obtain approximately 300 specimens per genus, when available. For samples with insufficient specimens in the larger size fractions, specimens from smaller fractions (>125 µm and >63 µm) were also picked for clumped isotope analysis.

2.2.2 The fine fraction sediment (<63 µm) is mainly made up of coccolith plates, though it also includes foraminiferal fragments, clays, and siliceous material in varying proportions depending on the sample. Detailed descriptions of the sediment composition for each site are available in shipboard publications (Bralower et al., 2002; Norris et al., 2014; Pospichal and Wise Jr., 1990; Sager et al., 1993; Zachos et al., 2004).

2.3 Clumped Isotopes - Sample Preparation:

2.3.1 Planktic foraminifera: Specimens were cleaned to remove clays and other potential contaminants. They were placed in 1.5 ml vials and ultrasonicated with deionized water for three 5-second intervals. After sonication, the supernatant was removed, and the samples were dried overnight at 40 °C (< 50 °C). The specimens were then powdered by gently crushing the foraminifera between weigh paper using a pestle and returned to the vials until ready for weighing and analysis.

2.3.2 Fine fraction sediment: Approximately 20 mg of sample were cleaned to remove organics by adding dilute (3%) H_2O_2 to the sediment for about 3 hours. The sediment was then rinsed three times with deionized water and left to dry overnight at 40 °C (< 50 °C). After drying, the samples were powdered using a mortar and pestle and collected for weighing.

2.4 Clumped Isotopes - Measurement Procedure:

Machine configurations are described in detail in Lucarelli et al. (2023). All data was processed using the software Easotope (John and Bowen, 2016) and is in the I-CDES reference frame (Bernasconi et al., 2021). Briefly, most samples (those that were run in 2019 or later) were run on the Nu Perspective configuration 1a and were weighed out to 5 replicates at 0.35 – 0.48 mg (or equivalent carbonate percentage) when sufficient material was present. The samples were

then run on three Nu Perspective Dual inlet mass spectrometers with secondary electron suppression (described in Lucarelli et al., 2023; Upadhyay et al., 2021). The samples were digested through custom-built common acid bath systems with 105% phosphoric acid held at 90 °C. Carbonate standards ETH-1 and ETH-2 were used for a non-linearity correction. ETH-1, ETH-2, ETH-3, CMTile, Carmel Chalk, Veinstrom, TV_ST and TV_BT were run as standards for the Empirical Transfer Function (ETF) (Chapter 2, Lucarelli et al., 2023; Upadhyay et al., 2021). Samples run on the Mat 253 configuration were weighed between 5-6 mg and run on a Thermo Mat 253 mass spectrometer (Lucarelli et al., 2023; Upadhyay et al., 2021). The samples were digested through custom-built common acid bath systems with 105% phosphoric acid held at 90 °C. The same published carbonate standards ETH-1 and ETH-2 as well as heated and non-heated gas standards with varying composition were used for non-linearity corrections (Lucarelli et al., 2023). ETH-1, ETH-2, ETH-3, ETH-4, CMTile, Carmel Chalk, and Veinstrom were used for the ETF (Chapter 2, Lucarelli et al., 2023; Upadhyay et al., 2021).

2.5 Clumped Isotopes - Quality control:

Data were screened based on instrument source stability, leaks in the acid digestion system, and standard data quality during correction intervals. Screening thresholds for Δ_{47} are based on what was reported by Lucarelli et al. (2023), Meinicke et al. (2020), and Upadhyay et al. (2021), and follow the protocol of Parvez et al. (2023). Replicates with incomplete gas transfer and Δ_{47}, $\delta^{13}C$, and $\delta^{18}O$ values that fall outside of a SD range of ±0.5‰ for $\delta^{13}C$ and $\delta^{18}O$ and ±0.05‰ for Δ_{47} were flagged. Of analyses conducted for this study, 2056 replicates were included, and 56 flagged replicates were excluded.

2.6 Temperature reconstructions

2.6.1 Clumped Isotopes

Mean sample Δ_{47} values were calculated and converted to temperature using the calibration of Anderson et al. (2021) with standard error from the replicate averages and regression propagated to a final temperature error (Equation 1).

$$\Delta_{47(ICDES)} = 0.0391 \pm 0.0004 \times 10^6/T^2 + 0.154 \pm 0.004 \quad \text{Equation 1}$$

T is the temperature in K and $\Delta_{47(ICDES)}$ is the clumped isotope value in the I-CDES reference frame (Anderson et al., 2021; Bernasconi et al., 2021). Other calibrations result in similar results and are reported in the supplementary data (Chapter 1, Supplemental Table 4.S.2).

2.6.2 $\delta^{18}O$

$\delta^{18}O$ values were measured concurrently with Δ_{47}. $\delta^{18}O_{carb}$ was converted to temperature using assumed $\delta^{18}O_{SW}$ and the modified equation of Kim and O'Neil (1997) from Bemis et al. (1998):

$$T = 16.1\text{-}4.64(\delta^{18}O_{carb}\text{-}\delta^{18}O_{SW}) + 0.09(\delta^{18}O_{carb}\text{-}\delta^{18}O_{SW})^2 \quad \text{Equation 2}$$

Where T is the temperature in Celsius, $\delta^{18}O_{carb}$ is the measured value from the carbonate (VPDB). $\delta^{18}O_{SW}$ is reported relative on a different scale (VSMOW). Values for $\delta^{18}O_{SW}$ for initial calculations are from Hollis et al. (2019) with an estimated global ice-free $\delta^{18}O_{SW}$ of -0.89 ‰ from Cramer et al. (2011). We also combine Δ_{47}-temperatures with $\delta^{18}O_{carb}$ to estimate $\delta^{18}O_{SW}$.

2.7 Electron Backscatter Diffraction (EBSD)

EBSD measurements were taken on specimens of *Acarinina* and *Morozovella* to estimate percent recrystallization at Sites 865 and 1209 because those are the sites with the poorest preservation based on lithology. EBSD measurements were made in 2014-2016 at the Central

Analytical Facility (CAF) of The University of Alabama. Full method description and results are in the supplementary information (Supplemental information S2). Briefly, specimens were picked and mounted in resin before being ground and polished up to 0.3 µm with alumina micropolish. Samples were rinsed with distilled water, dried, and then coated with a thin (2.5 nm) layer of carbon and surrounded by silver paint to avoid electron charging carbon. EBSD data were collected with OIM 7.0 software at high vacuum, 30 kV, large beam intensity (10), and a high spatial resolution of 0.2 µm step size for diffraction and crystallographic maps. Finally, data were analysed using OIM 5.3 from EDAX-TSL (Pérez-Huerta et al., 2011; Pérez-Huerta and Cusack, 2009).

2.8 Recrystallization calculations

To address the uncertainty in the extent and impact of recrystallization on Δ_{47}, we apply a non-linear mixing model from Leutert et al., (2019) which allows for the estimation of possible Δ_{47} derived temperatures at various percentages of recrystallization. Differences in $\delta^{13}C$ and $\delta^{18}O$ between originally precipitated calcite and diagenetic calcite are difficult to quantify without direct measurement (e.g. by in situ secondary ion mass spectroscopy, see discussion in Leutert et al., 2019), so we estimate $\delta^{13}C$ by assuming it is the same as the bulk/fine fraction composition from each site following Leutert et al. (2019). Values are estimated with a LOESS smoothing regression through the $\delta^{13}C$ with a span of 0.2. We use our own data for these smoothing regressions, except for at Site 865 where we use bulk values from Hupp et al. (2022) as we do not have fine fraction or bulk data at this site. $\delta^{18}O$ values are assumed to be similar to benthic $\delta^{18}O$. We use benthic $\delta^{18}O$ from Westerhold et al. (2020) for all sites, with the exception of Site 865 for which we use a constant value of 1.2 ‰ that was measured by Kozdon et al. (2013) using SIMS. If the $\delta^{13}C$ and $\delta^{18}O$ differences between primary calcite and diagenetic calcite is less than

2 ‰, then nonlinear mixing effects should not be significant (Defliese and Lohmann, 2015) and linear mixing can be assumed (Stolper et al., 2018). However, if $\delta^{13}C$ and $\delta^{18}O$ differences are larger than 2 ‰, then not factoring in the impact of mixing would tend to dampen the temperature change recalculated considering recrystallization from clumped isotopes (Leutert et al., 2019). The Δ_{47} composition of the diagenetic endmember calcite used in the mixing model is from the average Δ_{47} reported for the Late Paleocene and Early Eocene by Meckler et al. (2022), which was converted to temperature using the calibration from Anderson et al. (2021). Calculations were performed in R version 4.2.1 (R Core Team, 2022).

2.9 Statistical analysis

Comparisons between stable isotope systems across sample archives and between proxy reconstructions from the same samples are done through paired t-tests. Comparison between means are using Welch's t-tests. All statistical analyses were performed in R version 4.2.1 (R Core Team, 2022) except for model skill score performed in Python 3. Skill score is defined as a model's skill in capturing anomalies from a null hypothesis, in our case three times CO_2/late Paleocene temperatures, where a score of 1 reflects a perfect model, a score of 0 that the new model and null hypothesis perform equally well, and a negative score reflects a model error greater than that of the null hypothesis (see Hargreaves et al., 2013; Lora and Ibarra, 2019).

3. Results:

The warmest Δ_{47}-temperatures are reconstructed for the two low-latitude sites, tropical Pacific Sites 865 and 1209, while the coolest Δ_{47}-temperatures are inferred for the highest latitude site, Southern Ocean Site 690 (Table 4.2). Late Paleocene Δ_{47}-temperatures for foraminifera from Site 865 are 24 °C with no evidence for changes at the PETM. At Site 1209,

Late Paleocene Δ_{47}-temperatures from foraminifera are 22.3 °C, with a small shift at the PETM; fine fraction values are slightly cooler and also record a small PETM anomaly. At Site 1409, in the mid-latitude North Atlantic, Late Paleocene temperatures are 19.7 °C, indistinguishable from fine fraction, with no PETM samples analyzed here. These Late Paleocene temperatures are similar to what was reconstructed at Site 1263 in the mid-latitude South Atlantic, where PETM Δ_{47}-temperatures are ~4 °C warmer. At Site 690, on Maud Rise in the Atlantic sector of the Southern Ocean, Late Paleocene Δ_{47}-temperatures are 13.4 °C, and the PETM values are about 2.2 °C higher.

At Site 865, $\delta^{18}O_{carb}$-temperatures are ~3.1 °C lower than Δ_{47}-temperatures ($p < 0.01$) with no evidence for change across the PETM (Table 4.S.3). At Site 1209, they are ~4.5 °C lower ($p < 0.01$) and do support a PETM increase in temperature (Table 4.S.3). For Site 1409, temperatures calculated from $\delta^{18}O$ are on average 2.9 °C lower than those derived from Δ_{47} ($p < 0.01$). $\delta^{18}O_{carb}$-derived temperatures at Site 1263 are on average 3.3 °C lower than those derived from clumped isotopes ($p < 0.01$) and support a temperature increase across the PETM. At Site 690, Late Paleocene temperatures calculated from $\delta^{18}O_{carb}$ are on average 1.0 °C lower than those derived from clumped isotopes ($p < 0.01$). PETM samples do have lower $\delta^{18}O_{carb}$ values, which if there was no change in $\delta^{18}O_{sw}$ or pH, would support temperatures that are on average 2.3 °C higher (Table 4.3).

4. Discussion:

4.1 Δ_{47}-temperatures

Core-top studies and downcore studies show that Δ_{47}, like other temperature proxies, can be subject to non-thermal influences. To refine clumped isotope temperature estimates for the

Late Paleocene through early Eocene, we explore a range of assumptions regarding secondary effects and potential corrections to the data for each site.

4.1.1 Taxonomic offsets in Δ_{47}

Prior calibration tudies have shown that taxonomic differences in modern planktic foraminifera Δ_{47} values are not detectable (Meinicke et al., 2020; Chapter 1). No offset was observed in Δ_{47} between the mixed-layer taxa *Morozovella* and *Acarinina* at the three sites with sufficient sample density to perform robust comparisons of foraminiferal material (Sites 1263, 1409, and 865; Supplemental Table 4.S.1), so temperatures derived from analyses of mono-specific samples for these two foraminiferal taxa were averaged together (Tables 4.2, 4.3).

It is possible that Δ_{47} offsets exist between coccoliths and mixed-layer planktics. For example, different species of haptophyte algae and planktic foraminifera can have distinct depths of maximum abundance, and thus record different temperatures (Drury and John, 2016). A recent culturing study has suggested that coccolith calcite, a major component of sediment fine fraction in open ocean settings, may be offset from foraminiferal and inorganic calcite by approximately 0.008 ‰ (Clark et al., 2024). Drury and John (2016) described the potential influence of post depositional non-biogenic calcite on clumped isotope measurements of fine fraction sediments following observations showing that the relative percentage of non biogenic calcite is likely to increase at smaller size fractions, and may vary by site and time period as carbonate chemistry changes. We measured a large number of samples of both fine fraction and foraminiferal calcite from two sites: Sites 1263 and 1409. At Site 1263, discussed in Chapter 3, we identified a 0.006 ‰ offset between the fine fraction carbonate Δ_{47} values and foraminiferal carbonate values,, consistent with prior work. At Site 1409, there is a difference of 0.004 ‰ between fine fraction and foraminiferal calcite. Given the predictions from the prior body of work, and that the offset calculated at Site 1409 is close to the Site 1263 value of 0.006 ‰, but the latter site has a higher

sampling density and is more similar to the larger values reported by what was found in laboratory studies, we correct fine-fraction sediment data from all sites by adding 0.006 ‰ (the mid-range value) to measured Δ_{47}, which increases average Δ_{47}-temperatures from fine fraction by ~1-2 °C (Supplementary Figures 4.S.1-4.S.4, Supplemental Table 4.S.4).

4.1.2 Carbonate ion effect on calcification

To date, there has not been any work that supports a carbonate ion effect on planktic foraminifera. However, in Chapter 1, a small benthic carbonate ion effect of 0.0001 ‰ / µmol/kg $\Delta[CO_3^{2-}]$ was reported. pH effects are reported in planktic foraminifera on oxygen isotopes and a study on corals suggested that Δ_{47} values could be impacted similarly due to DIC speciation (Spero et al., 1997; Tripati et al., 2015; Zeebe, 1999). The response for Δ_{47} in benthics from Chapter 1, however, is in the opposite direction of the theorized relationship of Δ_{47} with pH, so it is likely not controlled by the same processes as the pH effect in oxygen isotopes. As a carbonate ion effect on Δ_{47} in planktic foraminifera has not been described, we do not consider the effects in our calculations.

However, if such an effect does exist for planktic foraminifera, with a similar sensitivity to benthic foraminifera, then given that background values of surface water $\Delta[CO_3^{2-}]$ were lower than today (Anagnostou et al., 2016; Gutjahr et al., 2017; Penman et al., 2014; Uchikawa and Zeebe, 2010), estimates of late Paleocene temperatures for all sites may be different than uncorrected values. To apply the offset in Δ_{47} found in benthic foraminifera from Chapter 1 we first must estimate $\Delta[CO_3^{2-}]$. Estimates of $\Delta[CO_3^{2-}]$ can be made if the temperature and salinity is known and estimates are available for two components of the carbonate system (e.g. pH, $[CO_3^{2-}]$, pCO_2). Estimates of pCO_2 for the late Paleocene range from 650 - 850 ppmv, and for the PETM from ~1500 - 2800 ppmv (CenCO2PIP, 2023). Estimates of late Paleocene pH are approximately

0.5 lower than today at 7.7 units, and for the PETM drop an additional 0.3 units to 7.4 (Anagnostou et al., 2016; Gutjahr et al., 2017; Penman et al., 2014; Uchikawa and Zeebe, 2010). We supply sensitivity calculations to explore the breadth of the potential scope of this effect. $\Delta[CO_3^{2-}]$ was calculated using CO2Sys by taking the value of $[CO_3^{2-}]$ at a given set of constraints, and subtracting $[CO_3^{2-}]_{sat}$ calculated at omega = 1 (Van Heuven et al., 2011). For these sensitivity tests, all calculations assume a salinity of 35 psu, late Paleocene calculations assume a pH of 7.7 and PETM calculations assume a pH of 7.4, and temperature and pCO_2 are varied.

$\Delta[CO_3^{2-}]$ estimates of surface water for the late Paleocene range from approximately -5 - 131 µmol/kg with the lowest values corresponding to SSTs of 5 °C and a pCO_2 of 650 ppmv and the highest value corresponding to SSts of 45 °C with a pCO_2 of 850 ppmv. Estimates from the PETM range from approximately -20 - 101 µmol/kg with the lowest values corresponding to temperatures of 5 °C with 1500 ppmv pCO_2 and the highest values to temperatures of 45 °C and a pCO_2 of 2800 ppmv. If we use these values in the multivariate benthic equation from Chapter 1, we can decrease temperatures in the late Paleocene by ~2 °C if using the lowest estimates for $\Delta[CO_3^{2-}]$ of -5 µmol/kg or increase them by ~5 °C if using the highest values. For the PETM, we may overestimate the temperature by ~4 °C (101 µmol/kg) or underestimate them by ~2 °C (-20 µmol/kg). Lowest $\Delta[CO_3^{2-}]$ values are expected at the highest latitudes while higher $\Delta[CO_3^{2-}]$ are expected at lower latitudes given temperature gradients, so if applied by site high latitude sites would be expected to decrease in estimated temperature, while low latitude sites may increase. However, given the uncertainties and the fact that this multivariate equation was based on benthics only, we do not apply a correction related to carbonate saturation on Δ_{47} in further comparisons.

4.1.3 Recrystallization

Prior work has explored the sensitivity of Δ_{47}-temperatures in foraminifera to recrystallization (Leutert et al., 2019; Stolper et al., 2018). They showed that recrystallization will impact foraminifera to differing extents, depending on the composition of primary and secondary calcite. The impact of recrystallization on the geochemistry of planktic foraminifera in sediments with low clay contents and higher porosity and permeability is thought to have discernable impacts. In particular, recrystallization is likely to have affected $\delta^{18}O$-based and Mg/Ca reconstructions from tropical open ocean successions for greenhouse intervals (Colosimo et al., 2005; D'Hondt and Arthur, 1996; Hollis et al., 2019; Kozdon et al., 2011, 2013, 2018; Leutert et al., 2019; Pearson and Burgess, 2008; Schrag et al., 1995; Sexton et al., 2006; Tripati et al., 2003). While this diagenetic process is hypothesized to explain why some carbonate-based proxies may be biased to apparently cool values during the early Cenozoic (termed the "cool tropics" paradox) (D'Hondt and Arthur, 1996; Pearson and Burgess, 2008; Tripati et al., 2003), it remains poorly quantified.

We hypothesize that Δ_{47} could be particularly sensitive to recrystallization given mechanisms for recrystallization explored for other proxies. Given that carbon and oxygen isotopes in bulk and fine fraction and foraminiferal carbonate at Sites 1209 and 690 all show clear evidence for changes across the PETM, we speculate the relatively small change in Δ_{47} at these sites across the PETM could also indicate there was sediment-buffered recrystallization occurring at cold temperatures. Recrystallization is known to impact sediments with atomic exchange with pore water towards an equilibrium state (Gorski and Fantle, 2017 and references therein). In biogenic sediments, fluid carbonate exchanges can occur along microstructure fractures and along organic layers (Cisneros-Lazaro et al., 2022). If fluid-carbonate exchange near equilibrium in these microstructure environments acts as a closed or near-closed system,

$\delta^{18}O$ and $\delta^{13}C$ signals of the pore water could become increasingly buffered within the sediment, similar to what is modeled for Mg/Ca in (Staudigel et al., 2022). Recrystallization would then rely on the closed $\delta^{18}O$ and $\delta^{13}C$ reservoir of the pore water for further exchange which could help to preserve the original $\delta^{18}O$ and $\delta^{13}C$ signals but could still continue to reprecipitate carbonate reflecting bottom water temperatures in clumped isotope signatures. If additional exchange near equilibrium continues to occur in the sediment past the intervals of typical sediment buffering, this could explain the relatively static clumped isotope temperature signals on long time scales and contribute to cool temperatures being recorded. If this type of recrystallization is occurring, it could mean that clumped isotopes are uniquely susceptible to recrystallization effects due to their independence of seawater chemistry. Substantial micrite has been found at Site 690 indicating continued dissolution and reprecipitation in the fine fraction that would record this signal, but less micrite is observed at Site 1209 which contains better preserved fine fraction than at Site 690 (Bralower et al., 2014).

Regardless, recrystallization is a factor that should be considered as a source of uncertainty. Techniques including SIMS and EBSD offer methods for detecting and quantifying the impacts of recrystallization on carbonates (Cummins et al., 2014; Cusack, 2016; Kozdon et al., 2013, 2011; Pabich et al., 2020; Procter et al., 2024). Both SIMS and EBSD show that within a given population of foraminifera in sediments, a range of preservational states can be observed. In each specimen, there are regions of tests that can preserve ultrastructure and crystallite orientation, and areas that can show evidence for complete recrystallization.

Generally, “frosty” textures are observed at Sites 1209, 865, 1263, and 690 and “glassy” tests at Site 1409 (Colosimo et al., 2005; Hollis et al., 2019; Kozdon et al., 2018, 2013, 2011; Leutert et al., 2019; Pearson and Burgess, 2008; Sexton et al., 2006). Percent estimates for recrystallization have been made for Site 865 with 15-50 % recrystallization constrained by

SIMS analyses (Kozdon et al., 2013, 2011). Figure 4.2 (and Supplemental Figure 4.5) shows estimates of area recrystallized for 161 specimens of *Morozovella* and *Acaranina* that are Late Paleocene to Middle Eocene in age, with 89 specimens from Site 865 and 72 specimens from Site 1209. The data support poorer preservation at Site 865 than Site 1209, with Morozovellids being the worst preserved taxa, and the Acaraninids being the best-preserved taxa. Figure 4.S.5 shows a histogram of the results.

Given the range of mean and median values, and the upper-level values, in concert with the SIMS data, we assume 10 % recrystallization across all sites as a minimum estimate and additionally discuss higher estimates for low latitude sites (25 and 50 % for Site 865, and 25 % for Site 1209). This level of recrystallization represents minimum temperatures. Applying the correction for recrystallization increases temperatures throughout the record with largest changes at the warmest intervals and sites (Site 865 and 1209) and slightly amplifies temperature trends in the records (Figure 4.3, Supplemental Figures 4.S.1-4.S.4, Supplemental Table 4.S.4). However, the only scenarios that yield plausible tropical temperatures are the higher recrystallization estimates for Sites 865 and 1209.

4.1.4 Dissolution

Recent work suggests there is a dissolution effect on foraminiferal Δ_{47} that could bias reconstructions to colder temperatures (Chapters 1-3). Dissolution has also been shown to affect Mg/Ca and $\delta^{18}O$ values in foraminifera, and bias temperature reconstructions toward colder values (Bonneau et al., 1980; Brown and Elderfield, 1996; Dekens et al., 2002; Fehrenbacher and Martin, 2014; Johnstone et al., 2011; McCorkle et al., 1995; Regenberg et al., 2014, 2006; Rosenthal et al., 2000; Rosenthal and Lohmann, 2002). While dissolution intensity can vary

regionally and as a function of temperature and respiration (Seibold and Berger, 2017; Zeebe and Zachos, 2013), the impacts can be difficult to quantify.

Site 865 is thought to have experienced increased dissolution at the beginning of the excursion, where sediments recording the transition to the PETM are missing (Hupp et al., 2022; Kelly et al., 1996). At Site 1209, the carbonate compensation depth (CCD) was estimated to have shoaled at least 500 m (Colosimo et al., 2005). Estimates of foraminiferal fragmentation at this site range from ~10 - 70% over the Late Paleocene and PETM, with $CaCO_3$ content dropping ~20% during the hyperthermal (Adebowale, 2021; Colosimo et al., 2005). Site 1263 was above the lysocline during the Late Paleocene, and the CCD shoaled to depths above the site during the PETM (Zachos et al., 2005). At Sites 689 and 690 on Maud Rise, the lysocline depth is thought to have shoaled to above ~1100 m across the PETM (Kelly et al., 2012). Estimates of percent foraminiferal fragmentation at this site range from ~5 - 40% over the Late Paleocene and PETM with $CaCO_3$ content dropping by ~20% during the hyperthermal (Kelly et al., 2005).

At each site, to correct for dissolution, we utilize the mean observed core-top Δ_{47} increase of 0.010 ‰ for different species across the carbonate saturation horizon from the Ontong-Java Plateau (Chapter 2). This increases PETM temperatures typically by ~4-5 °C (Supplementary Figures 4.S.4-4.S.7, Table 4.3). We note that larger dissolution increases were observed in experiments for some species, while in core-tops, some species do not exhibit a resolvable change (Chapter 2). Another caveat is that no data on dissolution impacts on Δ_{47} are available yet for coccoliths, which may be more resistant to dissolution than foraminiferal calcite (Schmidt et al., 2006; Subhas et al., 2019).

4.1.5 Mixing

The impact of mixing would be to potentially mute temperature excursions across the PETM, and bias low-latitude temperatures to colder values. In particular, clumped isotopes can be non-linearly affected by mixing of sample types when the bulk isotopic compositions of the archives differ by more than 2 ‰, and the mixing effects can be complex ((Defliese and Lohmann, 2015; Drury and John, 2016), although they can potentially be detected using other measurements such as Δ_{48} (Lucarelli et al., 2023) or through careful microscopy. There are two potential sources of mixing we discuss here. First, it is possible that changes in the Δ_{47} composition of fine fraction in sediments over time at any site, such as changing the fraction and composition of coccolith, foraminiferal, and abiotic calcite, may impact the measured Δ_{47} signal of the mixture (Drury and John, 2016).

Second, substantial amounts of winnowing and bioturbation, such as what has been reported for the PETM at Site 865 (Kozdon et al., 2011; Kozdon and Kelly, 2024), could also result in a muted temperature response. Sediments from this site have been observed to have foraminifera with isotopic signals similar to Late Paleocene values mixed with PETM samples over the excursion window (Hupp et al., 2022; Kelly et al., 1996; Kozdon et al., 2018; Kozdon and Kelly, 2024). The mixing can be avoided by picking solely excursion taxa, and we note that Mg/Ca data for the site do show evidence for a temperature change (Tripati and Elderfield, 2004). However, due to the relatively large sample size requirements required for Δ_{47} analysis, we picked at the genus level for this study. We hypothesize that the lack of significant change at Site 865 in the Δ_{47} record may be due to downcore sediment misplacement, and we exclude the PETM results for this site from further comparison. Future work at this site could aim to pick solely excursion taxa over the PETM interval to more accurately determine Δ_{47} temperatures at

this site. At the other sites we examined, sedimentation rates are higher and thus, this process is much less likely to impact the records (Bralower et al., 2014; Kelly et al., 2005; Stoll, 2005).

4.2 Comparison with other proxies

Below, we discuss Δ_{47}-temperatures estimated for Sites 865, 1209, 1409, and Site 690 and how values compare to $\delta^{18}O$ and Mg/Ca-based reconstructions (Figure 4.3). An in-depth discussion of different proxy reconstructions for Site 1263 is reported in Chapter 3.

4.2.1 Site 865

Late Paleocene Δ_{47}-temperatures for Sites 865 with the base corrections are warmer than $\delta^{18}O$-temperatures, and cooler than Mg/Ca temperatures, but are implausible, given models that would suggest tropical temperatures be much warmer (Figure 4.3a) (Sagoo et al., 2013; Zhu et al., 2019). The temperatures are lower than pre-industrial tropical temperatures for similar latitudes and oceanic regions. If higher levels of recrystallization are assumed that are consistent with the range of recrystallization inferred for these sites from SIMS and EBSD (Kozdon et al., 2013, 2010; Figure 4.2), the absolute temperatures from clumped isotopes increase to 27.0 °C and 32.6 °C for 25 % and 50 % respectively, at Site 865 (Figure 4.3b), which are more reasonable given what is understood about the CO_2 concentrations of the late Paleocene (CenCO2PIP, 2023; Lunt et al., 2017). At Site 865, Δ_{47}-SSTs at these higher levels of recrystallization also converge with recently published Mg/Ca estimates (Kozdon and Kelly, 2024), and with $\delta^{18}O$ estimates derived using SIMS data (Kozdon et al., 2013, 2011).

4.2.2 Site 1209

At Site 1209, as with Site 865, the absolute Δ_{47}-temperatures with base corrections are ~7 °C higher than $\delta^{18}O$-temperatures (Hollis et al., 2019; Thomas et al., 1999), and ~5 °C lower than

Mg/Ca-temperatures (Dunkley Jones et al., 2013; Hollis et al., 2019; Tripati and Elderfield, 2004). These Δ_{47}-temperatures are also likely implausible for the tropics, considering values simulated in models with similar boundary conditions (Figure 4.3; Sagoo et al., 2013; Lunt et al., 2021). However, if higher estimates of recrystallization (~25%) that are consistent with EBSD data are considered, then more reasonable absolute SSTs are calculated, with Late Paleocene values of 25.4 °C and PETM values of 29.0 °C. These are ~3 °C slightly cooler than Mg/Ca estimates (Hollis et al., 2019; Figure 4.3).

The PETM temperature anomaly at this site increases from 1.7 °C to 4.2 °C following corrections for dissolution effects and 10% recrystallization (Figure 4.4). It reduces to 3.6 °C if 25% recrystallization is assumed. The Δ_{47} estimates of PETM warming that are corrected for dissolution and recrystallization are similar to Mg/Ca estimates (~4 °C; Hollis et al., 2019; Penman et al., 2014; Zachos et al., 2003) for Site 1209 (Figures 4.3, 4.4).

4.2.3 Site 1409

We were unable to acquire samples corresponding to peak PETM conditions from Site 1409 (Penman et al., 2016), and thus focus on discussing the Late Paleocene and Early Eocene results. As with tropical Sites 865 and 1209 (this work), and mid-latitude Site 1263 (Chapter 3), absolute Δ_{47}-temperatures at mid-latitude Site 1409 are also substantially different from traditional $\delta^{18}O$-temperatures (Supplemental Table 4.S.3, 4.S.4) (Bornemann et al., 2016, 2014; Hollis et al., 2019), and Mg/Ca temperatures for the region (Bornemann et al., 2016, 2014; Gutjahr et al., 2017; Hollis et al., 2019), with mean offsets of ~5 and 7 °C, respectively. We calculate a $\delta^{18}O_{sw}$ using our corrected Δ_{47}-temperatures of ~0.20 ‰ VSMOW, which is higher than what was reported in a prior DeepMIP proxy synthesis (-0.81 ‰ VSMOW; Hollis et al., 2019) which is based on a latitudinal correction derived from modern data, adjusted for ice-free conditions

4.2.4 Site 690

At Site 690, as with the low and mid-latitude sites, Δ_{47}-temperatures are higher than $\delta^{18}O$-temperatures by ~4 °C (Figure 4.3) (Hollis et al., 2019; Kelly et al., 2005; Kozdon et al., 2020; Thomas et al., 2002), and lower than Mg/Ca temperatures by 10 °C (Kozdon et al., 2020). Late Paleocene Δ_{47}-SSTs are 15.3 °C and PETM values are 20.6 °C (Table 4.3). Average $\delta^{18}O_{sw}$ values for all samples calculated using Δ_{47}-SSTs are ~0.29 ‰ VSMOW, which is higher than the assumed latitudinally-adjusted ice-free value of -1.28 ‰ VSMOW (Table 4.3) (Hollis et al., 2019).

The PETM warming for Site 690 estimated from Δ_{47} is 5.3 °C, if non-thermal factors are considered (Figure 4.4). $\delta^{18}O$-based estimates of warming for Site 690 that have been published range from 3-7 °C (Figure 4.4) (Hollis et al., 2019; Kozdon et al., 2020). Mg/Ca estimates are ~4 °C (Figure 4.4) (Kozdon et al., 2020).

4.2.5 Impact of non-thermal effects on proxy comparison

As with Site 1263, we examined the impact on proxy agreement of considering non-thermal effects on planktic foraminiferal $\delta^{18}O$ and Mg/Ca, such as a pH effect (e.g, Spero et al., 1997, Zeebe et al., 1999) and dissolution effects (e.g. Brown and Elderfield, 1996; Dekens et al., 2002; Regenberg et al., 2014). Previous work has shown that pH corrections will increase $\delta^{18}O$-temperatures and decrease Mg/Ca-temperatures (Hollis et al., 2019). For a first-order set of calculations, we use the methods described in Chapter 3, including assuming a surface ocean pH of ~7.7 for the late Paleocene and early Eocene, and ~7.4 for the PETM (Anagnostou et al., 2016; Gutjahr et al., 2017; Penman et al., 2014; Uchikawa and Zeebe, 2010), and follow the correction procedure used in Hollis et al. (2019) for Mg/Ca and in Meckler et al. (2022) for $\delta^{18}O$. Dissolution corrections for $\delta^{18}O$ and Mg/Ca were also applied during the PETM window by

subtracting 0.30 ‰ and adding 0.54 mmol/mol for $\delta^{18}O$ and Mg/Ca respectively. These corrections, as with the Δ_{47} dissolution correction, are similarly based only on foraminifera and the difference between values above and below the carbonate saturation horizon from Chapter 2. With these corrections and a 10 % recrystallization correction, $\delta^{18}O$-temperatures increase by ~3 °C during the late Paleocene and by ~7 °C during the PETM at each site.

At all sites, the pH and diagenetically corrected values are closer to Δ_{47}-temperatures, with the average differences becoming < 1.5 °C, except for at Site 1209 where there is a difference of ~3.4 °C (Figure 4.4, Supplemental Table 4.S.3). Similarly, pH-corrected Mg/Ca temperatures have absolute values that are typically ~3-4 °C cooler (Chapter 3). Thus, factoring in pH effects helps to partially reconcile different proxy estimates of SST.

Just as absolute SSTs for each site, and the PETM anomalies, more closely align between proxies if pH effects and variable surface water $\delta^{18}O$ are considered, the SST gradients inferred from Δ_{47} more closely agree with $\delta^{18}O$ and Mg/Ca estimates. Differences may reflect factors such as variable $\delta^{18}O_{sw}$ that were not taken into account in calculations, and other factors influencing Mg/Ca. There is also a ~3 ^{o}C uncertainty in Mg/Ca-temperatures that arises from the value used for the H-factor (Hines et al., 2017), which reflects a biological and seawater Mg/Ca dependence of Mg/Ca incorporation (e.g. Segev and Erez, 2006; Stanley et al., 2005). Additionally, we can not preclude that diagenetic impacts (both dissolution and recrystallization) and other corrections are accounted for accurately at a given site for a specific proxy. For example, partial dissolution could occur outside of the PETM. The corrections used in all cases represent first-order estimates.

4.3. Implications

4.3.1 Climate model comparison

We compare Δ_{47}-temperatures for the late Paleocene and PETM to simulations from two DeepMIP models that have been run using the same boundary conditions for 3x and 6xCO_2 (Figure 4.5) (Lunt et al., 2021; Zhu et al., 2019). Both models have positive skill scores when compared with Δ_{47}. Δ_{47}-based temperature anomalies for the PETM are in better agreement with the GFDL CM2.1 model predictions for a doubling of CO_2 (Figure 4.5). The model skill score for GFDL CM2.1 is 0.781 and for CESM1.2 CAM5 is 0.534.

Late Paleocene temperatures (with higher estimates of recrystallization at Site 865 and 1209) agree well with the 3xCO_2 simulations in both models (Figure 4.3, 4.5). North Atlantic and tropical Pacific Δ_{47}-SSTs (from Sites 1409 and 1209, respectively) are slightly cooler than simulated values (Figures 4.3, 4.5). If the reconstructed Δ_{47}-SSTs are in fact robust, then it is possible that cooler temperatures may have occurred regionally associated with the North Atlantic Igneous Province (Gutjahr et al., 2017; Rampino, 2013; Saunders, 2016), due to aerosols blocking solar radiation (Saunders, 2016).

For the PETM values, Δ_{47}-temperatures for the mid- and high-latitude sites agree well with both models. However, Site 1209 is slightly cooler than is predicted by model simulations (29 °C as compared to 36.0 °C for GFDL CM1.2 and 34.6 °C for CESM2.1 CAM5) (Figure 4.5). Sediments at Site 1209 at the base of the PETM section are known to have undergone dissolution, which may have muted peak-PETM temperatures more than we have estimated (Bralower et al., 2014). It is also possible that larger amounts of recrystallization may have occurred.

4.3.2 Meridional SST gradients

Broadly, the clumped isotope gradients are in agreement with the multi-proxy average and model simulations (Figure 4.5), when non-thermal influences are considered for all proxies. The Δ_{47} estimates in Figure 4.5 support meridional temperature gradients for the Late Paleocene of ~16.7 °C that are more in line with model estimates for $3xCO_2$ (~ 21 °C) (Lunt et al., 2021; Steinig et al., 2024), assuming ~10% recrystallization at mid- and high-latitude sites, 25% recrystallization at Site 1209, and 50% recrystallization at Site 865. In contrast, if the Δ_{47} data are uncorrected for non-thermal effects, then the results would support a shallow temperature gradient of ~10.6 °C in the Late Paleocene, much shallower than those predicted by models or compared to modern temperature gradients (Lunt et al., 2021; Steinig et al., 2024). With the base corrections described in section 4.1 applied, the data would support a gradient of ~9.7 °C.

Meridional temperature gradients for the PETM from Δ_{47} (assuming 25 % recrystallization at Site 1209 and 10 % at Site 1263 and 690; extrapolated to 0 ° latitude) suggest pole to equator temperature gradients ~13 °C, shallower than what is calculated for the Late Paleocene. If no corrections are applied, this decreases to ~11 °C. The results support a decrease in latitudinal temperature gradients with increased temperatures, but a shallow value that is difficult to capture with models ($6xCO_2$ simulations estimate latitudinal gradients ~20 °C) (Lunt et al., 2021).

4.3.3 Meridional $\delta^{18}O_{sw}$ gradients

Estimates of mean ocean $\delta^{18}O_{sw}$ for ice-free conditions in the Late-Paleocene range from -0.89 ‰ to -1.11 ‰ VSMOW (Cramer et al., 2011; Hollis et al., 2019; L'homme et al., 2005). The $\delta^{18}O_{sw}$ estimates calculated using Δ_{47}-temperatures are on average higher than values calculated using the modern latitudinal adjustment (Broecker, 1989) to mean ice-free values for global ocean water (Tables 4.2 and 4.3) (Hollis et al., 2019). Table 4.3 also reports $\delta^{18}O_{sw}$ values

that are calculated by combining Δ_{47}-temperatures with recrystallization, dissolution, and pH-corrected $\delta^{18}O_{carb}$ values, which we assume are more robust. Figure 4.6 shows $\delta^{18}O_{sw}$ values as a function of latitude calculated with and without the pH correction for the Late Paleocene, PETM, and EECO compared to what would be predicted for an ice-free ocean using the modern gradient of LeGrande and Schmidt (2006) (Hollis et al., 2019). Our $\delta^{18}O_{sw}$ calculations with the corrections are more in-line with predicted values with slight variations between time intervals, most noticeably a drop in $\delta^{18}O_{sw}$ over the PETM at Site 1263 not reflected at other sites. Over the PETM and EECO $\delta^{18}O_{sw}$ values are also generally higher than that which would be predicted based on modern latitudinal gradients (Figure 4.6). These elevated values could be reflective of an intensified hydrologic cycle during these intervals or may be related to basin-specific effects not reflected in a modern latitudinal average. These calculations add to the discussion of whether latitudinal and regional $\delta^{18}O_{sw}$ gradients have been stable through time (Hollis et al., 2019; Roberts et al., 2009; Tindall et al., 2010).

5. Conclusions

The Late Paleocene and Early Eocene represent an important interval of Earth's history, characterized by elevated greenhouse gas concentrations, high global temperatures, and weak meridional sea surface temperature gradients. However, proxy estimates of sea surface temperatures and climate models disagree over the magnitude and patterns of warmth across different regions, and the nature of pole-to-equator temperature gradients, due to uncertainties in reconstructions and simulations. In this study, we applied the Δ_{47}-temperature proxy to planktic foraminifera and coccolith-dominated fine fraction in sediments to reconstruct SSTs and water $\delta^{18}O$ at multiple sites across varying latitudes and ocean basins, for the Late Paleocene, Paleocene-Eocene Thermal Maximum, and Early Eocene Climatic Optimum.

At all sites, Δ_{47}-temperatures fall between $\delta^{18}O$ and Mg/Ca estimates. If non-thermal factors, such as dissolution and recrystallization effects on Δ_{47}-based temperatures, and pH effects on $\delta^{18}O$ and Mg/Ca, are considered, then absolute SSTs and temperature anomalies are in closer agreement, which underscores the importance of accounting for these factors when reconstructing SST and comparing different proxies.

Δ_{47}-SSTs and PETM anomalies generally align with model simulations of temperatures at 3x and 6x pre-industrial CO_2 concentrations, when non-thermal effects on the proxy are considered. Δ_{47}-derived temperatures generally agree with model simulations, especially for mid- and high-latitude sections. In particular, incorporating higher levels of recrystallization at tropical Sites 865 and 1209 results in more plausible SSTs that align more closely with model predictions, and other proxy-based reconstructions.

The corrected Δ_{47}-SSTs support a more pronounced meridional gradient during the Late Paleocene (~16.7 °C), which is in closer agreement with model simulations at 3x CO_2, and a weaker gradient during the PETM, when we extrapolate values of 13 °C. Δ_{47}-constraints on seawater $\delta^{18}O$ also support changes in gradients compared to the present-day, potentially reflective of changes in the hydrologic cycle or basin specific effects.

This work highlights the potential for clumped isotopes and multi-proxy approaches in the study of paleoclimate. It highlights the importance of accounting for non-thermal effects such as recrystallization, dissolution, and pH changes on proxies to improve reconstructions and model-proxy comparisons.

Acknowledgements

This work was supported by Heising-Simons Foundation grant 2022-3314, DOE BES grant DE-FG02-83613ER16402, the Packard Foundation, and by NSF grants EAR-0949191, EAR-1352212, and RISE-228198. It was also supported by a Royal Society Wolfson Visiting Research Fellowship. We thank B. Elliot, H. Taylor, K. Miguel, and J. Rubi for lab support.

Open Research

All data are in the Supplementary information associated with this paper. In addition, on publication, all data will be archived in Pangaea and EarthChem.

6 Figures

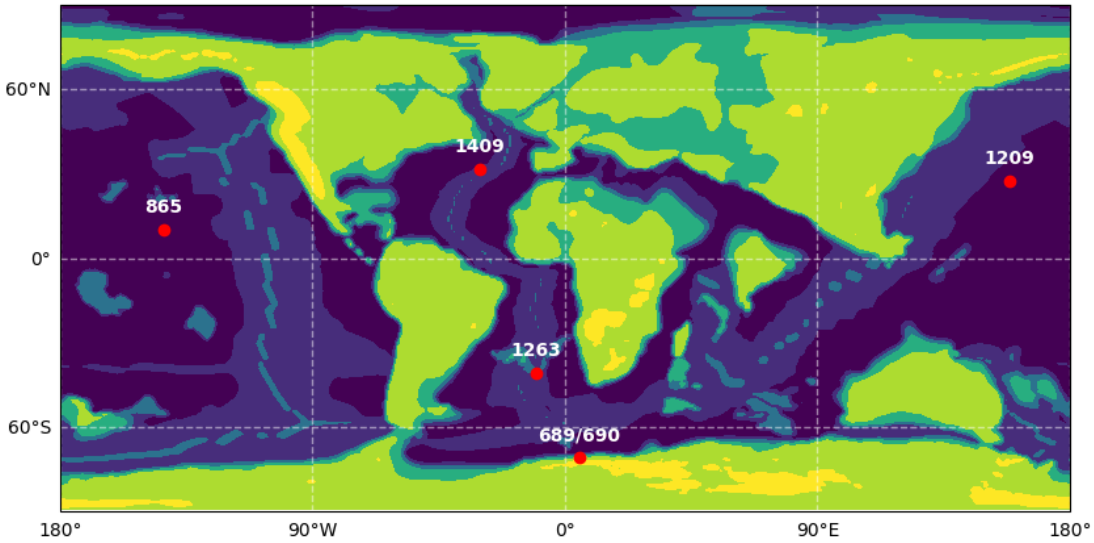

Figure 4.1: Paleogeographic site locations. Site locations are plotted on top of paleogeography for the early Eocene from Herold et al. (2014). Table 4.1 shows paleo-latitudes and paleo-water depths.

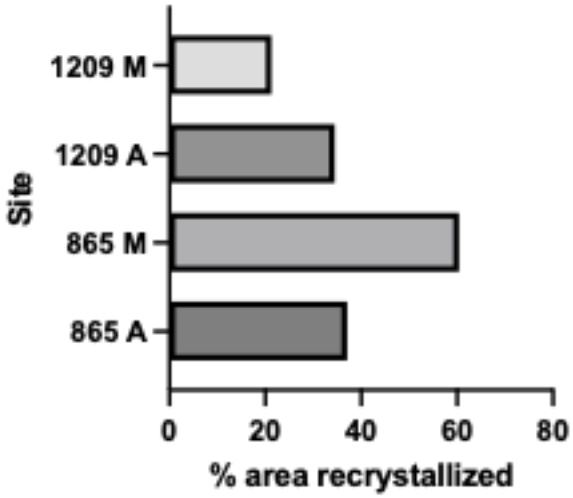

Figure 4.2: Full range of estimates from EBSD of area recrystallized for 161 specimens of Morozovella and Acaranina from Sites 865 and 1209. 89 specimens were measured from Site 865 (Acaranina n = 38; Morozovella n = 51) and 72 specimens from Site 1209 (Acaranina n = 40; Morozovella n = 32). Median values are Quartile 3 values are ~10-15%, and maximum values range from 20-35% at Site 1209, and 37-60% at Site 865. A histogram of the data is shown in Figure 4.S.6.

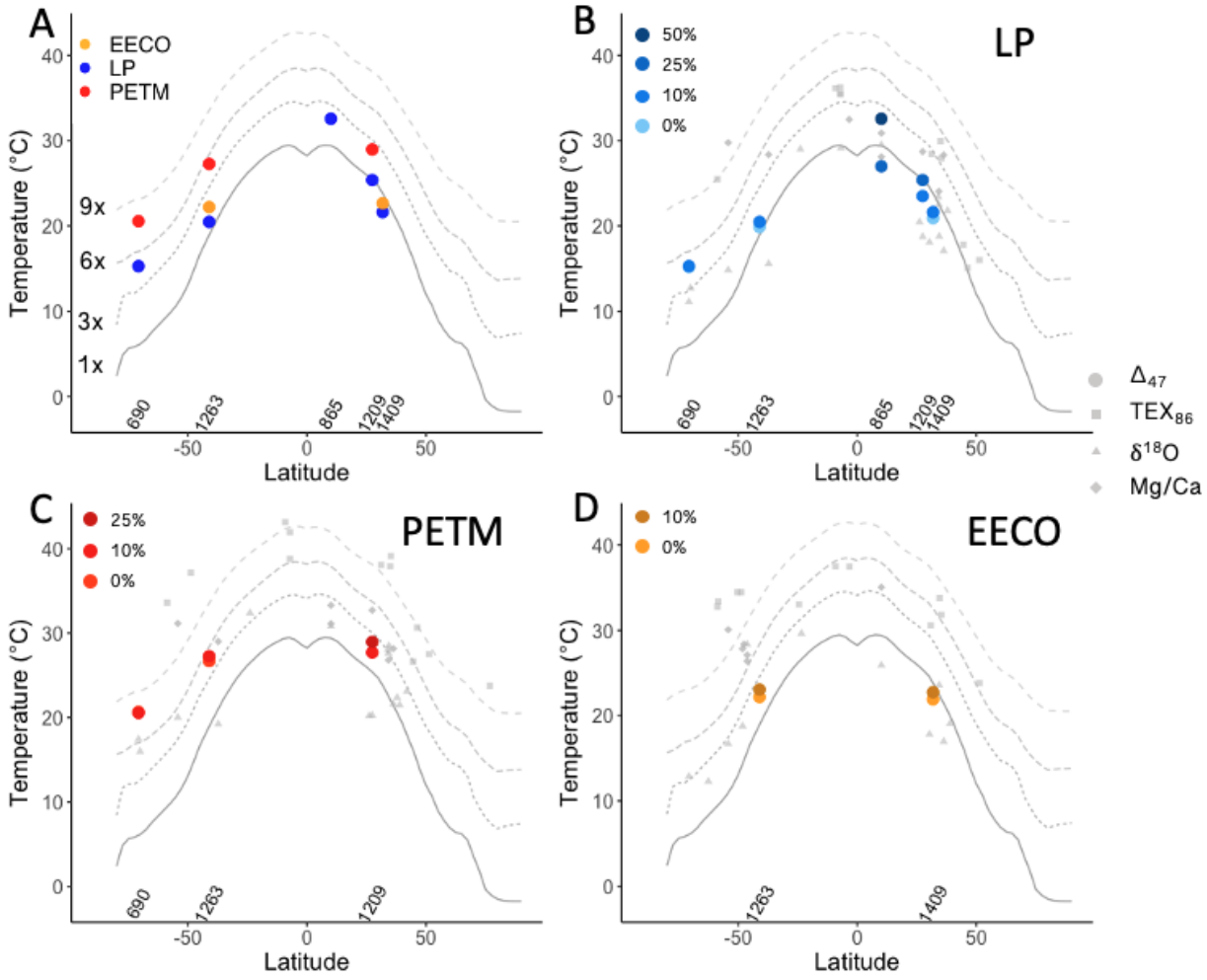

Figure 4.3: Comparison of Δ_{47}-temperatures and meridional temperature gradients for the Late Paleocene, PETM, and Early Eocene Climatic Optimum (EECO) to other proxies and to model simulations at varying CO_2. Δ_{47}-temperatures account for non-thermal influences. Model results at 1x, 3x, 6x, and 9x CO_2 are from the CESM1.2 CAM5 model (Lunt et al., 2021). Panel A assumes 10 % recrystallization at Sites 1409, 1263 and 690, 25 % recrystallization for Site 1209, and 50 % recrystallization for Site 865. Panels B-D assumes variable amounts of plausible recrystallization scenarios with prior proxy estimates from respective time periods. Panel B shows results for Late Paleocene. Panel C shows results for PETM. Panel D shows results for EECO. Δ_{47}-temperatures are generally warmer than $\delta^{18}O$-based temperatures and cooler than TEX_{86} and Mg/Ca for similar latitudes. Δ_{47}-temperature gradients are generally shallower than model simulations. Latitudinal gradients increase if more recrystallization is assumed. The best fit for the Late Paleocene data are the simulations with CESM 3x CO_2. Proxy temperatures from TEX_{86}, Mg/Ca, and $\delta^{18}O$ are compiled in Hollis et al. (2019).

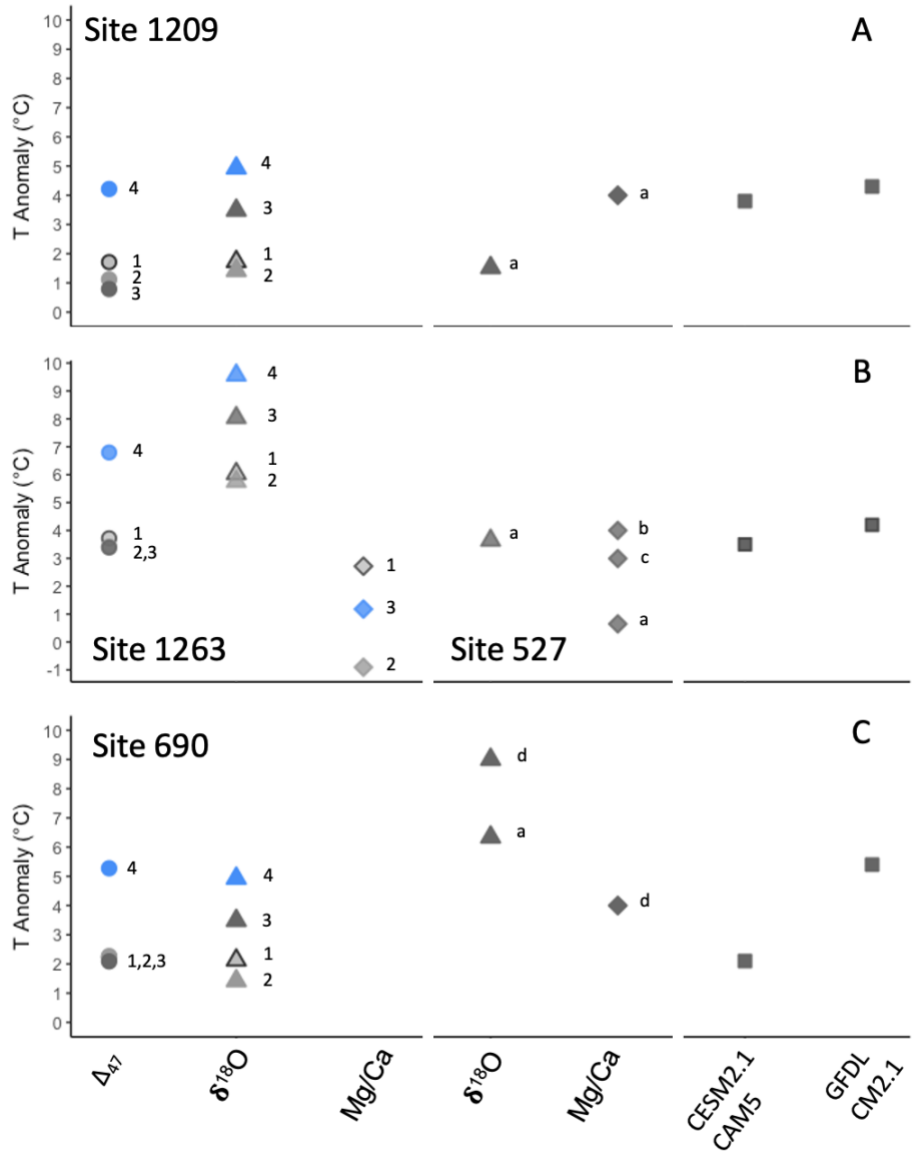

Figure 4.4: PETM warming calculated from different proxies and from DeepMIP models for different sites in this study. Results are shown for (A) Site 1209, (B) Site 1263, and (C) Site 690. Temperature anomalies are defined as PETM minus Late Paleocene values. Circles show Δ_{47} values with 1) no non-thermal effects, 2) fine fraction offset from foraminifera correction 3) same as 2 with 10 % recrystallization correction, 4) same as 3 with dissolution correction. Filled blue circle (4) shows the results of assuming there are non-thermal influences on Δ_{47}, and indicates a larger amount of warming than other reconstructions. Triangles are $\delta^{18}O$ with 1) no non-thermal effects, 2) 10 % recrystallization correction, 3) Same as 2 with pH correction, and 4) Same as 3 with dissolution correction. Diamonds are Mg/Ca at Site 1263 with 1) no non-thermal effects, 2) pH correction, and 3) same as 2 with dissolution correction. $\delta^{18}O$ and Mg/Ca temperatures are from (a) Hollis et al. (2019) (recalculated from Thomas et al. (2002), Kelly et al. (2005), Tripati and Elderfield (2004), Zachos et al. (2003) and Penman et al. (2014)), (b) Tripati and Elderfield (2004) (c) Dunkley-Jones et al. (2013) and (d) Kozdon et al. (2020) are shown. Data from different publications use different assumptions (see publications for details). DeepMIP values are from Lunt et al. (2021) and are based on the difference between $3xCO_2$ and $6xCO_2$ simulations at each site location.

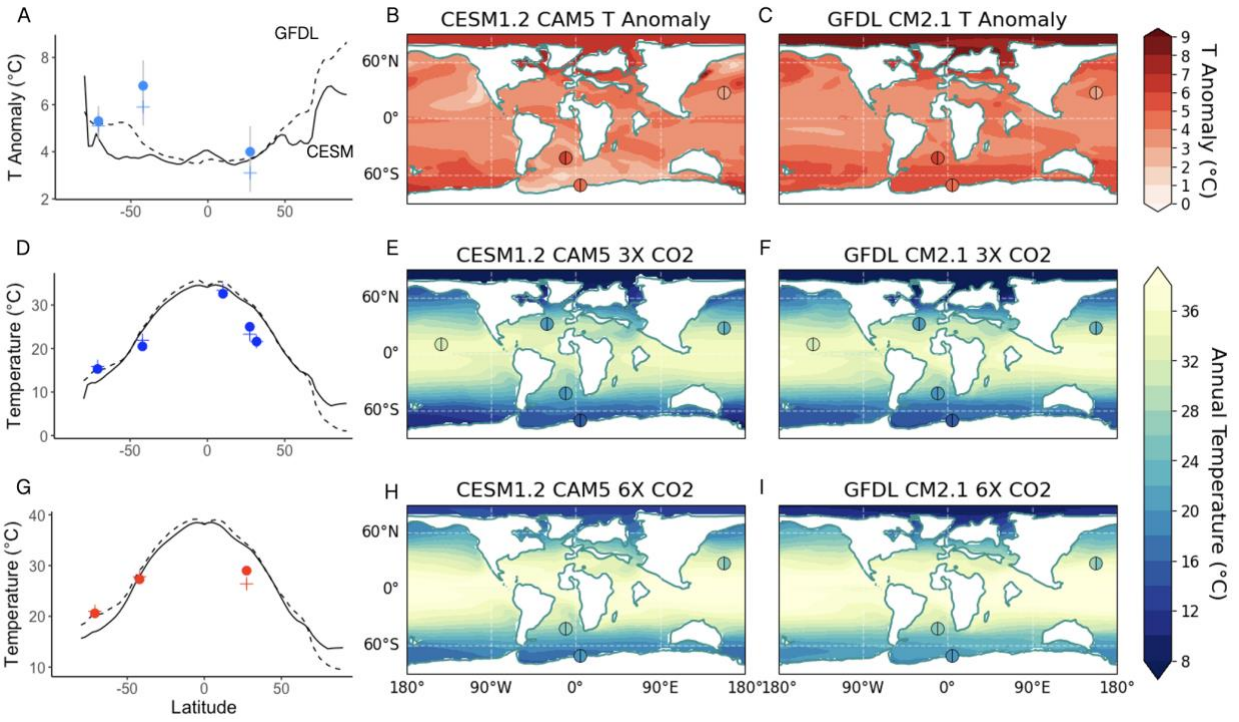

Figure 4.5: Δ_{47}-temperatures for the Late Paleocene and PETM compared with DeepMIP model simulations. Proxy reconstructions use values factoring in non-thermal influences. For Δ_{47}-temperatures this includes a 0.006 ‰ fine fraction correction, 10 % recrystallization at Sites 1263, 690, and 1409, 25 % recrystallization at Site 1209, 50 % recrystallization at Site 865, and a dissolution correction for the PETM at all sites. The left column with panels A, D, G show the absolute SSTs or temperature anomalies, and 1 SE error, where circles are Δ_{47}-temperatures and the cross is the multi-proxy mean. This comparison shows evidence for a convergence in the data, and more generally with model results, when non-thermal influences are considered. For the right two columns, with panels B, C, E, F, H, I) Left half of the symbol indicates mean Δ_{47}-temperatures for the E, F) Late Paleocene and H, I) PETM or the B, C) temperature anomaly from Δ_{47}-temperatures. The right half of the circles indicates the multiproxy average temperatures or multiproxy temperature anomalies for the same intervals. Model output is from DeepMIP (Lunt et al., 2021). 3X CO_2 simulations are compared to values from the late Paleocene, and 6X simulations are compared to values from the PETM. Temperature anomalies are given as the differences between 6X and 3X CO_2 simulations and PETM-LP temperatures from clumped isotopes. Model skill score for CESM1.2 CAM5 is 0.534 and for GFDL CM2.1 is 0.781 based on Δ_{47}-temperatures only, and 0.549 and 0.794 respectively for those with Δ_{47} and $\delta^{18}O$ averaged together.

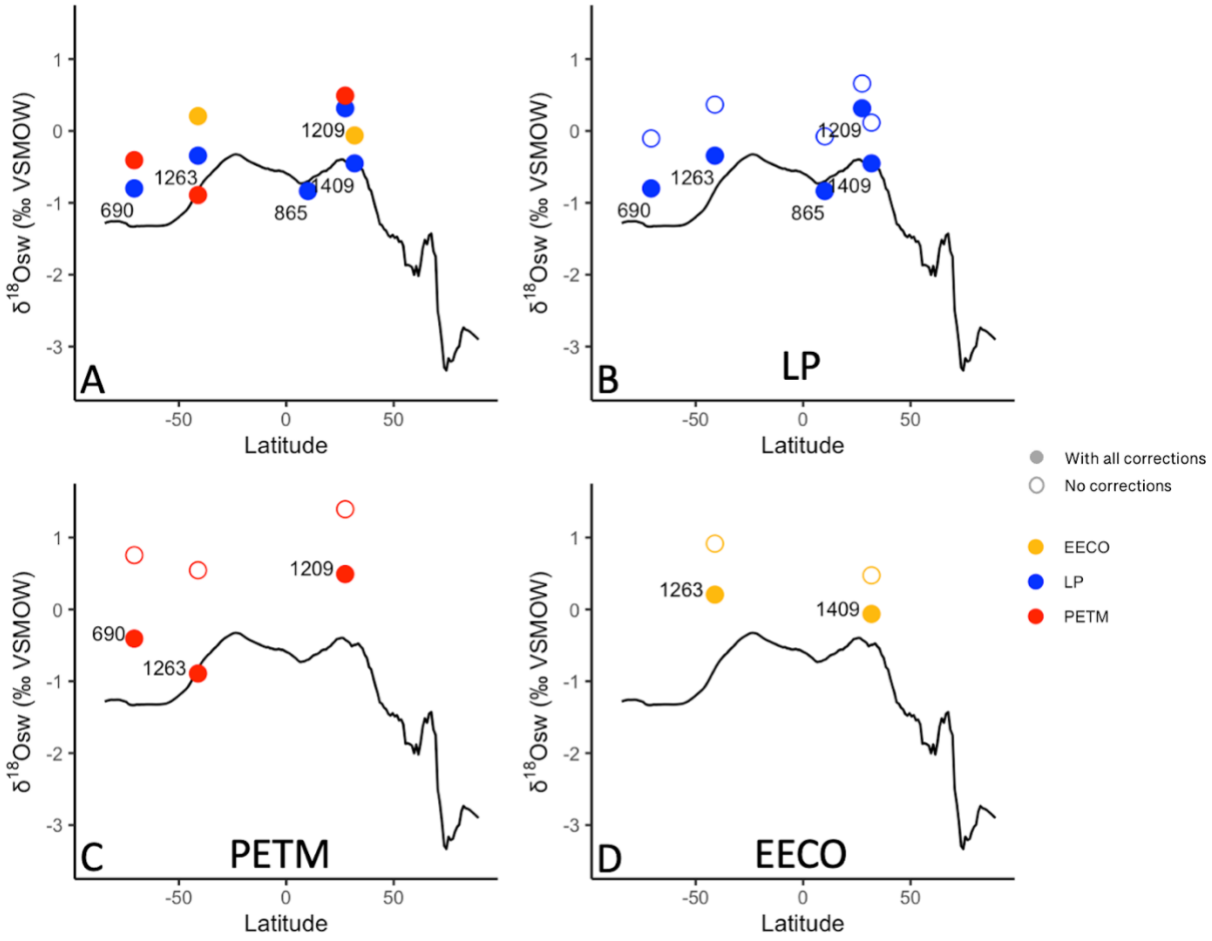

Figure 4.6: $\delta^{18}O_{sw}$ calculated from clumped isotopes. The line is the latitudinal $\delta^{18}O_{sw}$ from LeGrande and Schmidt (2006) offset by -1 ‰ to estimate ice-free values (as in Hollis et al., 2019). Panel A) Calculated values using the SSTs and same assumptions as in Figure 4.5. Δ_{47} values were corrected for a fine fraction offset, assuming 10 % recrystallization at Sites 690, 1263, and 1409, 25 % at Site 1209, and 50 % at Site 865 and a dissolution correction at the PETM. $\delta^{18}O_{carb}$ values were corrected assuming the same levels of recrystallization, a pH correction assuming values of 7.7 outside of the PETM window and 7.4 during the PETM, and a dissolution correction at the PETM. Panels B, C, and D compare corrected and uncorrected values for $\delta^{18}O_{sw}$ for the B) late Paleocene C) PETM and D) EECO. Corrected values are much closer to ice-free estimates of $\delta^{18}O_{sw}$.

7 Tables

Site	Paleolatitude[1]	Estimated Paleodepth (m)[2]
1409	31.7893 °N	3000
689	70.0962 °S	1100
690	70.7624 °S	1900
1209	27.4230 °N	1900
865	10.0790 °N	1300-1500
1263 (Chapter 3)	41.0937 °S	1500

[1]Paleolatitude calculated with (Hinsbergen et al., 2015)

[2]Estimates of paleodepth from (Bralower et al., 1995; Norris et al., 2014; Takeda and Kaiho, 2007; Thomas and Shackleton, 1996; Zachos et al., 2005)

Table 4.1: Site locations

Clumped isotope temperatures, uncorrected (°C)

		LP (55.93 - 56.05 Ma)				Peak PETM (55.82 - 55.89 Ma)				Post PETM (55.5 - 55.82 Ma)				EECO (51 - 54 Ma)			
Site	Archive	n	analyses	Mean	SE	n	analyses	Mean	SE	n	analyses	Mean	SE	n	analyses	Mean	SE
865	Foraminifera	11	64	24	0.8	13	21	24	0.8								
1209	Foraminifera	2	9	22.3	0.8	6	35	24.3	1.5	2	9	21.1	2.1				
	Fine fraction	14	160	20.6	0.6	8	93	21.2	0.8	28	156	20.9	0.4				
1409	Foraminifera	8	41	19.7	0.5					6	30	19.2	1	8	41	21.3	0.7
	Fine fraction	9	47	19.9	2.3					13	65	18.1	1.2	6	27	20.7	0.6
690	Fine fraction	11	113	13.4	0.5	12	130	15.6	0.4	34	172	16.2	0.5				
1263, Chapter 3	Foraminifera	15	75	19.4	0.7	17	67	23.4	1.2	29	131	20.3	0.5	4	20	20.8	1
	Fine fraction	19	96	18.3	0.7	11	59	21.2	1	21	112	18.5	0.5	3	17	20.3	2

$\delta^{18}O_{sw}$ with uncorrected clumped isotope values and no pH correction in $\delta^{18}O_{carb}$ (‰ VSMOW)

		LP (55.93 - 56.05 Ma)				Peak PETM (55.82 - 55.89 Ma)				Post PETM (55.5 - 55.82 Ma)				EECO (51 - 54 Ma)			
Site	Archive	n	analyses	Mean	SD	n	analyses	Mean	SD	n	analyses	Mean	SD	n	analyses	Mean	SD
865	Foraminifera	11	64	0.17	0.6	13	21	0.17	0.6								
1209	Foraminifera	2	9	0.37	0.1	6	35	0.47	0.8	2	9	0.07	0.8				
	Fine fraction	14	160	0.87	0.1	8	93	0.67	0.2	28	156	0.97	0.1				
1409	Foraminifera	8	41	-0.13	0.7					6	30	-0.13	0.6	12	58	0.17	0.7
	Fine fraction	9	47	0.57	1					13	65	0.17	1.3	10	17	0.97	0.6
690	Fine fraction	11	113	-0.13	0.1	12	130	-0.03	0.1	34	172	0.27	0.1				
1263, Chapter 3	Foraminifera	15	75	0.07	0.6	17	67	-0.03	0.7	29	131	0.37	0.6	4	20	0.47	0.4
	Fine fraction	19	96	0.67	0.6	11	59	-0.33	0.8	21	112	0.87	0.5	3	17	1.27	0.8

Table 4.2: Mean Δ_{47}-temperatures and $\delta^{18}O_{sw}$ for different intervals with no consideration of non-thermal effects on proxies

Clumped isotope temperatures, corrected (°C)

		LP (55.93 - 56.05 Ma)				Peak PETM (55.82 - 55.89 Ma)				Post PETM (55.5 - 55.82 Ma)				EECO (51 - 53 Ma)			
Site	Archive	n	analyses	Mean	SE	n	analyses	Mean	SE	n	analyses	Mean	SE	n	analyses	Mean	SE
865	Foraminifera	11	64	25	1	*13*	*21*	*28.1*	*0.9*								
	Foraminifera	2	9	23.1	0.9	6	35	28.5	1.7	2	9	21.8	2.4				
1209	Fine fraction	14	160	23.6	0.7	8	93	27.1	0.9	28	156	23.8	0.4				
	Foraminifera	8	41	20.3	1.2					6	30	19.7	1.1	8	41	22.1	0.8
1409	Fine fraction	9	47	22.7	1.9					13	65	20.7	1.4	6	27	23.6	0.6
690	Fine fraction	11	113	15.3	0.5	12	130	20.6	0.4	34	172	18.5	0.5				
	Foraminifera	15	75	20	0.8	17	67	27.4	1.4	29	131	21.1	0.6	4	20	21.5	1.1
1263, Chapter 3	Fine fraction	19	96	20.9	0.8	11	59	27.1	1.2	21	112	21	0.6	3	17	23.1	2.3

$\delta^{18}O_{sw}$ with corrected clumped isotope temperatures and pH correction in $\delta^{18}O_{carb}$ (‰ VSMOW)

		LP (55.93 - 56.05 Ma)				Peak PETM (55.82 - 55.89 Ma)				Post PETM (55.5 - 55.82 Ma)				EECO (51 - 53 Ma)			
Site	Archive	n	analyses	Mean	SD	n	analyses	Mean	SD	n	analyses	Mean	SD	n	analyses	Mean	SD
865	Foraminifera	11	64	-0.58	0.65	*13*	*21*	*-0.12*	*0.63*								
	Foraminifera	2	9	-0.37	0.12	6	35	0.22	0.82	2	9	-0.58	0.87				
1209	Fine fraction	14	160	0.21	0.53	8	93	0.5	0.52	28	156	0.35	0.5				
	Foraminifera	8	41	-0.87	0.74					6	30	-0.89	0.61	8	41	-0.54	0.52
1409	Fine fraction	9	47	-0.08	1.16					13	65	-0.46	1.44	6	27	0.57	0.25
690	Fine fraction	11	113	-0.8	0.42	12	130	-0.41	0.43	34	172	-0.35	0.66				
	Foraminifera	15	75	-0.72	0.59	17	67	-0.48	0.69	29	131	-0.36	0.63	4	20	-0.32	0.5
1263, Chapter 3	Fine fraction	19	96	-0.05	0.62	11	59	-0.77	0.79	21	112	0.08	0.53	3	17	1	0.17

Table 4.3: Mean Δ_{47}-temperatures and $\delta^{18}O_{sw}$ for different intervals with consideration of non-thermal effects as described in 4.1 and 4.3.2

Supplemental information Chapter 4

S1 Age model adjustments to CENOGRID

Ages for each core were roughly updated to the CENOGRID time scale through tie points in the carbon isotope records of each site to that of Site 1263 (Westerhold et al., 2020). Primary time points were the beginning of the carbon isotope excursion at 55.93 Ma and the minimum carbon isotope value representing the peak of the PETM tied to 55.87 Ma. Age models were adjusted to these time points across the PETM and otherwise used ages relative to the PETM boundary as published in prior studies (Bralower et al., 1995; Farley and Eltgroth, 2003; Kelly et al., 2012; Norris et al., 2014; Westerhold et al., 2018). Further age model refinement to the CENOGRID timescale is recommended if orbital scale variations are to be analyzed in the future, however, due to the long-term boxed averages used for analysis, detailed age model tuning was not necessary in this study.

S2 Electron Backscatter Diffraction

S2.1 Samples and Sample Preparation

Specimens of *Acaranina* and *Morozovella* were collected from Sites 865, 1209. 5-10 specimens of each species, per locality and horizon, were picked with a paint brush, and placed with different orientations with a needle, on a double-sided tape adhered to the base of a resin holder. Once the samples were adhered to the tape, they were covered with Buehler EpoThin epoxy resin. After the resin was cured and removal of the tape with a needle, samples with the foraminifera were manually grinded and polished following a series of modified steps from the protocol in Perez-Huerta and Cusack (2009), with Bueheler grinding (grit size) paper and polishing clothes, as follows: 1) 5 seconds intervals until the samples are exposed with 240/P280 size paper; 2) 30 seconds on 320/P400, 400/P800, 600/P1200 size papers; 3) 1 minutes on

800/P1500 size paper; 4) 10 minutes on 1200/P2500 size paper; 5) 10-15 minutes of polishing with 1 μm alumina micropolish; 6) 5-10 minutes of polishing with 0.3 μm alumina micropolish; and 7) 5 minutes of sample ultrasonication in distilled water.

S2.2 Electron Backscatter Diffraction (EBSD)

Electron backscatter diffraction (EBSD) is an *in situ* microscopy technique that provides high-resolution crystallographic information at nano- to micro-scales and it is widely used to characterize biomineral structures (see review in Cusack and Chung, 2014). Its expediency has been also demonstrated in detecting diagenesis in fossils (e.g., Dalbeck et al., 2011; Pérez-Huerta et al., 2012; Coronado et al., 2013; 2015). For EBSD analyses, samples were coated with a thin layer (2.5 nm) of carbon and surrounded by silver paint to avoid electron charging carbon (Pérez-Huerta and Cusack 2009). The EBSD study was carried out with a Hikari EDAX camera mounted on a Field Emission Scanning Electron Microscope (FIB-FESEM) TESCAN LYRA located in the Central Analytical Facility (CAF) of The University of Alabama. EBSD data were collected with OIM 7.0 software at high vacuum, 30 kV, large beam intensity (10), and a high spatial resolution of 0.2 μm step size for diffraction and crystallographic maps. Finally, data were analyzed using OIM 5.3 from EDAX-TSL. In this study, EBSD data are represented by diffraction maps, crystallographic maps and pole figures, which represent the stereographic projection of crystallographic planes in reference to the {0001} and {10-14} calcite planes (see further details in Pérez-Huerta and Cusack, 2008; Pérez-Huerta et al., 2011). Four to five specimens, with different orientations, were chosen from each species and site horizon for EBSD analyses for an inter-specimen comparison of sample preservation. Within a single specimen, 3-5 regions of the wall of the test were analyzed to determine the intra-specimen preservation and potential diagenetic alteration.

S2.3 Specimen Recrystallization Calculation

Only some specimens of *Morozovella* and *Acarinina* present significant diagenetic alteration. To calculate the percentage of recrystallization per specimen area in the analyzed polished test section by EBSD, the three most altered specimens in a sample were chosen. To double-check the results for a given collection site, specimens from two horizons of site 1209 [at intervals 110-112 cm (1209B13) and 118-120 (1209B14)] were analyzed. The areas that presented some alteration, were defined and the percentage calculated with ImageJ imaging software (Schneider et al., 2012). This approach allows for a semi-quantitative (analyzing a 2D section of a 3D object) calculation of the maximum percentage recrystallization of foraminifera specimens for a given location.

Supplementary Figures

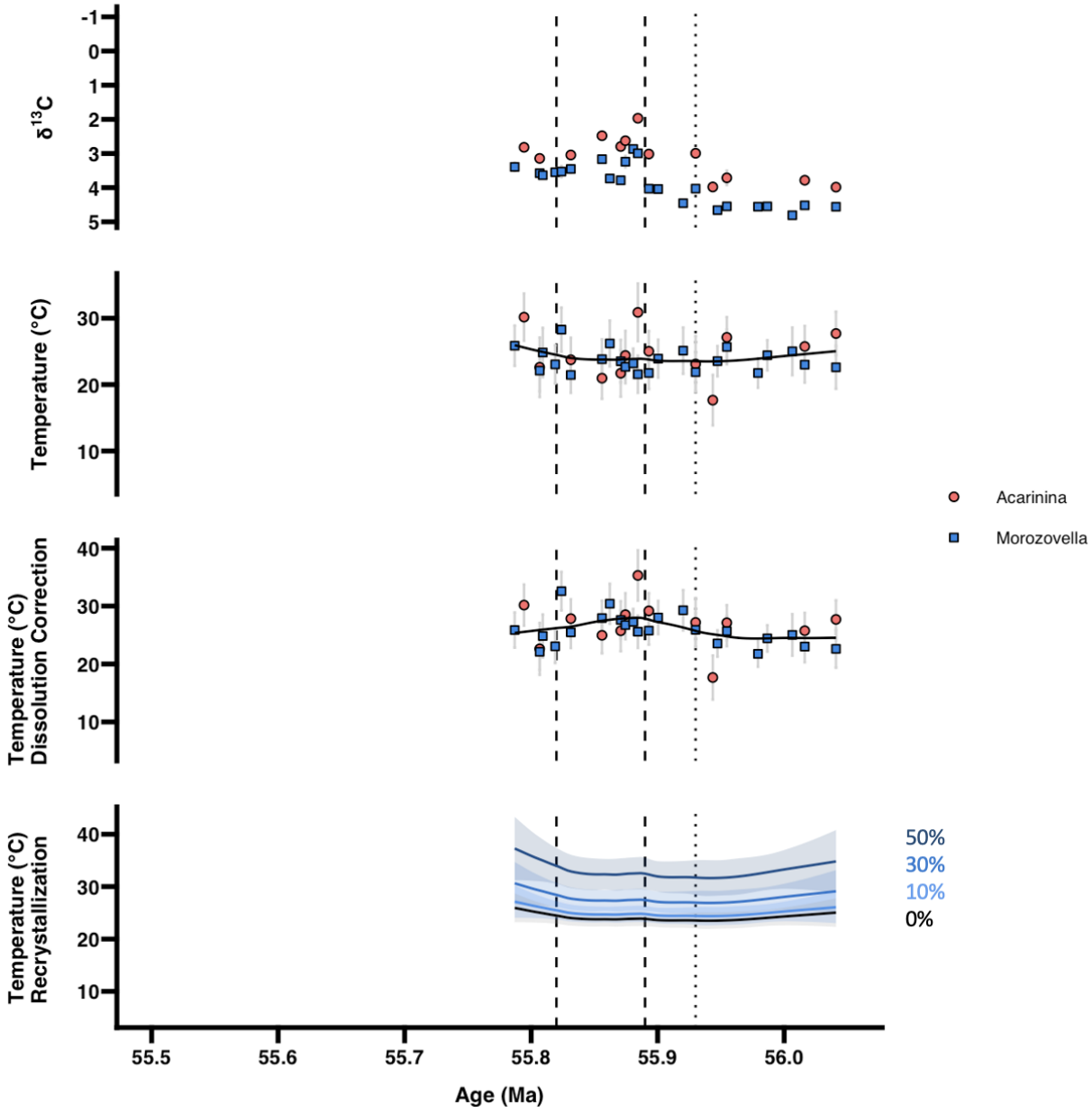

Figure 4.S.1: $\delta^{13}C$, temperatures, and applied corrections at Site 865. The vertical dotted line marks the start of the carbon isotope excursion, and the vertical dashed lines mark the Peak PETM interval as considered in this study.

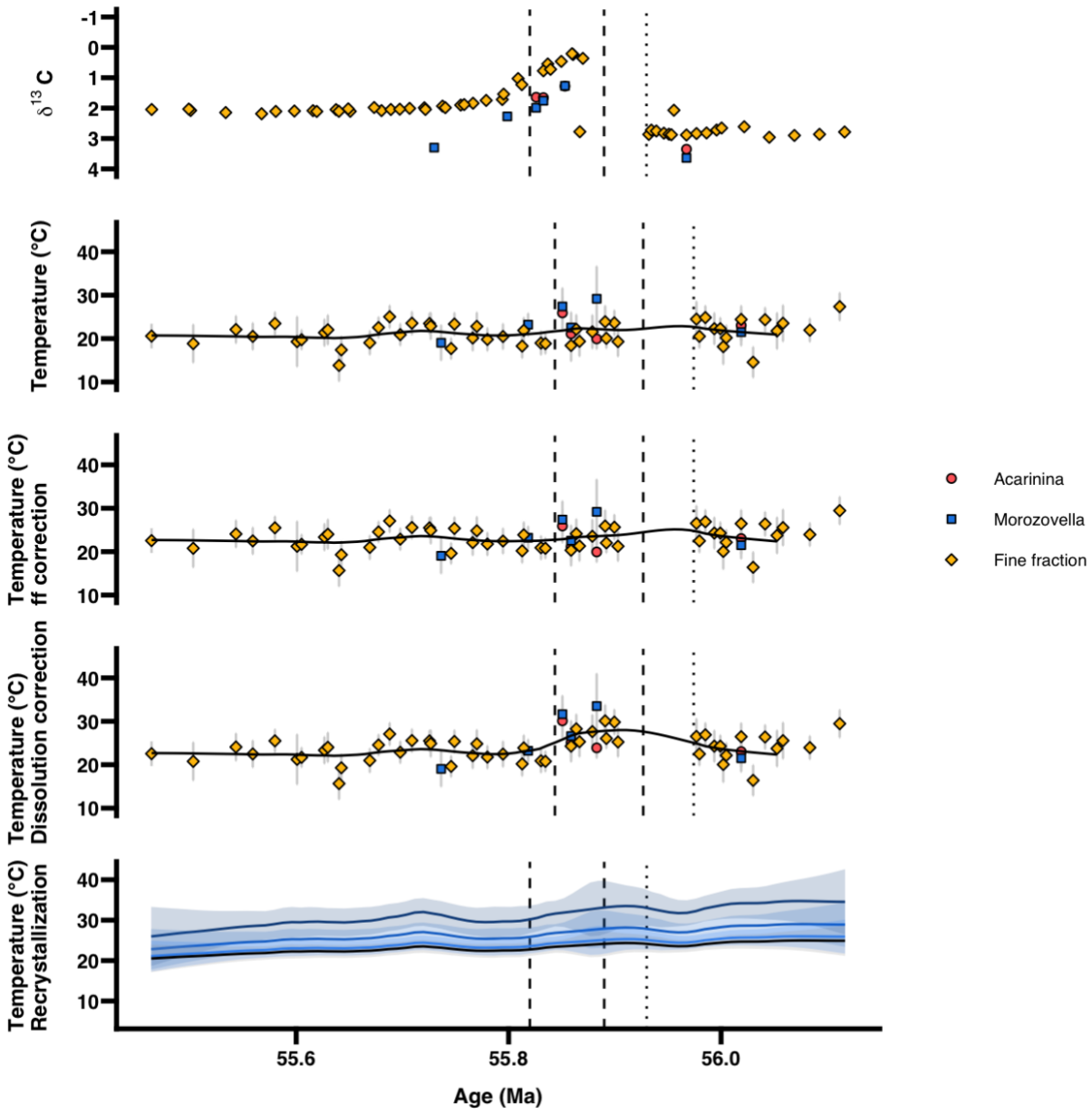

Figure 4.S.2: $\delta^{13}C$, temperatures, and applied corrections at Site 1209. The vertical dotted line marks the start of the carbon isotope excursion, and the vertical dashed lines mark the Peak PETM interval as considered in this study. Regressions are LOESS smoothing functions that have a span of 0.3.

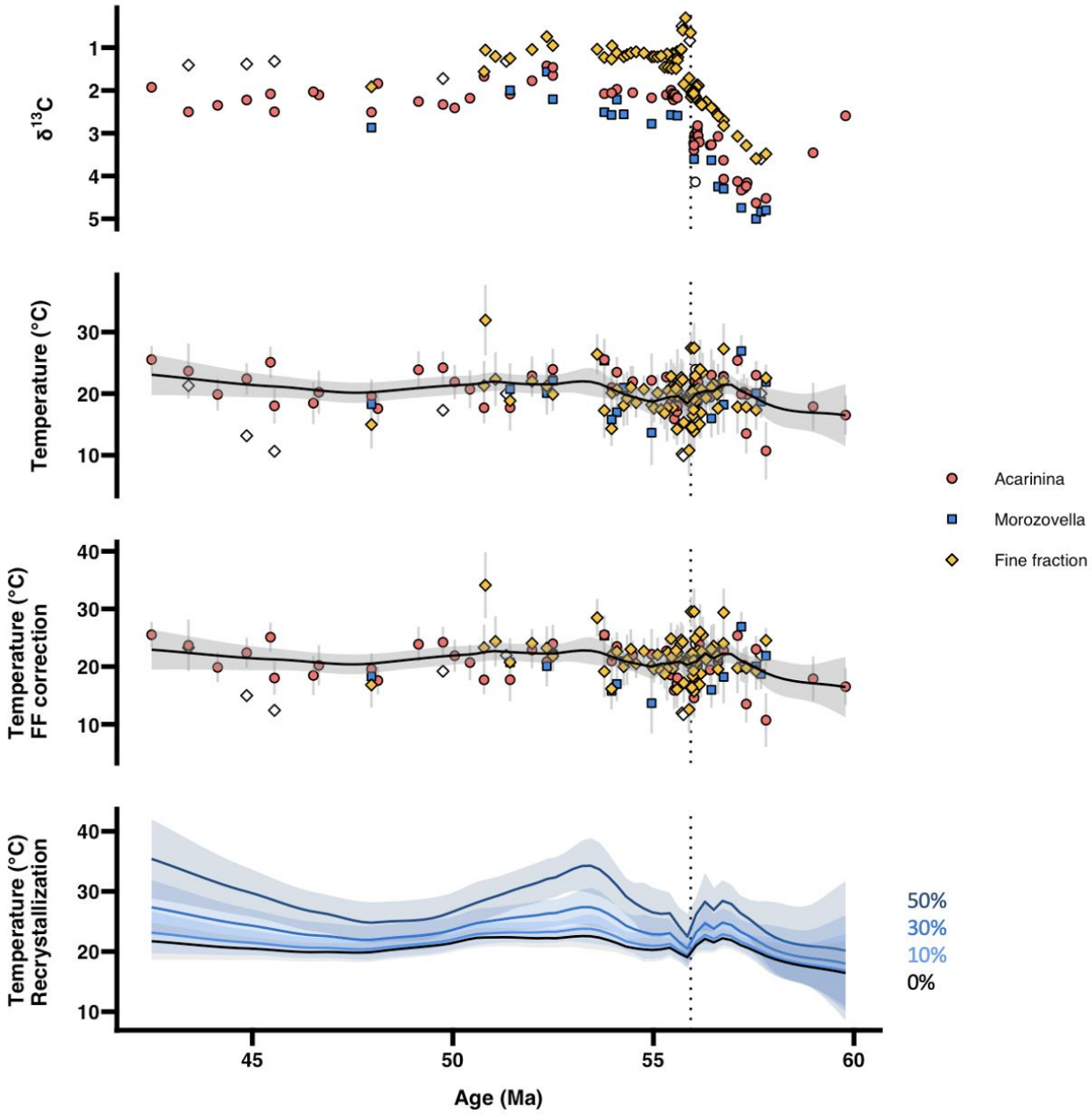

Figure 4.S.3: $\delta^{13}C$, temperatures, and applied corrections at Site 1409. The vertical dotted line marks the start of the carbon isotope excursion, not fully captured at this site. Regressions are LOESS smoothing functions that have a span of 0.2.

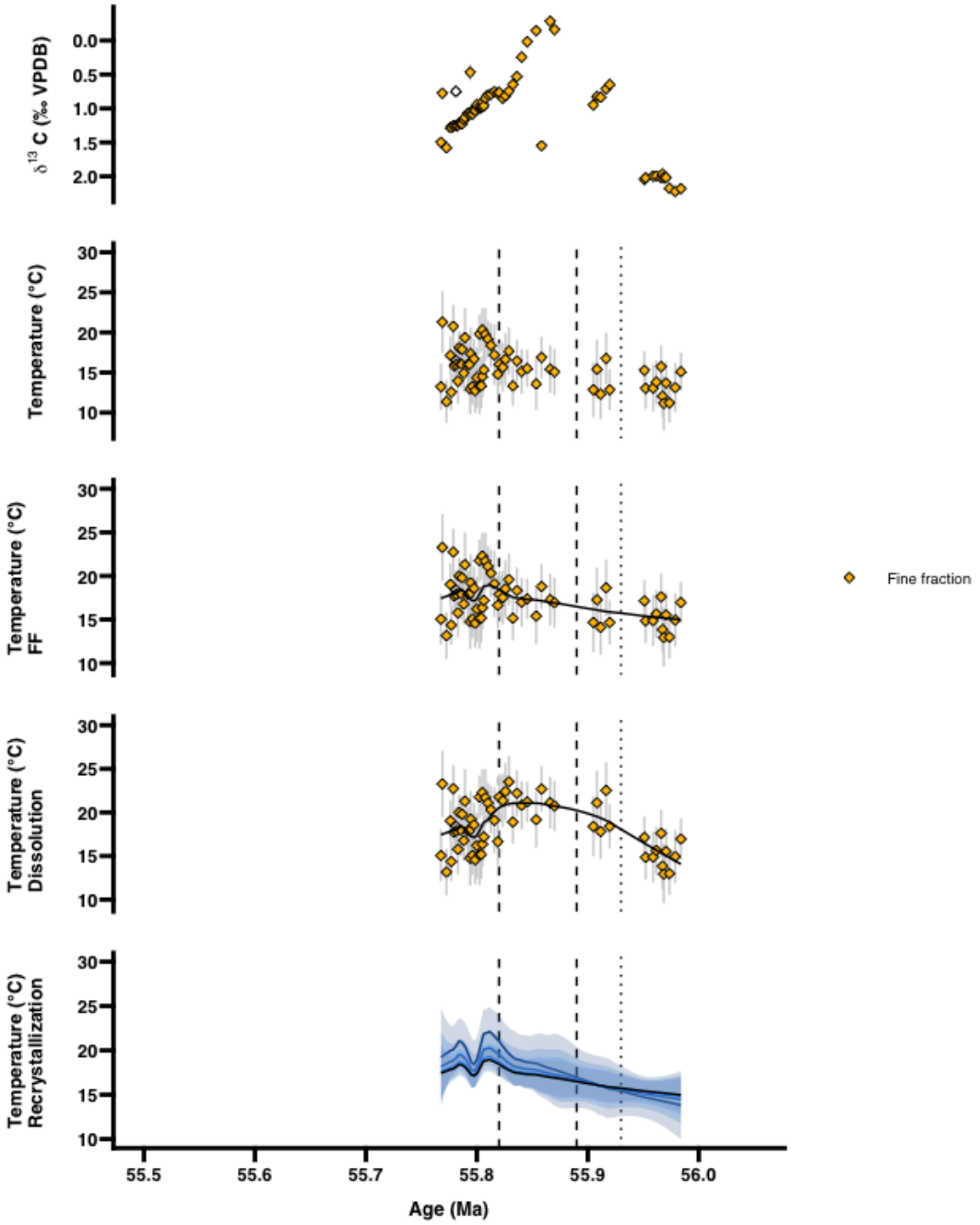

Figure 4.S.4: $\delta^{13}C$, temperatures, and applied corrections at Site 690. The vertical dotted line marks the start of the carbon isotope excursion, and the vertical dashed lines mark the Peak PETM interval as considered in this study. Regressions are LOESS smoothing functions that have a span of 0.3.

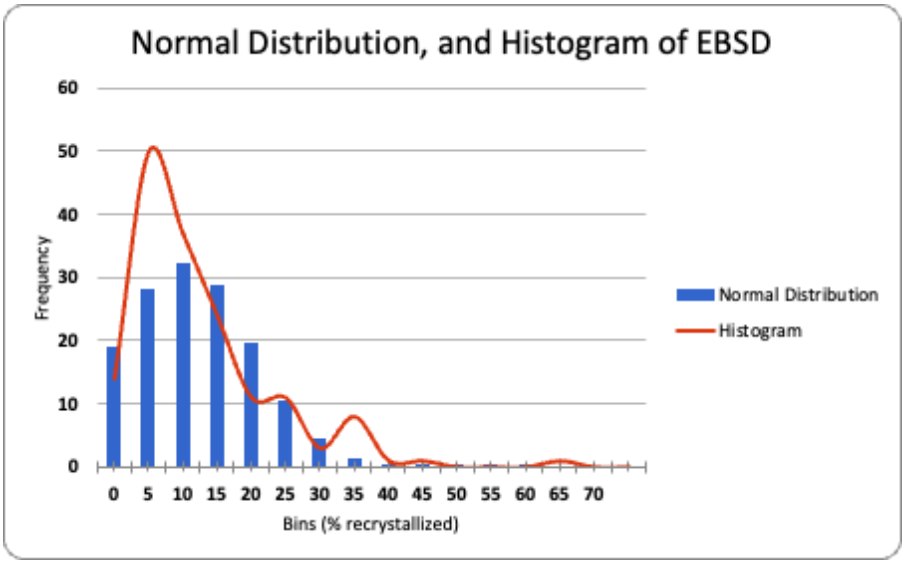

Figure 4.S.5: Histogram of EBSD results from Sites 1209 and 865 compared to a normal distribution. Mean 10%, median 7.2%, n = 161.

References

Adebowale, M., 2021. Rate and amplitudes of climate change – are there tipping points in marine ecosystems (Dissertation). University of Bristol.

Anagnostou, E., John, E.H., Edgar, K.M., Foster, G.L., Ridgwell, A., Inglis, G.N., Pancost, R.D., Lunt, D.J., Pearson, P.N., 2016. Changing atmospheric CO2 concentration was the primary driver of early Cenozoic climate. Nature 533, 380–384. https://doi.org/10.1038/nature17423

Anderson, N.T., Kelson, J.R., Kele, S., Daëron, M., Bonifacie, M., Horita, J., Mackey, T.J., John, C.M., Kluge, T., Petschnig, P., Jost, A.B., Huntington, K.W., Bernasconi, S.M., Bergmann, K.D., 2021. A Unified Clumped Isotope Thermometer Calibration (0.5–1,100°C) Using Carbonate-Based Standardization. Geophys. Res. Lett. 48, e2020GL092069. https://doi.org/10.1029/2020GL092069

Bemis, B.E., Spero, H.J., Bijma, J., Lea, D.W., 1998. Reevaluation of the oxygen isotopic composition of planktonic foraminifera: Experimental results and revised paleotemperature equations. Paleoceanography 13, 150–160. https://doi.org/10.1029/98PA00070

Bernasconi, S.M., Daëron, M., Bergmann, K.D., Bonifacie, M., Meckler, A.N., Affek, H.P., Anderson, N., Bajnai, D., Barkan, E., Beverly, E., Blamart, D., Burgener, L., Calmels, D., Chaduteau, C., Clog, M., Davidheiser-Kroll, B., Davies, A., Dux, F., Eiler, J., Elliott, B., Fetrow, A.C., Fiebig, J., Goldberg, S., Hermoso, M., Huntington, K.W., Hyland, E., Ingalls, M., Jaggi, M., John, C.M., Jost, A.B., Katz, S., Kelson, J., Kluge, T., Kocken, I.J., Laskar, A., Leutert, T.J., Liang, D., Lucarelli, J., Mackey, T.J., Mangenot, X., Meinicke, N., Modestou, S.E., Müller, I.A., Murray, S., Neary, A., Packard, N., Passey,

B.H., Pelletier, E., Petersen, S., Piasecki, A., Schauer, A., Snell, K.E., Swart, P.K., Tripati, A., Upadhyay, D., Vennemann, T., Winkelstern, I., Yarian, D., Yoshida, N., Zhang, N., Ziegler, M., 2021. InterCarb: A Community Effort to Improve Interlaboratory Standardization of the Carbonate Clumped Isotope Thermometer Using Carbonate Standards. Geochem. Geophys. Geosystems 22, e2020GC009588. https://doi.org/10.1029/2020GC009588

Bijl, P.K., Schouten, S., Sluijs, A., Reichart, G.-J., Zachos, J.C., Brinkhuis, H., 2009. Early Palaeogene temperature evolution of the southwest Pacific Ocean. Nature 461, 776–779. https://doi.org/10.1038/nature08399

Bornemann, A., D'haenens, S., Norris, R.D., Speijer, R.P., 2016. The demise of the early Eocene greenhouse – Decoupled deep and surface water cooling in the eastern North Atlantic. Glob. Planet. Change 145, 130–140. https://doi.org/10.1016/j.gloplacha.2016.08.010

Bornemann, A., Norris, R.D., Lyman, J.A., D'haenens, S., Groeneveld, J., Röhl, U., Farley, K.A., Speijer, R.P., 2014. Persistent environmental change after the Paleocene–Eocene Thermal Maximum in the eastern North Atlantic. Earth Planet. Sci. Lett. 394, 70–81. https://doi.org/10.1016/j.epsl.2014.03.017

Boucher, O., Randall, D., Artaxo, P., Bretherton, C., Feingold, G., Forster, P., Kerminen, V.-M., Kondo, Y., Liao, H., Lohmann, U., others, 2013. Clouds and aerosols, in: Climate Change 2013: The Physical Science Basis. Contribution of Working Group I to the Fifth Assessment Report of the Intergovernmental Panel on Climate Change. Cambridge University Press, pp. 571–657.

Bralower, T.J., Kelly, D.C., Gibbs, S., Farley, K., Eccles, L., Lindemann, T.L., Smith, G.J., 2014. Impact of dissolution on the sedimentary record of the Paleocene–Eocene thermal maximum. Earth Planet. Sci. Lett. 401, 70–82. https://doi.org/10.1016/j.epsl.2014.05.055

Brown, S.J., Elderfield, H., 1996. Variations in Mg/Ca and Sr/Ca ratios of planktonic foraminifera caused by postdepositional dissolution: Evidence of shallow Mg-dependent dissolution. Paleoceanography 11, 543–551. https://doi.org/10.1029/96PA01491

CenCO2PIP, 2023. Toward a Cenozoic history of atmospheric CO2. Science 382, eadi5177. https://doi.org/10.1126/science.adi5177

Cisneros-Lazaro, D., Adams, A., Guo, J., Bernard, S., Baumgartner, L.P., Daval, D., Baronnet, A., Grauby, O., Vennemann, T., Stolarski, J., Escrig, S., Meibom, A., 2022. Fast and pervasive diagenetic isotope exchange in foraminifera tests is species-dependent. Nat. Commun. 13, 113. https://doi.org/10.1038/s41467-021-27782-8

Clark, A.J., Torres-Romero, I., Jaggi, M., Bernasconi, S.M., Stoll, H.M., 2024. A clumped isotope calibration of coccoliths at well-constrained culture temperatures for marine temperature reconstructions. Clim. Past 20, 2081–2101. https://doi.org/10.5194/cp-20-2081-2024

Colosimo, A.B., Bralower, T.J., Zachos, J.C., 2005. Evidence for lysocline shoaling at the Paleocene/Eocene thermal maximum on Shatsky Rise, northwest Pacific, in: Proceedings of the Ocean Drilling Program: Scientific Results. Texas A & M University.

Cramer, B.S., Miller, K.G., Barrett, P.J., Wright, J.D., 2011. Late Cretaceous–Neogene trends in deep ocean temperature and continental ice volume: Reconciling records of benthic foraminiferal geochemistry (δ18O and Mg/Ca) with sea level history. J. Geophys. Res. Oceans 116. https://doi.org/10.1029/2011JC007255

Cummins, R.C., Finnegan, S., Fike, D.A., Eiler, J.M., Fischer, W.W., 2014. Carbonate clumped isotope constraints on Silurian ocean temperature and seawater δ18O. Geochim. Cosmochim. Acta 140, 241–258. https://doi.org/10.1016/j.gca.2014.05.024

Cusack, M., 2016. Biomineral electron backscatter diffraction for palaeontology. Palaeontology 59, 171–179. https://doi.org/10.1111/pala.12222

Defliese, W.F., Lohmann, K.C., 2015. Non-linear mixing effects on mass-47 CO2 clumped isotope thermometry: Patterns and implications. Rapid Commun. Mass Spectrom. 29, 901–909. https://doi.org/10.1002/rcm.7175

Dekens, P.S., Lea, D.W., Pak, D.K., Spero, H.J., 2002. Core top calibration of Mg/Ca in tropical foraminifera: Refining paleotemperature estimation. Geochem. Geophys. Geosystems 3, 1–29. https://doi.org/10.1029/2001GC000200

D'Hondt, S., Arthur, M., 1996. Late cretaceous oceans and the cool tropic paradox. Science 271. https://doi.org/10.1126/science.271.5257.1838

Drury, A.J., John, C.M., 2016. Exploring the potential of clumped isotope thermometry on coccolith-rich sediments as a sea surface temperature proxy. Geochem. Geophys. Geosystems 17, 4092–4104. https://doi.org/10.1002/2016GC006459

Dunkley Jones, T., Lunt, D.J., Schmidt, D.N., Ridgwell, A., Sluijs, A., Valdes, P.J., Maslin, M., 2013. Climate model and proxy data constraints on ocean warming across the Paleocene–Eocene Thermal Maximum. Earth-Sci. Rev. 125, 123–145. https://doi.org/10.1016/j.earscirev.2013.07.004

Gorski, C.A., Fantle, M.S., 2017. Stable mineral recrystallization in low temperature aqueous systems: A critical review. Geochim. Cosmochim. Acta 198, 439–465.

Gutjahr, M., Ridgwell, A., Sexton, P.F., Anagnostou, E., Pearson, P.N., Pälike, H., Norris, R.D., Thomas, E., Foster, G.L., 2017. Very large release of mostly volcanic carbon during the Palaeocene–Eocene Thermal Maximum. Nature 548, 573–577. https://doi.org/10.1038/nature23646

Herold, N., Buzan, J., Seton, M., Goldner, A., Green, J.A.M., Müller, R.D., Markwick, P., Huber, M., 2014. A suite of Early Eocene (~55 Ma) climate model boundary conditions. Geosci. Model Dev. Discuss. 7, 529–562. https://doi.org/10.5194/gmdd-7-529-2014

Hollis, C.J., Dunkley Jones, T., Anagnostou, E., Bijl, P.K., Cramwinckel, M.J., Cui, Y., Dickens, G.R., Edgar, K.M., Eley, Y., Evans, D., Foster, G.L., Frieling, J., Inglis, G.N., Kennedy, E.M., Kozdon, R., Lauretano, V., Lear, C.H., Littler, K., Meckler, N., Naafs, B.D.A., Pälike, H., Pancost, R.D., Pearson, P., Royer, D.L., Salzmann, U., Schubert, B., Seebeck, H., Sluijs, A., Speijer, R., Stassen, P., Tierney, J., Tripati, A., Wade, B., Westerhold, T., Witkowski, C., Zachos, J.C., Zhang, Y.G., Huber, M., Lunt, D.J., 2019. The DeepMIP contribution to PMIP4: methodologies for selection, compilation and analysis of latest Paleocene and early Eocene climate proxy data, incorporating version 0.1 of the DeepMIP database. https://doi.org/10.5194/gmd-2018-309

Huber, M., Caballero, R., 2011. The early Eocene equable climate problem revisited. Clim. Past 7, 603–633. https://doi.org/10.5194/cp-7-603-2011

Huber, M., Sloan, L.C., 2001. Heat transport, deep waters, and thermal gradients: Coupled simulation of an Eocene greenhouse climate. Geophys. Res. Lett. 28, 3481–3484. https://doi.org/10.1029/2001GL012943

Hupp, B.N., Kelly, D.C., Williams, J.W., 2022. Isotopic filtering reveals high sensitivity of planktic calcifiers to Paleocene–Eocene thermal maximum warming and acidification. Proc. Natl. Acad. Sci. 119, e2115561119. https://doi.org/10.1073/pnas.2115561119

John, C.M., Bowen, D., 2016. Community software for challenging isotope analysis: First applications of 'Easotope' to clumped isotopes. Rapid Commun. Mass Spectrom. 30, 2285–2300. https://doi.org/10.1002/rcm.7720

Katz, A., Bonifacie, M., Hermoso, M., Cartigny, P., Calmels, D., 2017. Laboratory-grown coccoliths exhibit no vital effect in clumped isotope (Δ47) composition on a range of geologically relevant temperatures. Geochim. Cosmochim. Acta 208, 335–353. https://doi.org/10.1016/j.gca.2017.02.025

Kelly, D.C., Bralower, T.J., Zachos, J.C., Silva, I.P., Thomas, E., 1996. Rapid diversification of planktonic foraminifera in the tropical Pacific (ODP Site 865) during the late Paleocene thermal maximum. Geology 24, 423–426. https://doi.org/10.1130/0091-7613(1996)024<0423:RDOPFI>2.3.CO;2

Kelly, D.C., Nielsen, T.M.J., Schellenberg, S.A., 2012. Carbonate saturation dynamics during the Paleocene–Eocene thermal maximum: Bathyal constraints from ODP sites 689 and 690 in the Weddell Sea (South Atlantic). Mar. Geol. 303–306, 75–86. https://doi.org/10.1016/j.margeo.2012.02.003

Kelly, D.C., Zachos, J.C., Bralower, T.J., Schellenberg, S.A., 2005. Enhanced terrestrial weathering/runoff and surface ocean carbonate production during the recovery stages of the Paleocene-Eocene thermal maximum. Paleoceanography 20. https://doi.org/10.1029/2005PA001163

Kiehl, J.T., Shields, C.A., 2013. Sensitivity of the Palaeocene–Eocene Thermal Maximum climate to cloud properties. Philos. Trans. R. Soc. Math. Phys. Eng. Sci. 371, 20130093. https://doi.org/10.1098/rsta.2013.0093

Kim, S.-T., O'Neil, J.R., 1997. Equilibrium and nonequilibrium oxygen isotope effects in synthetic carbonates. Geochim. Cosmochim. Acta 61, 3461–3475. https://doi.org/10.1016/S0016-7037(97)00169-5

Kozdon, R., Kelly, D.C., 2024. Hot Tropical Temperatures During the Paleocene-Eocene Thermal Maximum Revealed by Paired In Situ δ13C and Mg/Ca Measurements on

Individual Planktic Foraminifer Shells. Paleoceanogr. Paleoclimatology 39, e2023PA004834. https://doi.org/10.1029/2023PA004834

Kozdon, R., Kelly, D.C., Kita, N.T., Fournelle, J.H., Valley, J.W., 2011. Planktonic foraminiferal oxygen isotope analysis by ion microprobe technique suggests warm tropical sea surface temperatures during the Early Paleogene. Paleoceanography 26. https://doi.org/10.1029/2010PA002056

Kozdon, R., Kelly, D.C., Kitajima, K., Strickland, A., Fournelle, J.H., Valley, J.W., 2013. In situ δ18O and Mg/Ca analyses of diagenetic and planktic foraminiferal calcite preserved in a deep-sea record of the Paleocene-Eocene thermal maximum. Paleoceanography 28, 517–528. https://doi.org/10.1002/palo.20048

Kozdon, R., Kelly, D.C., Valley, J.W., 2018. Diagenetic Attenuation of Carbon Isotope Excursion Recorded by Planktic Foraminifers During the Paleocene-Eocene Thermal Maximum. Paleoceanogr. Paleoclimatology 33, 367–380. https://doi.org/10.1002/2017PA003314

Kozdon, R., Penman, D.E., Kelly, D.C., Zachos, J.C., Fournelle, J.H., Valley, J.W., 2020. Enhanced Poleward Flux of Atmospheric Moisture to the Weddell Sea Region (ODP Site 690) During the Paleocene-Eocene Thermal Maximum. Paleoceanogr. Paleoclimatology 35, e2019PA003811. https://doi.org/10.1029/2019PA003811

LeGrande, A.N., Schmidt, G.A., 2006. Global gridded data set of the oxygen isotopic composition in seawater. Geophys. Res. Lett. 33. https://doi.org/10.1029/2006GL026011

Leutert, T.J., Sexton, P.F., Tripati, A., Piasecki, A., Ho, S.L., Meckler, A.N., 2019. Sensitivity of clumped isotope temperatures in fossil benthic and planktic foraminifera to diagenetic alteration. Geochim. Cosmochim. Acta 257, 354–372. https://doi.org/10.1016/j.gca.2019.05.005

Lhomme, N., Clarke, G.K.C., Ritz, C., 2005. Global budget of water isotopes inferred from polar ice sheets. Geophys. Res. Lett. 32. https://doi.org/10.1029/2005GL023774

Lucarelli, J.K., Carroll, H.M., Ulrich, R.N., Elliott, B.M., Coplen, T.B., Eagle, R.A., Tripati, A., 2023. Equilibrated Gas and Carbonate Standard-Derived Dual (Δ47 and Δ48) Clumped Isotope Values. Geochem. Geophys. Geosystems 24, e2022GC010458. https://doi.org/10.1029/2022GC010458

Lunt, D.J., Bragg, F., Chan, W.-L., Hutchinson, D.K., Ladant, J.-B., Morozova, P., Niezgodzki, I., Steinig, S., Zhang, Z., Zhu, J., Abe-Ouchi, A., Anagnostou, E., de Boer, A.M., Coxall, H.K., Donnadieu, Y., Foster, G., Inglis, G.N., Knorr, G., Langebroek, P.M., Lear, C.H., Lohmann, G., Poulsen, C.J., Sepulchre, P., Tierney, J.E., Valdes, P.J., Volodin, E.M., Dunkley Jones, T., Hollis, C.J., Huber, M., Otto-Bliesner, B.L., 2021. DeepMIP: model intercomparison of early Eocene climatic optimum (EECO) large-scale climate features and comparison with proxy data. Clim. Past 17, 203–227. https://doi.org/10.5194/cp-17-203-2021

Lunt, D.J., Dunkley Jones, T., Heinemann, M., Huber, M., LeGrande, A., Winguth, A., Loptson, C., Marotzke, J., Roberts, C.D., Tindall, J., Valdes, P., Winguth, C., 2012. A model–data comparison for a multi-model ensemble of early Eocene atmosphere–ocean simulations: EoMIP. Clim. Past 8, 1717–1736. https://doi.org/10.5194/cp-8-1717-2012

Lunt, D.J., Huber, M., Anagnostou, E., Baatsen, M.L.J., Caballero, R., DeConto, R., Dijkstra, H.A., Donnadieu, Y., Evans, D., Feng, R., Foster, G.L., Gasson, E., von der Heydt, A.S., Hollis, C.J., Inglis, G.N., Jones, S.M., Kiehl, J., Kirtland Turner, S., Korty, R.L., Kozdon, R., Krishnan, S., Ladant, J.-B., Langebroek, P., Lear, C.H., LeGrande, A.N., Littler, K., Markwick, P., Otto-Bliesner, B., Pearson, P., Poulsen, C.J., Salzmann, U., Shields, C., Snell, K., Stärz, M., Super, J., Tabor, C., Tierney, J.E., Tourte, G.J.L., Tripati, A.,

Upchurch, G.R., Wade, B.S., Wing, S.L., Winguth, A.M.E., Wright, N.M., Zachos, J.C., Zeebe, R.E., 2017. The DeepMIP contribution to PMIP4: experimental design for model simulations of the EECO, PETM, and pre-PETM (version 1.0). Geosci. Model Dev. 10, 889–901. https://doi.org/10.5194/gmd-10-889-2017

Meckler, A.N., Sexton, P.F., Piasecki, A.M., Leutert, T.J., Marquardt, J., Ziegler, M., Agterhuis, T., Lourens, L.J., Rae, J.W.B., Barnet, J., Tripati, A., Bernasconi, S.M., 2022. Cenozoic evolution of deep ocean temperature from clumped isotope thermometry. Science 377, 86–90. https://doi.org/10.1126/science.abk0604

Meinicke, N., Ho, S.L., Hannisdal, B., Nürnberg, D., Tripati, A., Schiebel, R., Meckler, A.N., 2020. A robust calibration of the clumped isotopes to temperature relationship for foraminifers. Geochim. Cosmochim. Acta 270, 160–183. https://doi.org/10.1016/j.gca.2019.11.022

Pabich, S., Vollmer, C., Gussone, N., 2020. Investigating crystal orientation patterns of foraminiferal tests by electron backscatter diffraction analysis. Eur. J. Mineral. 32, 613–622. https://doi.org/10.5194/ejm-32-613-2020

Pearson, P.N., Burgess, C.E., 2008. Foraminifer test preservation and diagenesis: comparison of high latitude Eocene sites. Geol. Soc. Lond. Spec. Publ. 303, 59–72. https://doi.org/10.1144/SP303.5

Penman, D.E., Hönisch, B., Zeebe, R.E., Thomas, E., Zachos, J.C., 2014. Rapid and sustained surface ocean acidification during the Paleocene-Eocene Thermal Maximum. Paleoceanography 29, 357–369. https://doi.org/10.1002/2014PA002621

Penman, D.E., Turner, S.K., Sexton, P.F., Norris, R.D., Dickson, A.J., Boulila, S., Ridgwell, A., Zeebe, R.E., Zachos, J.C., Cameron, A., Westerhold, T., Röhl, U., 2016. An abyssal

carbonate compensation depth overshoot in the aftermath of the Palaeocene–Eocene Thermal Maximum. Nat. Geosci. 9, 575–580. https://doi.org/10.1038/ngeo2757

Pérez-Huerta, A., Cusack, M., 2009. Optimizing Electron Backscatter Diffraction of Carbonate Biominerals—Resin Type and Carbon Coating. Microsc. Microanal. 15, 197–203. https://doi.org/10.1017/S1431927609090370

Pérez-Huerta, A., Dauphin, Y., Cuif, J.P., Cusack, M., 2011. High resolution electron backscatter diffraction (EBSD) data from calcite biominerals in recent gastropod shells. Micron 42, 246–251. https://doi.org/10.1016/j.micron.2010.11.003

Procter, F.A., Piazolo, S., John, E.H., Walshaw, R., Pearson, P.N., Lear, C.H., Aze, T., 2024. Electron backscatter diffraction analysis unveils foraminiferal calcite microstructure and processes of diagenetic alteration. Biogeosciences 21, 1213–1233. https://doi.org/10.5194/bg-21-1213-2024

R Core Team, 2022. R: A language and environment for statistical computing.

Rampino, M.R., 2013. Peraluminous igneous rocks as an indicator of thermogenic methane release from the North Atlantic Volcanic Province at the time of the Paleocene–Eocene Thermal Maximum (PETM). Bull. Volcanol. 75, 678. https://doi.org/10.1007/s00445-012-0678-x

Regenberg, M., Regenberg, A., Garbe-Schönberg, D., Lea, D.W., 2014. Global dissolution effects on planktonic foraminiferal Mg/Ca ratios controlled by the calcite-saturation state of bottom waters. Paleoceanography 29, 127–142. https://doi.org/10.1002/2013PA002492

Roberts, C.D., LeGrande, A.N., Tripati, A.K., 2009. Climate sensitivity to Arctic seaway restriction during the early Paleogene. Earth Planet. Sci. Lett. 286, 576–585. https://doi.org/10.1016/j.epsl.2009.07.026

Sagoo, N., Valdes, P., Flecker, R., Gregoire, L.J., 2013. The Early Eocene equable climate problem: can perturbations of climate model parameters identify possible solutions? Philos. Trans. R. Soc. Math. Phys. Eng. Sci. 371, 20130123. https://doi.org/10.1098/rsta.2013.0123

Saunders, A.D., 2016. Two LIPs and two Earth-system crises: the impact of the North Atlantic Igneous Province and the Siberian Traps on the Earth-surface carbon cycle. Geol. Mag. 153, 201–222. https://doi.org/10.1017/S0016756815000175

Schmidt, D.N., Lazarus, D., Young, J.R., Kucera, M., 2006. Biogeography and evolution of body size in marine plankton. Earth-Sci. Rev. 78, 239–266. https://doi.org/10.1016/j.earscirev.2006.05.004

Schrag, D.P., DePaolo, D.J., Richter, F.M., 1995. Reconstructing past sea surface temperatures: Correcting for diagenesis of bulk marine carbonate. Geochim. Cosmochim. Acta 59, 2265–2278. https://doi.org/10.1016/0016-7037(95)00105-9

Seibold, E., Berger, W.H., 2017. The sea floor: an introduction to marine geology. Springer.

Sexton, P.F., Wilson, P.A., Pearson, P.N., 2006. Microstructural and geochemical perspectives on planktic foraminiferal preservation: "Glassy" versus "Frosty." Geochem. Geophys. Geosystems 7. https://doi.org/10.1029/2006GC001291

Spero, H.J., Bijma, J., Lea, D.W., Bemis, B.E., 1997. Effect of seawater carbonate concentration on foraminiferal carbon and oxygen isotopes. Nature 390, 497–500. https://doi.org/10.1038/37333

Staudigel, P.T., John, E.H., Buse, B., Pearson, P.N., Lear, C.H., 2022. Apparent preservation of primary foraminiferal Mg/Ca ratios and Mg-banding in recrystallized foraminifera. Geology 50, 760–764. https://doi.org/10.1130/G49984.1

Steinig, S., Abe-Ouchi, A., de Boer, A.M., Chan, W.-L., Donnadieu, Y., Hutchinson, D.K., Knorr, G., Ladant, J.-B., Morozova, P., Niezgodzki, I., Poulsen, C.J., Volodin, E.M., Zhang, Z., Zhu, J., Evans, D., Inglis, G.N., Meckler, A.N., Lunt, D.J., 2024. DeepMIP-Eocene-p1: multi-model dataset and interactive web application for Eocene climate research. Sci. Data 11, 970. https://doi.org/10.1038/s41597-024-03773-4

Stoll, H.M., 2005. Limited range of interspecific vital effects in coccolith stable isotopic records during the Paleocene-Eocene thermal maximum. Paleoceanography 20. https://doi.org/10.1029/2004PA001046

Stolper, D.A., Eiler, J.M., Higgins, J.A., 2018. Modeling the effects of diagenesis on carbonate clumped-isotope values in deep- and shallow-water settings. Geochim. Cosmochim. Acta 227, 264–291. https://doi.org/10.1016/j.gca.2018.01.037

Subhas, A.V., McCorkle, D.C., Quizon, A., McNichol, A.P., Long, M.H., 2019. Selective Preservation of Coccolith Calcite in Ontong-Java Plateau Sediments. Paleoceanogr. Paleoclimatology 34, 2141–2157. https://doi.org/10.1029/2019PA003731

Thomas, D.J., Bralower, T.J., Zachos, J.C., 1999. New evidence for subtropical warming during the Late Paleocene thermal maximum: Stable isotopes from Deep Sea Drilling Project Site 527, Walvis Ridge. Paleoceanography 14, 561–570. https://doi.org/10.1029/1999PA900031

Tierney, J.E., Zhu, J., Li, M., Ridgwell, A., Hakim, G.J., Poulsen, C.J., Whiteford, R.D.M., Rae, J.W.B., Kump, L.R., 2022. Spatial patterns of climate change across the Paleocene–Eocene Thermal Maximum. Proc. Natl. Acad. Sci. 119, e2205326119. https://doi.org/10.1073/pnas.2205326119

Tindall, J., Flecker, R., Valdes, P., Schmidt, D.N., Markwick, P., Harris, J., 2010. Modelling the oxygen isotope distribution of ancient seawater using a coupled ocean–atmosphere GCM:

Implications for reconstructing early Eocene climate. Earth Planet. Sci. Lett. 292, 265–273. https://doi.org/10.1016/j.epsl.2009.12.049

Tripati, A.K., Delaney, M.L., Zachos, J.C., Anderson, L.D., Kelly, D.C., Elderfield, H., 2003. Tropical sea-surface temperature reconstruction for the early Paleogene using Mg/Ca ratios of planktonic foraminifera. Paleoceanography 18. https://doi.org/10.1029/2003PA000937

Tripati, A.K., Eagle, R.A., Thiagarajan, N., Gagnon, A.C., Bauch, H., Halloran, P.R., Eiler, J.M., 2010. 13C–18O isotope signatures and 'clumped isotope' thermometry in foraminifera and coccoliths. Geochim. Cosmochim. Acta 74, 5697–5717. https://doi.org/10.1016/j.gca.2010.07.006

Tripati, A.K., Elderfield, H., 2004. Abrupt hydrographic changes in the equatorial Pacific and subtropical Atlantic from foraminiferal Mg/Ca indicate greenhouse origin for the thermal maximum at the Paleocene-Eocene Boundary: Abrupt Hydrographic Changes. Geochem. Geophys. Geosystems 5, n/a-n/a. https://doi.org/10.1029/2003GC000631

Uchikawa, J., Zeebe, R.E., 2010. Examining possible effects of seawater pH decline on foraminiferal stable isotopes during the Paleocene-Eocene Thermal Maximum. Paleoceanography 25. https://doi.org/10.1029/2009PA001864

Upadhyay, D., Lucarelli, J., Arnold, A., Flores, R., Bricker, H., Ulrich, R.N., Jesmok, G., Santi, L., Defliese, W., Eagle, R.A., Carroll, H.M., Bateman, J.B., Petryshyn, V., Loyd, S.J., Tang, J., Priyadarshi, A., Elliott, B., Tripati, A., 2021. Carbonate clumped isotope analysis (Δ47) of 21 carbonate standards determined via gas-source isotope-ratio mass spectrometry on four instrumental configurations using carbonate-based standardization and multiyear data sets. Rapid Commun. Mass Spectrom. 35, e9143. https://doi.org/10.1002/rcm.9143

Van Heuven, S., Pierrot, D., Rae, J.W.B., Lewis, E., Wallace, D.W.R., 2011. CO2SYS v 1.1, MATLAB program developed for CO2 system calculations.

Westerhold, T., Marwan, N., Drury, A.J., Liebrand, D., Agnini, C., Anagnostou, E., Barnet, J.S.K., Bohaty, S.M., De Vleeschouwer, D., Florindo, F., Frederichs, T., Hodell, D.A., Holbourn, A.E., Kroon, D., Lauretano, V., Littler, K., Lourens, L.J., Lyle, M., Pälike, H., Röhl, U., Tian, J., Wilkens, R.H., Wilson, P.A., Zachos, J.C., 2020. An astronomically dated record of Earth's climate and its predictability over the last 66 million years. Science 369, 1383–1387. https://doi.org/10.1126/science.aba6853

Zachos, J., Pagani, M., Sloan, L., Thomas, E., Billups, K., 2001. Trends, Rhythms, and Aberrations in Global Climate 65 Ma to Present. Science 292, 686–693. https://doi.org/10.1126/science.1059412

Zachos, J., Röhl, U., Schellenberg, S.A., Sluijs, A., Hodell, D.A., Kelly, D.C., Thomas, E., Nicolo, M., Raffi, I., Lourens, L.J., McCarren, H., Kroon, D., 2005. Rapid Acidification of the Ocean During the Paleocene-Eocene Thermal Maximum. Science 308, 1611–1615. https://doi.org/10.1126/science.1109004

Zachos, J., Wara, M.W., Bohaty, S., Delaney, M.L., Petrizzo, M.R., Brill, A., Bralower, T.J., Silva, I.P., 2003. A Transient Rise in Tropical Sea Surface Temperature During the Paleocene-Eocene Thermal Maximum. Science 302, 1551–1554. https://doi.org/10.1126/science.1090110

Zeebe, R.E., 1999. An explanation of the effect of seawater carbonate concentration on foraminiferal oxygen isotopes. Geochim. Cosmochim. Acta 63, 2001–2007. https://doi.org/10.1016/S0016-7037(99)00091-5

Zeebe, R.E., Zachos, J.C., 2013. Long-term legacy of massive carbon input to the Earth system: Anthropocene versus Eocene. Philos. Trans. R. Soc. Math. Phys. Eng. Sci. 371, 20120006. https://doi.org/10.1098/rsta.2012.0006

Zeebe, R.E., Zachos, J.C., Dickens, G.R., 2009. Carbon dioxide forcing alone insufficient to explain Palaeocene–Eocene Thermal Maximum warming. Nat. Geosci. 2, 576–580. https://doi.org/10.1038/ngeo578

Zhu, J., Poulsen, C.J., Tierney, J.E., 2019. Simulation of Eocene extreme warmth and high climate sensitivity through cloud feedbacks. Sci. Adv. 5, eaax1874. https://doi.org/10.1126/sciadv.aax1874

SUMMARY

In Chapter 1, we report new measurements and a compilation of clumped isotope data for 260 samples of planktonic and benthic foraminifera, and 118 synthetic calcite measurements, in the I-CDES reference frame. We used this data to conduct a meta-analysis of foraminiferal clumped isotope signatures and investigate for non-thermal effects. We created a new regression based on the foraminiferal calcite measurements and found that foraminiferal calcite signatures are not significantly different from synthetic calcite. We did, however, find evidence for a possible dissolution effect on planktic foraminifera, and report a weak carbonate ion effect in benthic foraminifera. We applied our new regressions to published Cenozoic datasets. We report evidence for cooler temperatures and seawater oxygen isotope values that are more plausible given independent proxy constraints.

In Chapter 2, we quantified a dissolution effect on clumped isotopes in foraminifera by examining samples of six species from sediment cores taken at different water depths along the Ontong Java Plateau, and by conducting dissolution experiments. We found that clumped isotope values generally increased below the carbonate saturation horizon with a significant difference in three of the species studied: *G. siphonifera*, *P. obliquiloculata*, and *G. tumida.* From these species, we calculated a normalized pooled slope -0.0006 ‰ / μmol/kg $\Delta[CO_3^{2-}]$. These observations facilitate the quantification of impacts of dissolution on clumped isotope-based paleo-records. The clumped isotope correlation with increased dissolution is hypothesized to be related to the higher dissolution susceptibility of poorly crystallized high-Mg calcite.

In Chapter 3, we applied our findings to sediments from Ocean Drilling Program Site 1263 located in the South Atlantic to reconstruct temperature and seawater chemistry over the Paleocene-Eocene Thermal Maximum (PETM). We observed reductions in Δ_{47} corresponding to temperature increase in both foraminiferal calcites and fine fraction (primarily coccolith calcite)

archives. Absolute temperatures are lower than those predicted by Mg/Ca and higher than foraminiferal $\delta^{18}O$ estimates. Our results suggest that gradients in $\delta^{18}O_{sw}$ may have changed, and/or that published $\delta^{18}O$ reconstructions are biased from changes in seawater pH effect.

In Chapter 4, we expanded our reconstructions of the PETM and Early Eocene by applying the clumped isotope paleothermometer to five Ocean Drilling Program Sites globally. With the exceptions of Sites 690 and 1263 (Chapter 3), the Δ_{47} records for other sites show limited amounts of warming across the PETM, possibly due to dissolution. We then applied various corrections for known effects such as offsets between foraminiferal and coccolith clumped isotope values, recrystallization, and the dissolution effect from Chapter 2. These corrections increase temperatures compared to the initial reconstructed values especially over the PETM where higher rates of dissolution occurred. We compared the final corrected values to temperatures from other proxy archives and models to interpret implications of the clumped isotope predicted temperatures. Overall, the clumped isotope reconstructed temperatures indicate a shallow temperature gradient from low to high latitudes, though exact interpretations of climate sensitivities from this proxy will depend on better constraints for the secondary effects of recrystallization, dissolution, and mixing at each site.